Advancing Multi-Messenger Astrophysics and Dark Matter Searches with XENONnT and the Top SiPM Array of Xenoscope

Dissertation
zur
Erlangung der naturwissenschaftlichen Doktorwürde
(Dr. sc. nat.)

vorgelegt der
Mathematisch-naturwissenschaftlichen Fakultät
der
Universität Zürich

von
Ricardo José Mota Peres
aus
Portugal

Promotionskommission

Prof. Dr. Laura Baudis (Vorsitz)
Prof. Dr. Ben Kilminster
Dr. Michelle Galloway

Zürich, 2023

Abstract

Numerous astrophysical observations point to the existence of a stable, non-luminous, non-baryonic, and not yet identified kind of matter: dark matter. The elusive dark matter corresponds to $\sim$84 % of the total matter content of the Universe. Among the particle candidates of dark matter, the weakly interacting massive particle (WIMP) is one of the most viable options.

XENONnT is the fourth detector of the XENON dark matter project and a leading experiment in the direct detection of dark matter. The first part of this thesis covers several topics related to this detector and its first science run. The description of the XENONnT facility is presented, followed by the Boundary Element Method 3D electric field simulations of the time projection chamber (TPC) in its nominal configuration. The first science run of XENONnT explored both the low-energy electron recoil (ER) and low-energy nuclear recoil (NR) regions. An event selection criterion for accidental coincidence events based on the charge signal properties was developed in the context of this work and reported in conjunction with the main science results. No evidence was found of an excess of low-energy ER events, as previously seen in XENON1T. The observed ER background rate was 15.8 events/$(t \cdot y \cdot keV)$, the lowest ever achieved in liquid xenon (LXe) time projection chambers (TPCs). No significant excess was found in the WIMP search data, setting new upper limits on the cross-section for WIMP-nucleon interactions, with a minimum of 2.58×10^{-47} cm^2 for a WIMP mass of 28 GeV/c^2.

The capacity of the facility as an observatory for astrophysical neutrinos from core-collapse supernovae (SN) and their direct application in multi-messenger astrophysics is presented next. In current condi-

tions, XENONnT is able to detect an average of 137 ± 5 events from a SN progenitor of 27 $M_\odot$ at 10 kpc, approximately ten times above background level. It may observe SNe events up to $\sim$30 kpc with 3 σ significance. Next-generation LXe TPCs will be able to double XENONnT's reach by profiting from larger active target masses, considering the background conditions can be maintained. If the rate of few-electron events, corresponding to the dominant background in the region of interest, can be suppressed by an order of magnitude, the possible reach is increased four-fold, up to $\sim$120 kpc for a 27 $M_\odot$ progenitor.

In the second part of this thesis, the focus is a future dark matter detector, DARWIN. Xenoscope, a full-height vertical demonstrator for DARWIN at the University of Zurich, is described. The first science results of Xenoscope regarding electron transport properties measured with a purity monitor are introduced. This is followed by a description of the top silicon photomultiplier (SiPM) array that instruments the liquid xenon column of the detector in its upgrade to a dual-phase TPC. A characterisation campaign of all the SiPM units used in the top array was done and a summed readout solution of several units in one signal channel was tested and benchmarked. The results obtained explore the different properties of interest of SiPMs in rare event searches, such as gain, dark count rate, cross-talk probability, and single photoelectron resolution. The study characterises not only a single VUV4 MPPC unit from Hamamatsu, but a large set of sensors and their variability. The array was installed and the first successful test results in air are reported. Lastly, a toy-Monte Carlo simulation framework developed to study the expected signals of the top array is also described. The framework will inform future design choices with respect to tiling and granularity of the SiPMs and be used to study electron diffusion properties, in particular electron transverse diffusion.

Preface

This thesis describes my work within the context of the XENON and DARWIN dark matter projects during my doctoral studies in the group of Prof. Dr. Laura Baudis. For completeness, this work not only presents my specific contributions but also includes the work from the collaborations as a whole. My specific contributions in each chapter are as follows:

- Chapter 3, *3D electric field simulations of the XENONnT TPC*: All the geometry, simulations and analysis are my own work. The BEM simulation software was adapted by Dr. J. Wulf [1] from [2] and further developed by me in the context of this thesis.
- Chapter 4, *Analysis and results from the first science run of XENONnT*: The low-energy ER and WIMP searches were the main results from XENONnT first science campaign, involving efforts from the whole collaboration, from design, construction, cleaning, assembling, commissioning, ensuring data taking, and analysis. Apart from smaller roles in all these different steps, my direct contribution reported here is the S2 Width cut (Section 4.2.4), developed in partnership with Dr. V. D'Andrea.
- Chapter 5, *Multi-messenger astronomy in XENONnT*: The work described in this chapter is from a core of people invested in expanding the XENONnT science program to supernova neutrinos and, in particular, to make XENONnT the first dark matter-based experiment to actively contribute to SNEWS. My contributions to this work are on the simulations shown in Section 5.3.2 (in collaboration with M. Kara), the sensitive study shown in Section 5.3.3, the absolute timing correction for XENONnT shown in Section 5.4 (in collaboration with Dr. A. Mollinario), and early development of the active trigger system described in Section 5.4.2. The analysis cuts described in Section 5.3.2 are the work of Dr. A. Baxter and the work on the communication between XENONnT and SNEWS, briefly described in Section 5.4.2, are the work of Dr. A. Baxter and M. Kara.

- Chapter 6, *Xenoscope, a full-height DARWIN demonstrator*: The assembly, operation, and analysis of the purity monitor setup described in Section 6.3.1 was led by Dr. Y. Biondi, with contributions from myself and the rest of the Xenoscope team. My contributions were of particular importance to the single-wire cabling of the purity monitor setup, and to filling, operating, and recuperating the xenon from the facility in the purity monitor runs. The electron lifetime fit is the work of Dr. F. Girard.
- Chapter 7, *The top SiPM array of Xenoscope*: The main design of the SiPM array is the work of N. McFadden, to which I have contributed with minor modifications. Everything else described is my own work. I would like to credit Dr. F. Girard for introducing and helping me with the DAQ system assembly and commissioning, as well as planning and machining the PTFE cover of the SiPM array with me.

Contents

À Leonor,
Aos meus pais,
Aos meus avós,

O Universo é feito essencialmente de coisa nenhuma.
Intervalos, distâncias, buracos, porosidade etérea.
Espaço vazio, em suma.
O resto, é a matéria.
Daí, que este arrepio,
este chamá lo e tê-lo, erguê-lo e defrontá-lo,
esta fresta de nada aberta no vazio,
deve ser um intervalo.

António Gedião, *Máquina do Tempo*

Chapter 1.

The search for dark matter

Over the millennia of humankind, the stars and the Universe have been at the centre of astonishing accomplishments in understanding the mechanisms of Nature. Yet, when looking up into the night sky, only a small percentage of all the observed matter is known. The large majority, unknown, is dark matter (DM). Evidence for the existence of a stable, non-luminous, non-baryonic, and massive matter component in the Universe has been around for almost a century. In current understanding, baryonic matter accounts for 5.0 % of the total energy content of the Universe, DM for 26.5 %, and dark energy, responsible for the accelerating expansion of the Universe, for the remaining 68.5 % [3]. As a long-standing mystery in particle physics and cosmology, several particle and non-particle candidates have been introduced to explain the presence of DM. Although none of the particles in the Standard Model of particle physics (SM) is considered a viable dark matter candidate, a large set of hypotheses have been presented in beyond the Standard Model (BSM) physics.

In this chapter, the main evidence supporting the existence of dark matter is reported in Section 1.1, followed by an overview of potential dark matter candidates, mainly focusing on weakly interacting massive particles (WIMPs), in Section 1.2. Section 1.3 presents an overview of dark matter detection methods, in particular direct detection, and the current status of the field.

1.1. Evidence for dark matter

Evidence for the existence of dark matter has been reported since the beginning of the 20^{th} century [4–7]. In 1933, by studying the Coma cluster, the Swiss-American

astronomer Fritz Zwicky determined the velocity dispersion of individual galaxies in the galaxy cluster. His observations could not be explained solely by the visible matter content of the galaxies [8], leading him to coin the term "dunkle Materie" for the missing mass.

In current studies, the effect of DM in galaxy clusters is studied by comparing the distribution of baryonic mass with the observed total mass. The baryonic matter is detected by electromagnetic telescopes, typically from X-rays emitted from hot intracluster gas [9], while the total matter mass can be determined by gravitational lensing [10]. A striking example, shown in Figure 1.1a, is the 1E 0657-558 cluster merger [11]. From two colliding galaxy clusters, a region of hot gas, detectable by X-rays, slows down considerably due to electromagnetic interactions. Although the gas represents most of the baryonic matter of the cluster pair, gravitational lensing surveys identify a large portion of the total mass in two separated regions, coincident with the location of the galaxies, which did not collide considerably (and do not account for enough baryonic mass to explain the effect). Other examples of the described effect can by found in [12–14].

At the galactic scale, evidence of the existence of DM arises from the study of the rotation curves, pioneered in the 1970s [15, 16]. As predicted by Newtonian mechanics and Kepler laws, the rotational speed, $v(r)$, of stars at the distance r from the galaxy centre, described by their matter distribution $M(r)$, is given by:

$$v(r) = \sqrt{\frac{GM(r)}{r}}\,, \tag{1.1}$$

where G is the gravitational constant. It follows that the expected rotational velocity falls proportional to $1/\sqrt{r}$. However, the rotation curves display a flat behaviour instead of a decrease in rotational velocity, as shown in Figure 1.1b. These observations suggest the existence of a DM component with a density proportional to $1/r^2$. Following the initial observations, other examples were identified in subsequent studies [17].

Further resounding evidence for the existence of dark matter emerges at the cosmological and non-local scales through the interpretation of the Cosmic Microwave Background (CMB). Discovered in 1965 [19], the CMB is the relic electromagnetic radiation emitted of the recombination phase after the Big Band. At this phase, where the Universe had cooled down to a temperature of around 3000 K and free electrons and protons could combine to form neutral atoms, photons were able to propagate

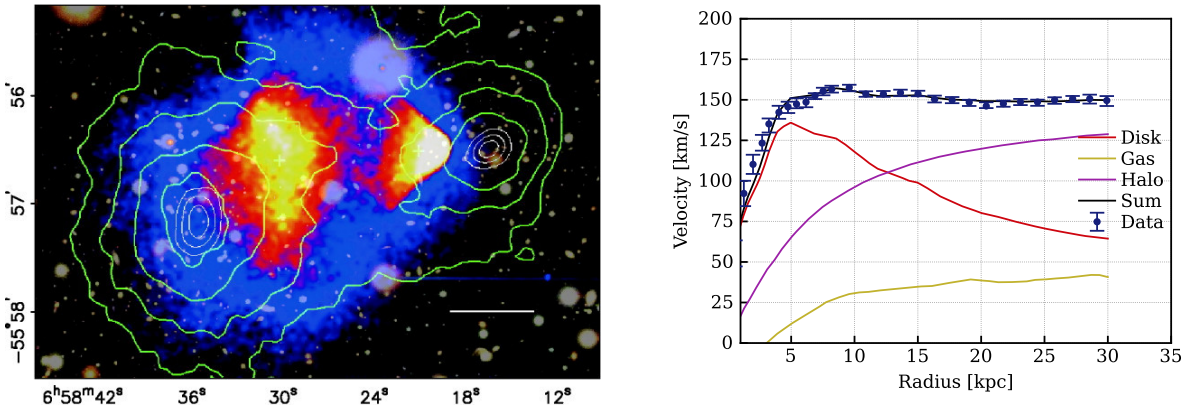

Figure 1.1.: (a) The cluster 1E 0657-558 with visible (semi-transparent, cool X-rays (in blue), hot X-rays (in red). Shown in green contours are the weak-lensing outer contour levels. Figure adapted from [11]**(b)** Rotational velocity distribution curve of the NGC 3198 galaxy as a function of the distance to the galactic centre. The figure shows the contributions from the disk (dashed line), the gas (dotted line), and the DM halo (dot-dashed line), as well as their sum (solid line). Figure from [18].

through the matter, previously hot plasma. The light has been travelling through the Universe ever since. Currently redshifted due to the expansion of the Universe, the CMB can be observed in the microwave region of the electromagnetic spectrum as if emitted by a black body with a temperature of $(2.7255 \pm 0.0006)\,\mathrm{K}$ [20]. The CMB temperature shows anisotropies only on the order of $\delta T/T \approx 10^{-5}$ [21] that can be used to study matter density at the time of recombination and explore the process of formation of large-scale structures in the Universe. Moreover, the CMB is of particular interest because it provides quantitative constraints and expectations on the abundance and density of, at the same time, baryonic matter, dark matter, and dark energy [22,23].

The latest measurements of the anisotropies of the CMB by satellite missions such as WMAP and Planck [3,25–27] are well explained by the six-parameter Λ cold dark matter (ΛCDM) model[1]. Figure 1.2 shows the CMB temperature power spectrum, where particularly the third peak relates to the abundance of DM. Measurements from [3] indicate a dark matter relic density of $\Omega_c h^2 = 0.120 \pm 0.001$, where $h = H_0/100\,\mathrm{km\,s^{-1}\,Mpc^{-1}}$ is the reduced Hubble constant, which is $\sim$5.4 times larger than the baryonic matter density, $\Omega_b h^2 = 0.0224 \pm 0.0001$.

[1] "Λ" refers to dark energy and "cold" specifies that the DM has non-relativistic speeds at the time of decoupling.

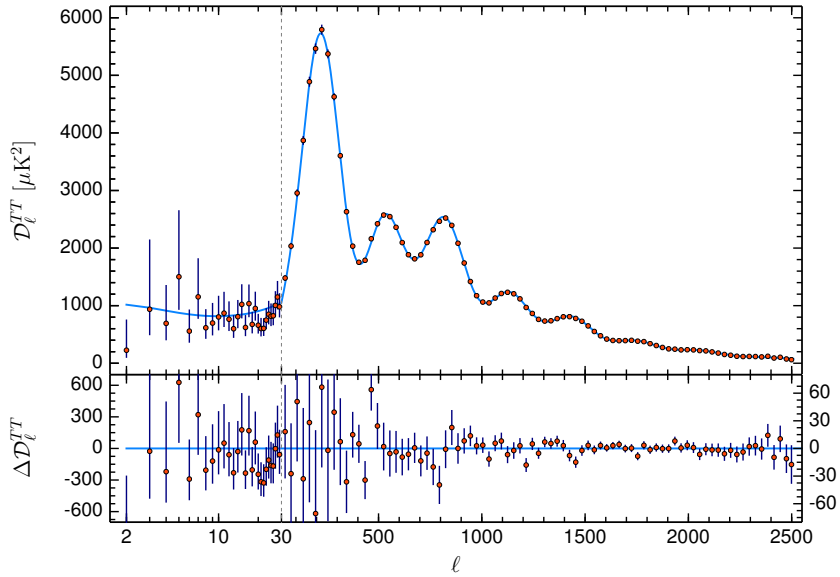

Figure 1.2.: The CMB temperature power spectrum as a function of the angular scale. Figure from [24].

1.2. Dark matter candidates

The compelling case for the existence of dark matter leads to the natural question of its composition. The candidate options are vast, requiring or less extensions to the current SM [28, 29]. From the set of evidence presented, several basic properties of dark matter can be outlined:

- DM must be massive and interact via the gravitational force;
- DM must be neutral or have a very small electric charge to avoid cooling by radiating energy electromagnetically;
- DM must be non-relativistic at the time of decoupling in order to explain the formation of large-scale structures [30];
- DM must be stable or with a lifetime considerably longer than the age of the Universe, with a current lower bound at 160 Gyr [31];

1.2.1. The Standard Model of particle physics

The Standard Model of particle physics is a very successful theory of modern physics describing elementary particles and their interactions. Developed in the early 1970s, it

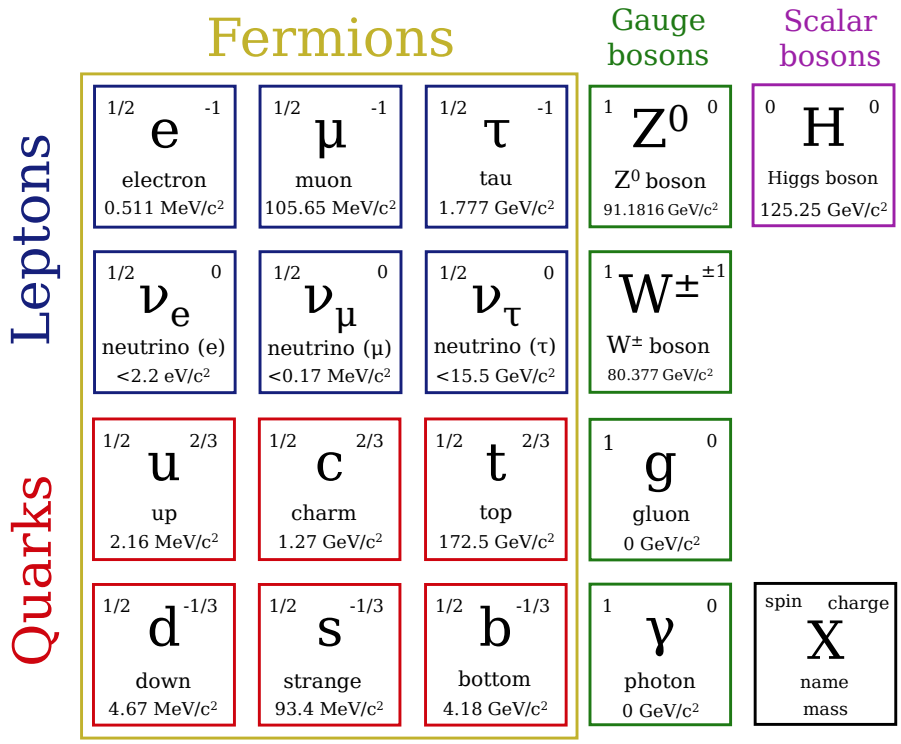

Figure 1.3.: The particles of the Standard Model of particle physics. Values on particle properties from [36].

has explained most of the observed experimental results in the field, and predicted the existence of the top quark, tau neutrino, and Higgs boson before they were discovered in 1995 [32], 2000 [33], and 2012 [34, 35], respectively. A schematic view of the SM constituent particles is shown in Figure 1.3.

In the SM, there are two types of elementary particles: fermions and bosons [37]. Fermions have spin $s = \frac{1}{2}$, and are further classified into six leptons and six quarks. The leptons are: the electron, e^-, the muon, μ^-, the τ, and their respective neutrinos, ν_e, ν_μ, and ν_τ. The former three have charge $Q = -1$ (in units of elementary charge, e), while their neutrinos are neutral particles. As for the quarks, these are: up, u, down, d, charm, c, strange, s, top, t, and bottom, b. Their charges are the fractional values $Q = \frac{2}{3}$ for u, c, and t, and $Q = -\frac{1}{3}$ for d, s, and b. All the fermions have an analogous anti-particles with opposite charge. In the SM, unlike all the other fermions, the neutrinos are massless particles. The discovery of neutrino oscillations at the beginning of the 21st century [38, 39] categorically proves that at least two of the three neutrinos have a quantifiable mass, albeit yet undetermined. The current most sensitive measurement sets the upper limit for the absolute mass scale of neutrinos at m_ν <1.1 eV [40].

Bosons are divided into the gauge bosons with $s = 1$ and the scalar boson with $s = 0$. The gauge bosons mediate the interactions between particles: the photon, γ, is exchanged in electromagnetic interactions, the gluons, g, are exchanged in strong interactions between quarks, and the bosons $W^{\pm}$ and Z are exchanged in weak interactions. The only scalar boson is the Higgs boson, required to explain the massive nature of the weak gauge bosons and fermions [37].

For all its correct predictions and overall success, the SM has several problems motivating physics BSM. The hierarchy problem questions why the mass of the Higgs boson, $(125.25 \pm 0.17)\,\mathrm{GeV/c^2}$, is so small in comparison to the Planck mass, $\sim 1.22 \times 10^{19}\,\mathrm{GeV/c^2}$. Such a difference is only explained by terms almost perfectly cancelling out in various loop-level corrections without clear reason. This problem highly motivates dark matter candidates such as WIMPs and superWIMPs. The strong charge-conjugation parity (CP) symmetry problem is another "fine-tuning" issue of the SM. While CP violation is observed in weak interactions and is allowed in strong interactions, it has not been observed in the latter. While this is possible within the SM, it requires that the coupling angle parameter of the strong interactions is extremely small. The strong CP problem motivates axions as dark matter candidates. A last problem of the SM of relevance to dark matter is the neutrino mass problem. In the SM, fermion masses arise in quantum field theory by coupling left- and right-handed fields together, but no right-handed neutrino fields are observed, and, hence, neutrinos are massless. Since the discovery of neutrino oscillations [38,39], at least two of the three neutrinos must be massive, contradicting the prediction of the SM. This provides evidence of the incompleteness of the SM and motivates the keV-scale sterile neutrino as a dark matter candidate [41].

In the end, no particle in the SM is a suitable candidate to make up all of the needed DM. As most of the matter particles decay with shorter lifetimes than the age of the Universe, only the electron, the up and down quarks, and the three neutrinos could be considered. Electrons could contribute to dark matter density if bound to protons, but protons are accounted for in the baryonic energy density, Ω_b, which is too small to explain observations. Neutrinos, on the other hand, are simply too light to account for a significant part of the expected dark matter [42].

1.2.2. The WIMP

The classification of weakly interacting massive particle refers not to one particle in particular but to a set of particle candidates with masses between $\mathcal{O}(1)$ GeV/c^2 and $\mathcal{O}(100)$ TeV/c^2 [43]. Example of candidate particles considered as WIMPs are the lightest supersymmetric particle in supersymmetric theories (commonly, the neutralino) [44, 45] or the lightest Kaluza-Klein particle in theories with extra spacetime dimensions [46].

WIMPs exist as thermal relics of the Big Bang, resulting from the freeze-out mechanism [47]. Right after the Big Bang, WIMPs and standard matter were in thermal equilibrium, as the annihilation and production rates cancelled each other out. As the thermal energy of the Universe, $k_B T$, decreased below the DM rest mass, $m_\chi c^2$, the annihilation of WIMPs was preferred over their creation, leading to an exponential decrease in the number of dark matter particles proportional to $e^{-m_\chi/T}$. If only the described process is taken into consideration, the DM density would progressively diminish until there is no dark matter remaining. However, due to the expansion of the Universe, the dark matter particles become so diluted that their probably of interaction progressively decreases. By the effect of freeze-out, the number of DM particles will asymptotically approach their relic density. The effect is shown as a function of time, or the temperature of the Universe, in Figure 1.4. The DM relic density can be expressed as a fit of its cross-section [28, 48]:

$$\Omega_\chi \approx \frac{x_f T_0^3}{\rho_c M_{PI}} < \sigma_A v >^{-1} , \tag{1.2}$$

where the subscripts f and 0 denote the time at the moment of freeze out and at present day, respectively, $x_f = T_f/m_\chi \sim 1/25$ is the freeze-out temperature scaled to the DM mass, ρ_c is the critical density, σ_A the WIMP annihilation cross-section, v is the relative velocity of the particles in the interaction, and the brackets, $<>$, represent the average over the Boltzman thermal distribution.

From the expression, it follows that the thermal relic density is independent of the mass of the DM and inversely proportional to the annihilation cross-section, $< \sigma_A v >$. Moreover, when the expected value for the relic density of dark matter is considered in the above relation, the interaction cross-section is found at the weak scale ($\sim 10^{-36}$cm^2) for particles with a mass in the range of the electroweak scale. This "coincidence" is named the WIMP miracle and motivated the searches of DM particles related to new

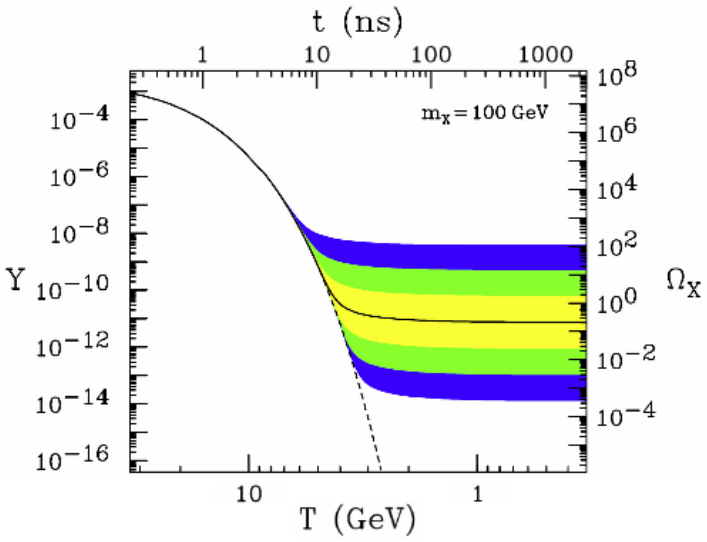

Figure 1.4.: Normalised dark matter density (left axis), and resulting thermal relic density (right axis) given a 100 GeV WIMP particle as a function of temperature (bottom) and time (top). The dashed line corresponds to a particle that remains in thermal equilibrium, and the solid line is for a particle at frozen-out with the observed relic density of DM. Shaded regions differ from this value by 10, 10^2, and 10^3. Figure from [28]

electroweak physics, which were already expected to occur [49]. Careful evaluation, however, reveals that only the ratio between the coupling of the process, g, and the mass of the WIMP are not fixed and can be satisfied for a wide range of values [49,50]:

$$\sigma_A \propto \frac{g^4}{m_\chi^2} \,. \tag{1.3}$$

1.2.3. Other dark matter candidates

Apart from the aforementioned WIMPs, the list of dark matter candidates is long. A schematised diagram of various dark matter particle candidates can be found in Figure 1.5.

As particles, alternative production mechanisms to the WIMP freeze-out, such as freeze-in, lead to feebly interacting massive particles [51], and freeze-out with subsequent decay to lighter particles to superWIMPs [52,53]. Another alternative particle candidate is the ultralight ($<1\,\mathrm{eV/c^2}$) axion [48,54,55], initially thought to solve the strong CP problem and the more general set of axion-like particles (ALPs). Still below the typical WIMP mass range, light dark matter candidates ($<1\,\mathrm{GeV/c^2}$) populate the

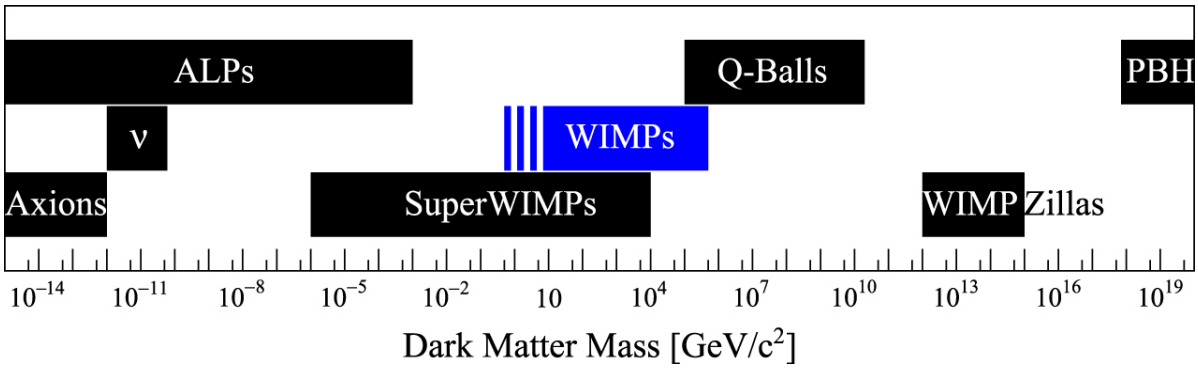

Figure 1.5.: A set of the most researched dark matter particle candidates as distributed at their predicted mass range. The WIMP, shown in blue, for masses below 10 GeV/c^2, considered the "low-mass region", is shown as a dashed bar. Figure from [63].

hidden-sector, such has sterile neutrinos [56] and dark photons [57, 58]. Above the mass range of WIMPs, the particle spectrum is dominated by WIMPzillas [59] and composite dark matter, such as Q-balls [60–62].

Outside the dark matter particle hypothesis, alternative explanations for the effects of dark matter can be found. In particular, theories describing massive astrophysical compact halo objects (MACHOs), such as primordial black holes, neutron stars and macroscopic dark matter, provide suitable candidates. However, observations of the Milky Way show that only ∼8 % of the total halo mass can be explained by MACHOs [64]. One final alternative and non-particle hypothesis is that the underlying gravitational theory is not applicable at large scales and must be corrected. An example of such theories is the Modified Newtonian Dynamics hypothesis and its relativistic extension Tensor-Vector-Scalar gravity. A recent observation of a galaxy containing no indication of presence of DM [65] highly disfavours any modified gravity theory.

1.3. Detecting dark matter

All the evidence detailed before point to effects of a dark matter component in the Universe. If DM was in thermal equilibrium with SM particles in the early Universe, then non-gravitational interactions between the two matter components must be possible and, potentially, observable. There are three classes of experiments searching for these interactions and its corresponding DM particles: direct detection, indirect detection, and production. A schematic view of these three detection channels can be

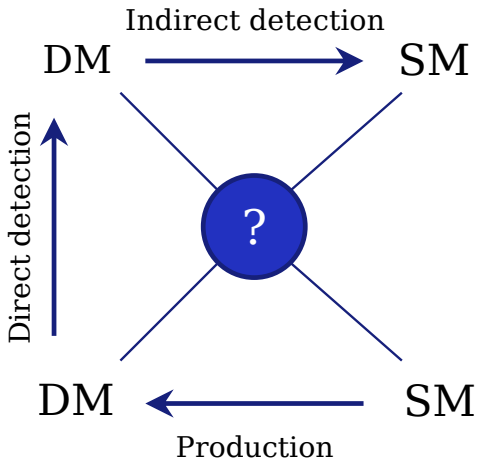

Figure 1.6.: Schematic of the couplings of dark matter particles to Standard Model particles and their detection channels. Details are presented in the text.

found in Figure 1.6. Direct detection of dark matter particles, looking for signals of an interaction of DM particles in a particle detector is the subject of Subsection 1.3.1.

Indirect detection of DM focuses on the search for observable SM particles which could be products of DM annihilation. The annihilation rate is dependent on the local DM density, making regions such as the like galactic centres, prime candidates for an enhancement of the process. The resulting particles could be photons, neutrinos, electron-positron pairs, proton-antiproton pairs, and other exotic pairs ($W^+W^-, Z^0Z^0, q\bar{q}$) [66]. These can be detected by particle detectors and telescopes, both ground-based and space-based. Examples of such experiments are the Fermi-LAT space telescope [67] (looking for gamma-rays), HESS [68] and the future CTA [69,70] (looking for cosmic-ray showers), Super-Kamiokande [71,72], and IceCube [73] (both looking for neutrinos).

Searching for DM by means of production entails creating DM particles from SM particles at sufficiently high energy in a controlled environment such as the Large Hadron Collider (LHC) [74,75] and conducted by experiments like ATLAS [76] and CMS [77]. The produced DM particles are expected to not interact substantially with SM particles after production and hence be detected as missing transverse energy and momentum. In this detection channel, any detected DM particles can not be guaranteed stable.

1.3.1. Direct dark matter detection

Direct detection of DM particles, particularly of WIMPs, entails the search for their scattering events with SM particles in ultra-sensitive low-background experiments. Such interactions can, in principle, happen with the atomic nuclei of the target material or with their electron clouds. Given the neutral charge of the WIMP, the main interaction of interest is the elastic scattering with the atomic nucleus itself, giving rise to a nuclear recoil (NR).

The differential rate of WIMP scattering events in a target is given by [78]:

$$\frac{\mathrm{d}R}{\mathrm{d}E_R} = \frac{\rho_0 M}{m_N m_\chi} \int_{v_{min}}^{v_{esc}} v f(v) \frac{\mathrm{d}\sigma}{\mathrm{d}E} \mathrm{d}v \ , \tag{1.4}$$

where E_R is the recoil energy, m_n the mass of the target nucleus, m_χ the WIMP mass, M the total target mass of the detector, and σ is the scattering cross-section of the WIMP-nucleus interaction. The WIMP distribution is described by the normalised WIMP velocity, $f(v)$, and the local dark matter density, ρ_0. Additionally, v is the incident velocity of the WIMP particle, with the escape velocity as v_{esc} and the minimum velocity required for a WIMP-nucleus interaction represented as v_{min}, calculated from the kinematics of a non-relativistic back-to-back recoil:

$$v_{min} = \sqrt{\frac{E_R m_N}{2\mu^2}} \ , \tag{1.5}$$

where μ denotes the reduced mass of the WIMP-nucleon system $\mu = m_\chi m_N / \left(m_\chi + m_N\right)$.

For the purpose of comparing different experimental results, a standard set of WIMP-related astrophysical parameters was established, known as the Standard Halo Model [79][2]: $\rho_0 = 0.3\,\mathrm{GeV/c^2/cm^2}$ [78], $v_{esc} = 544\,\mathrm{km\,s^{-1}}$ [80]. The velocity distribution, $f(v)$, is considered to have a Maxwell-Boltzman distribution with a most probable speed of $v_0 = 238\,\mathrm{km\,s^{-1}}$ [79,81,82] and a cut-off at the escape velocity value:

$$f(v) \propto \begin{cases} \exp\left(-\dfrac{v^2}{v_0^2}\right) & , v < v_{esc} \\ 0 & , v \geq v_{esc} \ . \end{cases} \tag{1.6}$$

[2] In the same cited work, [79], members of the majority of the direct detection experiments also outline procedures and recommendations on the statistical inference treatment to use for both upper limits and discovery claims.

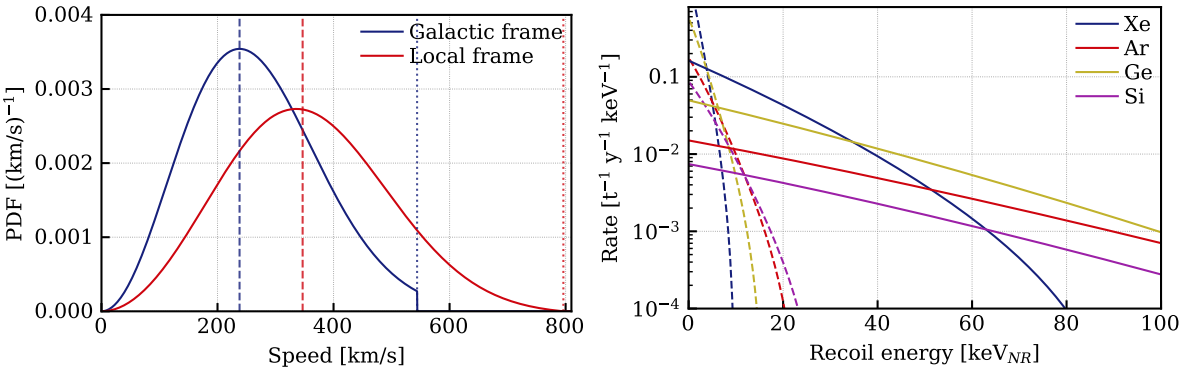

Figure 1.7.: **(a)** Distribution of WIMP speeds as modelled by the Standard Halo Model in the Galactic and local frames. Vertical dashed and dotted lines depict the maximum and escape velocities of both cases, respectively. **(b)** Nuclear recoil spectra for common target materials for a 10 (dashed lines) and 100 GeV/c^2 (solid lines) WIMP assuming a cross-section $\sigma_{SI} = 1 \times 10^{-47}$ cm^2. The decrease at higher energies is due to form factor suppression. Figures made using [83].

The distribution of WIMP velocities as seen from the rest frame of the Earth is influenced by the speed at which it travels while orbiting the Milky Way, changing the distribution anisotropically. The distribution of velocities as seen from the Galactic rest frame and from the local rest frame is depicted in Figure 1.7a.

Due to the translational movement of the Earth in the solar system, the speed at which the Earth moves through the DM halo changes throughout the year. The amplitude of the modulation is $\sim$15 km s^{-1} [84]. The annual modulation of observed DM rate over the course of one year, on the order of $\sim$5 %, is a strong method of searching for DM, often considered necessary for an ultimate confirmation of any observed signal as a DM signature [63]. A similar effect happens due to the rotational movement of the Earth over a period of one day but is dependent on the location of the detector on the globe.

In elastic WIMP recoils with a target material, two specific interactions are usually considered: spin-independent (SI) and spin-dependent (SD) interactions. The total cross-section can then be split into two factors:

$$\frac{\mathrm{d}\sigma}{\mathrm{d}E_R} = \frac{m_N}{2v^2\mu^2}\left(\sigma_{SI}F_{SI}^2(E_R) + \sigma_{SD}F_{SD}^2(E_R)\right) , \tag{1.7}$$

where F_{SI} and F_{SD} are the SI and SD nuclear form factors, respectively, and μ is the WIMP-nucleus reduced mass. The two cross-sections can be treated separately. The SI

WIMP-nucleus cross-section is given by:

$$\sigma_{SI} = \sigma_n \frac{\mu^2}{\mu_n^2} \frac{\left(f_p Z + f_n (A - Z)\right)^2}{f_n^2} \,, \tag{1.8}$$

where σ_n is the WIMP-nucleon cross-section, and μ_n is the WIMP-nucleon reduced mass. The WIMP coupling strengths to protons and neutrons are described with f_p and f_n, respectively. Z and A are, respectively, the number of protons and the total number of nucleons in the nucleus. The two couplings are usually assumed to be the same, leading to Equation 1.8 being rewritten to emphasise the A^2 dependence of the cross-section:

$$\sigma_{SI} = \sigma_n \frac{\mu^2}{\mu_n^2} A^2 \,. \tag{1.9}$$

The above expression suggests that a target of heavier nuclei results in higher rates than one of lighter nuclei. While this is true, the recoil energies are smaller, which can be challenging for experimental detection due to the need for lower detector thresholds. Figure 1.7b shows the expected interaction rates for both a 10 and a 100 $\mathrm{GeV/c^2}$ WIMP in different target materials. The expected dependence on A^2 is observed, putting heavier nuclei at an advantage. Due to form factor suppression, which results in the loss of coherence of the process at large momentum transfers, the rates of heavy elements are greatly reduced at high energies. The form factor for SI interaction is commonly approximated as the Helm form factor [85], which is in good agreement with shell-model calculations [86].

The SD cross-section, on the other hand, has no A^2-scaling due to coherence effects. On the contrary, only unpaired nucleons contribute meaningfully to the process by totalling a non-zero net spin of the nucleus. The cross-section for SD interactions can be written as [87]:

$$\sigma_{SD} = \frac{32}{\pi} \mu^2 G_F^2 \left(a_p \langle S^p \rangle + a_n \langle S^n \rangle\right)^2 \frac{J+1}{J} \,, \tag{1.10}$$

where G_F^2 is the Fermi constant, J is the total nuclear spin, a_p (a_n) the effective proton (neutron) couplings, and $\langle S^p \rangle$ ($\langle S^n \rangle$) are the expectation value of the nuclear spin content due to the proton (neutron) group. Despite heavy nuclei being more sensitive to SI interactions, for SD interactions, the spin of the nucleus is determinant for the cross-section of the interaction. The prime case is of ^{19}F that, while having a rather

light nucleus, is very sensitive to SD WIMP-proton scattering. Because protons and neutrons have different contributions to the total spin of the target, SD cross-section results are often given assuming couplings only to protons ($a_n = 0$) or only to neutrons ($a_p = 0$).

1.3.2. Direct detection experiments

Dark matter detectors looking for recoil signals in their target mass use one or a combination of heat, light, and charge signals. The achievable energy threshold, energy resolution, and discrimination between electron and nuclear recoils are dependent on the target material and detection technology employed by each experiment.

Currently, most experiments aim to detect more than one of the signal channels. Experiments focusing on detection through only heat are confined to bubble chambers, such as PICO-40L [88]. The target is kept in a superheated liquid in a metastable state, which undergoes a phase transition from particle interactions, creating a bubble detectable by its acoustical signal and cameras on the outside of the chamber. The energy threshold is $\sim$1 keV. The next phase of the project is the PICO-500 [89].

While still detecting phonons, several experiments are able to additionally detect either charge or light. Examples of charge and phonon experiments are SuperCDMS [90–92], EDELWEISS-III [93], and CDEX-10 [94], all using cryogenic germanium crystals. The energy threshold in these experiments is $\mathcal{O}$(10-100) eV, enhancing sensitivity to low-mass WIMPs. Other experiments complement the heat signal by detecting photons from the interaction. It is the case of CRESST-III [95], which operates scintillating $CaWO_4$ crystals as cryogenic calorimeters. In a similar fashion, the COSINUS [96, 97] project uses a NaI crystal target as a calorimeter. The energy threshold of these calorimeter-based experiments is, once-again, $\mathcal{O}$(10-100) eV. A different type of experiment using both heat and photons is the liquid noble bubble chamber, such as the SBC experiment [98, 99], which operates a scintillating bubble chamber of xenon-doped liquid argon.

Charge-based detectors often use charge-couple devices (CCDs), in which an interaction causes an electron-hole pair subsequently drifted by an applied electric field. The charges are read on a pixelated readout for precise position reconstruction. These are among the lowest thresholds achieved, around $\mathcal{O}$(10)eV. Examples of such detectors are DAMIC/DAMIC-M [100, 101], SENSEI [102], and CoGenT [103, 104]. Still

as charge-based detectors, gas proportional counters are also used to look for WIMPs with low-thresholds, $\mathcal{O}(100)$eV, in experiments such as NEWS-G [105].

Detectors relying on the light signal channel are either scintillating crystals or liquid noble element detectors. The prime example of the former is the DAMA/LIBRA detector [106], which operates 242.5 kg of NaI(Tl) as a scintillating target. Famously, DAMA/LIBRA reports evidence of an annual fluctuation of background rate in concordance with what is expected from DM at a 12.9 σ significance [107]. The claim is in strong tension with the many limits set by other experiments looking for the expected absolute rate. Nonetheless, the DAMA/LIBRA result remains a puzzling mystery. Soon, the COSINE-100 [108, 109], ANAIS-112 [110], and KIMS [111] experiments, using the same target and technology as DAMA/LIBRA, will definitively confirm or deny the claimed positive result. Light-based liquid noble element detectors use either xenon or argon as scintillating material. This is the case of the DEAP-3600 [112] experiment, operating 3.3 t of liquid argon, and the XMASS [113] experiment, that operated 832 kg of liquid xenon.

Sensitive to both light and charge, liquid noble element time projection chambers (TPCs) have, in particular from LXe TPCs, lowered the upper limits on SI WIMP-nucleus interaction by $\sim$6 orders of magnitude in 15 years. The detection concept and emerging signals in dual-phase LXe TPCs are discussed in the next chapter. The main experiments using xenon TPCs for DM searches are the XENONnT [114], LZ [115], and PandaX-4T [116] multi-tonne experiments. The next-generation LXe TPC, DARWIN [117], will be able to reach the neutrino fog [118], where coherent elastic neutrino-nucleus scattering (CEνNS) interactions from solar and atmospheric neutrinos start to dominate the background of the experiment. The DARWIN project is further described in Chapter 6. Recent argon-based TPCs are the DarkSide-50 experiment [119], WArP [120], and ArDM [121]. Given the logistical and funding problems in the scalability of both xenon- and argon-based DM searches, both communities are making steps towards common monolithic detectors. It is the case of the XLZD consortium [122] and the Global Argon Dark Matter Collaboration [123, 124]. Outside of xenon or argon, the proposed CYGNO [125] experiment, currently in prototype phase, is a gas TPC with a helium/fluorine-based gas mixture at atmospheric pressure. The future experiment aims to be capable of directionality detection, providing unambiguous validation in the case of a DM candidate signal.

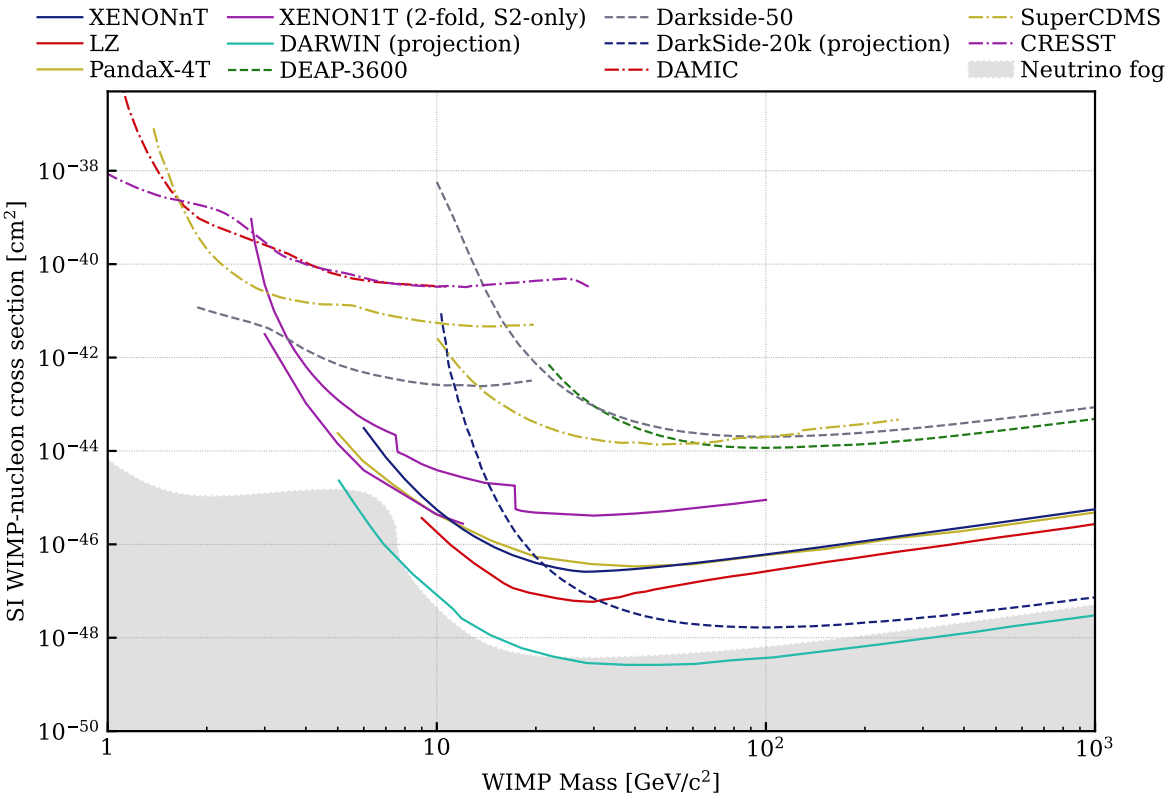

Figure 1.8.: Current upper limits from the leading dark matter experiments and the projected DARWIN and DarkSide-20K sensitivities for spin-independent WIMP-nucleon interaction cross-section. Results for xenon dual-phase TPCs are shown in solid lines (XENONnT [114], XENON1T [126, 127], LZ [115], PandaX-4T [116], and the projection for DARWIN [117]), for argon-based experiments in dashed lines (DEAP [128], Darkside-50 [129,130], and the projection for DarkSide-20K [124], and for experiments using other technologies in dot-dashed lines (DAMIC [100],SuperCDMS [91, 92], CRESST [95]. The neutrino fog [118] region is shown in light grey.

Figure 1.8 shows the most recent and stringent SI WIMP-nucleon upper limits as a function of the WIMP mass, as well as the projection for the baseline scenario of DARWIN.

Chapter 2.

The XENONnT experiment

XENONnT is the fourth detector in a series of liquid xenon (LXe) TPCs of the XENON project to be hosted in Hall B of Laboratori Nazionali del Gran Sasso (LNGS) [131–133]. The XENON10 detector, operated between 2005 and 2007, instrumented 14 kg of LXe, was the precursor of XENON100, operated between 2008 and 2016 with 16 kg of LXe instrumented. XENON1T was the first tonne-scale LXe dual-phase TPC, operated between 2013 and 2018 with 2 t of LXe instrumented. Following a one-year upgrade of XENON1T, XENONnT has been operating since 2020 with an active target of 5.9 t. Figure 2.1 summarises the XENON project timeline. The 400-fold increase in active mass from XENON10 has been accompanied by a reduction of background in the WIMP region of interest (ROI) of five orders of magnitude, from $\sim 1 \times 10^{3}\,\mathrm{cts}/(\mathrm{t}\cdot\mathrm{d}\cdot\mathrm{keV})$ to $\sim 4 \times 10^{-2}\,\mathrm{cts}/(\mathrm{t}\cdot\mathrm{d}\cdot\mathrm{keV})$.

The main characteristics of xenon as a target material in particle detectors are reviewed in Section 2.1. Section 2.2 describes the dual-phase TPC working principle, and Section 2.3 details the features of the XENONnT TPC in particular. An overview of the other XENONnT sub-systems is provided in Section 2.4.

2.1. Xenon as a particle detector target

2.1.1. Overview of xenon properties

Xenon is used as a target in particle detectors in a large range of science searches. In other fields, xenon is used as an anaesthetic, as a propellant in the spacecraft industry, as a medical radioisotope marker (^{133}Xe), and as a light emitter in xenon lamps and

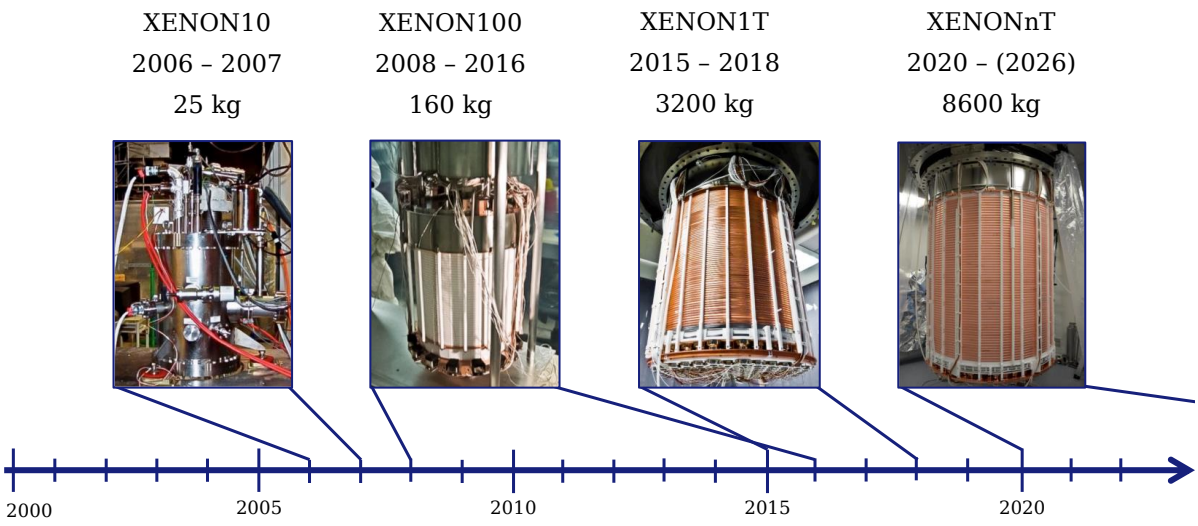

Figure 2.1.: Timeline of the XENON project and total xenon mass operated in each XENON detector. More information on the history of the project and the different XENON detectors can be found in [134]. Pictures by the XENON Collaboration.

photographic flashes. In nature, it is a rare gas diluted in the air at a concentration of 0.087 ppm. Most of the commercially available xenon is obtained through fractional distillation in large air separation unit (ASU) in a several-step process: first, nitrogen and oxygen are separated. Then, the resulting liquid oxygen contains a mixture of krypton and xenon, which can be extracted by distillation. Finally, krypton and xenon undergo one last fractional distillation process to be separated, purified, and bottled.

In the search for DM, some key characteristics make xenon stand out as an excellent choice of detection medium. Xenon is the heaviest noble gas with few naturally occurring radioisotopes that would contribute to the overall background level. The main exceptions are the ^{124}Xe and ^{136}Xe double-weak decays with half-lives of $(1.10 \pm 0.03) \times 10^{22}$ years [135] and $(2.27 \pm 0.13) \times 10^{21}$ years [136], that become increasingly important for the larger volumes of xenon targets in next-generation experiments [137, 138].

The density of xenon in liquid form is $2.861\,\mathrm{g\,cm^{-3}}$ at 177 K and 2 bar [139, 140], the operating temperature and pressure of XENONnT. The high-density medium and high atomic number translate into a high stopping power for radiation, making self-shielding highly effective. Figure 2.2 shows the xenon absorption coefficient for photons in a wide range of energies. The photoelectric effect is dominant up to

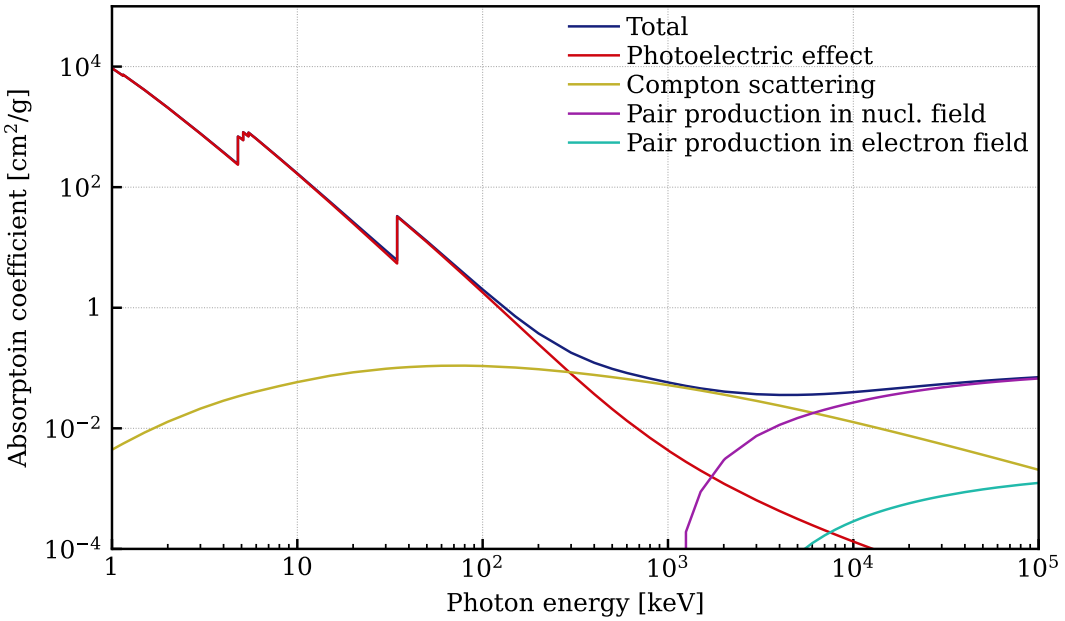

Figure 2.2.: Photon absorption coefficient as a function of the incident photon energy for liquid xenon. The several interaction mechanisms' contributions (photoelectric, Compton and pair production) are depicted, as is the total absorption coefficient. The two sudden increases in the absorption coefficient at low photon energy are due to the K-shell and L-shell absorption edges of xenon. Data from [141].

$\sim$300 keV, where Compton scattering becomes the main mechanism, only surpassed by pair production at $\sim$6 MeV.

Moreover, xenon makes large target masses available in relatively small geometries. It has a relatively high boiling point, around 163 K at 1 atm [139, 142], when compared with other cryogenic fluids. This feature allows the use of liquid nitrogen (LN_2) as a coolant, despite current experiments often employing active cooling with pulse tube refrigerators (PTRs).

Xenon has an atomic number, Z, of 54 and an average atomic mass, A, of 131.290 g mol^{-1} [143]. As detailed in Chapter 1, the large atomic mass enhances the sensitivity to coherent SI scattering of WIMPs, at the same time as odd isotopes allow SD WIMP interactions to also be studied.

Table 2.1.: Main properties of xenon in the context of dual-phase LXe TPCs.

Property	Value	Unit	Notes	Reference
Atomic number, Z	54			
Average mass number, $\bar{A}$	131.293(6)	$\mathrm{g\,mol^{-1}}$		[143]
Boiling point	165.02(5)	K	at 1 atm	[139, 142]
Melting point	161.25(5)	K	at 1 atm	[139, 142]
Triple point	161.38(2)	K		[139, 144]
	0.816 000(2)	bar		[139, 145]
Density, ρ	2.8609(57)	$\mathrm{g\,cm^{-3}}$	at 177 K, 2 bar	[139, 140]
Abundance in air	0.087 ppm			[146]
Scintillation wavelength	174.8(2)	nm	at 168-169 K, 1.10-1.17 bar	[147]
Dielectric constant, ϵ_r	1.95			[148]

2.1.2. From interaction to signal

Upon a particle interaction with a xenon atom, the deposited energy, E_0, is shared between excitation, ionisation, and heat, such that:

$$E = N_{exc}\bar{E}_{exc} + N_{ion}\bar{E}_{ion} + N_{ion}\bar{\epsilon}\ , \tag{2.1}$$

where N_{exc} (N_{ion}) is the number of excited (ionised) atoms, $\bar{E}_{exc}$ ($\bar{E}_{ion}$) is the average energy expended on exciting an atom (creating an electron-ion pair), and $\bar{\epsilon}$ is the average sub-excitation energy carried through heat. The ratio N_{exc}/N_{ion} is dependent on the type of interaction, the electric field and the deposited energy. For interactions via scattering off electrons, named electronic recoils (ERs), the excitons to electron-ion pairs ratio is 0.06 to 0.20, while for interactions via scattering off nuclei, named NRs, the ratio is 0.9 to 1.1 [149–151]. This difference can be used for background discrimination.

In LXe TPCs, only the excitation and ionisation fractions are measured. The excitation process leads to the creation of excited Xe_2^* dimers, which emit scintillation light, $h\nu$, when returning to xenon atoms in their ground state:

$$\begin{aligned} \mathrm{Xe}^* + 2\mathrm{Xe} &\rightarrow \mathrm{Xe}_2^* + \mathrm{Xe} \\ \mathrm{Xe}_2^* &\rightarrow 2\mathrm{Xe} + h\nu \ . \end{aligned} \tag{2.2}$$

The xenon excimers, Xe_2^*, responsible for the scintillation process, can form a spin-singlet or spin-triplet state, with decay times of $\sim$2 ns and $\sim$27 ns, respectively [152]. The ratio between the populations of the two excited states depends on the type of interaction and could conceptually be used for particle discrimination through pulse shape discrimination (PSD). Measurements of the single-to-triplet ratio in liquid xenon yielded $0.042^{+0.098}_{-0.040}$ for ER and $0.269^{+0.204}_{-0.105}$ for NR [153]. However, the difference in timing is too small to be experimentally distinguished. In the case of argon, the singlet (2 ns) and triplet (1950 ns) lifetimes are orders of magnitude apart, and PSD is widely and efficiently used for recoil discrimination [124,154–156]. The xenon dimers produce vacuum ultraviolet (VUV) photons with an average wavelength of $\sim$175 nm [147]. As the VUV photons are a product of excimer states and not directly from excited atomic states, they are not absorbed by the xenon atoms, making xenon transparent to its own scintillation light.

In the absence of an applied electric field, or if the field is not strong enough to separate all the ion-electron pairs, a fraction of the xenon ions, Xe^+, will undergo recombination, leading to more scintillation light from Xenon dimers:

$$\begin{aligned} \mathrm{Xe}^+ + Xe &\rightarrow \mathrm{Xe}_2^+ \\ \mathrm{Xe}_2^+ + e^- &\rightarrow \mathrm{Xe}^{**} + \mathrm{Xe} \\ \mathrm{Xe}^{**} &\rightarrow \mathrm{Xe}^* + \mathrm{heat} \\ \mathrm{Xe}^* + 2Xe &\rightarrow \mathrm{Xe}_2^* + \mathrm{Xe} \\ \mathrm{Xe}_2^* &\rightarrow 2\mathrm{Xe} + h\nu \end{aligned} \tag{2.3}$$

While in an excited state, the xenon excitons can combine to form an electron-ion pair and a xenon atom in the ground state. This process, which is energy and recoil-type dependent, is known as bi-excitonic quenching or Penning quenching and is responsible for reducing the number of measurable quanta produced from the interaction. This effect is most prevalent in high-density tracks of highly ionising

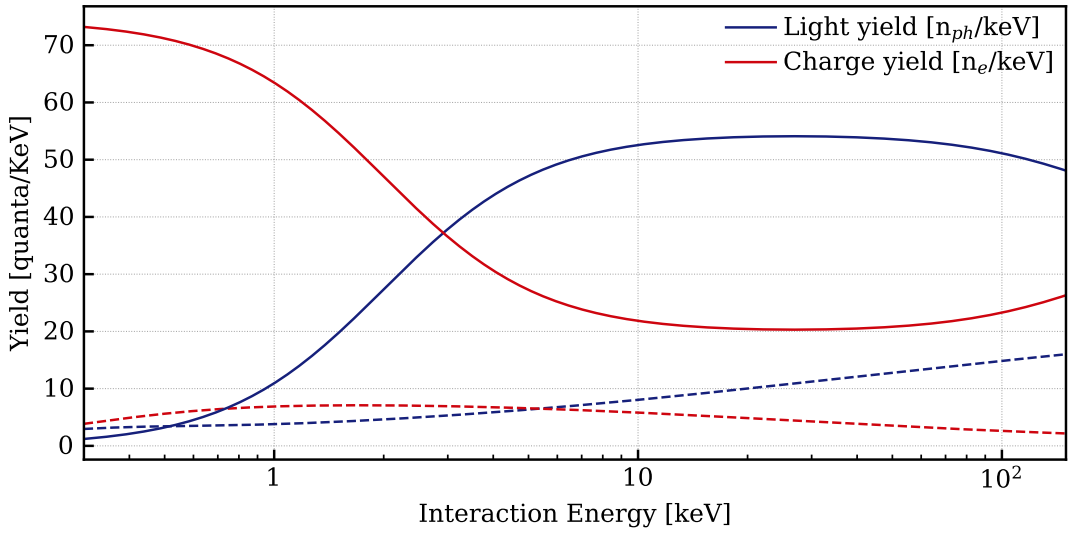

Figure 2.3.: Light (blue) and charge (red) yields for an electron recoil interaction from a gamma-ray (solid lines) and nuclear recoil interaction (dashed lines). The values are calculated for an applied electric field of 200 V/cm using NEST v2.3.12 [157, 158].

particles, such as those from alpha particles, while contributing negligibly to ER interactions.

The expected number of quanta from an interaction is dependent on both the energy of the interaction, the type of recoil, and the electric field. The number of photons and electrons produced per unit of recoil energy are named light yield, L_y, and charge yield, Q_y, respectively. Figure 2.3 shows the light and charge yields for NR and gamma interactions as provided by Noble Element Simulation Technique (NEST) [157, 158] in the main range of interest for DM search in dual-phase xenon TPCs.

The majority of the excited dimers produce photons, but a large number of electron-ion pairs do not contribute to extracted charges. Instead, they undergo the above-described recombination and Penning quenching processes. The number of electrons extracted from the interaction site by the electric field is governed by the recombination probability, r, through:

$$N_{el} = (1 - r)N_i \,, \tag{2.4}$$

where N_{el} is the number of resulting free electrons. As the total number of quanta must be conserved, the number of photons, N_{ph}, and electrons relate to the number of

excitons and electron-ion pairs created by

$$N_{exc} + N_{ion} = N_{ph} + N_{el} \ . \tag{2.5}$$

In terms of deposited energy, the following relation arises:

$$E_{ER} = W(N_{ph} + N_{el}) \ , \tag{2.6}$$

where W is defined as the average energy needed to produce a single free quantum in LXe, also known as the work function. The expression above is a good approximation for ER interactions, where quenching effects are negligible and total quanta production is linearly dependent on the deposited energy. However, for NR interactions, the previously mentioned energy-dependent quenching effects require the introduction of the energy-dependent Lindhard factor, $\mathcal{L}$ [151, 159]:

$$E_{NR} = W\frac{(N_{ph} + N_{el})}{\mathcal{L}} \ . \tag{2.7}$$

The value of W taken as standard in the field for liquid xenon is (13.7 ± 0.2) eV [160]. However, recent results have measured values around 11.5 eV [161, 162]. Further independent measurements are needed to resolve the $\sim$20 % difference.

2.2. The dual-phase TPC

All of the detectors of the XENON project are dual-phase time projection chambers filled with xenon in liquid and gaseous forms. In these detectors, most of the volume is occupied by the liquid phase, which acts as the target material. Figure 2.4 depicts the different components, electric field regions, and operating principles of a TPC.

The standard TPC used in DM experiments such as in XENONnT [163], LZ [164], or PandaX-4t [165], has a cylindrical shape with two arrays of photosensors, both below and above the target volume. A set of electrodes defines two main electric field regions: between the cathode and gate extends the drift field region, E_{drift}, from the bottom of the target to a few mm below the liquid-gas interface; between the gate and the anode extends the extraction field region, $E_{extraction}$, from a few mm below the liquid-gas interface to a few mm above it. While the drift field has an applied

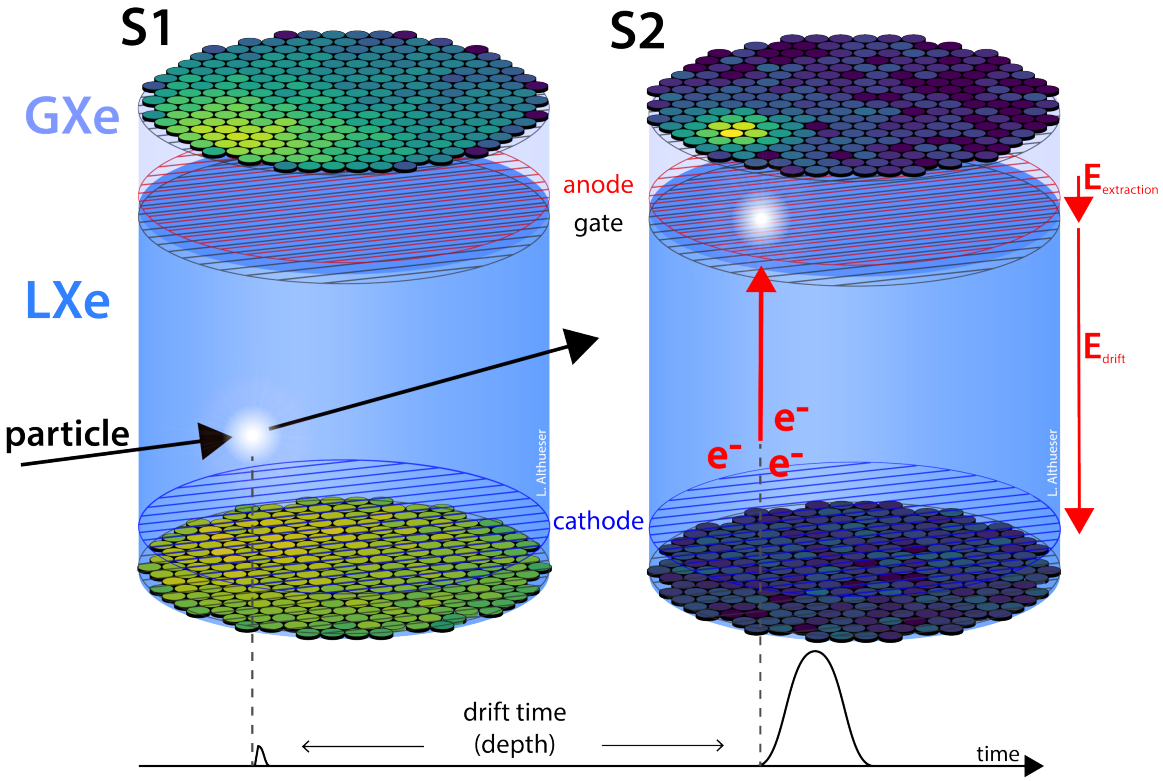

Figure 2.4.: Dual-phase TPC working principle. A particle interacts within the liquid xenon target, creating a prompt scintillation signal (S1) detected in the top and bottom PMT arrays and electron-ion pairs. The electrons that do not undergo recombination drift towards the gate by the effect of the applied E_{drift}. The electrons are extracted from the liquid phase by the $E_{extraction}$ and, now in gas, the accelerated charges induce proportional scintillation, giving origin to the S2 signal. This secondary scintillation signal is again detected by the top and bottom PMT arrays. Figure by L. Althüser/XENON collaboration.

field of $\mathcal{O}(10-100)$V/cm, the magnitude of the extraction field is much higher, at $\mathcal{O}(1-10)$kV/cm.

As detailed in the previous section, when an electronic or nuclear recoil occurs, both scintillation photons and ionisation electrons are generated. Since xenon is transparent to its own scintillation light, the prompt photons can be detected in arrays of photosensors, giving origin to the primary scintillation signal, S1. The S1 signal is mainly collected in the bottom photosensor array due to total internal reflection at the liquid-gas interface. As a result of the applied E_{drift}, the electron-ion pairs that did not undergo recombination are separated, and each charge follows the field in opposing directions. The formed electron cloud drifts upwards towards the gate

electrode. Upon reaching the gate, the electrons are pushed out of the liquid phase to the gas phase due to $E_{extraction}$, applied between the gate and the anode. The velocity at which the electron cloud moves through the liquid xenon is dependent on the intensity of the applied field, the xenon purity, and the conditions of the medium, such as temperature and pressure. The typical range of electron drift speeds is between 0.2 and 2 mm μs^{-1} [166–168]. Detailed information on electron transport can be found in Chapters 6, Figure 6.6, and in the last section of Chapter 7.

In the gas phase, the electrons are continuously accelerated up to a terminal velocity by the strong electric extraction field up, gaining enough energy between collisions with xenon atoms to excite them, producing scintillation photons once again. This second signal is named S2. The proportional scintillation process in the gas makes the S2 signal 100 times larger than the typical S1 signal while remaining proportional to the number of extracted electrons. The relative gain of this process is named electroluminescence gain. For sufficiently strong electric fields, around $\sim$10 kV/cm, the extraction efficiency is $\sim$100 % [169, 170].

The combined analysis of the S1 and S2 signals can yield valuable information of the event: energy reconstruction, position reconstruction, and ER/NR discrimination. First, the energy deposited in the interaction can be determined by the number of quanta produced and, therefore, by the size of the S1 and S2 signals. Taking detector effects on the conversation of quanta to S1 and S2 signals, Equation 2.6 can be rewritten as:

$$E = W \left(\frac{S1}{g_1} + \frac{S2}{g_2} \right) , \tag{2.8}$$

where g_1 and g_2 are detector-dependent parameters defining a linear relationship between the number of quanta produced by the interaction and the number of photoelectron (PE)[1] detected. The g_1 value includes the spatial-dependent probability that a photon produced at a given position hits a photosensor, named light collection efficiency (LCE), and the probability that the photosensor detects the hit, named quantum efficiency. Accordingly, it has units of photoelectrons per photon, PE/ph. The g_2 value includes the extraction efficiency, the electroluminescence gain, and the aforementioned quantum efficiency of the photosensors. Signifying the number of

[1] Photoelectrons are electrons detected in the photosensors after photon detection efficiency considerations. While in the proportional range of the photosensor, the number of PE is proportional to the number of incident photons hitting the photosensor, and often used here as a unit of detected photons.

photons detected per electron reaching the gate, it has units of photoelectrons per electron, PE/el, respectively. The energy of an interaction can also be reconstructed from just the S1 or S2 signal. However, the combined energy scale of Equation 2.8 achieves the highest resolution given the anti-correlation of light and charge, resolving the recombination fluctuations on S1 and S2 signals.

Second, as scintillation light production and detection are almost simultaneous, the time difference between the S1 and S2 signals is mainly due to the drift time of the electron cloud through the TPC. Disregarding local field non-uniformities, the drift velocity, v_e, is constant, and the drift time, t_d, is then proportional to the depth of the interaction, z:

$$z = v_e \cdot t_d \ . \tag{2.9}$$

Moreover, the localised light pattern on the photosensor arrays, in particular on the top, can be used to reconstruct the (x,y) position of the event. The three-dimensional position reconstruction of events within the active target enables fiducialisation of the volume, i.e., defining an inner fiducial volume with a highly reduced radiogenic background from materials due to the self-shielding power of liquid xenon.

Position resolution is a result of both diffusion processes of the electron clouds during the drift path and limitations due to the granularity of the photosensor array. In XENONnT, the latter is the dominating factor in (x,y) position resolution, given the cm-scale distance between photosensors when compared to mm-size electron clouds after transverse diffusion effects [167,171]. For small S2s, random fluctuations in the patterns originating also play an important role in limiting the achievable position resolution. The transverse position resolution is $\sim$1 cm [172]. In the z direction, however, since reconstruction depends only on the timing of the electron cloud, greater resolution can be achieved, turning the longitudinal diffusion process into the limiting factor. Longitudinal diffusion concerns the stochastic process of the random walk of electrons in addition to their group drift. The longer an electron cloud drifts, the longer it diffuses. Consequently, the z resolution is dependent on the depth of the interaction, from $\sim$1 mm at the top to a few mm at the bottom of the TPC [172].

Third, the ratio between the S2 and S1 signals can be used to discriminate between ER and NR events, which is key to the discrimination of backgrounds. As discussed in the previous section, ER and NR interactions result in different relative numbers of photons and electrons due to recoil-dependent quenching effects. As a result, the

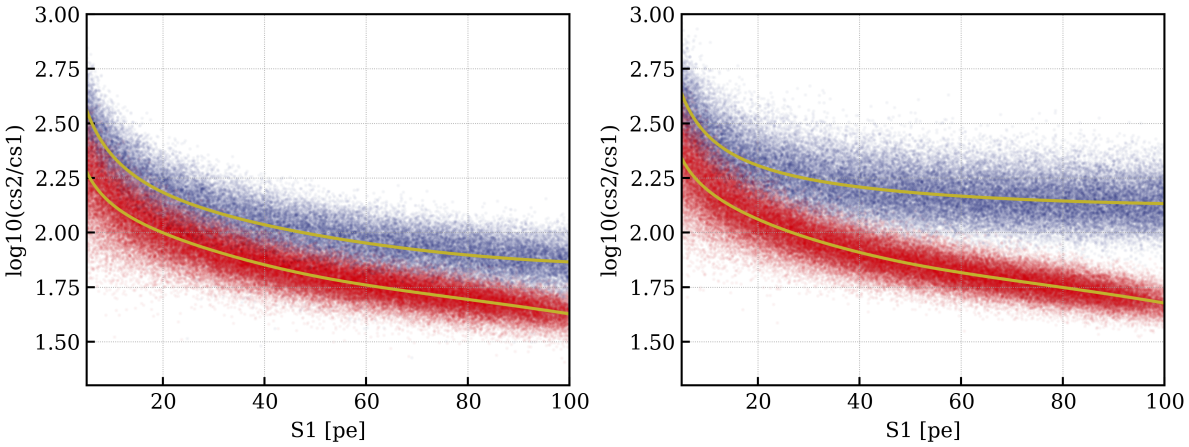

Figure 2.5.: Simulated ER (blue) and NR (red) bands obtained from uniformly distributed deposited energies for a field magnitude of 20 V/cm **(a)** and 200 V/cm **(b)**. The median values of the distributions are shown as solid gold lines. Simulated with NEST v2.3.12 [157, 158].

S2/S1 ratio from an ER event is much larger than the analogous signal from an NR event. The distribution of ER and NR events in S2/S1 as a function of S1 space is shown in Figure 2.5. The relative position of the ER and NR bands and, therefore, the discrimination capability of the detector is highly dependent on the drift field due to its role in the recombination probability. High drift fields result in lower recombination probability and a larger separation of the ER and NR bands, while for low drift fields, the bands tend to be closer together and leakage events, i.e., ER events below the median value of the NR band, are more probable. Experimentally, the distribution of ER and NR events is obtained by calibrating the detector with ER-inducing neutron sources such as ^{220}Rn and NR-inducing sources such as ^{241}AmBe.

2.3. The XENONnT TPC

The XENONnT TPC follows the same broad design and improves upon its predecessor, XENON1T [133]. The TPC has a quasi-cylindrical shape with 1613 mm of height and 1327 mm of diameter. All the TPC components hang from the top flange of the stainless steel inner cryostat vessel, which holds 8.6 t of xenon in total. From the full amount, 5.9 t are used as an active target, while the rest stands above, below, and around the TPC, between its walls and the wall of the inner vessel. A render of the XENONnT TPC and its main components is depicted in Figure 2.6.

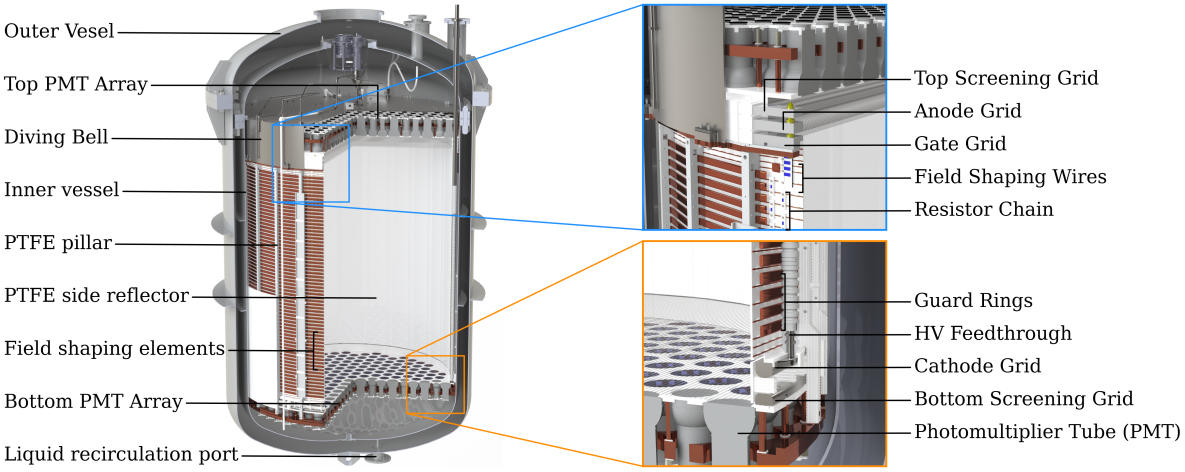

Figure 2.6.: CAD render of the XENONnT TPC. Details of the top and bottom parts of the TPC are shown as insets on the right side.

The walls enclosing the active region are made from 3 mm-thick polytetrafluoroethylene (PTFE), forming an icositetragon (24-sided polygon). The PTFE is diamond polished on all the surfaces facing the interior of the TPC to improve the reflectivity of the walls to the ∼175 nm scintillation light of xenon to ∼97 % [173, 174]. Special care was taken during design to minimise the amount of PTFE used, as it is a source of neutron background via (α,n)-reactions [175, 176] and a major source of outgassing, which negatively influences the xenon purity.

The TPC hosts two arrays of photomultiplier tubes (PMTs): 253 on the top and 241 on the bottom, for a total of 494 units. The PMTs are the VUV-sensitive and low-background cryogenic model Hamamatsu R11410-21 [177], developed in partnership between Hamamatsu Photonics and the XENON collaboration [178–180]. This model shows an average quantum efficiency of 34.1 % at xenon scintillation wavelength, and an average collection efficiency of 90 %. All the PMTs were thoroughly tested in liquid xenon conditions to detect units with increased signs of potential failure such as leaks in PMT vacuum and high afterpulse rate. Of the 494 PMTs used in XENONnT, 153 had previously been operated successfully in XENON1T. Both arrays have the PMTs arranged in a hexagonal pattern to achieve maximum photocathode coverage and are fixed in place by a PTFE disc. A disc of oxygen-free high thermal conductivity (OFHC) copper provides mechanical support to each array.

The different electric field regions of the TPC are defined by five parallel wire grid electrodes. From bottom to top: bottom screening grid, cathode, gate, anode, top screening grid. The wires are stretched under tension and secured in stainless steel

frames. The drift region, defined between cathode and gate as described in Section 2.2, is 1468 mm-long, and the extraction field region, between gate and anode, 8 mm, with the TPC at LXe temperature. All the electrodes are individually biased by CAEN A1526P [181] (anode), Heinzinger PNChp 150000-1 neg [182] (cathode), and CAEN A1580HDM [183] (all other electrodes) power supplies. At a late stage of design, a set of four (two) transverse wires was mounted on the anode (gate) electrodes to minimise sagging and prevent discharges between the biased grids. More details on the electrodes and electric fields of XENONnT are provided in Chapter 3.

The uniformity of the drift field is ensured by two sets of concentric field-shaping electrodes. The innermost set of shaping electrodes is attached to the backside of the PTFE walls, consisting of 72 2 mm OFHC copper wires. Radially outwards from the wires, the second set of field-shaping electrodes is composed of 64 OFHC copper "guard" rings with a 15 mm$\times$5 mm cross-section (see insets in Figure 2.6). The field-shaping elements are connected through two redundant resistive chains to both the cathode (on the bottom) and a dedicated power supply (on the top). The possibility to independently bias the field shaping chain allows fine-tuning of the electric field during operation and has proven to be a key parameter in achieving high field uniformity close to the gate. More details on the field cage of XENONnT are provided in Chapter 3 and can be found in [184].

During normal operation, the liquid-gas interface stands at $\sim(5.02 \pm 0.20)$ mm above the gate electrode. The monitoring of the liquid level is done by four parallel-plate capacitive level metres, which are also responsible for measuring the tilt of the TPC. The liquid level is set by a pressurised diving bell that surrounds the top part of the TPC (see Figure 2.6). Other level metres around at centre height and the bottom of the TPC monitor the LXe level during filling and recuperation.

2.4. The XENONnT facility

The XENONnT experiment is a complex cryogenic facility. Several systems provide the conditions for physics searches and safe operation of the detector: data acquisition (DAQ), slow control (SC), cryogenics and xenon handling, xenon storage, xenon purification, Kr and Rn removal, and veto detectors. Most of these subsystems are located in the XENON service building, next to the water tank, as shown in Figure 2.7.

Figure 2.7.: XENON water tank and service building in Hall B of LNGS. The canvas print hung on the front of the water tank depicts a rendering of the inside, where the muon veto, neutron veto, calibration, and TPC structures are shown. The rooms in the service building are used as follows: upper left – cryogenics, gaseous xenon (GXe) purification, gas xenon pumping; upper right – radon distillation column; centre left – DAQ and power supplies; centre right – office space, top part of the krypton distillation column; bottom left – ReStoX1, LXe purification; bottom right – bottom part of the krypton distillation column, GXe bottles. Picture by H. Schulze/XENON Collaboration.

Cryogenics, xenon handling and purification

The cooling of xenon is handled away from the cryostats, inside the second floor of the XENON service building. A 6 m long vacuum-insulated cryogenic pipe connects the cooling station to the cryostat. Two redundant cooling towers with 250 W PTRs PTRs [185] liquefy the xenon. A heater band around the cold head allows for the precise control of cooling power via a controller [186]. The cold head can also be cooled by LN_2 in the case of electrical failure of the controller or heater.

In XENONnT, both xenon gas and liquid are circulated for purification (impurities removal, Kr removal, and Rn removal). For gas purification, LXe is extracted from the cryostat, evaporated in a heat exchanger, and guided through two parallel high-temperature PS4-MT50-R getters from SAES [187]. The flow of xenon is controlled mass flow controllers and driven by two magnetically-coupled piston pumps [188].

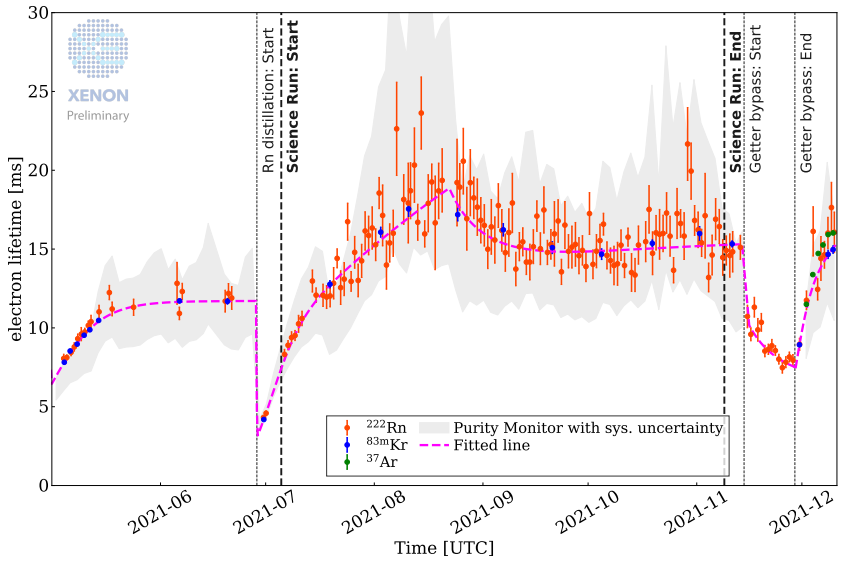

Figure 2.8.: Electron lifetime evolution during the first science run of XENONnT. Data points with error bars correspond to the electron lifetime calculated during calibration campaigns with data from the TPC, while the grey background shows the electron lifetime measured in a dedicated purity monitor in the cryogenics room.

These novel pumps have proven to be both chemically cleaner and more radiopure than the previously used Q-drive pumps [189]. The average total flow of xenon in gas is ∼80 SLPM. For liquid purification, the xenon is extracted from the bottom of the cryostat and routed to the ground floor of the service building. There, it is driven by a clean cryogenic liquid pump [190] for flows up to 4 LPM (∼18hours to circulate the entire volume) [191] and purified in custom-made filters containing SAES St707 getter pills [192]. After an initial week of purification using an Engelhard Q-5 filter to bring the impurity level down, the SAES St707 filter is installed and, over a week, the liquid purification system can purify the entire XENONnT xenon inventory down to <0.1 ppb of O_2-equivalent impurities. A direct result of the more efficient and complete purification is the unprecedented electron lifetime[2] achieved during the first science run, above 10 ms [114, 193], as shown in Figure 2.8.

To reduce radioactive krypton and radon contaminants, two distinct distillation columns are in place. The krypton column was developed, commissioned, and operated for XENON1T [133, 194] and further used in XENONnT to purify the full inventory of xenon. The main target of the removal is ^{85}Kr, which undergoes beta decay with a half-life of 10.74 years [195], and is present in commercial xenon as a trace contaminant. The achieved concentration during the first science run of XENONnT

[2]Electron lifetime is defined by the drift time after which the number of electrons is attenuated to 1/e.

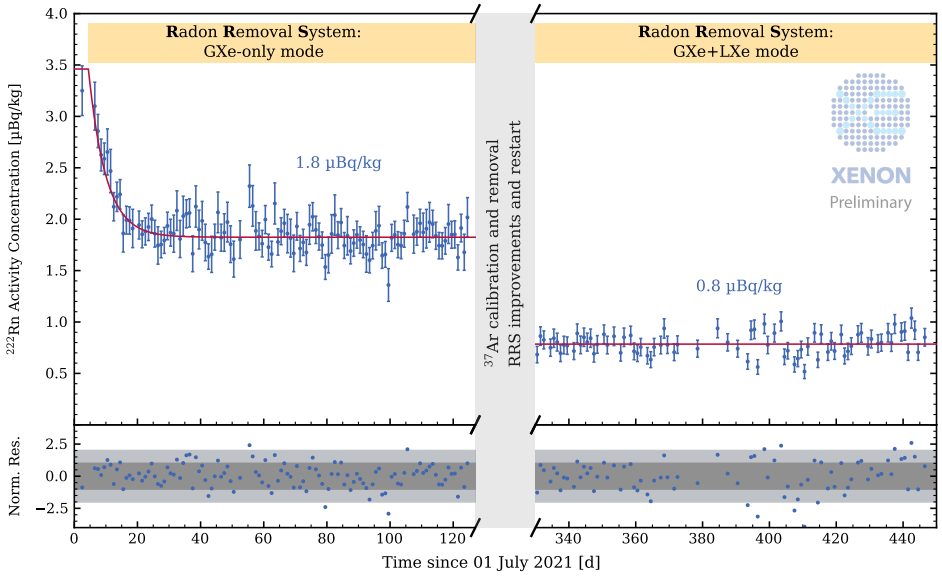

Figure 2.9.: Evolution of the ^{222}Rn activity concentration as a function of time with gas-only circulation (left) and gas and liquid circulation (right) over the radon removal system.

was (56 ± 36) ppq $^{\text{nat}}$Kr/Xe, measured by rare gas mass spectroscopy (RGMS) [196]. As for radon reduction, a fractional distillation column for high flows was developed to allow the removal of radon online during operation. It addresses the main source of ER background in XENON1T: ^{214}Pb decays originating from ^{222}Rn emanated from materials [197]. With online distillation in "gas-only" mode, where only the xenon extracted for gas purification is distilled, the measured radon concentration was 1.8 µBq/kg. Using also xenon extracted for liquid purification, the radon concentration achieved is 0.8 µBq/kg [191, 198]. The evolution of the radon activity concentration during the operation of the radon removal system is shown in Figure 2.9. Further information on radon mitigation and the radon removal system can be found in [198–200].

As previously mentioned, xenon is a rare gas and an expensive asset. To safely store the xenon when not in use in the cryostat or purification plant, and allow rapid transfer to safe conditions in case of an emergency, XENONnT makes use of two xenon storage units: ReStoX1 and ReStox2. With a capacity for 7.6 t of xenon as a cryogenic liquid or supercritical gas at room temperature, the former was designed, commissioned, and operated for XENON1T [133]. It is a vacuum-insulated stainless steel sphere and is located on the ground floor of the XENON service building (see Figure 2.7). ReStoX2 was built to hold the entire XENONnT xenon inventory and is operated alongside ReStoX1. The ∼5.5 m-high pressure vessel is placed close to the rest

of the XENON infrastructure in Hall B of LNGS (to the right of the space pictured in Figure 2.7). Its maximum rating is for 60 bar, for a total of $\sim$10 t of xenon. In a recovery scenario, either emergency recovery or draining the cryostat after an operation period, recuperation is possible both in liquid and gas phases. Liquid recuperation is handled solely by ReStoX1.

Active veto systems

The TPC is enclosed within two active water Cherenkov detectors: the muon veto (MV) and the neutron veto (nV).

The MV is kept from XENON1T [201], featuring 84 8 ″ PMTs model R5912ASSY from Hamamatsu [202]. The tagging efficiency for muons is expected to be $>$99.5 % and for showers of secondary particles interacting in the rock of the cavern walls it is $>$70 % [201].

The novelty of the veto sub-systems lies in the nV. An octagonal structure surrounding the outer vessel with high-reflectivity expanded PTFE walls is instrumented with 120 8 ″ PMTs model R5912-100-10 from Hamamatsu [203], as pictured in Figure 2.10. In parallel, a gadolinium water purification system (GdWPS) was constructed and connected to the water tank to, in the near future, dope the pure deionised water with gadolinium sulphate octahydrate ($Gd_2(SO_4)_3 \cdot 8\,H_2O$). This gadolinium salt enhances the neutron tagging capabilities of the vetoes by capturing neutrons on ^{157}Gd and ^{155}Gd, leading to the emission of 7.9 MeV and 8.5 MeV gammas, which, after Compton scattering, create free electrons that generate Cherenkov light [204]. The tagging of neutrons in the nV is correlated with potential neutron events inside the TPC, helping to reduce this background, often indistinguishable from DM interactions. During SR0, using only pure deionised water, the neutrino tagging efficiency was measured to be (53 ± 3) % [114]. The expected tagging efficiency after the introduction of the gadolinium salt is $\sim$87 % [114].

Callibration system

To fully characterise the detector response of XENOnNT, several internal and external sources are used. In this context, internal sources refer to radioactive isotopes that are injected into the gas xenon during recirculation and spread uniformly throughout

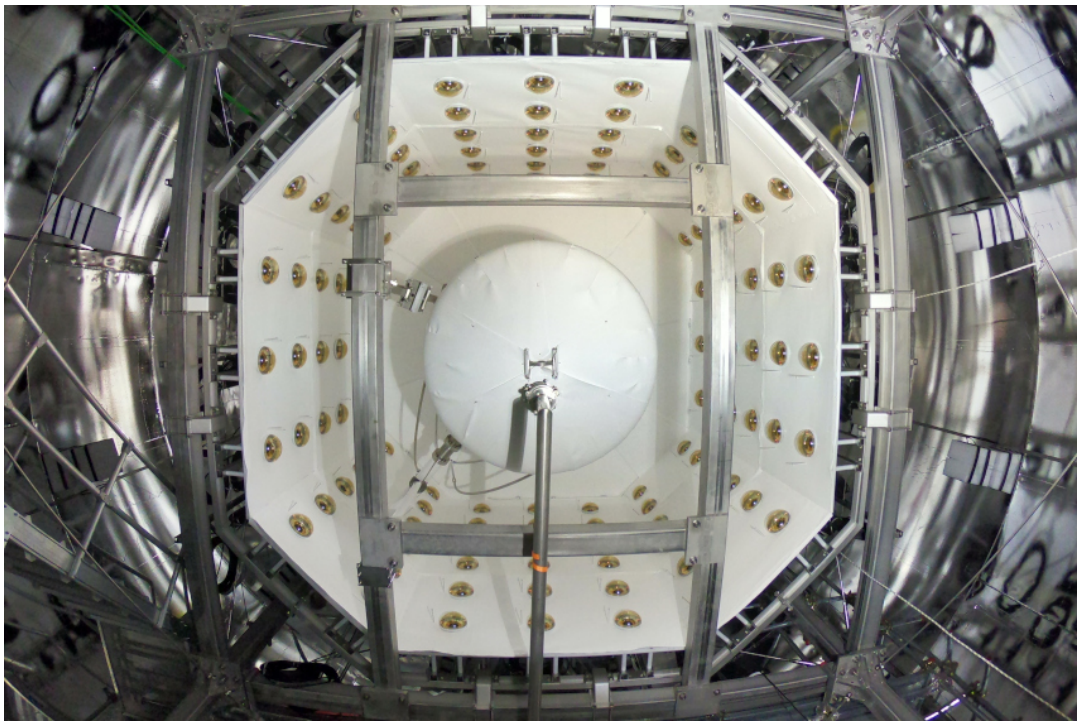

Figure 2.10.: Neutron veto system as seen from below during assembly, before the bottom panels were put in place. The 120 8 ″ PMTs' windows can be seen standing out of the expanded PTFE walls. From the bottom of the cryostat, the liquid xenon recirculation pipe can also be seen. Picture by the XENON Collaboration.

the active volume. On the other hand, external sources are deployed in dedicated structures inside the water tank and close to the outside wall of the cryostat.

Three internal sources were used during the SR0 science campaign of XENONnT: ^{83m}Kr, ^{220}Rn, and ^{37}Ar. ^{83m}Kr is a metastable isomer state with a half-life of 1.83 h, decay product of the long-lived ^{83}Rb, which decays emitting a 32.2 keV conversion electron, followed by another 9.4 keV conversion electron with a half-life of 154 ns. This source is used to study the spatial effects of the electric field and monitor the electron lifetime throughout the science run [172, 205, 206]. ^{220}Rn is used to characterise the ER band using the decay of ^{212}Pb, one of its daughter isotopes [172, 207]. ^{212}Pb decays via beta decay with a Q value of 560 keV. The third source utilised, ^{37}Ar, was successfully tested at the end of XENON1T and employed from the start of XENONnT [208]. The radioactive isotope undergoes electron capture and has a half-life of 35.01 days, ultimately decaying to ^{37}Cl with a Q-value of 813.9 keV. The vacancy created triggers electron rearrangement and, subsequently, the emission of x-rays and Auger electrons, resulting in lines at 2.82 keV (90.2 %), 0.27 keV(8.7 %), and 0.01 keV(1.1 %). Although the latter is below the energy threshold of XENONnT, the former two are used to

calibrate the detector response close to the energy threshold ($\sim$1 keV), in particular the charge-only channel.

As for the external sources, ^{228}Th was used to provide high-energy gammas to the TPC and nV, and an ^{241}AmBe source was used to calibrate the NR band and the neutron tagging efficiency of the nV [114, 209]. The ^{241}AmBe source is composed of ^{241}Am, which is an alpha-emitter, and ^{9}Be, which by an (α,n)-reaction to ^{12}C releases neutrons and a characteristic 4.4 MeV gamma-ray.

Apart from radioactive sources, the use of a D-D neutron generator to provide high-statistics neutron calibration is foreseen for the near future. The generator, unlike the one used in XENON1T, emits 2.2 to 3 MeV and 14 MeV neutrons in short-time pulses [210].

Data acquisition and slow control systems

The DAQ is responsible for recording data from the three detectors of XENONnT (TPC, MV, and nV). From the TPC, all analogue PMT signals are connected to dual-gain linear amplifiers with a $\times$10 and a $\times$0.5 output [1]. The addition of the low-gain data stream is aimed at high-energy studies, such as double-beta decay of ^{136}Xe, where the signals from the PMTs easily exceed the dynamic range of the digitisers [211]. Both high and low gain signals are read by v1724 flash Analog-to-Digital Converters (ADCs) from CAEN [212]. Ancillary data from the TPC, such as the summed signal from the low-gain outputs, the GPS synchronisation pulses, busy state signals, and veto triggers are collected in a separate v1724 digitiser named Acquisition Monitor. Details on the GPS synchronisation and absolute timing in XENONnT can be found in Section 5.4.1 of Chapter 5. The main novelty of the XENONnT DAQ is the introduction of a truly triggerless data stream, recording any pulse from any photosensor. The raw data stream is processed online in real-time by Strax [213] and its XENONnT-specific adaption straxen [214]. More information regarding the triggerless DAQ of XENONnT can be found in [215].

In parallel to data-taking, the control and monitoring of all the experiments' sensors are done by a SC system expanded from the one developed for XENON1T [133, 216]. The system automates numerous tasks, such as the tuning of cryogenic control parameters, changes in the high voltage of the PMTs, and LED calibration sequences

for the TPC PMTs. If the values of the monitor parameters fall outside the set range, automatic alerts are sent to the users on-site and to remote experts.

Chapter 3.

3D electric field simulations of the XENONnT TPC

Accurate electrostatic field simulations are essential to fully comprehend the XENONnT detector performance. There are several solutions available commercially available for such a task, mainly relying on Finite Element Method (FEM) simulations [217], such as COMSOL Multiphysics [218], ADINA Multiphysics [219], or Ansys Maxwell [220]. Often these solutions struggle to handle the full 3-dimensional (3D) geometry of the increasing size of LXe TPCs. However, using a Boundary Element Method (BEM) framework [221], volume-intense geometries are more efficiently handled and a simulation of the full 3D geometry becomes accessible. A 3D electrostatic simulation of the XENONnT TPC using BEM was developed in parallel to efforts conducted through 2D-axial symmetric simulations with COMSOL by the XENON collaboration. The BEM simulations presented here were performed with a custom version of the KEMField software, part of the Kassiopeia package [2], initially developed for the KATRIN experiment [222]. The computation was conducted on the computing infrastructure of the University of Zurich using several Nvidia V100 [223] and Nvidia T4 [224] Graphics Processing Units (GPUs). A full 3D geometry model of all electrodes and other relevant parts of the detector was constructed, and, as a result, a full description of the electric potential and field inside the TPC was simulated.

In Section 3.1, the BEM framework and the computation of the electric fields in KEMField are introduced. The implemented geometry of the XENONnT TPC is described in Section 3.2 and the results of the electrostatic simulation are presented in Section 3.3. An outlook of the developed work, main challenges encountered,

and future perspectives on 3D field-simulation for LXe dual-phase TPCs is given in Section 3.4

3.1. BEM for electrostatic field simulation

For a full 3D electrostatic simulation of the XENONnT detector, FEM-based simulation frameworks need to discretize the entirety of the volume. To achieve high levels of accuracy, the resulting mesh often becomes too large to be handled, requiring large amounts of memory and processing power, although possible [225]. More commonly, this method is used when simplifying the complexity of the problem by simulating only a 2D axial-symmetric representation of the actual geometry of the TPC. Although large accuracy can be reached in these simulations, and often sufficient to achieve the desired detector understanding and overall science goals, they remain an approximation of the true local electric fields, as the non-axial-symmetric elements are by definition not properly treated. Examples of such elements are the wires of the electrode grids or the 24 PTFE panel walls of the TPC. In the BEM [221], however, only the surfaces are discretized and meshed. Therefore, large-volume regions are not impeditive to the method and do not increase the complexity of the computation, making it a suitable choice for a volume-intensive design such as the one of XENONnT and, in general, current and next-generation LXe TPCs. Moreover, BEM simulations have proven to be faster at reaching the same level of accuracy in most geometries when compared with analogous FEM simulations [226].

In a BEM simulation, the geometry of the overall surface of electrodes and dielectric boundaries, S, is meshed into a finite set of non-overlapping sub-elements, S_i:

$$S = \bigcup_{i}^{N} S_i \ , \tag{3.1}$$

where N is the total number of sub-elements S_i in the surface S. For each sub-element, the charge density is assumed to be constant and uniformly distributed throughout the region. The size of the sub-elements can vary throughout the surface, allowing for a varying level of detail in different regions. Despite the fact that the charge density is unknown, the applied voltage is given *a priori*. The relation between the potential and charge density of each sub-element S_j is given by introducing the Coulomb matrix, where each element, C_{ij}, represents the electric potential, U_i, of the sub-element S_i at

the centre of the sub-element S_j and is given by:

$$U_i = \sum_{j=1}^{N} C_{ij}\sigma_i \ , \tag{3.2}$$

where σ_i is the charge density of the sub-element S_i. The elements C_{ij} of the Coulomb matrix can be obtained by integrating over the geometrical shape of S_i:

$$C_i\left(\vec{r}_j\right) = \frac{1}{4\pi\epsilon_0}\int_{S_i}\frac{1}{\vec{r}_j - \vec{r}_{S_i}}d^2\vec{r}_{S_i} \ , \tag{3.3}$$

where ϵ_0 is the electric permittivity, $\vec{r}_j$ is the centre point of sub-element S_i, and $\vec{r}_{S_i}$ is a point on the sub-element S_i. The sub-elements could assume any arbitrary voxel shape but are usually restricted to triangles, rectangles, or trapezoids so that their Coulomb matrix element can be easily calculated [227].

For dielectric boundaries, which also get meshed into sub-elements, S_i, the boundary condition is applied in the corresponding matrix element as:

$$\epsilon_i^+\vec{E}_i^+\vec{n}_i + \epsilon_i^-\vec{E}_i^-\vec{n}_i = 0 \ , \tag{3.4}$$

where $\vec{n}_i$ is the surface normal vector of the sub-element S_i, $\vec{E}$ is the electric field, ϵ the dielectric constant, and the signs $+/-$ are with respect to the above and below of the surface of the sub-element, considering its normal vector.

Given the potential applied to each surface and the computed Coulomb matrix elements, equation 3.2 can be numerically solved for the charge densities of each sub-element. The framework employed, a C++ custom version of KEMField [2,228], uses the Robin Hood method [229,230] as an iterative solving technique until all individual electric potentials of each sub-element, calculated by their computed charge densities, are within a user-defined limit of the applied voltages. The accuracy of the calculation, at any iteration, is calculated as the relative error of the potential of each sub-element, U_i, in relation to the applied potential to the element it belongs, U_0, defined as

$$\theta = \frac{U_0 - U_i}{U_o} \ , \tag{3.5}$$

The iterative process ends when the largest accuracy calculated is below a user-defined accuracy limit.

The Robin Hood method has the advantage over other suitable algorithms in that its memory use scales linearly with the number of sub-elements and it can be highly parallelised, decreasing computation time. For further details on the BEM implementation and the Robin Hood method, the reader is directed to references [1,2, 227,231,232].

After the iterative calculation converges, the charge density of all the sub-elements of the geometry is known, and the main computation is finished. At this stage, both the electric potential and field can be calculated at any given point in space by the superposition of the individual contributions of the sub-elements given by:

$$U(\vec{r}) = \frac{1}{4\pi\epsilon_0}\sum_{i}^{N}\sigma_i \int_{S_i}\frac{1}{\vec{r}-\vec{r}_{S_i}}d^2\vec{r}_{S_i}\ , \tag{3.6}$$

$$\vec{E}(\vec{r}) = \frac{1}{4\pi\epsilon_0}\sum_{j}^{N}\sigma_j \int_{S_j}\frac{\vec{r}-\vec{r}_{S_j}}{\left(\vec{r}-\vec{r}_{S_j}\right)^3}d^2\vec{r}_{S_j}\ . \tag{3.7}$$

where $U(\vec{r})$ is the electric potential and $E(\vec{r})$ the electric field at any point in space, $\vec{r}$.

3.2. The XENONnT geometry

All the parts of the XENONnT detector relevant to the full 3D simulation were considered and their geometry was implemented in the simulation framework. For simple geometries, such as planes and wires, native functions from KEMField were used to mesh the surface with a defined level of granularity[1]. For more complex shapes, such as the stainless steel holders of the electrodes or the 12-sided wires and guards of the field cage, the computer-aided design (CAD) drawings were meshed with the software Gmsh [233] and Fusion360 [234] and later imported into the framework. Before meshing, the CAD drawings of the parts were simplified to avoid an excessive amount of sub-elements, which would hinder the computation without any impact

[1] In this context, "granularity" is referring to the size of each sub-element described in the mesh. High granularity stands for highly-meshed, meaning smaller sub-elements and, in principle, a more realistic geometry description.

Table 3.1.: Elements of the XENONnT detector considered in the KEMField implementation. The type of meshing elements used and the number of discretised sub-elements are presented for each part.

Part		Meshing type	Number of sub-elements
Electrodes	Top screen	Grid: Parallel wire mesh Holder: CAD import	30 293
	Anode		38 218
	Gate		30 482
	Cathode		31 658
	Bottom screen		30 293
Liquid-gas boundary		Circular plate mesh	149 700
Field shaping elements	Wires	CAD import in two halves	359 260
	Guards	CAD import	405 504
Other elements	PMT arrays	Simple geometry: Circular plate mesh	161 260
		Complex geometry: CAD import and detail modelling	2 373 839
	Inner cryostat	CAD import	198 120
	Bell	CAD import	188 760
	Outer cryostat	CAD import	386 880

on the TPC's electric fields. An example of these simplifications is the removal of the holes in the electrode holders where the wires for the grids are secured, as well as the grooves that keep the wires in the correct position during stretching. The different elements considered in the simulation and the specific method or class employed for their meshing are detailed in Table 3.1.

There are a total of 4 223 007 surface sub-elements in the final geometry model. However, some elements are suppressed or simplified for the calculation: the cryostats and bell are not present, and, for the main simulations, the PMT arrays are only considered as discs. In the simplified model used, the total number of sub-elements to

compute is 1 236 668. The computing time varied depending on the complexity of the geometry, averaging ∼1.9 sub-elements per GPU, per second.

The reference frame used in the KEMField model has the origin at the centre of the gate electrode, similar to the coordinate system used for XENONnT analysis. However, contrary to the normal orientation in analysis, the parallel wires of the electrode grids are parallel to the x axis and the perpendicular wires are parallel to the y axis. A representation of the full model of XENONnT implemented in KEMField is shown in Figure 3.1, done with the VTK [235] software in ParaView [236].

Liquid-gas boundary

The liquid-gas boundary is implemented as a dielectric boundary, defining the regions of the liquid and the gas xenon as the two distinct dielectric regions of the TPC. The element is approximated as a circular surface with infinitesimal height and radius up to the inner radius of the inner vessel of the cryostat. The dielectric constants used were 1.95 for liquid and 1 for gaseous xenon [237]. The implementation of the geometry uses the *XDisk* class with discretisation both radially (250 steps) and axially (200 steps).

Electrodes

As summarised in Table 3.1, all the electrodes have two distinct parts: the wire grids and the stainless steel holders. The holders are imported from externally meshed and simplified CAD drawings based on the ones used for production. On the other hand, the wire grids of the electrodes are implemented as *XWireMesh* objects, which define a set of straight, parallel wires with an outer circular shape and user-defined mesh granularity of the wire sub-elements. The diameter of the wires, the pitch of the grid, and the voltage applied to the electrode are also defined by the user, corresponding to the values of the respective parts in XENONnT. The specification of each simulated electrode can be found in table 3.2.

At the final stages of XENONnT's design, two sets of perpendicular wires were added to reduce the sagging effect resulting from the electrostatic force between the gate and the anode. Sagging could realistically lead to the meshes of the two electrodes becoming too close and creating electrical discharges from one to the other, resulting

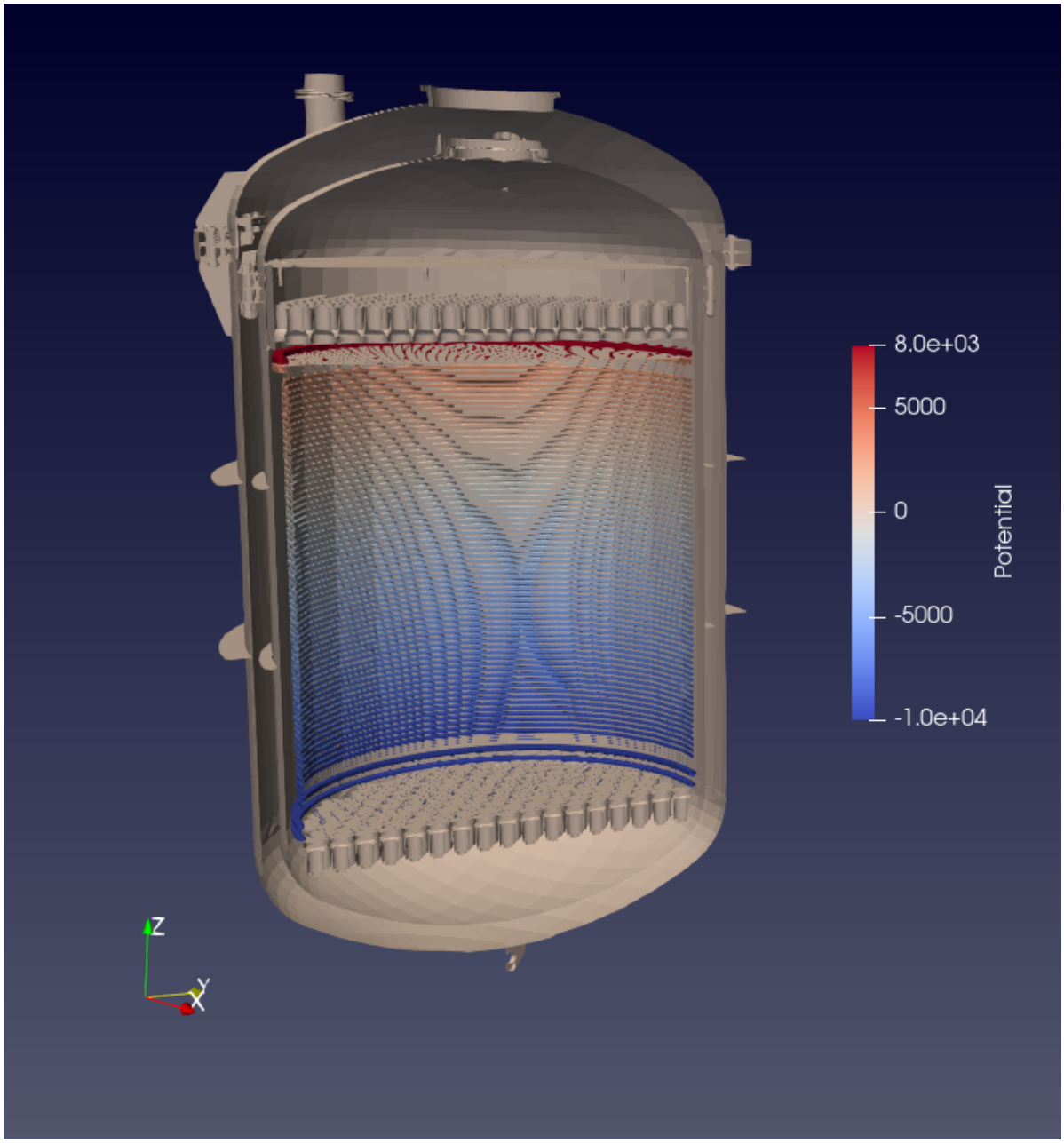

Figure 3.1.: Full detector geometry implemented in KEMField, containing all the elements of Table 3.1: electrodes (wires and holders), PMT arrays, field shaping elements, inner cryostat, bell, and outer cryostat. The model reflects the nominal electric field considered during XENONnT's design phase. For the electric field simulations executed, only a simplified model without vessels and simplified PMT arrays was considered, as described in the text.

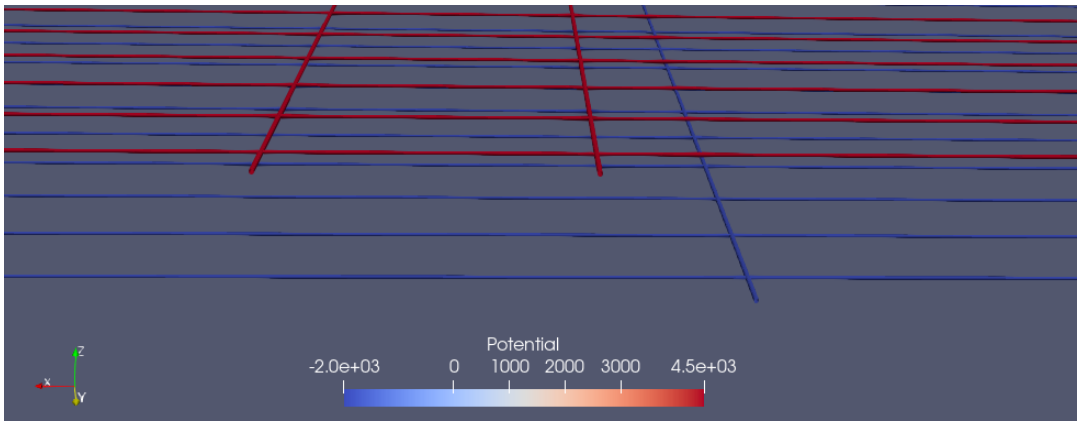

Figure 3.2.: Detail on the geometry of the perpendicular wires. Another set of one wire on the gate and two on the anode is located on the symmetrically opposite side of the electrodes

in light-intense incidents, damage to the wires, or even a constant current discharge between the electrodes. The extra pair of perpendicular wires were inserted in the mesh in such a way that they support the rest of the parallel wires and prevent major outliers in the sagging of the electrodes. The overall mesh is still expected to sag up to a certain degree, but an on-site test proved that the average sagging decreased and the risk of discharges was greatly reduced [184]. Two perpendicular wires were added to the gate and four perpendicular wires were added to the anode, all with a diameter of 0.304 mm. These are implemented individually in the simulated detector's geometry as meshed wires with the *XWireGeo* class. A representation of the implemented geometry can be found in Figure 3.2.

Table 3.2.: Designed voltages and sizes of XENONnT electrodes.

Electrode	Nominal voltage [kV]	SR0 voltage [kV]	Wire diameter [mm]	Wire pitch [mm]
Top screen	−1.5	−0.9	0.216	5
Anode	8	4.9	0.216	5
Gate	0	0	0.216	5
Cathode	−30	−2.7	0.304	7.5
Bottom screen	−1.5	−2.7	0.216	7.5

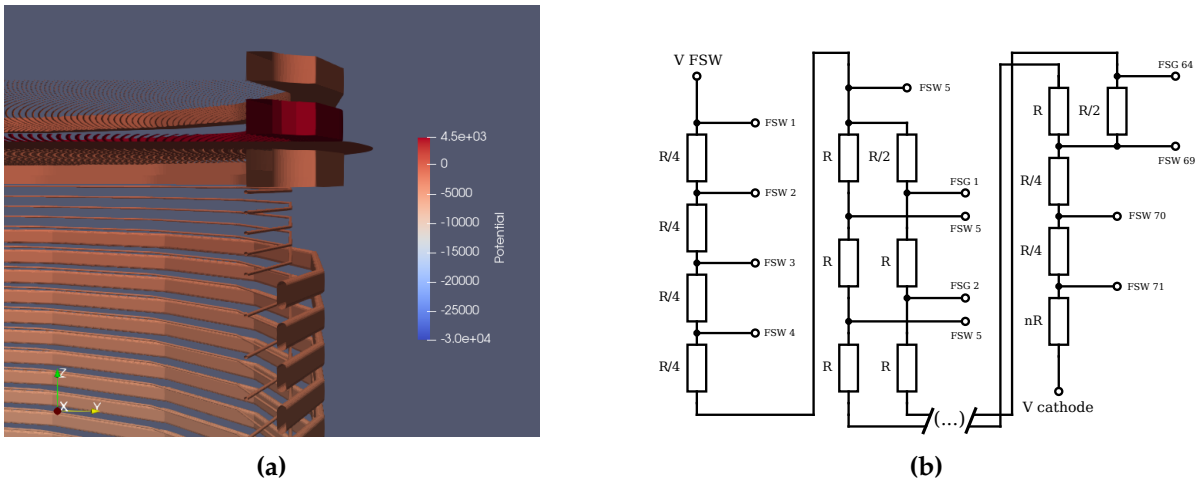

(a) **(b)**

Figure 3.3.: **(a)** Detail of the top corner of the TPC with the field cage elements implemented. From top to bottom, the different elements present are the top screen mesh and holder, the anode mesh and holder, the liquid-gas dielectric boundary, the gate mesh and holder, and the field shaping elements (wires and guards). The extra four field-shaping wires are visible before the first field-shaping guard. **(b)** Electric circuit schematic of the field elements' resistor chain. R is a selected resistance value, which, for the case of XENONnT, was 1 GΩ.

The Field Shaping Elements

The field shaping elements are responsible for ensuring a close-to-uniform electric field through the active volume of the TPC, minimising the volume in which charges are not drifted up to the liquid-gas interface. The XENONnT TPC has a more intricate design regarding its field-shaping elements than its ancestors [132, 133]. To improve the uniformity of the field close to the walls and avoid charge-up of the PTFE, two different elements are in place: a set of 71 wires in contact with the PTFE walls and a set of 64 guards placed 12 mm outwards and between the wires. Near the gate, from top to bottom, there are five wires until the guards start, and three wires after the guards end, near the cathode. All the elements are connected through two redundant resistor chains from the first wire (on top, near the gate) down to the cathode. Changing the applied voltage on the first wire (or the cathode) adjusts the voltage of all the field shaping elements, a powerful tool to tune the drift field uniformity, especially in the corner region near the gate.

In the KEMField framework, both the field shaping wires and guards are implemented as imported external meshes in order to properly describe their 24-sided polygon shapes. The voltage is set individually for each of the elements with a con-

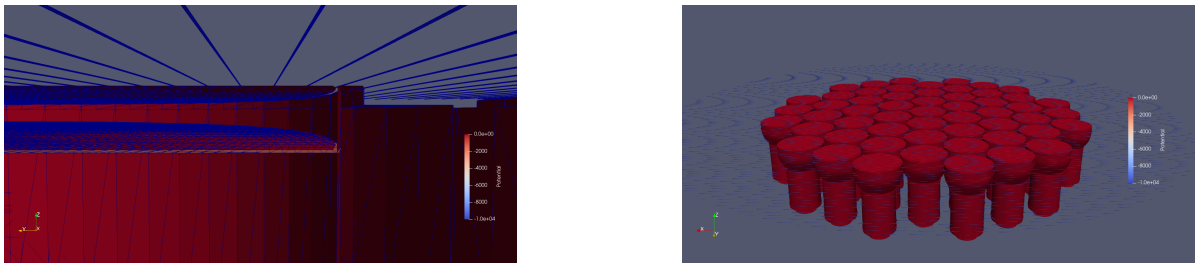

(a) **(b)**

Figure 3.4.: **(a)** Detail of the implemented PMT model with different dielectric boundaries that form the PMT window and photocathode, meshed as discs, and the PMT shell imported from a simplified version of the R11410 Hamamatsu PMT. **(b)** Geometry of the detailed PMT array model and a screening mesh.

stant voltage drop for each consecutive wire and guard in the main section of the field cage, ΔV, is given by:

$$\Delta V = \frac{V_{FSW_0} - V_{cathode}}{N_{wires} + n}\,, \tag{3.8}$$

where V_{FSW_0} is the voltage applied to the top-most wire, $V_{cathode}$ is the voltage applied to the cathode, N_{wires} is the total number of wires, and n is a term accounting for a different resistor type on the connection to the cathode in order to achieve a more uniform field in the bottom corner of the TPC.

Detailed modelling of the PMT arrays

The PMT arrays are simulated as simple meshed planes with a set voltage equal to the expected voltage of a PMT photocathode. In KEMField, the circular discs of the PMT arrays were constructed with the *XDisk* class and set to $-1.5\,\mathrm{kV}$. This approximation is justified by the presence of the top and bottom screen meshes, which considerably shield the active volume of the TPC from the local field of the PMT arrays.

However, for detailed studies of the field effects close to the PMTs, a more accurate and structured geometry of the PMT arrays is needed. More detail is also required if the shielding meshes become defective, such as the bottom screen mesh in XENONnT, and one wants to better predict the electric field close to the photosensors.

In the detailed model, each PMT has three parts:

- The PMT body: the geometry of the PMT is taken from a CAD drawing of the R11410 Hamamatsu PMT, made hollow and without a window. The voltage on the body of the PMT is set at 0 V.
- The PMT window: the quartz window of the PMT is reproduced with two discs representing both dielectric boundaries: from liquid (gas) xenon for the bottom (top) array and the quartz, and from the quartz to vacuum.
- The photocathode: the photocathode stands right after the window and is implemented as a disc for the purposes of the simulation. The voltage applied to the photocathode is by default -1.5 kV but it can be tuned specifically for each PMT to follow the set voltage on the detector itself.

A PMT array is then composed by placing the PMT models at their defined positions and defining their individual voltages. To study the field effects close to the PMTs, a smaller array was implemented to reduce the computation time required, as shown in Figure 3.4b. While the effects on the active region of the TPC are lost, in particular close to the edges, for local effects near the PMTs this smaller model is sufficient

3.3. Results of the 3D electrostatic field simulations

For a given geometry, the simulation and output-processing framework is similar. First, KEMField is used to compute the charge density of all the meshed sub-elements given a certain accuracy, as described in 3.1. In the simulations of the drift field, extraction field, and field near the perpendicular wires, the accuracy of the calculation, as defined in Equation 3.5, was set to 0.01 %. From equation 3.6, the potential of any point can then be computed. From the available methods in KEMField, this calculation is done for a rectangular grid of points of varying grid step granularity. Close to the walls or electrodes, the grid is set to high density ($\sim$1 mm step), while for the bulk of the volume the density of points is lower ($\sim$8 mm step) to expedite the calculation. The computation time scales linearly with the number of sub-elements in the meshed geometry and the number of points requested for calculation.

The resulting set of points with electrode potential values is then processed with a dedicated package, PyKeField [238], to compute the electric field, determine the electric field lines (streamlines), and generalise both the electric potential and field to

any point within the volume. The components of the electric field are calculated for each point where the electric potential is defined as:

$$\vec{E}(x_i, y_i, z_i) = -\nabla U(x_i, y_i, z_i) \ , \tag{3.9}$$

where $\vec{E}$ is the electric field vector, U is the electric potential, and (x_i, y_i, z_i) is a point on the initial grid of computed U values. To account for miscalculated points on the grid, the potential and electric field functions are generalised in two steps. A finer grid at each calculated z value plane is constructed by interpolating the initial values. Then, the values of U and $\vec{E}$ per z slice computed on a regular grid of user-defined size and boundaries are set as the basis for 3D interpolative functions. In particular, the value at any given point in between the base grid points is computed by trilinear interpolation [239] using the RegularGridInterpolator class from the SciPy open-source package [240, 241]. The resulting well-behaved functions, $U(x, y, z)$, $E_x(x, y, z)$, $E_y(x, y, z)$, $E_z(x, y, z)$, provide the electric potential and electric field for any point in the 3D volume in question.

In the following subsections, the results obtained with the geometries described in the previous section are presented and discussed. In particular, they cover the drift field and electron drift paths in the active region of the TPC at the described nominal setup of XENONnT in Subsection 3.3.1. The results on the extraction field are reported in Subsection 3.3.2, and the effects arising from the extra perpendicular wires in Subsection 3.3.3. Finally, in Subsection 3.3.4, the electric field near the bottom PMT array in the case of applied high-voltage on the bottom screening mesh is studied.

3.3.1. Drift field

The drift field is at the core of functioning TPC. It is responsible for preventing the total recombination of the ionised atoms and drifting the resulting electron clouds. Both the magnitude and the direction of the electric field at any given point in the active volume are important, determining the following properties:

- Electron drift velocity: the magnitude of the drift field determines the velocity of the drifting electron clouds and, therefore, the drift time, which is used to reconstruct the z coordinate of a given event.

- Field streamlines and electron loss: the drift field is never completely uniform up to the edge of the walls due to the finite geometry of the detector. In reality, some of the field streamlines cross the walls, leading to a partial or even total loss of the drifting charges. In the case of a partial loss, the resulting S2 signal is then smaller than expected, and the event possibly contributes to ER leakage into the NR band. On the other hand, in the case of a total loss of the drifting charges, no S2 signal will be observed, and its unpaired S1 counterpart, which could get mistakenly paired with an uncorrelated S2 signal, is a prime example of a potential accidental coincidence event.
- Local charge yield: the charge yield of an interaction in the liquid xenon target depends on the local electric field. Although in normal conditions the field is sufficiently uniform that this difference is negligible, in specific conditions and parts of the active volume where the field misbehaves, this effect can be relevant.
- Correction of reconstructed positions: the observed position for an event is inferred by its hit pattern in the PMT top array. However, due to the non-uniformities of the drift field, the reconstructed position of the events requires a spatially dependent correction to determine the true position of the interaction site.

The obtained results are shown in Figure 3.5. Since representing the values of the electric potential and field in a three-dimensional plot is difficult without relying on interaction by the observer, the results are shown in the $R^2 \times Z$ space[2], where each point on the 2D plane is an average value of the potential or field over the azimuthal angle.

The average drift field value in the z direction is 181.5 V/cm with a standard deviation of 16.6 V/cm. Within a cylindrical fiducial volume of 4 t, the average drift field becomes 185.0 V/cm with a much reduced standard deviation of 5.3 V/cm. With this fiducial condition, the average electric field in the x direction is 0.02 V/cm with a standard deviation of 0.08 V/cm, and in the y direction is 0.03 V/cm with a standard deviation of 0.09 V/cm. The larger field non-uniformities are present close to the walls ($<$5 cm) and on the top and bottom corners of the TPC. In these regions, the influence of the finite geometry of the meshes and the presence of the electrode holders become dominant factors in the field direction.

[2]Here, R^2 is the radial projection into the xy plane, such that $R^2 = x^2 + y^2$

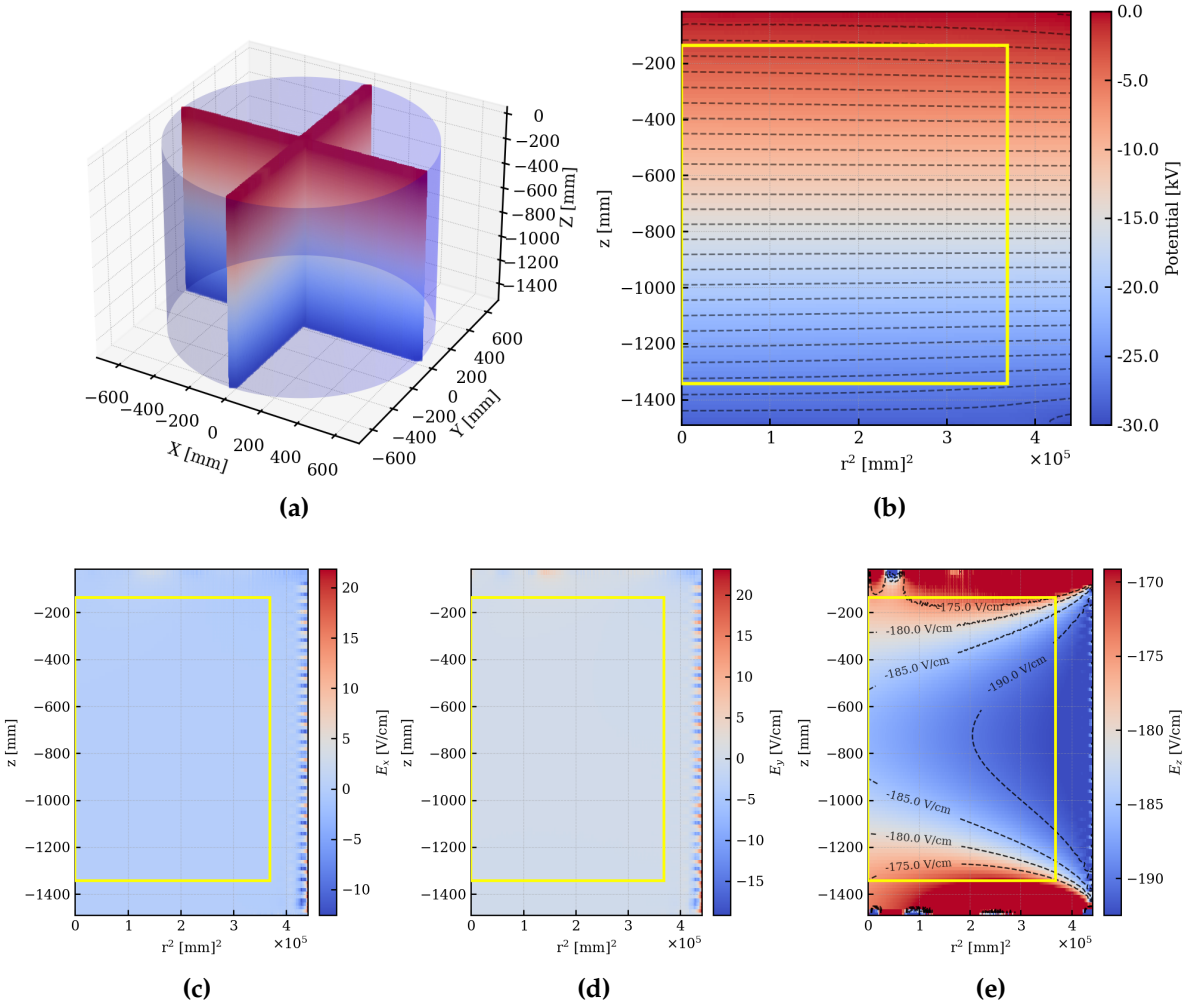

Figure 3.5.: **(a)** Values of the electric potential computed in the planes $x = 0$ and $y = 0$, with the TPC edges represented as surfaces in blue. In the figures **(b)** to **(e)**, the 2D projection of the simulated electric potential and electric field components (E_x, E_y, and E_z) of the drift region of the TPC are shown, respectively. The dotted lines are contours of the same potential or field. For reference, the edges 4 t cylindrical volume are shown in yellow. For the projection of E_z, in **(e)**, the color scale was constrained to the electric field values within the 4 t fiducial volume in order to emphasise the differences within the inner region of the TPC.

A direct result of such non-uniformities is the previously mentioned distortion of the field lines and the increase of electron loss regions. Without the presence of magnetic fields, the electric field streamlines coincide with the electron drift path. To compute such lines, a simple discrete algorithm was used to follow the direction of the field from a start point, $\vec{r}$, up to a final position at the wall of the TPC or the gate electrode plane: To compute the field lines, and therefore the electron drift path, the following algorithm is followed:

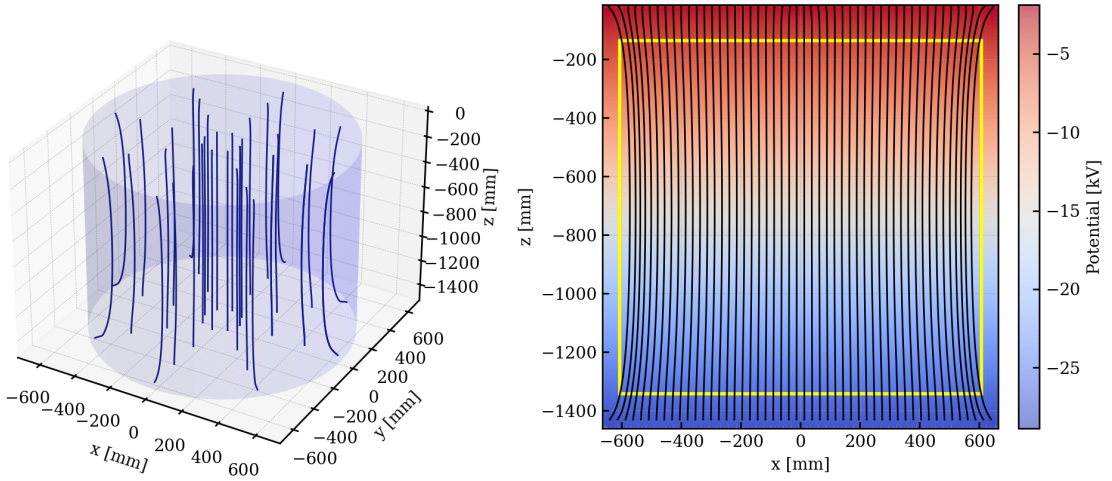

(a) **(b)**

Figure 3.6.: **(a)** A 3D representation of a set of 28 field streamlines radially and azimuthally distributed in the active region of the TPC. **(b)** Potential and streamlines on the plane $y = 0$. The fiducial volume of a 4 t cylinder is shown in yellow. Although high uniformity is achieved in the large majority of the plane, streamlines near the wall have a high chance of not reaching the gate electrode and are overall more likely to have a larger change between the initial and final x and y coordinates.

1. Define a starting position, $\vec{r}$;
2. Determine the normal vector, $\vec{n} = \frac{\vec{E}}{\|\vec{E}\|}$;
3. Calculate $\vec{r'} = \vec{n} \cdot dL$;
4. Save $\vec{r'}$;
5. Repeat with steps 2 to 4 with new $\vec{r}$ as $\vec{r} = \vec{r'}$ until the calculated position is outside the defined boundaries;

where dL is the defined discrete step taken in each iteration of the algorithm. The electric field components at each step are calculated from the previously described generalised 3D functions of the field. An example of the computed streamlines is shown in Figure 3.6.

Since each field line is unique when computed sufficiently accurately, the reconstructed initial position can be determined by a distortion function, S:

$$(x, y, z) = S^{-1}(x', y', z') \tag{3.10}$$

where x' and y' are the observed position at the gate, z' is the drift length calculated with the drift velocity and time, and (x, y, z) is the true interaction site. Note that the value of z' can be used to determine the length, which, in conjunction with the local drift velocity, provides a more accurate calculation of the drift time than solely the height of the track (the projection on the z axis).

The distortion correction function, in the same fashion as the 3D field functions, can be calculated in a grid of points and generalised for the entire volume. For initial positions from which the field streamlines converge with the walls of the TPC, S is not defined, signifying a charge-insensitive region of the detector.

The behaviour of the field close to and above the gate also has a great influence on the behaviour of the electron clouds and the generation of the S2 signal. Effects in these regions are discussed in the following sections.

3.3.2. Extraction field

The extraction field, defined between the gate and anode electrodes, is responsible for the extraction of the electron clouds from the liquid to the gas phase and for the secondary scintillation process leading to the S2 signals. Similarly to the drift field, both the direction and magnitude of the vector field are important to the resulting signals. In particular, they influence the following parameters:

- Extraction field uniformity and loss of charges: since the extraction field is much stronger and much shorter in length than the drift field, field uniformity is usually easier to achieve. However, in the corners of the TPC and near the perpendicular wires, the uniformity needs accurate study.
- Extraction efficiency: the electron extraction efficiency is dependent on the local electric field intensity at the liquid-gas boundary. Due to geometry effects such as those from the perpendicular wires and sagging of the electrode wires (not treated in this study), the extraction efficiency can have different values throughout the boundary plane.
- Electron multiplication and S2 generation: when extracted from the liquid, the electron clouds start an ionisation and multiplication process in the gaseous xenon phase that also produces scintillation light, creating the S2 signal. The multiplication factor, often referred to as "single electron gain", depends on the

magnitude of the electric field throughout the drift path of the electron clouds from the gate to the anode region.

The electric potential and field were simulated using the procedure described in Section 3.1 and in the beginning of the current section. A finer grid of points was considered to compute the electric potential from the charge density than had previously been used for the drift field. In the nominal configuration used, the gate electrode is placed at $z = 0$ mm, the anode at 8 mm, and the liquid-gas interface is in between the two at $z = 4$ mm. The results for the simulated electric field regarding the extraction region are shown in Figure 3.7.

The average extraction field in the liquid phase is 3.71 kV/cm with a standard deviation of 0.53 kV/cm and 7.24 kV/cm with a standard deviation of 1.26 kV/cm in the gas phase. At the nominal pressure of 2 bar, the average extraction efficiency for this range of electric field magnitudes is (95 ± 2) % [170].

3.3.3. Field near perpendicular wires

As described in Section 3.2, six additional wires, perpendicular to the alignment of the grids, were added to the electrodes of the XENONnT TPC. The field effect of perpendicular wires is not negligible and became one of its distinct characteristics. Due to the lack of symmetry in the position and orientation of such wires, the electric field in this region is a prime example where 3D simulation is required. 2D axial-symmetric models, such as the ones largely studied with BEM, are insufficient to tackle this problem. Below, the perpendicular wires field region is studied and discussed in the context of KEMField.

To study the perpendicular wires region at the top of the TPC, a simplified geometry model was considered, consisting of the cathode, gate, and anode wires – one perpendicular wire on the gate and two on the anode –, and the liquid-gas boundary. The perpendicular wires are centred around $x = 0$, unlike in the full XENONnT geometry. In the full geometry, each set of wires is symmetrically placed at $x = 130.6$ mm, $x = 139.95$ mm, and $x = 158.65$ mm. For most of the cross-sectional plane, the wires are far enough from the edges that no effect from the finite edges of the grids will be a major contribution to the local field. In the modelled geometry, the relative distance between the wires is accurate, but an offset of $+144.625$ mm is needed to switch to the proper x coordinates in the XENONnT geometry. In the studied geometry the gate

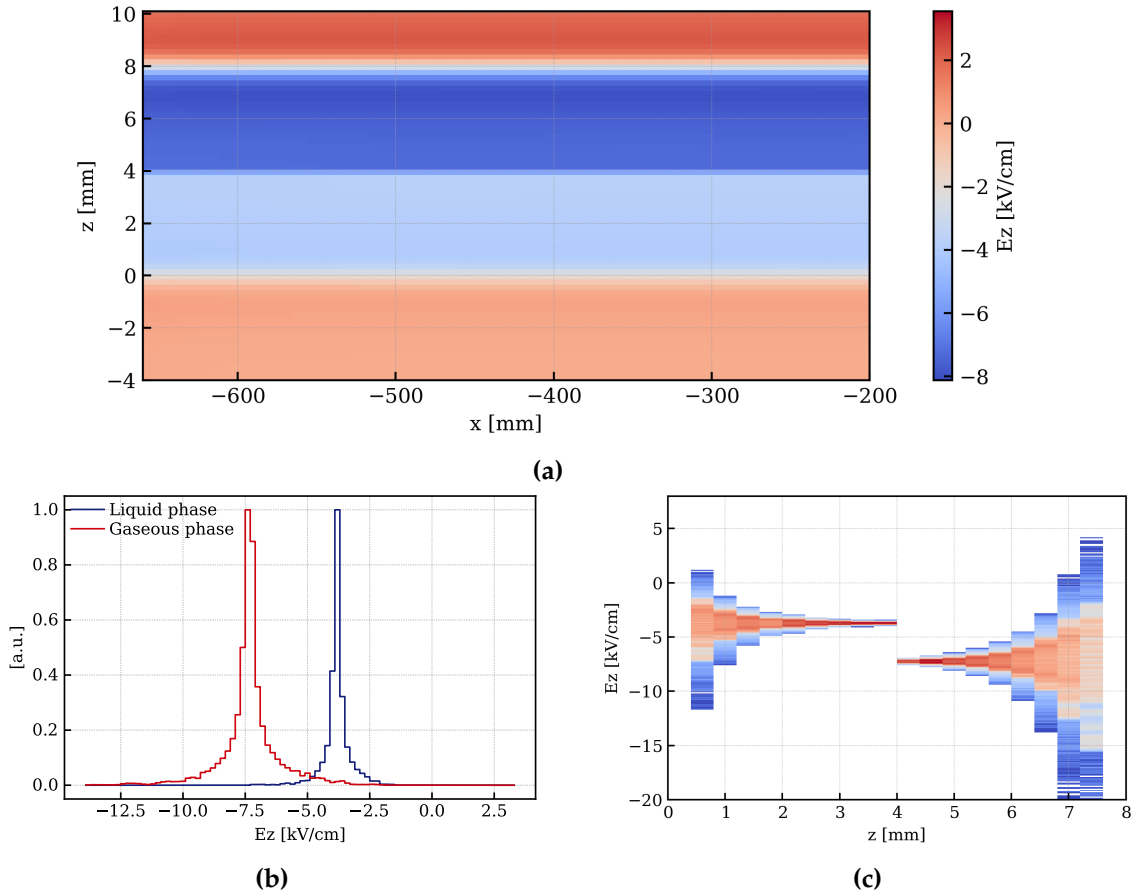

Figure 3.7.: **(a)** Distribution of the vertical component of the electric field, E_z, at the plane $y = 0$. The different field regions are clearly and correctly seen between the different electrodes: the high region of the drift field at $z < 0$mm, the extraction field in liquid at $0 < z < 4$mm, the extraction field in gas at $4 < z < 8$mm, and the field between the anode and the top screening mesh at $z > 8$mm. **(b)** Histogram of the vertical component of the electric field, E_z, in the liquid and gas regions of the extraction region. The average E_z values of these distributions are 3.71 kV/cm and 7.24 kV/cm, respectively. **(c)** Values of E_z in function of z, emphasising the discontinuity of the field at the liquid-gas dielectric boundary and the effect of the distance to the grids on the variance of the electric field magnitude.

wire stands at $x = -14.025$ mm, inner anode wire at $x = -4.675$ mm and outer anode wire at $x = 14.025$ mm. The electric potential and field were computed following the same procedure detailed above and the results can be seen in Figure 3.8a and 3.8b.

From the electric potential and field, it is clear that the perpendicular wires have a strong local influence, in particular on the x and y directions of the electric field. However, their effect is limited to a few cm around these elements. The electric field streamlines were computed for a set of initial positions, far and close to the affected

region, to study the direct impact on the drift path of the electron clouds. The results are shown in Figure 3.8.

The effects of the perpendicular wires on the electron cloud paths are consistent with what is observed in real data: electrons underneath the wires are repulsed away, leaving a region with a lack of events (Figure 3.8c). In simulation coordinates, the region extends between $x = -29$ mm and $x = 6$ mm. In height, the field streamlines are close to vertical up to $z \approx -4$ cm, where they rapidly change direction. Large electron clouds could be split into two different sites, leading to events likely tagged as two different interactions and potentially mimicking a multiple scatter event. Moreover, there is an agglomeration of streamlines at the outer anode perpendicular wire, which would translate into an increased rate of events in this region. Apart from the repulsion effect of the perpendicular wires, the focusing effect between the gate wires in the y direction is also visible (Figure 3.8d).

As mentioned at the end of section 3.3.1, making use of the computed streamlines, one can correlate the initial position, $\vec{r} = (x, y, z)$, with the expected position at the anode plane, $\vec{r'} = (x', y', z')$. A map of the distortion function is then made from a fine grid of initial positions and the computed correction vector, $\Delta\vec{r}$. This function provides the expected difference. It is worth noting that, although in the x and y coordinates the correction correlates with the direct physical meaning of the difference between the expected and observed position, the correction value for the z coordinate does not, as all electron clouds end at the anode. In this case, the correction in z is the difference between the length of the simulated path and the length if the path were strictly vertical. This quantity describes, from a particular initial position, how further an electron cloud travels in the simulated configuration in comparison to a homogeneous field. The mapped correction function for the simulated perpendicular wires region is shown in Figure 3.9.

Moreover, it is of interest to study how well the simulated behaviour matches the effect encountered in the XENONnT data. For field-distortion-related studies, calibration data with ^{83m}Kr injected in the active volume is extremely useful, as detailed in Chapter 2. The source spreads throughout the volume, reaching a uniform spatial distribution in a short time. After applying a set of selection cuts to the recorded events, the non-corrected volume of the active volume can be determined. A prominent feature of the summed xy distribution of events is the presence of two parallel gaps due to the perpendicular wires. Moreover, on the outer side of the gaps, there is an agglomeration of events in two distinct stripes (see figures 3.10b).

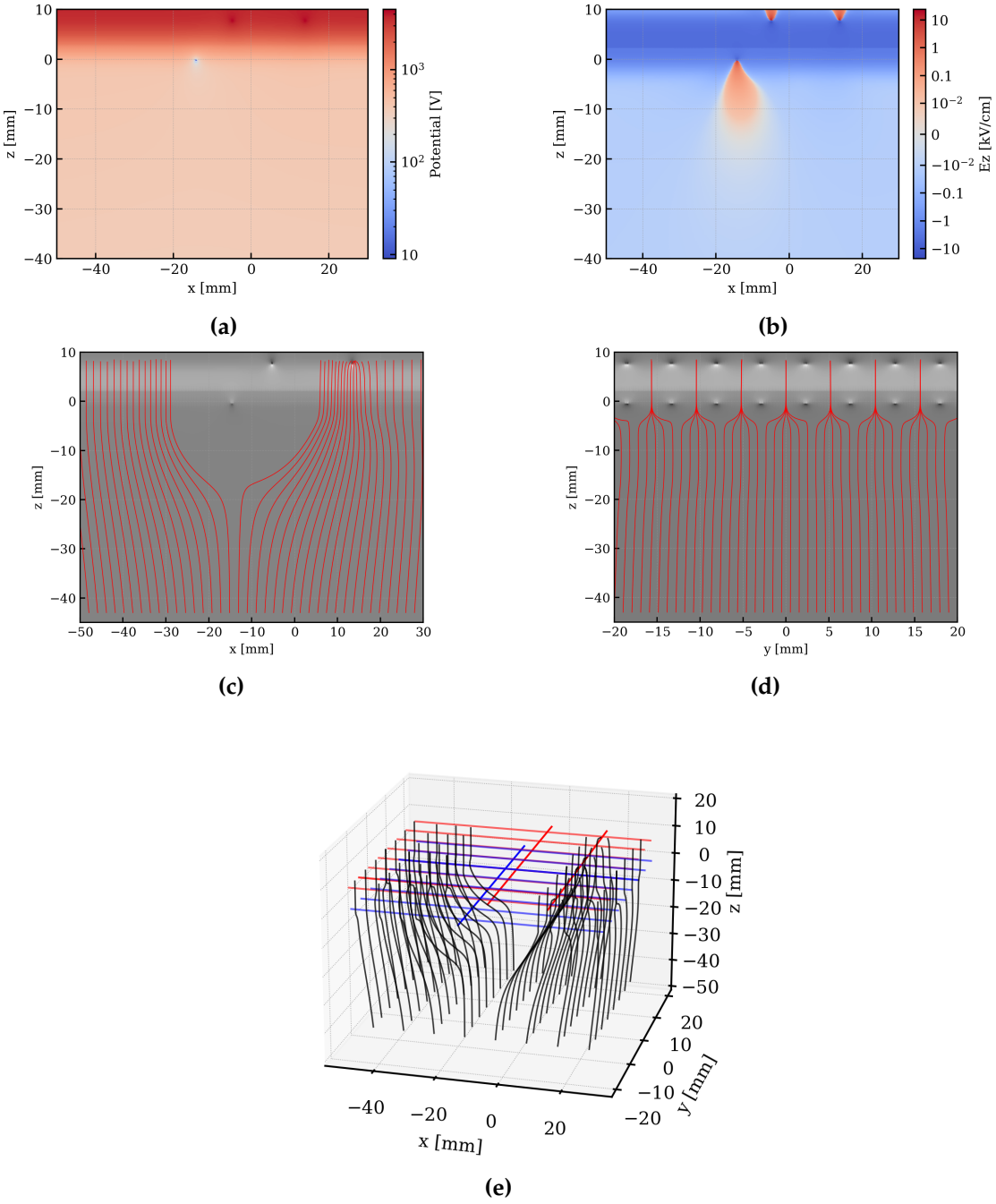

Figure 3.8.: The values of the electric field potential **(a)** and and vertical **(b)** component calculated for the plane $y = 0$. The effect of the perpendicular wires on the local field breaks the uniformity observed in other regions of the TPC. A set of streamlines is shown in **(c)** and **(d)** for the $y = 0$ and $x = 0$ planes, where the features of the electron cloud paths are observed. In the x direction, a region with no streamlines connected with the rest of the TPC is formed, while in the y direction, the focusing between gate wires is observed. Although in the simulated geometry the gate and anode wires stand above one another, in XENONnT they are misaligned by half a pitch. **(e)** displays a 3D rendition of a set of streamlines where the same features can be seen.

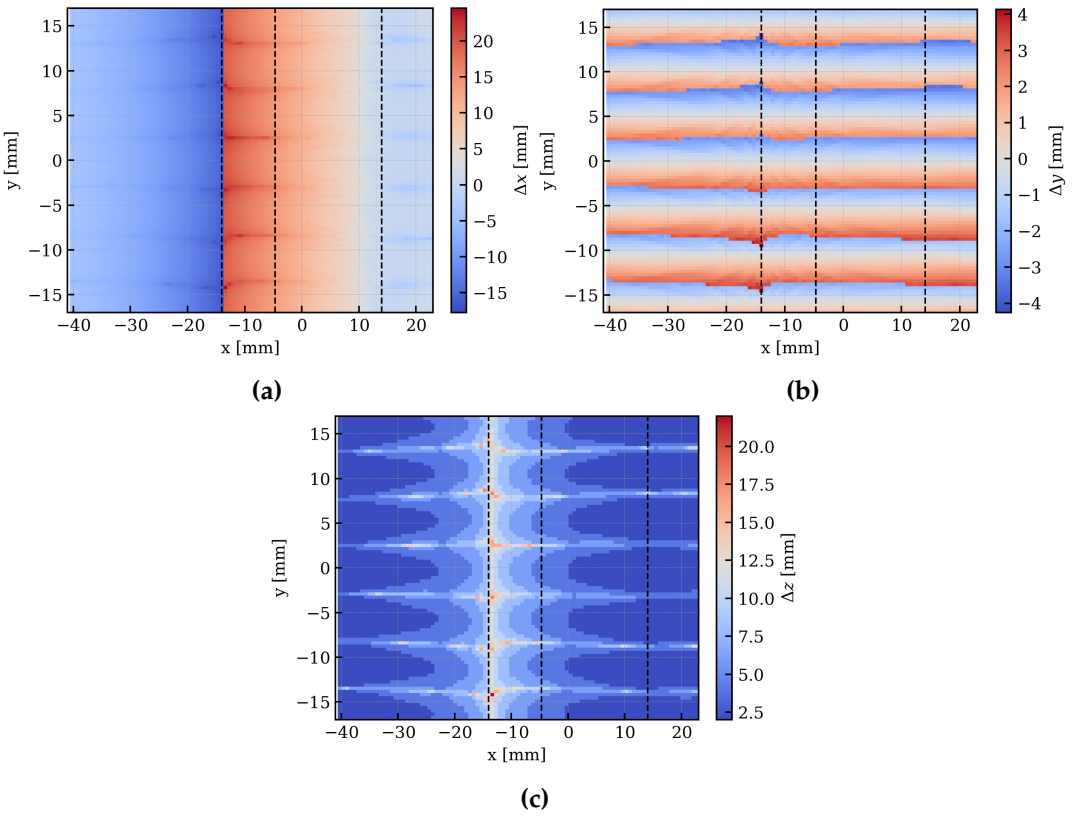

Figure 3.9.: Distortion correction function in the region of the perpendicular wires calculated from $z = -40$ mm. The correction differences for x, y, and z coordinates are shown in **(a)**, **(b)**, and **(c)**, respectively. Dashed lines mark the perpendicular wires' positions.

To compare the simulation results with the calibration data, a set of uniformly distributed events was simulated. Their initial z coordinate was -45 mm, where the field is still not highly affected by the local non-uniformity of the perpendicular wires. The effect of position reconstruction was addressed by applying Gaussian smearing of 1.3 cm to the final positions. Finally, to compare both simulated and real data, the number of events was normalised.

Figure 3.10 shows the comparison of the normalised rate of events expected if the field followed the KEMField simulations with the observed ^{83m}Kr rate. There is a clear mismatch between the two. While ^{83m}Kr data shows a double peak structure to the right of the valley, the expected rate from the simulation does not. In the data, the valley appears shifted to the right by $\sim$5 mm and centred on the gate wire position. Finally, from the simulation, an increased rate is expected on both sides of the valley, albeit larger on the outer side of the perpendicular wires. Such a feature is not as clear in the data regarding the inner edge.

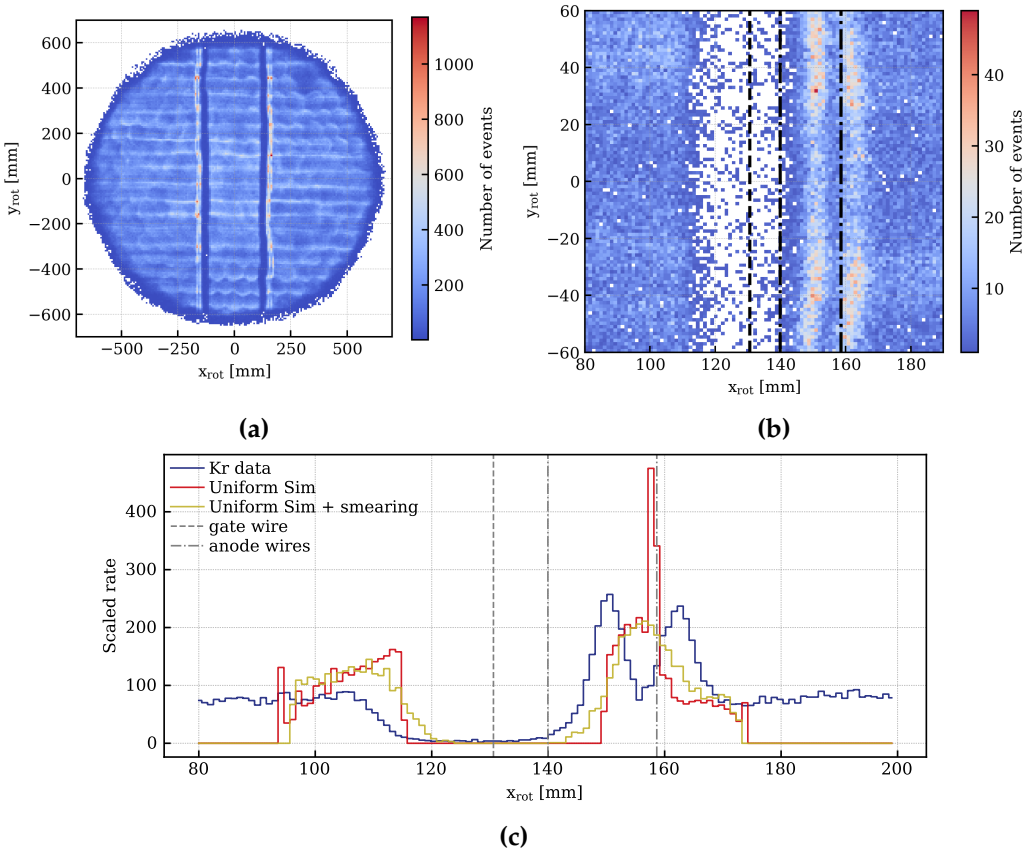

Figure 3.10.: Uncorrected xy distribution of ^{83m}Kr events in the full XENONnT TPC **(a)** and close to a set of perpendicular wires **(b)**. The nominal positions of the perpendicular wires are shown in dashed (gate) and dot-dashed (anode) lines. **(c)** Scaled rate of events in function of their reconstructed x coordinate for both ^{83m}Kr and simulation from a uniform distribution.

In summary, the perpendicular wires geometry was successfully implemented in KEMField, and the simulation provides reasonable results. It predicts a gap in the possible positions of extracted electrons of $\sim$35 mm, which is observed in ^{83m}Kr data from XENONnT. However, the simulation does not replicate other features seen in the data, such as the double peak structure in the event rate on the outer side of the perpendicular wires. Given the distance between the two peaks in rate, a likely cause of the mismatch is the coordinates used for the wires. The perpendicular wires were simulated at their nominal positions, but either due to issues during the assembly of the TPC or due to sagging effects, the effective position of the wires appears to be different.

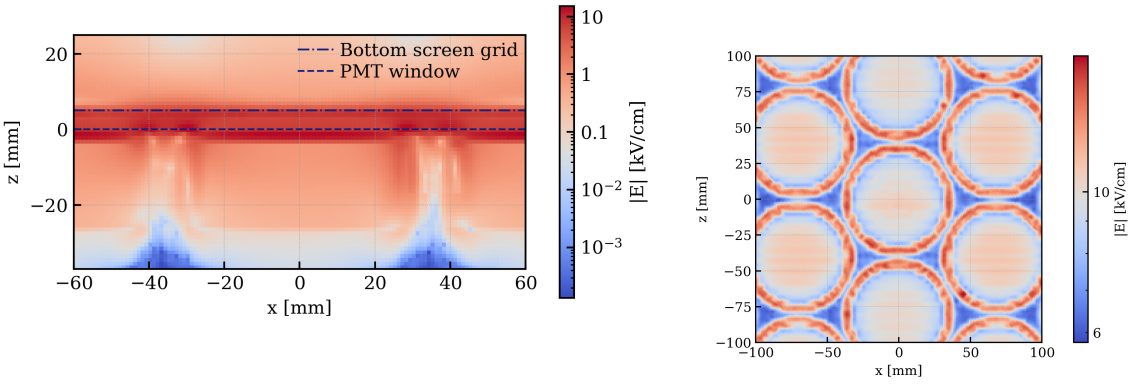

(a) **(b)**

Figure 3.11.: **(a)** Magnitude of the electric field in the plane $y = 0$, where the shape of the PMTs' bodies and the high field region between the bottom screen and the quartz window are depicted. **(b)** Magnitude of the electric field in the xy plane 0.1 mm above the quartz window of the PMTs.

3.3.4. Field near PMT arrays

During XENONnT's early commissioning, an unknown event forced the cathode and bottom screen mesh to be in short circuit. In this case, if the cathode is operated at its nominal voltage, the bottom screen would be subject to very high voltage while being in close proximity to the PMTs, about 5 mm away. To investigate the magnitude of the electric field close to the PMTs in this scenario, the geometry of a small PMT array, shown in Figure 3.4b, was simulated with a calculation accuracy of 0.1 %.

The resulting electric field around and inside the PMTs can be seen in Figure 3.11. The maximum value of the electric field is 18 kV/cm, which is insufficient for electron multiplication and avalanche in liquid xenon [242]. Such high fields are reached right above the window and on the inner border of the PMT, where the photocathode is closer to the PMT body. The x and y components of the field are, for the large majority of the geometry, an order of magnitude below the z component. The resulting field streamlines are, therefore, vertical, and any electron cloud forming between the screening mesh and the PMT array will be propelled downwards towards the quartz windows.

Since no electron avalanche and proportional scintillation are likely to happen in liquid xenon at the electric field observed, the TPC could be run with nominal fields and high-voltage applied at the bottom screen via the cathode. However, the effects of

a high rate of accelerated electrons hitting the quartz windows could lead to a highly accelerated deterioration of the PMTs. Despite the possibility, it was quickly found that no high voltage could be supplied to the cathode without triggering the current limit of the power supply, indicating a short to ground. As a result, the cathode and bottom screen mesh were operated at a reduced voltage (more details on the operation conditions are given in Chapter 2).

3.4. Outlook

In this chapter, the BEM full 3D simulations of the XENONnT detector in its nominal configuration were reported and discussed. It is noteworthy the absence of direct comparison with data from the detector or with the mentioned 2D axisymmetric simulations done with COMSOL. This limitation arises from the difficult process of making the simulations converge. The BEM method is particularly sensitive to the meshing of surfaces, in particular in regions such as the perpendicular wires and the ending of the electrode wires on the electrode holders, where elements of different surfaces can easily overlap. Despite following the best practices described in [2, 227] and in private communications with Kassiopeia developers, the meshing of the XENONnT geometry was nevertheless unstable, making convergence of the charge density calculation highly dependent on both fine-tuning the mesh and the set voltages.

At the same time, COMSOL Multiphysics works as a full-stack simulator, with an included geometry meshing tool, has been established both in academia [133, 172, 225] and industry [243–245] for several years. Another asset of COMSOL when compared to Kassiopeia/KEMField is the possibility to define the charge distribution in certain regions or surfaces. This feature can be used to simulate different levels of charge-up of the PTFE walls and, by comparison with data, estimate the true value of the accumulated charge [184]. Such a procedure is unnatural in BEM methods, where the charge density is the unknown parameter to optimise based on the set voltages. Albeit conceptually possible, Kassiopeia/KEMField does not provide the tools necessary for field calculation with priors on the charge distribution, and their development surpasses the extent of this work.

During the commissioning and first science run of XENONnT, COMSOL-driven field maps described the observed behaviour of data with sufficient accuracy. A case

still stands for certain regions of the TPC not conveyed by the 2D axial-symmetric geometry, such as the field close to the perpendicular wires. For that case in particular, the simulations presented in Section 3.3.3 were determinant to understand the process and used to define a preliminary region where the effect was dominant[3]. Analogous simulations were done using COMSOL Multiphysics and its 3D FEM module, with high adaptability to the changing conditions of the detector in early stages of data taking. Due to the aforementioned meshing and convergence issues, KEMField-driven simulations struggle to provide the same level of throughput.

As a concluding remark, the question "are 3D BEM electrostatic simulations the right fit for the needs of current and next-generation LXe TPCs" comes naturally. As in all good questions, the answer is complex. The case made in Section 3.1 on the lack of scalability of FEM simulations and the advantages of BEM in geometries with large volumes is definitively compelling. The work here presented is a concrete basis for future work, both from the geometry implemented, the computation procedures adopted, and the analysis framework developed. However, in order to use the method to its full capacity, further development is needed to better adapt the Kassiopeia software to the specific needs of dual-phase TPCs, or a different software employed in the efforts. Recently, COMSOL has released a BEM extension to its AC/DC module in COMSOL Multiphysics version 5.3 [246], including support for an hybrid BEM/FEM solver. Although preliminary studies with the module show unnatural behaviour of electric fields, especially very close to thin wires [247], it is expected for the module to undergo further development. Depending on the geometry chosen for future detectors, 2D axial-symmetric simulations might continue to prove sufficient for the needs of characterising the electric fields in the active region of their TPCs. However, if local effects only described by a 3D geometry are of concern, as with the perpendicular wires case in XENONnT, a robust solution for 3D simulations must be found or developed. Such a tool would provide the means to properly model the electric field and streamlines in regions of large non-uniformity. The electron diffusion properties can then be modelled and realistic S2 signal shapes simulated, allowing for the exploration of the detector's sensitivity in complex field regions of the TPC.

[3]Later on, the "near-wire" region was also defined in a data-driven way using the spatial distribution of S2 signal shape parameters, as described in Section 4.2.4 of Chapter 4.

Chapter 4.

Analysis and results from the first science run of XENONnT

The XENONnT detector, described in Chapter 2, was assembled during the first half of 2020, less than two years after the decommissioning of XENON1T. With its larger target mass and numerous upgrades to its ancillary systems, the experiment had two main goals for its first science run (SR0): explore the low-energy ER excess of XENON1T [248], and detect or constrain the cross-section of WIMP-nucleon interactions.

In this chapter, Section 4.1 details the configuration at which the XENONnT detector was operated during SR0 and the types of data acquired. Section 4.2 gives an overview and discusses the analysis of SR0, with an emphasis on the S2 width selection criteria. Given the low drift field and the perpendicular wires features present in XENONnT, the S2 width cut has a significant impact on the science reach of the experiment, as will be detailed. Finally, the results on the low-energy ER and low-energy NR dark matter searches are discussed in Sections 4.3 and 4.4, respectively.

4.1. SR0 conditions and acquired data

In the fall of 2020, the TPC was filled with LXe. Subsequently, the many sub-systems were commissioned and the first data was acquired. However, after normal operation at nominal conditions over several weeks, in November 2020, a short circuit occurred between the cathode and the bottom screening mesh, which then limited the cathode voltage to $-2.75\,\mathrm{kV}$, instead of the design voltage of $-30\,\mathrm{kV}$. From then on, the

electrodes were maintained at the following potentials: $V_{\text{anode}} = 4.9\,\text{kV}$, $V_{\text{gate}} = 0.3\,\text{kV}$, $V_{\text{cathode}} = -2.75\,\text{kV}$, and $V_{\text{FSR}} = 0.65\,\text{kV}$[1]. These voltage values corresponded to a drift field of 23 V/cm and an extraction field of 2.9 kV/cm [114, 193].

After Kr distillation, the low-energy ER background in XENON1T was dominated by ^{214}Pb, a β-emitter from the chain of ^{222}Rn, which comes from the emanation of materials. To suppress this background, a strict material radioassay campaign to select and clean materials [249] and a ^{222}Rn removal cryogenic distillation column were employed [198] (see Chapter 2). During the commissioning of the new radon removal plant, it was found that its operation in LXe mode resulted in a drastic drop in xenon purity. Therefore, the system was used only in GXe mode for SR0, resulting in a ^{222}Rn level of $1.7\,\mu\text{Bq}\,\text{kg}^{-1}$ [193].

Science data was entirely blinded in the ROI for both the ER and NR searches. The detector ran in stable conditions during the entire period. The temperature and pressure of the detector remained stable at $(176.8 \pm 0.4)\,\text{K}$ and $(1.890 \pm 0.004)\,\text{bar}$, respectively. The liquid level above the gate electrode was set and maintained at $(5.02 \pm 0.20)\,\text{mm}$, resulting in an electron extraction efficiency into the gas phase and single electron (SE) gain[2] of 53.3 % and (31.2 ± 1.0) PE, respectively. The TPC PMTs were operated at a gain of $\sim 2 \times 10^6$, showing stability within 3 % throughout SR0. Due to internal vacuum degradation, high noise or light emission, 17 PMTs were excluded from the analysis.

Several episodes of "hotspots" and "warmspots" were registered, characterised by the localised and intermittent high-rate emission of S2 signals from single or few electrons. To safeguard the electrodes and PMTs, the common response was to ramp-down the anode and steadily bring it back to operational condition. The method proved reliable enough to acquire quality data and for any remaining effect to be corrected in the analysis.

Several sources were used to calibrate the response of the detector. Figure 4.1 shows the different periods of data taking in SR0. Before the beginning of the run, the NR response was calibrated with an ^{241}AmBe source, and the ER response with the ^{212}Pb beta spectrum from an injected ^{220}Rn source. After all the science data was acquired, an ^{37}Ar source was injected to further characterise the detector response to ERs at low

[1] As discussed in Chapter 2 and 3, the topmost field shaping ring has a dedicated power supply such that the voltage of the chain can be independently set from the voltage of the gate.

[2] The SE gain is defined as the number of photoelectrons detected from the extraction of a single electron.

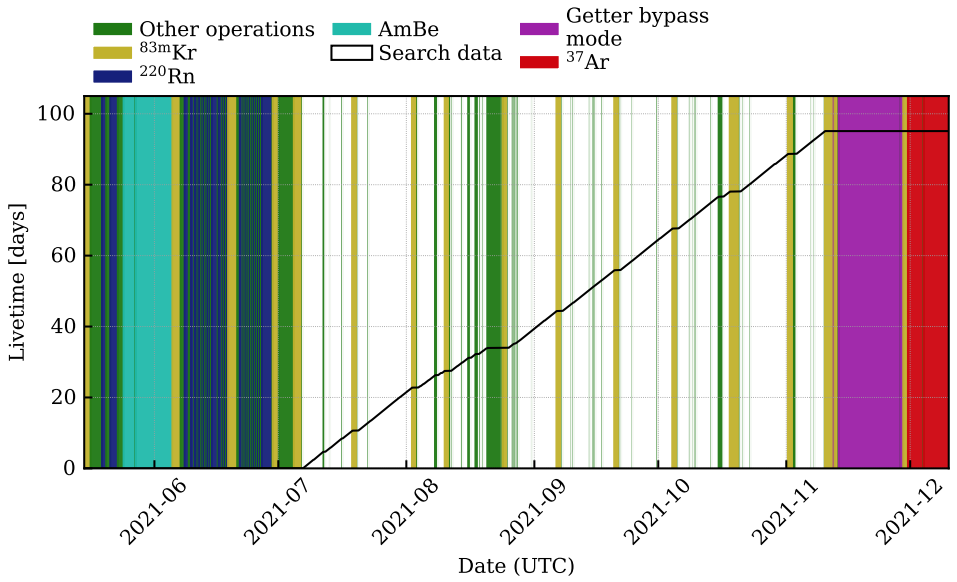

Figure 4.1.: Cumulative livetime of SR0 science data corrected for DAQ deadtime. The different calibration periods and periods of operations not suitable for science data are marked in coloured patches.

energy. ^{83m}Kr was injected every other week to monitor detector stability and tune time- and position-dependent corrections. More details on the calibration methods can be found in Chapter 2 and in [206–209]. At the end of the science run, in an effort to rule out the tritium hypothesis put forth to explain the XENON1T excess, the detector was run in "tritium-enhanced" mode by bypassing the GXe-dedicated getter [193]. In total, SR0 data was acquired from July 6, 2021, to November 10, 2021, with a total live time of 97.1 days, or 95.1 days after deadtime corrections (see Figure 4.1).

As detailed in Chapter 2, the energy of a recorded event can be reconstructed with Equation 2.8. The detector-specific values of $g1$ and $g2$ were obtained by using the calibration sources ^{37}Ar and ^{83m}Kr. Additionally, the xenon activation lines ^{131m}Xe, and ^{129m}Xe could be used on the fit as inputs for the high-energy regime. For the fit used in the science searches, these were excluded. The photon and electron gains are determined to be $g1 = (0.151 \pm 0.001)$ PE/photon and $g2 = (16.5 \pm 0.6)$ PE/electron [114, 193], respectively, assuming an energy of 13.7 eV [160] per quantum of charge or light. The linear fit of the charge yield as a function of the light yield used to estimate the $g1$ and $g2$ parameters is shown in Figure 4.2. These values are corrected for an energy-dependent "reconstruction bias", which arises due to nonlinearity in the S1 and S2 reconstructions. This nonlinearity is the result of the single-PE threshold effect and PMT afterpulsing. The effect, which is $\sim$1 % at 41.5 keV

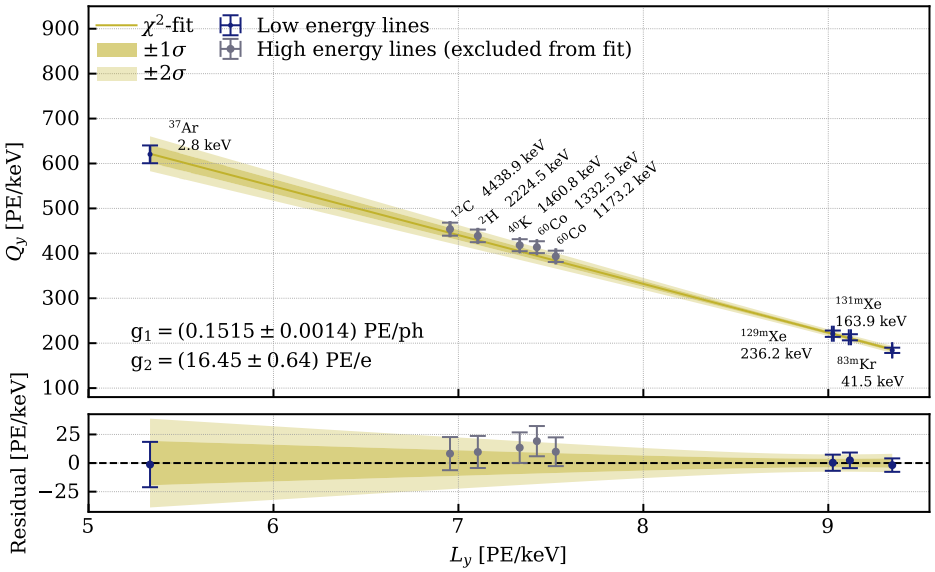

Figure 4.2.: Charge yield, Q_y, as a function of the light yield, L_y, for several monoenergetic calibration lines, commonly referenced as the Doke plot. For the linear fit, the high-energy lines shown in grey datapoints are not considered.

(^{83m}Kr) and ∼2 % at 236.1 keV (^{129m}Xe), is modelled empirically with input from both data and simulation.

4.2. Analysis of SR0

The XENONnT data analysis process is split into several steps: data taking, processing, correction, selection, and statistical inference. First, data is acquired over a given period of time, divided into "runs" of, typically, 30 minutes or 1 hour. A database of the runs, implemented in NoSQL-based MongoDB [250], automatically stores information for each run: a unique run number, type of data (background or calibration type), start and end times of acquisition, and where the raw and processed data can be found. The database can be easily accessed and queried from a front-end website [215].

The raw data stream acquired, composed of the amplitudes of the PMT signals recorded by the digitisers over time, is then processed on-site with the generic framework strax [213], in particular its XENONnT implementation straxen [214]. Details on data processing and event reconstruction are given in Subsection 4.2.1. During regular operation, straxen fully processes all the data $\mathcal{O}(10)$ s after the interactions happen in the TPC, and the data is partially online for monitoring purposes within $\mathcal{O}(30)$ s. This

allows for constant monitoring of data quality and detector stability, especially during operations that entail the change of detector conditions, such as ramping of electrode voltages or calibration source injections. The raw and processed data are subsequently automatically transferred to redundant remote storage elements, both in Europe and in the United States of America. The management of data is done by a custom code using the Rucio software [251].

The next step is data correction, where the reconstructed events are corrected to account for effects such as electron lifetime, field non-uniformity, and position-dependent light collection efficiency (LCE). Data corrections are discussed in Subsection 4.2.2. After data correction, the data undergoes a selection process to identify events of interest from what could be considered background. Details on data selection can be found in Subsection 4.2.3. Finally, when the interactions in the detector are sufficiently characterised and livetime accumulated, the data in the ROI is unblinded. Subsequently, the results are determined by statistical inference, as broadly detailed in [79]. The results of the low-energy ER and low-energy NR searches can be found in [114, 193] and here discussed in Sections 4.3 and 4.4, respectively.

4.2.1. Event reconstruction

During the event reconstruction process, a series of output files are generated with increasing levels of data reduction and abstraction, named “datakinds”. These are: raw records, records, peaklets, peaks, and events[3]. If only information from the later stages is required, it is possible to process each of the intermediate datakinds using strax, which can greatly reduce processing time and the needed computing resources. As an example, to process events given a different configuration without changing the way peaks are built, the new events can be created from the available peaks instead of reprocessing from the raw records base.

The process of reconstructing interactions is done in multiple steps, correlated to the different data kinds mentioned. It begins by identifying “hits” within each time sequence, corresponding to where the PMT signals go above the expected baseline level. If a number of hits, N_{hits}, is observed over a number of PMTs, N_{PMT}, in a coincidence window, T_{coin}, these are clustered and split into peaklets by a natural

[3]Apart from the general meaning of "interaction" used up to this point, in the context of straxen and the XENONnT analysis framework, "event" is a highest-level datakind. Events are defined after S1 and S2 signals pairing and have available their properties after corrections

breaks goodness of fit algorithm. For a standard analysis, the variables take the values $N_{\text{hits}} = 3$, $N_{\text{PMT}} = 3$, and T_{coin} =100 ns. The identified peaklets are then classified as an S1-, S2- or unknown-like signal peaks based on their rise time[4], the fraction of the total signal seen by the top array, named area fraction top (AFT), and N_{PMT}. Since S2 signals can often be several µs long, they usually consist of several S2 peaklets. Therefore, S2 peaklets and neighbouring signals are merged into a single S2 peak.

At the peak stage, the signals have maintained their peaklet classification but are not yet combined into S1-S2 pairs. At this point, the horizontal $(x_{\text{uncorrected}}, y_{\text{uncorrected}})$ position of the S2 peaks is reconstructed from the PMT hit pattern on the top array by three simulation-trained position reconstruction algorithms based on a Convolutional Neural Network (CNN), a Multilayer Perceptron (MLP), and a Graph Convolutional Network (GCN) [172, 252]. By default, the MLP-reconstructed position is used, but the difference between the three different reconstructed positions can later be used as a selection criterion for poorly reconstructed events. The horizontal position reconstruction resolution achieved, for a 1000 PE S2 signal, is ∼1 cm [114]. Moreover, at this stage, a simulation-trained Naive Bayes Classifier (NBC) computes the probability of each peak being classified as S1, S2, or unknown, which can be used as an alternative classification method. Further details and results obtained from using this classification method are reported in [253].

Finally, the peaks are clustered into "events" by pairing S2 signals with candidate S1 signals, if possible. The time interval considered to form an event is constrained to the maximum drift time registered in the TPC, ∼2.2 ms, as detailed further in Subsection 4.2.4. The values used are 2.45 ms before and 0.25 ms around the identified main S2 peak. Furthermore, as conditions for the event pairing, the S2 peak must be larger than 100 PE, and, within a 10 ms window, have less than seven other peaks larger than half of its area. An example waveform of a $^{83\text{m}}$Kr calibration event is shown in Figure 4.3. For events with paired S1 and S2 signals, the drift time is defined by the time difference between the centres of both peaks, and subsequently, the (uncorrected) depth of the interaction, z, is calculated using the electron drift velocity, as in Equation 2.9 of Chapter 2.

[4]Straxen uses a non-standard definition of rise time. In this context, rise time is calculated by the time between the first and fifth area deciles, i.e. the time it takes for the signal to go from 10 to 50 % of its total waveform area.

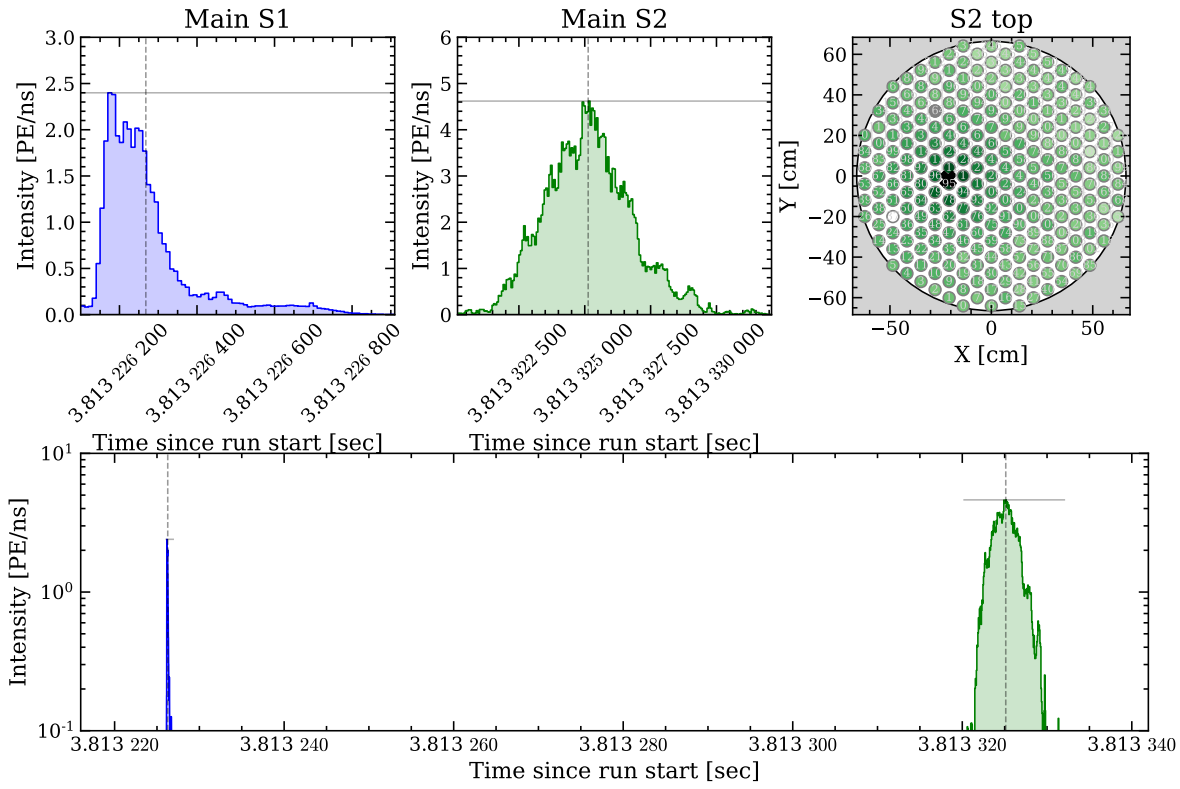

Figure 4.3.: Example waveform of a ^{83m}Kr event in the XENONnT detector. The top left corner shows the S1 signal (blue), characterised by its short rise time and short duration (width). In the centre upper panel, the S2 signal (green) is depicted, characterised by the large width. Notice the axis scale difference between the S1 and S2 plots. The top right corner shows the hit pattern on the top array, meaning the distribution the S2 signal over the different PMTs, used for position reconstruction. The reconstructed x, y position is marked with a dark cross. The bottom panel shows the waveform of the full event with both the S1 and S2 signals. The time difference between the signals is the drift time, in this example $\sim$100 µs.

4.2.2. Event correction

The set of corrections applied to the reconstructed events can be divided into corrections on the area of the signal (both S1 and S2) and corrections to the reconstructed position of the event.

The electric field non-uniformities affect the path of the drifting electron clouds, deviating from pure vertical drift. This effect is corrected by a field distortion correction map of the drift field based on COMSOL simulations and using uniformly-distributed ^{83m}Kr calibration data to tune the charge accumulation on the PTFE surface. An average surface charge density of $<0.5\,\mathrm{C\,m^{-2}}$ was estimated from the data-simulation

matching [184]. Some electron paths, especially from the bottom edge of the TPC, end at the PTFE walls, creating events without S2 signals and defining the charge-insensitive region of the TPC. In the SR0 electrode configuration, the charge insensitive region is estimated to be $\sim$112 kg, or 1.9 % of the active target [184].

The geometry of the detector, together with the optical properties of the PTFE walls and the xenon medium itself, affect the quantity of scintillation light (S1) that is detected from a given interaction position. To account for this spatial dependence, LCE maps for the top and bottom array are constructed based on ^{83m}Kr data by normalising the observed light yield (LY) to the mean LY inside the fiducial volume (FV). In addition, differences in the local electric field lead to spatial-dependent values of the LY up to 1 % [254]. The field-dependent effect in the LY is removed by using tuned electric field maps from COMSOL [218] simulations, decoupling the two effects and guaranteeing that the LCE correction map only depends on geometric effects. Using this construction, the LCE maps are valid at any energy. The corrected scintillation signal is denoted cS1.

On the other hand, for the ionisation-based signal (S2), the correction is two-fold. Due to the presence of electronegative impurities in the xenon bulk, some of the electrons in drifting electron clouds are lost to attachment. Such process is characterised by the electron lifetime, as defined in Chapter 2, and further discussed in Chapter 6. The direct effect in the observed signals is the exponential reduction of the S2 peak area for interactions deeper in the detector. Because xenon purification can change over time, this is a time-dependent effect. The electron lifetime can be measured with injected internal sources (^{83m}Kr and ^{220}Rn) and the new purity monitor in the xenon purification path, based on [255]. Also here, the effect of local variations of the charge yield, which could extend up to 5 %, is taken into account using the COMSOL-simulated electric field map. Both internal sources and the independent purity monitor are consistent with each other and register electron lifetime values of $>$10 ms, displaying an unprecedented level of purity in dual-phase LXe TPCs (see Figure 2.8 in Chapter 2).

The S2 response is also influenced by the local electric field of the extraction region and its impact on the extraction efficiency and local electroluminescence amplification. In particular, close to the perpendicular wires, the extraction efficiency and SE-gain are much higher than in the rest of the TPC. These effects are modelled by a data-driven (x, y)-dependent extraction efficiency and SE-gain normalised map, obtained from ^{83m}Kr calibration. The spatially-dependent model is time-dependent to account for the

electrode ramping operations described before, which drastically change the electron extraction conditions of the TPC. The area of the S2 signals corrected for both these effects and summed from the bottom and top arrays is denoted cS2.

4.2.3. Event selection

Once events have been reconstructed and corrected, a set of selection criteria, commonly referred to as "cuts", is applied to include only well-reconstructed events (i.e. not unphysical) and suppress backgrounds in the final science-search dataset. The choice of cuts to be applied in the analysis depends on the specific physics objective and the associated event population. For instance, the cuts required to study WIMP-nucleon interactions, which are expected to be low-energy and single scatter NR events, are distinct from those used in the search for $0\nu\beta\beta$ decay, which are high-energy electron recoil (ER) events. In the particular studies presented in this work, the relevant signals are from single-scatter events and the cuts are set accordingly.

In general, the selection criteria can be classified into three broad categories: livetime cuts, S1-based cuts, and S2-based cuts. Livetime cuts directly reduce the total livetime of the science run (or calibration campaign) by removing events which take place when the DAQ is in "busy" state[5], events in coincidence with a muon or neutron veto trigger, and small events following a large recorded signal. The latter targets specifically accidental coincidence (AC) events, where an S1 and an S2 signal are wrongly reconstructed as correlated to an event. After a previous large S1 or S2 signal a high rate of single electrons is observed [256, 257], which are then vetoed by the cut.

Both S1- and S2-based quality cuts remove events considered unphysical or outliers based on their distribution in particular parameter spaces. These cuts are tuned to provide high acceptance, i.e., event survival probability, to signal-like events, assessed either with calibration data (^{220}Rn, ^{37}Ar, ^{241}AmBe) or simulation-driven data, while maximising rejection power. The event simulation is done using the WFSim [258] package, a data-tuned waveform simulator which provides an output that can be processed in the same way as acquired data. Accurately describing the acceptance value for each cut is crucial in order to estimate the number of signal events and modelled background events that can be expected during the science run. For SR0,

[5] "Busy" state refers to a condition in which the DAQ system is unable to accept new data because it is in the process of reading out or processing previously acquired data in any of its digitisers. Events acquired in this state may be truncated or only partially recorded by some digitisers.

with both low-ER and low-NR searches in mind, these are the S1-based data quality cuts used in the analysis:

- S1 single scatter: aims to select events with only one valid interaction between the largest S2 signal of the event and any S1 signals that occurred prior to it, removing any event where the primary S1 signal could be ambiguous, such as in the case of multiple scatter interactions;
- S1 width[6]: rejects SE events or large afterpulse events misclassified as S1 signals by correlating the area and width of the peak;
- S1 area fraction top: identifies and removes misreconstructed events by comparing the fraction of observed light in the top PMT array to the total amount of light detected and its correlation with the reconstructed position of the interaction;
- S1 pattern: identifies and removes events with anomalous S1 light pattern distributions;
- S1 naive Bayesian score: uses the NBC score introduced in Subsection 4.2.1 to remove events whose S1 peak shows a low S1-likeness;
- S1 maximum PMT: this cut removes events where an excessive fraction of the S1 area is contributed from a single PMT, as in the case of a PMT flash.

The S2-based selections developed are often analogous to their S1-counterpart. The employed cuts were:

- S2 single scatter: aims to reject multiple scatters by identifying and excluding events with multiple physical S2 signals;
- S2 width: identifies and removes unphysical events based on the expected and observed width of the S2 signal; Subsection 4.2.4 describes and reports on this cut further;
- S2 area fraction top: analogous to the S1 area fraction top cut;
- S2 pattern: analogous to the S1 pattern cut;
- S2 naive Bayesian score: analogous to the S1 NBC score cut;

[6]In the context of straxen, the width of a peak is defined as the time between the 25^{th} and the 75^{th} area percentiles of the waveform, or between the 5^{th} and the 95^{th} area percentiles of the waveform. Unless otherwise stated, the term "width" of a peak refers to the former.

- S2 reconstructed position difference: removes events whose reconstructed position significantly differs when computed by the CNN, MLP, and GCN algorithms;
- Boosted Decision Tree (BDT): aims at suppressing the AC background by means of a trained BDT model. The model uses S2-shape parameters, such as S2 width (both 50 percentile range and 90 percentile range) and S2 rise time, S2 area and reconstructed depth. Details on the method and its previous application in XENON1T can be found in [127].

The developed cuts were used identically both for the low-energy ER and WIMP-nucleon interaction searches, with the exception of the S2 width cut, which was tightened for the NR search, and the BDT cut, which was only used in the NR search. The collective acceptance of the described selection is reported in Sections 4.3 and 4.4, respectively, for low-energy ER and low-energy NR results.

A final selection criterion, not qualified as a data quality cut, is the fiducial volume. The fiducial volume cut is indispensable to reduce backgrounds such as gas events (events arising from interactions in the gas phase), "wall" events (ER events arising from radioactive decays in the TPC materials that may mimic NR events due to ionisation electrons collected on the walls [172]), gamma-rays, and neutrons. In XENONnT, another constraint to the fiducial volume was the non-negligible charge-insensitive region (introduced in 4.2.2), which leads to events without or with only partial ionisation signal. The final shape optimisation in the $x - y$ and $r^2 - z$ space is later shown in Figures 4.7c and 4.8c.

4.2.4. The S2 width cut

As described in Chapter 2, the S2 signal arises from proportional scintillation in the gas phase, after ionisation electrons have been drifted through the TPC and extracted from the liquid phase. During the drifting process, the electron clouds undergo diffusion effects which impact the shape of the S2 signal. In particular, diffusion occurs both in the direction of the drift field (longitudinal diffusion, in z) and perpendicular to the drift field (transversal diffusion, in (x, y)). While transversal diffusion impacts the hit pattern and position reconstruction of the S2, longitudinal diffusion impacts its time distribution, mainly reflected in the width of the S2. As the electron cloud diffuses over time, the width of the S2 signal is highly correlated with the drift time

of the events. The S2 width cut evaluates if such correlation is satisfied and excludes events for which it is not.

The main targets of the S2 width cut are AC events, gas events, multiple scatters when their S2 signals are merged to a wide signal, and overall other events with unphysical S2 signal width and drift time correlation. Given the low value of the drift field in SR0, the accidental coincidence rate is expected larger than on past XENON detectors. This arises from the larger drift time window, increasing the probability of a spurious S1 or S2 signal between true S1 and S2 pairs. The AC rate in XENONnT is also driven by the strange topology of events near the perpendicular wires (see Section 3.3.3 of Chapter 3). This background, while not as crucial for the low-energy ER search, completely overlaps the WIMP ROI in the low-energy regime [114]. Constraining the AC component is, therefore, essential, making the S2 width cut determinant to the final science results. Apart from the S2 width cut, the previously mentioned BDT cut specifically targets AC events. However, due to the lack of accurate simulation of events near the two sets of perpendicular wires, the BDT model could not be trained in this region, making the S2 width the main selection criterion to remove AC events.

The S2 width model

For low-energy interactions, in particular NRs, the spatial distribution of initial charges n_0 is <1 µm (RMS) [160], justifying the treatment of the initial electron cloud as point-like. In that case, the distribution of charges n over the drift time t_d can be written as a Gaussian distribution [259]:

$$n = \frac{n_0}{\sqrt{4\pi D_L t_d}} \exp\left(\frac{-(v_d t_d)^2}{4 D_L t_d}\right) , \tag{4.1}$$

with the drift-time-dependent standard deviation

$$\sigma = \sqrt{\frac{2 D_L t_d}{v_d^2}} , \tag{4.2}$$

where D_L is the field-dependent longitudinal diffusion coefficient and v_d the drift velocity. In view of the practical definition of width previously mentioned, a conversion from Gaussian standard deviation to the 50^{th} area range, $\sigma_{r_{50}} \approx 1.35$ is used. Moreover, the observed drift time must be corrected for the drift within the extraction field, from the gate to the liquid-gas interface, t_{gate}. By adapting Equation 4.2, the expected width

of an event as a function of the drift time can then be written as:

$$r_{50} = \sigma_{r_{50}} \sqrt{\frac{2D_L(t_d - t_{gate})}{v_d^2}} \, . \tag{4.3}$$

It stands from the equation above that three parameters are required to model the S2 width: the position of the gate in units of drift time (t_{gate}), the electron drift velocity (v_d), and the diffusion coefficient (D_L). While the first is strictly dependent on the detector effects, the last two are properties of electron transport in LXe, mainly the drift field.

Electron transport properties

Events originating on the gate can be identified by a sudden change in the cS2/cS1 ratio at low drift times. This change is due to the increase of the electric field magnitude, which, for the same type of events, suppresses recombination and induces bigger S2 signals at the expense of smaller S1 signals. t_{gate} is then determined by the maximum slope in the Gaussian-filtered median of the distribution, as shown in Figure 4.4a. For SR0, the average t_{gate} was (4.4 ± 0.5) µs.

The electron drift velocity is calculated from the known gate to cathode distance when cooled at LXe temperature, 1485.6 mm, and the drift time observed for events at the cathode during ^{83m}Kr runs, where the events are uniformly distributed throughout the active region. Since interactions below the cathode do not have S2 signals, and, therefore, no associated drift time, the distribution of all the known drift times drops in this region, as seen in Figure 4.4b. The drift time of events at the cathode level is calculated as the point of maximum slope in the Gaussian-filtered drift-time distribution. For SR0, the "cathode drift time" was (2.204 ± 0.001) ms. The resulting electron drift velocity, taking into account the previously calculated "gate drift time", is 675 mm ms^{-1}.

Given the calculated t_{gate} and v_d, the longitudinal diffusion coefficient can be determined by fitting Equation 4.3 to the observed data. As previously done, ^{83m}Kr calibration data is used due to its homogeneous distribution throughout the active region, and, consequently, at the full extent of possible drift times. Figure 4.4c shows the distribution of the observed S2 width (r_{50}) as a function of the drift time of the

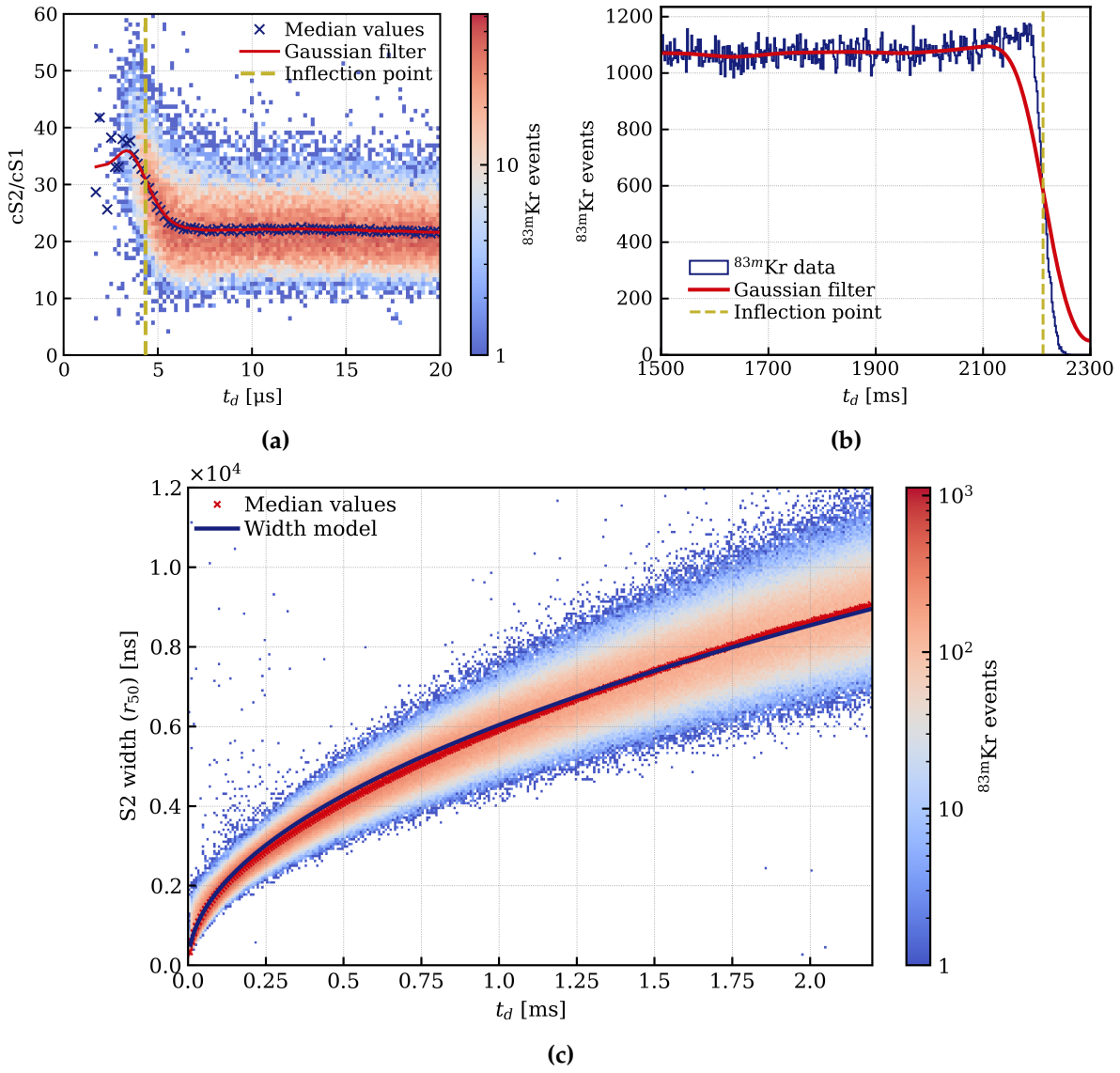

Figure 4.4.: **(a)** Distribution of the fraction cS2/cS1 as a function of drift time for a set of ^{83m}Kr events close to the gate, with an applied pre-selection based on the ^{83m}Kr peak energy and S1 signal quality. In blue cross markers are shown the median values of the distribution for each bin of drift time, in red solid line the result of a Gaussian filter to these points and as a dashed gold line the determined t_{gate}. **(b)** Number of ^{83m}Kr events (with the same pre-selection criteria of **(a)**) as a function of the drift time for events close to the cathode (solid blue line). The result of the Gaussian filter is shown as a solid red line and its first derivative as a dashed gold line. In addition, a vertical dashed-gold line marks the minimum of the derivative, corresponding to the drift time position of the cathode. **(c)** Distribution of the S2 width (r_{50}) as a function of drift time for a set of 1 million ^{83m}Kr events. The median values of the S2 width for each drift time bin are shown as blue cross markers and the tuned width model of Equation 4.3 with the parameters detailed in the text is shown as a solid blue line.

events and the fit of Equation 4.3 to the median values of the distribution. The resulting longitudinal diffusion coefficient D_L is $(45.6 \pm 0.1)\,\mathrm{cm^2\,s^{-1}}$, for a drift field of 23 V/cm.

Definition of the S2 width cut

While the average expected value of the S2 width of an event depends only on the drift time, the spread of the distribution of expected values is highly dependent on the size of the S2 signal. If this effect was neglected, the cut acceptance would be highly dependent on the energy of the interaction. Since the S2 width and the depth of the interaction are intrinsically correlated, the dimension of the problem can be reduced by introducing the concept of "normalised width", r_{50}^{norm}. This quantity is calculated as the ratio between the observed width of an event and the width expected from the width model, r_{50}^{model} (Equation 4.3):

$$r_{50}^{norm}(t_d) = \frac{r_{50}(t_d)^2 - (r_{50}^{SE})^2}{r_{50}^{model}(t_d)^2}\,, \tag{4.4}$$

where r_{50}^{SE} is the SE width, introduced to correct the width model at small number of electrons in the electron cloud. The r_{50}^{SE} value observed in SR0 was $\sim$375 ns, calculated on the SE population of events. By removing the dependence on the depth, the cut can be defined as a selection in the normalised width versus the S2 signal area parameter space.

The boundaries of the S2 width cut were defined in two distinct regions. The separation in these two regimes is due to a systematic increase of S2 width at high energies, arising from a reconstruction bias outside the ROI. The effect is depicted in Figure 4.5c. Up to S2 areas of 10^4 PE, the upper and lower boundaries were modelled by the functions:

$$f^{UB}(S2_{area}) = \frac{a_1}{\exp\left[a_2\left(\log_{10}(S2_{area})\right) - a_3\right]} + a_4 \tag{4.5}$$

$$f^{LB}(S2_{area}) = \frac{b_1}{2}\,\mathrm{erf}\left[\frac{\sqrt{2}\left(\log_{10}(S2_{area})\right) - b_2}{b_3}\right]\,, \tag{4.6}$$

where UB and LB stand for upper and lower boundary, respectively. Above 10^4 PE, the S2 width cut boundaries were modelled by parabolas:

$$f^{high-E}(S2_{area}) = p_0 + p_1 \log_{10}(S2_{area}) + p_2 \log_{10}(S2_{area})^2 \, . \tag{4.7}$$

A comprehensive schematic of the cut parameter space and the different cut lines is shown in Figure 4.5a.

The boundaries of the cut are set on percentiles of the distributions obtained from signal-like WFSim simulated data for the "low-energy" region (up to S2 signal areas of 10^4 PE) and on ^{220}Rn data for the "high-energy" region (S2 signal areas above 10^4 PE). The two cases are depicted in Figures 4.5b and 4.5c, respectively.

The percentiles used to fit the boundary functions varied depending on the event belonging to "near" the perpendicular wires or far from the perpendicular wires. For the "far from wires" region, the boundaries were fitted to the 1^{st} and 99^{th} percentiles, excluding only clear outliers and maintaining a high acceptance. However, for events under the perpendicular wires, the observed S2 widths are larger than in the rest of the TPC due to longer drift times and different electric field conditions. This effect can be seen in Figure 4.5d, where, around $x^{rotated} = \pm\, 13.06\,\text{cm}$[7], the observed normalised width of the events completely deviates from 1 and increases locally. The extent of this effect defines the previously mentioned "near-wires" region at $\sim$4.45 cm around the perpendicular wires. This region corresponds to a volume of $\sim$850 kg of active volume close to the centre of the TPC ($\sim$15 % of the total active volume). In this region, the S2 width cut maintains its lower boundary (Equation 4.6) and is fitted to the 1^{st} and 5^{th} percentile of observed data for the low-energy ER and WIMP searches, respectively. The choice to have two distinct lower boundaries for the different analyses relates to the aimed suppression of AC events, a more harmful background for the WIMP searches. Since the other main anti-AC cut, the BDT cut, cannot be applied on the near-wires regions, the S2 width balances the difference in background suppression by assuming a more strict boundary. Given the anomalous distribution of widths, the upper boundary needs distinct modelling. Instead of following the normalised width boundaries, the events in this region are selected based on the difference between the observed and expected width as a function of their distance to the perpendicular

[7] In the nominal coordinate system, the perpendicular wires stand at a 60° angle in relation with the x axis. $x_{rotated}$ represents the x coordinates of the events rotated such that the perpendicular wires stand parallel to the y axis. See Figure 3.10a in Chapter 3 for a visualisation of the wires in rotated coordinates

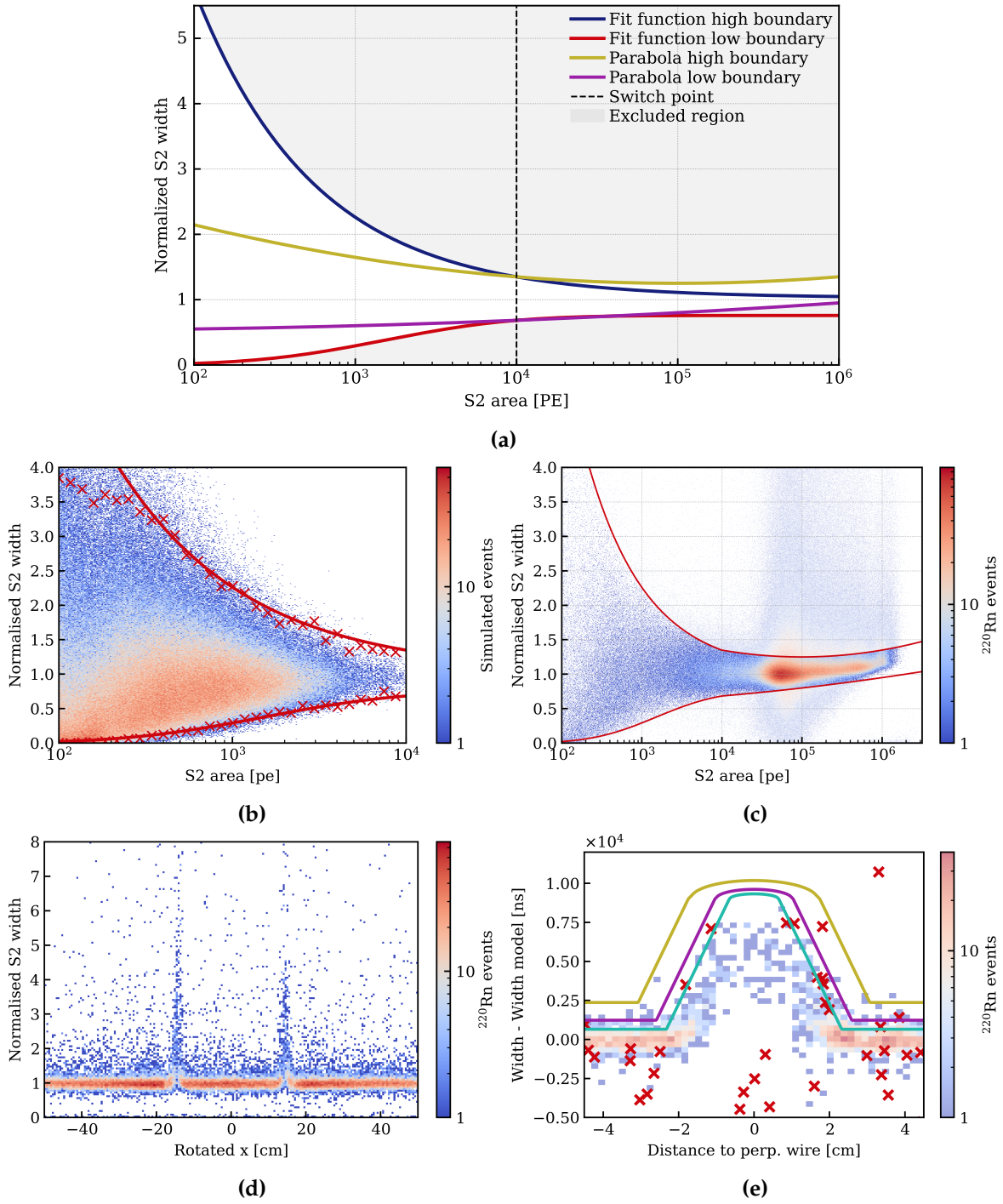

Figure 4.5.: **(a)** S2 width cut parameter space, boundaries, and excluded region. **(b)** Fit of the cut boundaries to signal-like WFSim simulated data. the 1st and 99th percentiles of each S2 signal area bin are shown as red crosses. **(c)** Effect of the S2 width cut in ^{220}Rn data, which was used to fit the cut boundaries for S2 signal areas above 10^4. **(d)** Distribution of the normalised width as a function of the position of the events in $x_{rotated}$ for ^{220}Rn data. **(e)** Definition of the S2 width cut upper boundary in the relevant parameter space. Three lines are shown for different S2 signal areas: 10^3 PE (gold), $10^{3.5}$ PE (purple), 10^4 PE (cyan). Red cross markers show events removed by the S2 width cut.

Table 4.1.: Tuned parameters of the S2 width cut corresponding to the terms of Equations 4.5, 4.6, and 4.7. UP and LB reference the upper and lower bound of the cut. In general, the parameters are used for the both the low-energy ER and WIMP version of the cut, except for the particular case of the near-wire region of the WIMP search, specified on the table.

Parameter	Value	Parameter	Value
a_1	4.744	p_0^{UB}	3.738
a_2	1.341	p_1^{UB}	-0.995
a_3	1.996	p_2^{UB}	0.099
a_4	1.025	p_0^{LB}	0.551
b_1	0.757	p_1^{LB}	-0.033
b_2	3.182	p_2^{LB}	0.016
b_3	1.263	p_0^{LB} (WIMP near wires)	1.450
b_1 (WIMP near wires)	0.774	p_1^{LB} (WIMP near wires)	-0.363
b_2 (WIMP near wires)	2.927	p_2^{LB} (WIMP near wires)	0.046
b_3 (WIMP near wires)	1.223		

wires and their area. The model and its effects are shown in Figure 4.5e, where the cut boundary in the parameter space of interest is shown for three distinct S2 signal areas.

The complete set of tuned parameters of the cut for the far and near wire regions and low-energy ER and WIMP searches are detailed in Table 4.1.

Cut performance

The S2 width cut acceptance was tested and tuned with ^{220}Rn and ^{37}Ar data. In general, cut acceptances are calculated using the N-1 method described in [172]: fraction of surviving events from the cut in question, with all the other selection cuts already applied. However, the data-driven acceptance of the S2 width cut displayed a large difference at low S2 signal areas when calculated with ^{220}Rn data or ^{37}Ar data. In order to describe the acceptance using both datasets, the following empirical model was fitted:

$$\mathcal{S}(S2_{area}) = a - \exp\left(\frac{-(S2_{area} - b)}{c}\right)) \, . \tag{4.8}$$

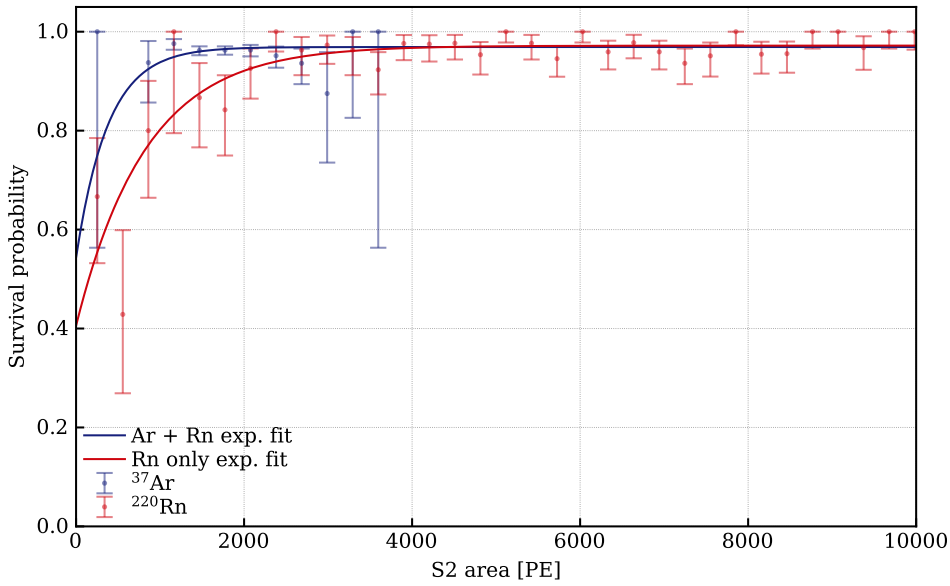

Figure 4.6.: Survival probability of events as a function of the S2 signal area for the S2 width cut using the N-1 method in ^{37}Ar (blue markers) and ^{220}Rn data (red markers). The fit to the ^{37}Ar+^{220}Rn dataset is shown as a solid blue and the fit to the ^{220}Rn-only dataset is shown as a solid red line.

The acceptance model used in the final analysis follows a fit of Equation 4.8 to a dataset containing both ^{220}Rn and ^{37}Ar data (blue line in Figure 4.6) and uses the fit to only ^{220}Rn data as the lower bound for the uncertainty (red line in Figure 4.6). The rejection of accidental coincidence events was tested with simulation and yields 82.5 % rejection of this background. The events rejected by the S2 width cut for both unblinded science search datasets can be found in Figures 4.7 and Figure 4.8 for the low-energy ER and WIMP search, respectively. These figures show that the S2 width plays a determinant role in removing key events in both searches. As the only anti-AC cut in the low-energy ER search, it removes events on the critical low-S1 signal area region. The waveforms of the excluded events were investigated after unblinding and confirmed as AC-like events. As for the WIMP search, most of the identified AC events are cut removed by both the S2 width cut and the BDT cut (purple stars in Figure 4.8), showing their complementarity. However, there are many events that are solely excluded by the S2 width cut (red crosses in Figure 4.8) and not by the BDT cut, making it essential to the results. These are mostly present in the near-wire region, as expected, and two others in the far-wire region.

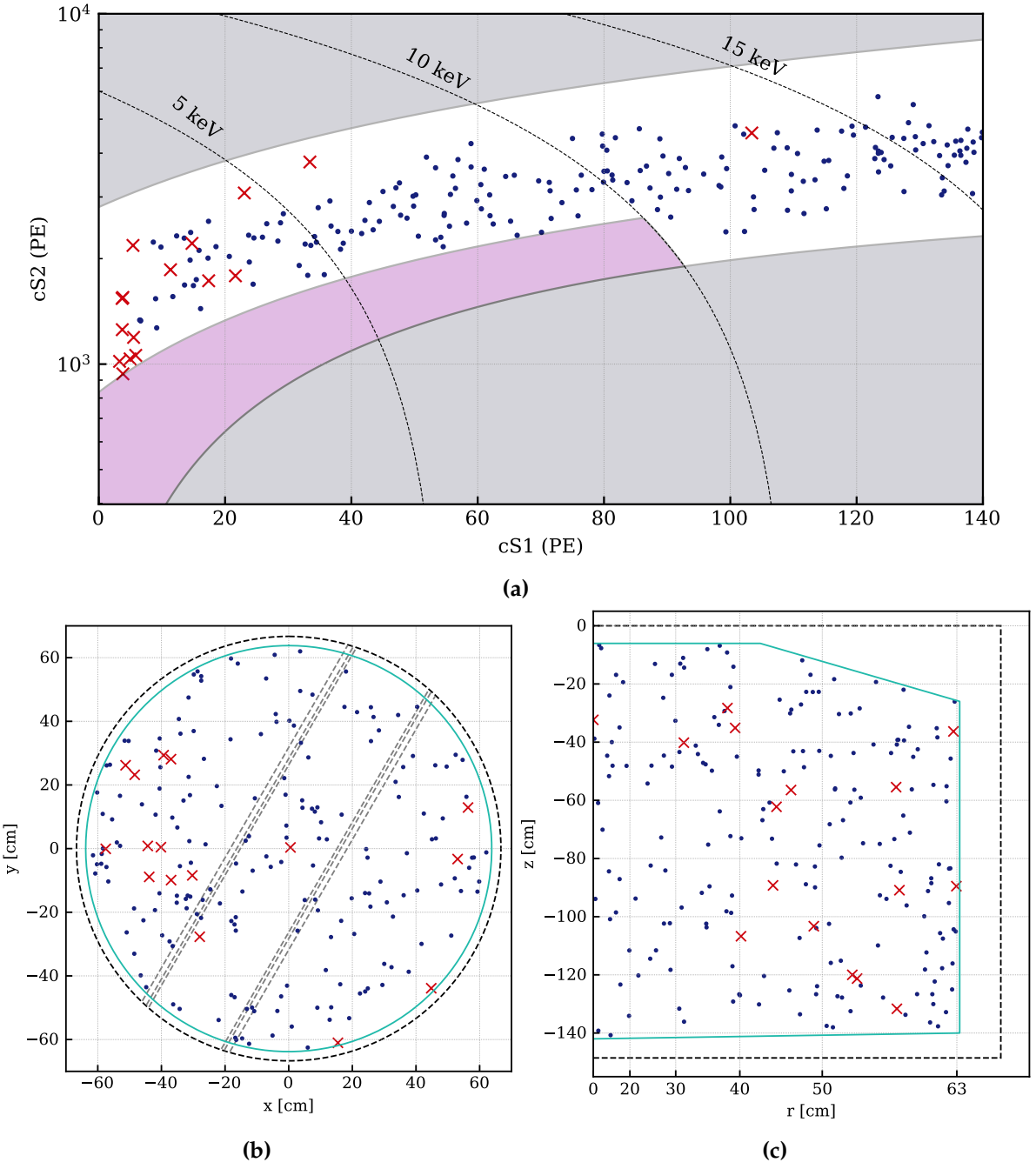

Figure 4.7.: ER dataset in cS2-cS1 space **(a)**, x-y **(b)**, and r-z **(c)**. The events removed by the S2 width cut are marked as red crosses and the surviving events of the dataset as blue dots. In **(a)**, the grey shaded regions correspond to parameter space excluded from the analysis (2σ above and below the ER median) and the purple shaded region to part of the WIMP search parameter space, which remained blinded on the time of ER unblinding. In **(b)** and **(c)**, the dashed grey line shows the external boundary of the TPC and the solid cyan line the defined fiducial volume. In **(c)**, the dotted grey lines depict the position of the perpendicular wires.

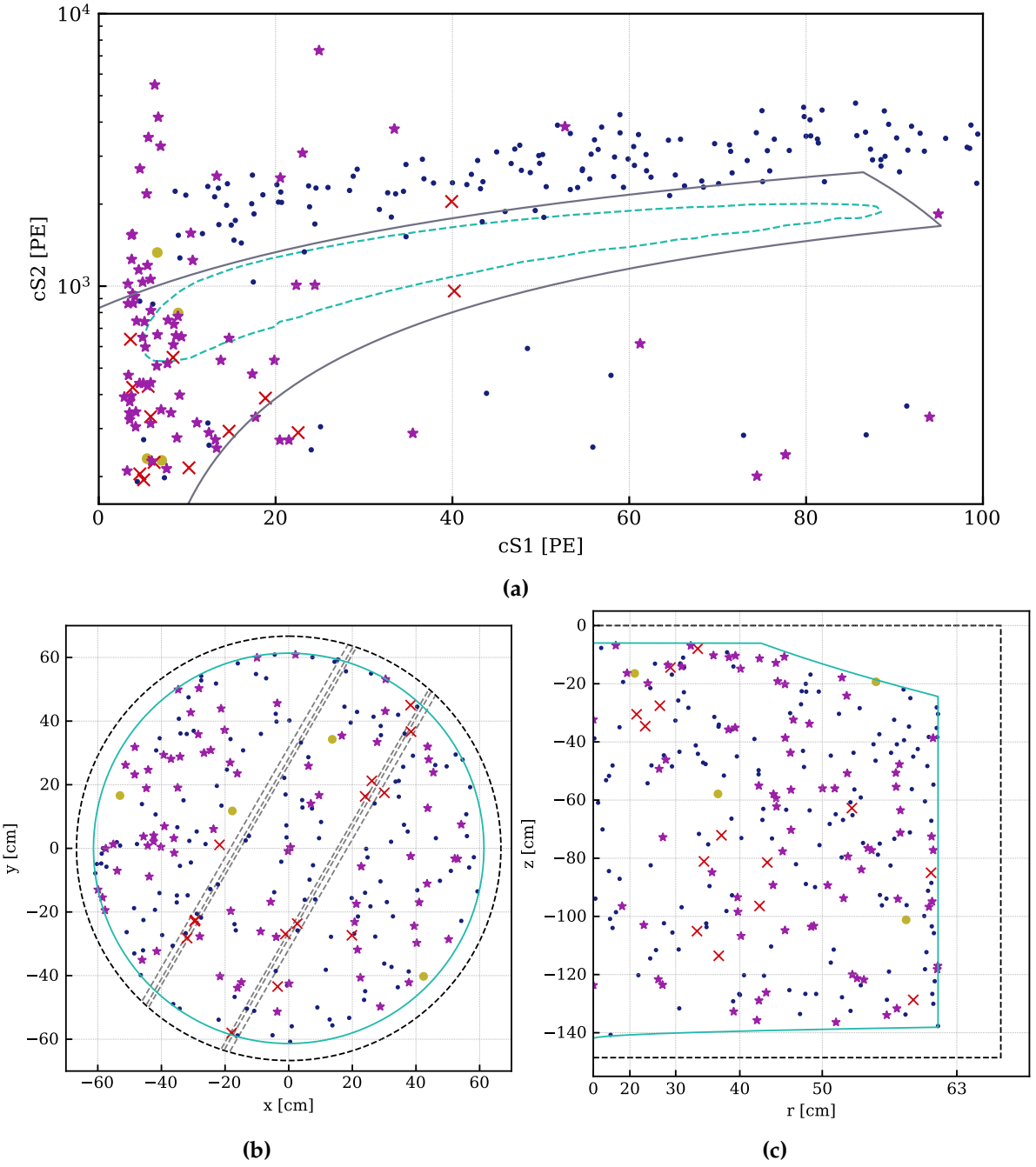

Figure 4.8.: WIMP search dataset in cS2-cS1 space **(a)**, *x*-*y* **(b)**, and *r*-*z* **(c)**. The events removed by only the S2 width cut are marked as red crosses, the events rejected by both the S2 width and the BDT cut are marked as purple stars, events remove only by the DBT cut are marked as gold circles, and the surviving events of the dataset as blue dots. In (**(a)**), the grey line remarks the previously blinded region and the dashed cyan line the contour of a signal-like region which is constructed to contain 50 % of a 200 GeV/ c2 WIMP signal. In (**(b)**) and (**(c)**), the dashed grey line shows the external boundary of the TPC and the solid cyan line the defined fiducial volume. In (**(c)**), the dotted grey lines depict the position of the perpendicular wires.

4.3. Results of the low-energy ER search

The ROI for the low-energy ER analysis extends from 1 to 140 keV in reconstructed energy, with particular attention to the events with energy below 10 keV, where XENON1T reported an excess of events [248]. As with XENON1T, three potential BSM signals were considered: solar axions, solar neutrinos with an enhanced magnetic moment, and bosonic DM, in particular axion-like particles and dark photon DM. Additionally, the presence of tritium as a possible cause of the XENON1T excess could not be ruled out. The energy-dependent detector efficiency is estimated as detailed in [172] and is shown in Figure 4.9a.

In total, nine components are included in the background model, B_0, summarised in Table 4.2. The main background at low energy is, as in XENON1T, the beta decay of ^{214}Pb, with an activity between 0.777 ± 0.038 and $(1.691 \pm 0.078)\,\mu\mathrm{Bq\,kg^{-1}}$, constrained by the α-decay rates of ^{218}Po and ^{214}Po. The ^{85}Kr rate is constrained by measurements of $^{\mathrm{nat}}$Kr concentration in the xenon. The fraction of ^{85}Kr in $^{\mathrm{nat}}$Kr was measured at 2×10^{-11}, compatible with [260]. Decays in the detector materials were accurately simulated in Geant4 [261] after a thorough screening campaign [163, 249]. From simulations, the resulting single-scatter gamma-ray background spectrum shows a flat behaviour below 140 keV within the fiducial volume with an expected rate of $(2.1 \pm 0.4)\,\mathrm{events/(t \cdot y \cdot keV)}$. The spectrum induced by the two neutrino double-beta decay ($2\nu\beta\beta$) of ^{136}Xe is present throughout the energy ROI and its rate is constrained by measurements of the xenon isotopic abundance and the half-life of the process from [262]. The $2\nu\beta\beta$ spectrum becomes the dominant background above 40 keV. The double-electron capture in ^{124}Xe, modelled as reported in [135], is left unconstrained. The previously discussed AC events, although not dominant, can overlap with the ER ROI. The expected AC rate is $(0.61 \pm 0.03)\,\mathrm{events/(t \cdot y \cdot keV)}$. The solar neutrino-electron scattering energy spectrum was obtained using the standard neutrino flux in the Large Mixing Angle Mikheyev–Smirnov–Wolfenstein (MSW) model and cross-section given by the SM [263, 264]. A 10 % uncertainty on the solar neutrino flux based on the Borexino measurement [265] was assumed. Trace amounts of $^{83\mathrm{m}}$Kr and ^{133}Xe, produced by neutron activation during ^{241}AmBe calibrations, can be found as residual background contaminants and their rate was left unconstrained in B_0.

The fitting of the background model to the data in reconstructed energy space was performed using an unbinned maximum likelihood approach, as described in

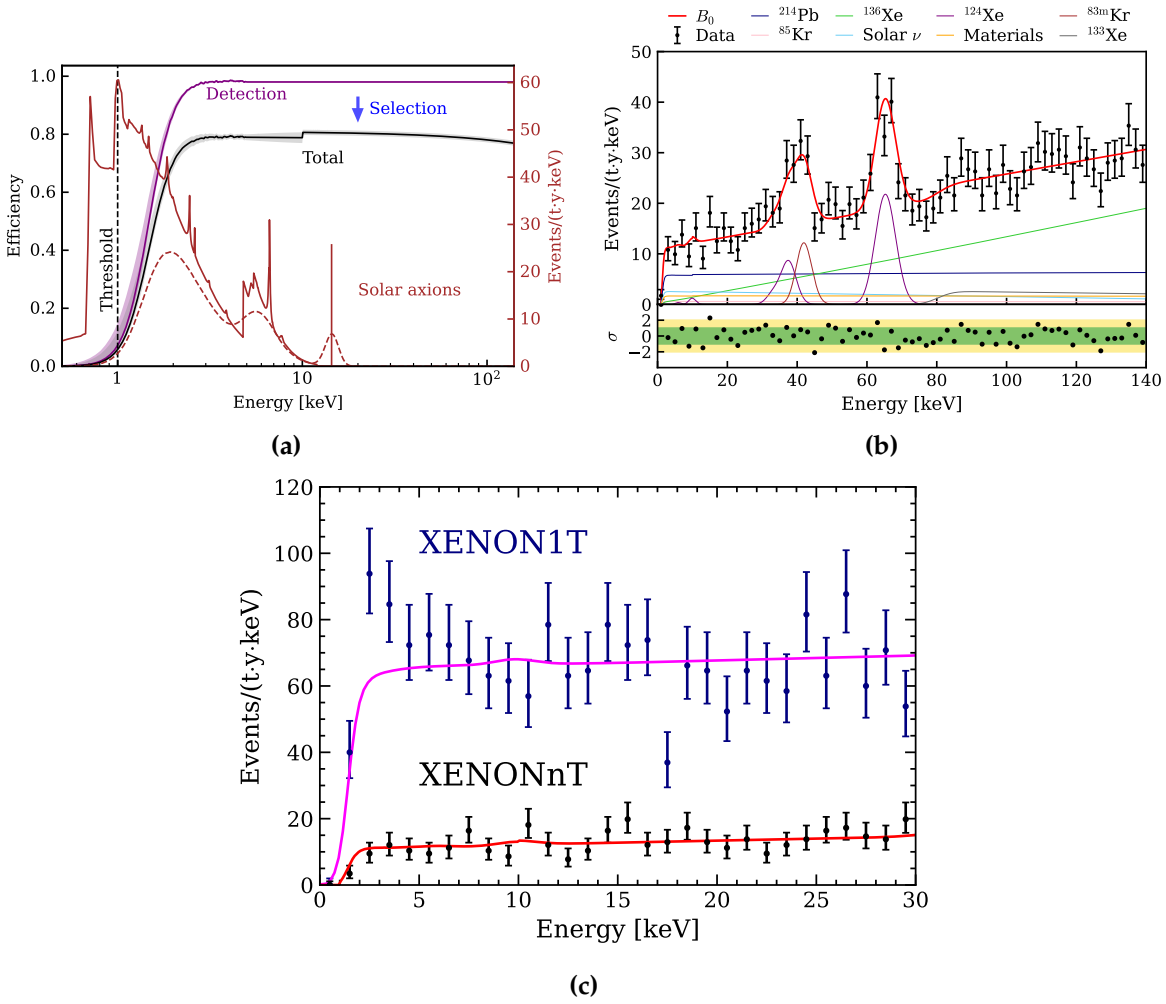

Figure 4.9.: **(a)** Acceptance of signal-like events as a function of the recoil energy for the low-energy ER search. The purple curve represents the detection efficiency. The black curve is the total efficiency, which is a combination of the detection and event-selection efficiencies. The discontinuity at 10 keV is caused by the blinded WIMP search region, as shown in Figure 4.7. The black dashed line shows the 1 keV energy threshold of the low-energy ER search. Efficiencies in reconstructed energy and the solar axion signal in true (red solid) and reconstructed energy (red dashed) as a function of the energy of the recoil. Figure from [193].**(b)** Fit to SR0 data using the background model B0. The fit result of B0 is the red line. The subdominant AC background is not shown. Figure from [193]. **(c)** Comparison between the XENON1T and XENONnT low-energy ER spectra.

Table 4.2.: Background model B_0 with fit constraints and best-fit number of events for each component in (1, 140) keV for the whole SR0 exposure (1.16 t · y). Table from [193].

Component	Constraint	Fit
^{214}Pb	(570, 1200)	960 ± 120
^{85}Kr	90 ± 60	90 ± 60
Materials	270 ± 50	270 ± 50
^{136}Xe	1560 ± 60	1550 ± 50
Solar neutrinos	300 ± 30	300 ± 30
^{124}Xe	-	250 ± 30
AC	0.70 ± 0.04	0.71 ± 0.03
^{133}Xe	-	150 ± 60
^{83m}Kr	-	80 ± 16

detail in [248]. The data agrees well with the background model, no excess was found, and a BSM interpretation of the XENON1T excess excluded. The fitted background model is shown in Figure 4.9b and the best-fit values for each of the background model components are reported in Table 4.2.

The average measured rate of low-energy ER events between 1 and 30 keV was (15.8 ± 1.3) events/$(\mathrm{t \cdot y \cdot keV})$, roughly five times lower than the rate measured in XENON1T [248] of (76 ± 2) events/$(\mathrm{t \cdot y \cdot keV})$, as shown in Figure 4.9c. The unprecedented low-energy ER background rate is a direct result of the use of the radon removal system (see Chapter 2), and the thorough material selection and cleaning. By treating tritium as a candidate signal, the resulting best-fit rate is 0 events, with an upper limit (90 % C.L.) of 15 events/t · y. Based on this result, new parameter spaces were excluded by upper limits on solar axions, bosonic dark matter, and solar neutrinos with an enhanced magnetic moment, as detailed in [193].

4.4. Results of the low-energy NR search

The low-energy NR search is conducted in the (cS1, cS2) space and the main signal model is the standard WIMP, probed both through elastic spin-independent and spin-dependent scattering. The ROI is contained between 0 PE and 100 PE in cS1 and between 126 PE and 12 589 PE in cS2, as shown in Figure 4.8. The signal NR

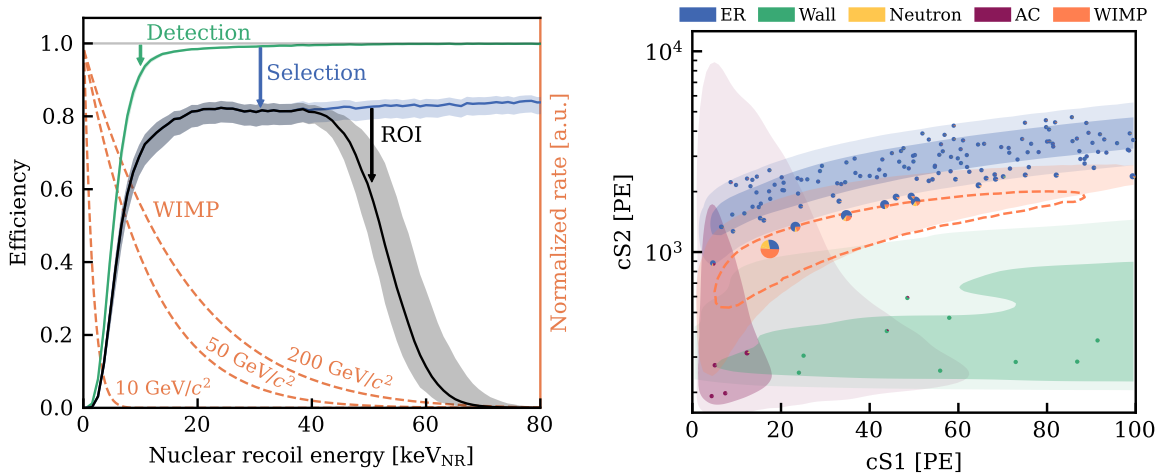

Figure 4.10.: **(a)** Detection and selection efficiency for NR events in the WIMP search as a function of the NR recoil energy. The total efficiency in the WIMP search region (black) is dominated by the detection efficiency (green) at low energies and event selections (blue) at higher energies. Normalised recoil spectra for WIMPs with masses of 10 GeV/c^2, 50 GeV/c^2, and 200 GeV/c^2 are shown with orange dashed lines for reference.**(b)** DM search data in the cS1-cS2 space. Each event is represented with a pie chart, showing the fraction of the best-fit model including a 200 GeV/c^2 WIMP (orange) evaluated at the position of the event with the size of the pie charts proportional to the signal model at that position. Background probability density distributions are shown for ER (blue), AC (purple) and surface (green, "wall"). The neutron background (yellow in pies) has a similar distribution to the WIMP (orange-filled area showing the 2σ region). The orange dashed contour contains a signal-like region which is constructed to contain 50 % of a 200 GeV/c^2 WIMP signal with the highest possible signal-to-noise ratio. Figures from [114].

spectrum uses the Helm form factor for the nuclear form factor [78] and follows the recommendations and conventions defined in [79]. The signal model in the (cS1, cS2) space is constructed via a LXe and detector response model fitted to NR calibration data from ^{241}AmBe. The energy-dependent detection efficiency is calculated by WFSim- and data-driven methods [172, 266] and is shown in Figure 4.10a.

The background model is constituted of five components. Their expected number of events can be found in Table 4.3 and their distribution in the (cS1,cS2) parameter space in Figure 4.10b. The main NR background of the WIMP search are radiogenic neutrons from (α,n) reactions. The neutron budget is estimated via a custom framework based on the fitted NR model [163, 267] with inputs from Geant4 simulations. This estimate was then compared with a data-driven method using the neutron veto

Table 4.3.: Expected number of events for each model component and observed events. The nominal column shows expectation values and uncertainties, if applicable, before unblinding. The nominal ER value is the observed number of ER events before unblinding. Expectation values for the best fit including a $200\,\mathrm{GeV/c^2}$ WIMP, with a cross-section of $3.22 \times 10^{-47}\,\mathrm{cm^2}$, are shown both for the ROI, and for the signal-like region indicated in Figure 4.10a (orange dashed contour). The best-fit and pre-unblinding values agree within uncertainties for all components which include an ancillary constraint term. Table from [114].

	Nominal	Best Fit	
		ROI	Signal-like
ER	134	135^{+12}_{-11}	$0.86^{+0.08}_{-0.07}$
Neutrons	$1.1^{+0.6}_{-0.5}$	1.1 ± 0.4	0.42 ± 0.17
CEνNS	0.23 ± 0.06	0.23 ± 0.06	0.022 ± 0.011
AC	4.3 ± 0.2	4.32 ± 0.15	0.366 ± 0.013
Surface	14 ± 3	12^{+0}_{-4}	$0.35^{+0.01}_{-0.11}$
Total background	154	152 ± 12	2.0 ± 0.2
WIMP	-	2.6	1.3
Observed	-	152	3

tagging capabilities, differing by a factor of $\sim$6. The total neutron expectation is $1.0^{+0.6}_{-0.5}$ events. The other NR background contribution are CEνNS events from ^{8}B solar neutrinos, yielding 0.23 ± 0.06 expected events. As for the total ER background, it follows the one described in the previous section, with the updated ER model including the different event selection cuts and efficiency curve of the WIMP search.

The AC background is of particular concern in the WIMP search due to its overlap with the signal region in (cS1, cS2), as shown in Figure 4.10b. As detailed in Section 4.2.4, given the lack of modelling of the S2 shape close to the perpendicular wires, the active volume of the TPC is split into near- and far-wire regions, with independent modelling. In the near-wire region, the AC rate was expected to be $\sim$6 times higher than for the far-wire region. The combined number of expected AC events is 4.3 ± 0.2 in the ROI.

Finally, the surface background is modelled from ^{210}Po events coming from the walls of the TPC and validated with a partial unblinding of events outside of the fiducial volume.

The search data is statistically interpreted using an unbinned extended likelihood, which is based on three-dimensional models in cS1, cS2, and radius, following the procedures outlined in [79,172]. The models are constructed by toy Monte Carlo (MC) simulations using fitted yields and efficiencies. A total of 152 events were found within the ROI, 16 of which were in the blinded WIMP region. No significant excess was found and the profile log-likelihood test is used to place constraints on the interaction WIMP-nucleon interaction cross-section for the range of WIMP masses of interest for both spin-independent and spin-dependent interactions, shown in Figure 4.11. For the former, the lowest upper limit observed was 2.58×10^{-47} cm^2 for a WIMP mass of 28 GeV/c^2.

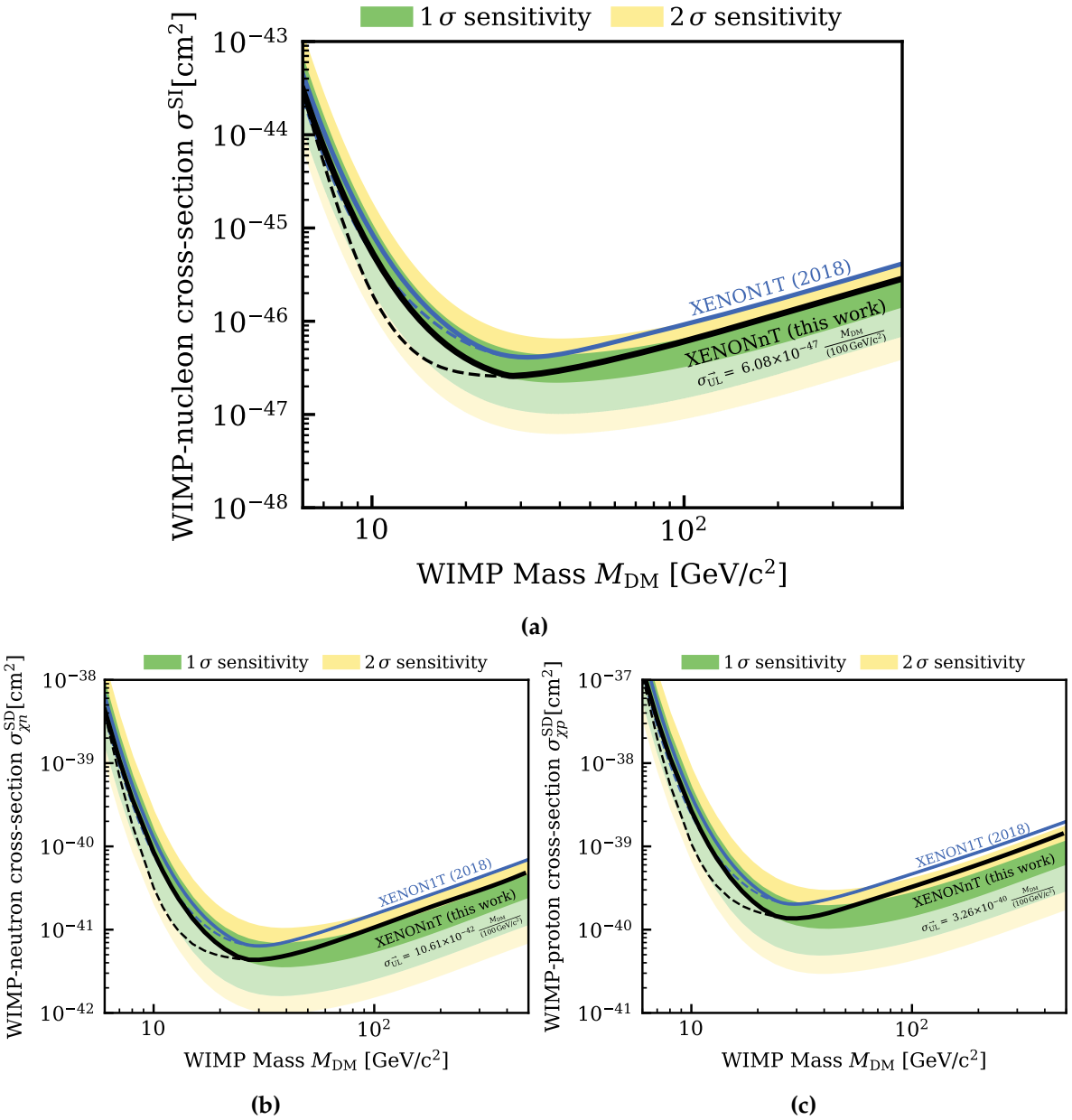

Figure 4.11.: Upper limit on spin-independent WIMP-nucleon cross-section at 90 % confidence level as a function of the WIMP mass with (solid lines) and without (dashed lines) a power-constraint applied (**a**). The 1σ (green) and 2σ (yellow) sensitivity bands are shown as shaded regions. The analogous limits for spin-dependent WIMP-neutron (**b**) and spin-dependent WIMP-proton (**c**) are also shown. Figures from [114].

Chapter 5.

Multi-messenger astrophysics in XENONnT

Multi-messenger astrophysics is a fast-expanding field. They combine information from single cosmic sources provided by different mediators: photons, gravitational waves, neutrinos, and cosmic rays. Parallel to their role in the hunt for DM, experiments such as XENONnT are sensitive to neutrinos coming from supernovae within and beyond the Milky Way, given their tonne-scale active target mass and low energy threshold. In this chapter, the potential for detection of neutrinos from supernova (SN) events in the XENONnT detector is discussed, as well as the infrastructure which makes XENONnT the first DM experiment to contribute to Supernova Early Warning System (SNEWS).

Section 5.1 introduces the SN process as a prime source of neutrinos of all flavours and the important role they portray in the astrophysical event. In Section 5.2, the SNEWS network goals and general procedures are described. The processes and prospects of SN neutrino detection in LXe TPCs are discussed in Section 5.3. Section 5.4 describes the particular adaptations and procedures developed to support the implementation of the XENONnT experiment in the SNEWS network.

5.1. Supernova neutrinos

A SN[1] is a powerful and luminous stellar explosion that occurs when a star with $\sim$8 to 110 $M_\odot$ [268] has exhausted its fuel for nuclear fusion in its core, resulting in the

[1] In this work, SN refers specifically to the subset of core-collapse supernovae.

sudden and catastrophic collapse of its core. The resulting remnant is, typically, a neutron star (NS) or a black hole (BH). In the first $\sim$10 s of a SN burst, around 99 % of the gravitational binding energy of the progenitor is converted into neutrinos with energies of $\mathcal{O}(10)$ MeV [269,270]. These neutrinos precede the emission of light and other particles by minutes to hours.

Although the SN process is dependent on the progenitor and not completely understood, the role of neutrinos throughout the process is undeniably important. The delayed neutrino-driven mechanism, first proposed by H. Bethe and J. Wilson in 1985 [271], has been the standard description of the SN process [272]. Still, both numerical and theoretical modelling, as well as observations, struggle to undoubtedly prove the mechanism [270]. When the oxygen-neon-magnesium cores of massive stars gravitationally collapse, a NS starts to form. Electron neutrinos are produced by electron captures on nuclei and free protons ($p + e^- \rightarrow n + \nu_e$), accelerating the implosion and converting the lepton-rich post-collapse remnant to a deleptonised NS. As a result of the repulsive forces between the nucleons, an intense bounce projects a shock wave into the supersonically collapsing outer shells of the dying star. However, only milliseconds after the core bounce, the energy of the shock is weakened by iron photo-disintegration and the emission of a large burst of neutrinos (see Figure 5.1), becoming an accretion shock [268,273,274]. In the following $\mathcal{O}(100)$ms, the neutrinos from the proto-NS deposit energy behind the shock front, or gain layer, through charged-current (CC) reactions with free nucleons:

$$\nu_e + n \rightarrow p + e^- \tag{5.1}$$

$$\overline{\nu}_e + p \rightarrow n + e^+ \, . \tag{5.2}$$

If the transferred neutrino energy and momentum are sufficient to raise the post-shock pressure to trigger re-acceleration of the shock front going outwards, a SN explosion takes place [271]. The critical threshold where the neutrino luminosity surpasses the mass-accretion rate of the stalled shock is often referred to as the critical luminosity condition [275]. Which parameters accurately define this condition is still widely discussed [276–278].

To conclude on the importance of neutrinos in the SN process, the intense neutrino and anti-neutrino radiation also define the neutron-to-proton ratio of the medium, determining the nucleosynthesis in the core of the SN explosion, as well as provoke nuclear spallation on the outer stellar shells, giving origin to further nuclides. While

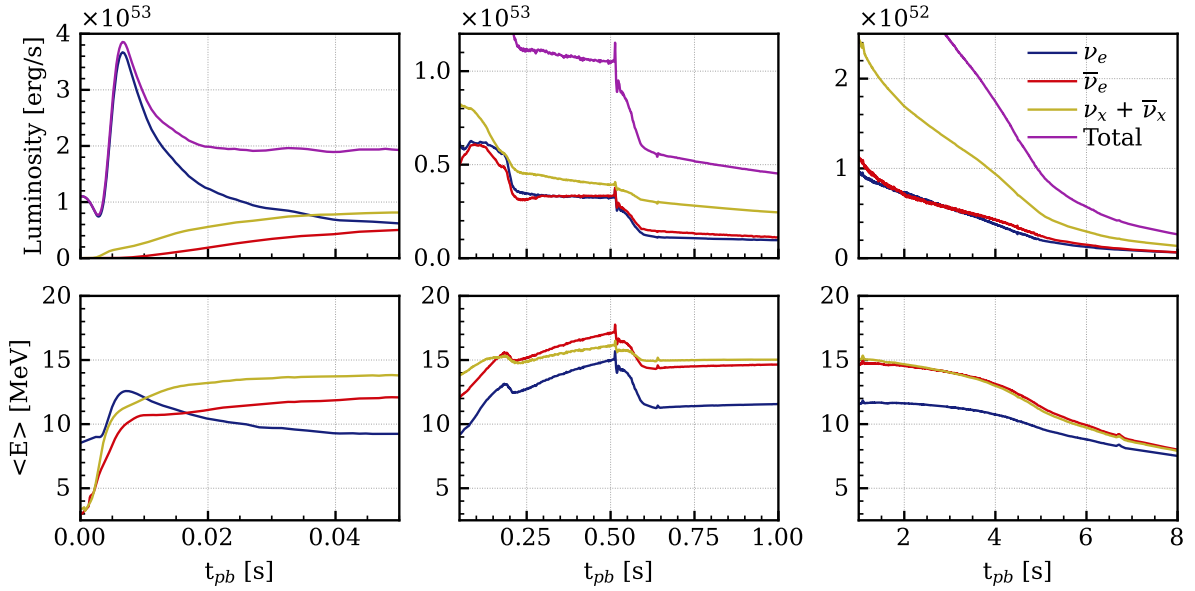

Figure 5.1.: Neutrino luminosity and mean neutrino energy for a 27 $M_\odot$ progenitor assuming a LSS220 equation of state (EOS) (model LS220-s27.0c, 1D computation) as a function of the time after the bounce. The three phases of the SN neutrino emission process are shown, from left to right: shock-breakout, accretion phase, and Kelvin-Helmotz cooling. The explosions of the displayed 1D model were artificially triggered at 0.5 s post-bounce. Model from the Garching Supernova archive [282], reported in [270].

traversing the remnant medium, both the MSW matter-effect [279,280] and neutrino-flavour oscillations can affect the described processes and, therefore, the observed neutrino signal [270,281].

Regardless of the complex process described above, the emitted neutrino signal can be divided into three main phases [269,270,273]:

1. The *shock-breakout*, characterised by the high-luminosity emission of ν_e;
2. The *accretion phase*, defined between the shock stalling and the final explosion;
3. The *Kelvin-Helmoltz cooling phase*, where the newly formed NS slowly cools into a deleptonised compact remnant. During this phase, the neutrino luminosity is shared between all flavours.

These three distinct phases are shown in figure 5.1 for a 27 $M_\odot$ progenitor from a isotropic, radius-dependent, simulation reported in [270]. The upper panels depict the neutrino luminosity for each neutrino flavour, where, as previously discussed, a sharp rise in the emission of electron neutrinos characterises the first phase of the

event, followed by a $\mathcal{O}(10)$s tail of emission of all neutrino flavours. The bottom panels depict the neutrino mean energies, expected around 10 MeV throughout the majority of the process, with a decrease down to $\sim$5 MeV at the end. The luminosity curves often display the same features associated with each phase, regardless of the model or the progenitor star [270, 273]. The differences become clearer the more time passes after the core bounce, as the outer shells of the dying star collapse inwards [283].

The first and only time SN neutrinos have been observed was for the SN1987A. It was the brightest SN registered in more than three centuries, originating from a blue supergiant in the Large Magellanic Cloud (LMC), $\sim$50 kpc away from Earth [284]. The incoming neutrinos were detected in four different detectors throughout the world: Kamiokande-II [285] (water Cherenkov) observed 11 events [286], the Irvine-Michigan-Brookhaven (IMB) [287] experiment (water Cherenkov) observed 8 events [288] and Baksan Neutrino Observatory [289] (crystal scintillator) observed 5 events [290]. The Mont Blanc Underground Neutrino Observatory (liquid scintillator) also reported on 5 events [291] but from several hours prior to the others, making the claim highly disputed. The neutrino interactions happened $\sim$2.5 h before the light front was detected in telescopes, but were only identified by the neutrino experiments days after during offline data analysis. Using real-time analysis, the neutrino signal can serve as an early warning for astronomers measuring the electromagnetic (EM) counterpart.

5.2. The supernova early warning system

SNe within the Milky Way are expected to occur only 1.63 ± 0.46 times per century [292]. As a rare astronomical event, the scientific community is always eager to extract as much information as possible from it and to avoid not recording such an event. As discussed in the previous section, neutrinos are promptly emitted in case of a SN event, while its electromagnetic counterpart may appear only after several hours or even days, depending on the progenitor star [293]. Neutrinos could then provide an early warning of an incoming SN signal and give time to prepare and fine-tune EM radiation and cosmic ray detectors. Based on this premise, SNEWS is an international network of neutrino observatories with the aim of detecting SN neutrinos and providing an early warning to astronomers in case of a SN event [294].

The first implementation of the SNEWS network was established in 1998 as a tiered alarm system based on three core principles: “prompt”, “pointing”, and “pos-

itive" [294]. The warning system works by running a 10 s coincidence trigger with inputs from the different neutrino observatories and is designed to minimise the chance of sending a false alarm to the astronomical community. For an alarm to be sent to astronomers, denominated "GOLD alert", several conditions need to be met: there must be at least a 2-fold coincidence in a 10 s window from different experiments, at least two of the experiments need to be located in different laboratories, at least two of the experiments need to tag their trigger as "GOOD", and, for at least two of the experiments issuing the trigger, the false-alarm rate preceding the alarm must be lower than 1 false alarms per week. If a 2-fold coincidence between experiments is found but at least one of the other criteria is not met, a second tier of alarms, denoted "SILVER", is circulated among the experiments. After the individual experiments check their alerts and data, the alarm is either upgraded to to GOLD or discarded as false-alarm. In twenty-five years of operation, SNEWS has never issued a "GOLD alert". Currently seven experiments actively contribute to SNEWS alerts [295]: Super-Kamiokande [296], LVD [297], IceCube [298], KamLAND [299], HALO [300], SNO+ [301] and Nova [302] (LVD [297], Borexino [303], and the Daya Bay [304] experiments previously contributed). Several experiments are "express-line" listeners of alerts, which receive "SILVER alarms" [305]: LIGO [306], KM3NET [307], GCN [308], Nova [302], XENONnT.

With the direct observation of gravitational waves in September of 2015 by the LIGO and Virgo collaborations [309], the multi-messenger astrophysics field leapt forward into a new paradigm: the same astrophysical event can now be observed through the four forces of the standard model [310]. Moreover, developments in the instrumentation of EM telescopes loosened their requirements regarding false-alarm rates of possible astronomical events. The SNEWS network adapted to the changing standards by developing SNEWS 2.0 [305].

In contrast to the first iteration of the platform, SNEWS 2.0 strives to send more alarms to the community. It aims to achieve this goal by lowering the threshold for generating alerts in order to gain sensitivity and by adding alerts based on pre-supernova neutrinos. Moreover, it plans to combine the timing information from individual experiments in order to provide pointing by triangulation. Another novel goal of SNEWS 2.0 is the addition of large DM detectors, where CEνNS flavour-insensitive neutrino detection provides a measurement of the total energy independent from neutrino oscillations [311,312]. The expected SN neutrino signals in current and

next generation LXe TPCs, in particular in XENONnT and DARWIN, are the subject of the next sections.

5.3. Supernova neutrinos detection in LXe TPCs

In xenon targets, MeV neutrinos interact primarily through CEνNS. At these energies, the recoils induced in the xenon target are on the order of a few keV, requiring a low energy threshold to be detected. Unlike the main WIMP analysis, to achieve the lowest possible detection threshold, an S2-only analysis can be conducted. In this analysis framework, the need for non-amplified primary scintillation light (S1) is dropped, accepting events whose only detectable signal is from the ionisation and gas electron amplification (S2). An implementation of the S2-framework to search for light DM with XENON1T can be found in [126].

When a SN neutrino burst reaches the active target, the rate of events is expected to increase to tens or hundreds of hertz and decrease again in less than 10 seconds. In stable science-run conditions, a sporadic increase in rate is possible but unlikely, usually associated with single electron trains after large S2 signals, which can be vetoed, or with hotspots (see Chapter 2). A restricted set of cuts tuned to select the expected SN neutrino signal over normal background conditions allows for the identification of such events a few minutes after the data is acquired.

In Subsection 5.3.1, the CEνNS process is described in more detail, followed by the description of the developed framework to simulate the expected signal of neutrinos from a SN burst in XENONnT in Subsection 5.3.2. Although the framework is capable of dealing with several different SN models, the previously presented Bollig2016 model from [270, 282] in Figure 5.1, is here used as a benchmark. To conclude, the detection significance of neutrinos from a SN event by current and next generation DM experiments is discussed in Subsection 5.3.3

5.3.1. CEνNS

As mentioned above, $\mathcal{O}(10)$MeV neutrinos interact with xenon mostly through coherent elastic neutrino-nucleus scattering [313–315]. In this process, the neutrino interacts coherently with an entire nucleus via a neutral-current interaction mediated by a Z bo-

son, resulting in a nuclear recoil. The CEνNS interaction is independent of the flavour of the neutrino up to next-to-leading order (NLO) radiative corrections, resulting in a common scattering cross-section for all the different flavours of neutrinos and anti-neutrinos. For a target made of xenon atoms, the CEνNS cross-section of the process is enhanced by its total number of neutrons, making it larger than the cross-section of the charge-current counterparts, such as electron scattering and inverse beta decay, by over an order of magnitude [316]. The differential cross-section for the CEνNS process of a neutrino energy E_ν and recoil energy E_R is given by [314]:

$$\frac{\mathrm{d}\sigma(E_\nu, E_R)}{\mathrm{d}E_R} = \frac{G_F^2 M}{4\pi} Q_W^2 \left(1 - \frac{ME_R}{2E_\nu^2}\right) F^2(q^2) \,, \tag{5.3}$$

$$Q_W = N - \left(1 - 4\sin^2\theta_w\right) Z \,, \tag{5.4}$$

where G_F is the Fermi constant, M is the total mass of the target, N and Z are the number of neutrons and protons in the target nucleus, $\sin^2\theta_w \approx 0.2386$, is the sine of the weak mixing angle at small momentum transfer, $F(q^2)$ is the nuclear form factor, and $q^2 = 2ME_R$ is the momentum transfer. For the xenon atom and the small values of E_R considered, the Helm form factor [85] is considered a good approximation with an algebraically closed form:

$$F(q^2) = \int \mathrm{d}r \; e^{iq\cdot r}\rho(r) \approx \frac{3j_1(qr_0)}{qr_0} e^{-\frac{1}{2}(qs)^2} \,, \tag{5.5}$$

where j_1 is the Spherical Bessel function of the first kind, $r_0 \approx$42.16 fm is the nuclear radius parameter, and $s = 0.9$ fm is the nuclear skin thickness parameter, both for the xenon atom.

Figure 5.2a shows the Helm form factor calculated for the most common xenon isotopes up to 200 keV and Figure 5.2b shows the calculated differential cross-section presented in Equation 5.3 in a heat map as a function of the energy of the incoming neutrino and of the energy of the recoiling xenon nucleus. This emphasises the low-energy recoils expected on the $\mathcal{O}$(10)MeV energy range of the neutrinos. Recent results using effective field theory (EFT) computations [317] give more precise values for the neutrino-nucleus form factor for xenon atoms, showing differences of $\mathcal{O}$(1)%.

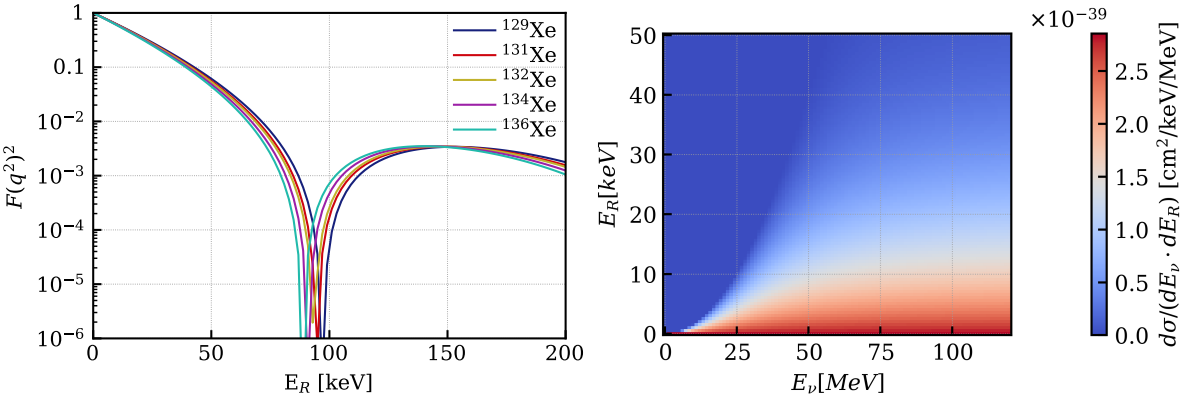

Figure 5.2.: **(a)** Square of the Helm form factor for the more naturally abundant xenon isotopes. **(b)** Differential cross-section of the CEνNS process as a function of incident neutrino energy and recoil energy for the ^{131}Xe isotope.

5.3.2. Simulation of SN neutrinos in XENONnT

The SN neutrino signal expected in a given detector is dependent on several factors: interaction type, size of the detector, distance to progenitor and the SN neutrino luminosity. In the case of LXe TPCs, the differential rate of expected events, $\frac{\mathrm{d}R_0}{\mathrm{d}E_R}$, can be calculated using the CEνNS cross-section from Equation 5.3 and the neutrino luminosity curve, $f_i(E_\nu)$, where i are the different neutrino and antineutrino flavours. Taking into account a SN neutrino light-curve defined between the initial time t_0 and final time t_f, the differential rate of interactions is given by [312]:

$$\frac{\mathrm{d}R_0}{\mathrm{d}E_R} = \frac{MN_A}{A4\pi d^2} \sum_{i=\nu_e,\nu_{ae},\nu_x} \int_{E_{min}} \int_{t_0}^{t_f} \frac{\mathrm{d}\sigma}{\mathrm{d}E_{min}}(E_\nu, E_R) f_i(E_\nu) \mathrm{d}E_\nu \mathrm{d}t \tag{5.6}$$

where A is the atomic mass of the target, N_A is Avogadro's number, d is the distance to the SN, and $E_{min} = \frac{1}{2}\left(E_R + \sqrt{2\,E_R + 2mE_R}\right)$ is the minimum energy of the neutrino for the interaction to occur.

An example of a neutrino luminosity curve, $f_i(E_\nu)$, can be found in Figure 5.1. Figure 5.3 shows the differential rate as a function of time when integrated over energy and as a function of energy when integrated over time. Without concern for detector limitations, the light curve naturally resembles the neutrino luminosity curve in its shape. Due to energy threshold, trigger efficiency and detector effects, experiments have an intrinsic detection efficiency, usually energy dependent, $\epsilon(E_R)$, such that the observed differential event rate spectrum, integrated over the duration of the neutrino

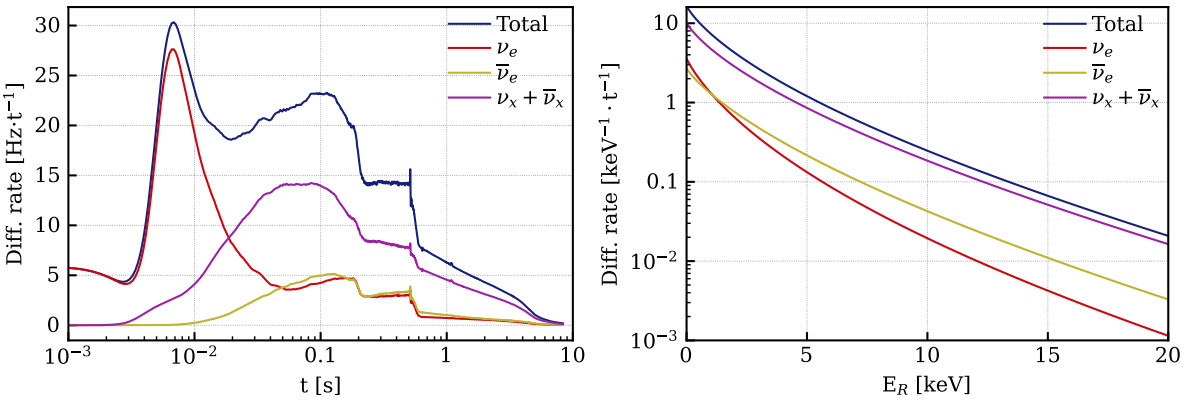

(a) **(b)**

Figure 5.3.: Differential rate per active target mass as a function of time, integrated over recoil energy up to 20 keV **(a)**, and as a function of recoil energy, integrated over time from 0 to 10 s **(b)**. The sharp increase at $t = 0.5$ s in **(a)** is due to the artificial triggering of the SN in this particular model. Rates from the Bollig2016 SN model for a SN progenitor of 27 $M_\odot$ at 10 kpc [270, 282]. Same model as in Figure 5.1.

emission period, is given by:

$$\frac{dR}{dE_R}(E_R) = \epsilon(E_R)\frac{dR_0}{dE_R}(E_R) \ . \tag{5.7}$$

Finally, the total number of observable events, N_{obs}, is obtained by integrating over the full energy spectrum:

$$N_{obs} = \int \frac{dR}{dE_R}(E_R)dE_R \ . \tag{5.8}$$

Figure 5.4 shows the number of expected CEνNS interactions without considering the detector-specific efficiency factor $\epsilon(E_R)$ introduced in Equation 5.7. Even though LXe TPCs won't be able to detect the magnitude of neutrino interactions as dedicated observatories [318, 319], the current generation of experiments can already expect >10 neutrino interactions for SN within the Milky Way[2], increasing ten-fold for the next generation of experiments.

Detector effects and threshold limitations are key in the low-energy regime of CEνNS interactions. To simulate a realistic signal model, a simulation using the

[2]The diameter of the Milky Way is a complex subject which exceeds the aim of this work. The commonly accepted value is ∼30 kpc, but up to where the stellar disk and halo extend is a highly debated and researched subject [320]

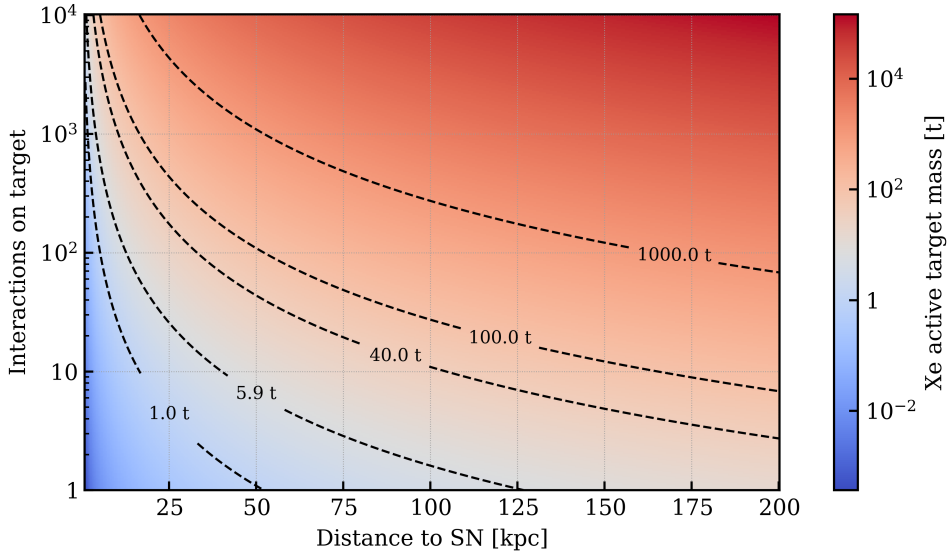

Figure 5.4.: Heatmap of the number of interactions expected in a xenon target as a function of distance for a range of target masses. Several benchmark target masses are highlighted as dashed lines.

WFSim package [258] was carried out. WFSim is a tool developed by the XENON collaboration to simulate waveforms, which can be processed in the same way as acquired data. The simulation package takes a set of instructions regarding the initial interactions to handle, such as their times, positions, recoil energies, and recoil types, and computes the different processes throughout the TPC up to waveform creation. These include, but are not limited to, the photon propagation and scaling by local LCE, electron diffusion, single photoelectron (SPE) shape smearing, SE gain corrections, field distortion correction, zero length encoding (ZLE) by the digitisers, and the ten-fold linear amplification by the amplifiers of the DAQ system. Most of the parameters have been tuned using measured data and the results, when compared with calibration data [114, 193]. In the case of SN neutrinos simulations, the main advantages of using a full-stream waveform simulator are the introduction of detector threshold effects and the realistic response to the signal.

The instruction file for the simulator is constructed by sampling times from the energy-integrated time curve (Figure 5.3a), energies from the time-integrated energy spectrum (Figure 5.3b), and positions uniformly distributed within the active volume of the TPC. The total number of events sampled is the number of expected interactions on the detector given by Equation 5.8. The light yield, charge yield, and quanta generation are provided by NEST [157] through nestpy [158]. The ∼150 interactions of the model in Figures 5.1 and 5.3 take less than 10 minutes to compute and can be

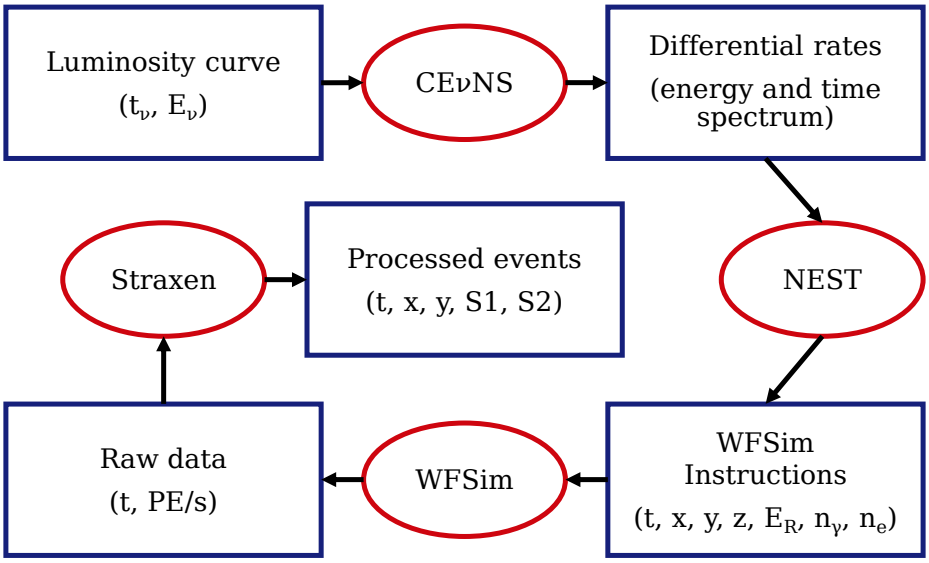

Figure 5.5.: Flow-chart of the SN simulation framework. The blue boxes depict data types and the red ellipses software/code steps, as described in the text.

streamlined by parallelising the simulation of several SN events in different processes. Since each simulation only provides $\mathcal{O}(100)$ events, a large number of independent simulations are required to accumulate enough statistics to accurately model the expected signal shape. These are always executed with a realistic number of interactions in the active volume, as previously described, instead of sampling a large number of isolated recoil times and energies. In this manner, the simulated waveforms and their subsequent processing always simulate a realistic SN neutrino signal in XENONnT. A comprehensive flow-chart of the different steps in the SN simulation framework developed is shown in Figure 5.5.

For the Bollig2016 model for a SN progenitor of 27 $M_\odot$ at 10 kpc, an average of 137 events are expected to occur, with a standard deviation of 4.5. After simulation and processing, using the same methods as for acquired data, 126 S2 signals are, on average, identified, with a standard deviation of 5.3 identified signals. The observed loss is the sum of several processes: events from which the initial electrons did not reach the extraction region (captured by electronegative impurities or interaction within a charge-insensitive volume), incorrectly paired events (AC), or incorrectly classified events. The resulting event reconstruction efficiency is (91.97 ± 0.22) % and the average expected rate over the duration of the SN duration (18.00 ± 0.03) Hz.

The signal is composed primarily of single and few electrons with a tail of events with S2 areas up to ∼1000 PE. In XENONnT, the background rate in the low-energy ROI is dominated by single electron events and it is ∼220 Hz. In runs populated by warmspots or hotspots, the rate of single and few electrons rises one or more orders of magnitude. In order to distinguish the SN signal from the background, a series of events selection criteria was developed based on the work of the collaboration on single and few-electron signals [256]. The set of selections is composed by:

- A volume cut, removing any events within 10 cm of a hotspot or warmspot.
- A timing cut, requiring that the small S2 signals are separated in time from interactions with large energy deposits in the TPC. The target of this cut is the single electron emission observed after large events, as reported in [126, 256, 257, 321].
- A position cut, analogous to the timing cut above, based on the position difference to any previous large event.
- A cut based on the spatial uniformity of the identified events, targeting muons which deposited energy within the TPC. Unlike the expected neutrino signal, the muons leave a track-like signal, which impacts the background level considerably several times per hour. As, in the case of a real SN, the neutrinos will also be detected in the veto systems, they can not be used to exclude muon events, as with other science searches.

Not considering the warm/hotspot cut, the background is highly mitigated by the other cuts, with only 3.7 % of the background events surviving selection, while the impact on the signal is negligible, with 97 % of the signal events passing all cuts. Figures 5.6a and 5.6b show the simulated signal shape compared to the background in the ROI. The two clearly distinct populations are the single electron population (lower area, lower width) and the two electrons population followed by the few-electrons population. The single electron region is where 13.9 % and 35.1 % of the total number of events identified as an S2 are located for the simulated SN signal and background data, respectively. Above two electrons, the SN signal shape supersedes the background spectrum two-fold. Above this threshold, ∼100 signal events can be identified. For S2 areas above ∼1000 PE, the average background is again larger than the expected signal with ∼2 neutrino events expected in this region. Figure 5.6c shows the evolution of the background rate, with and without cuts applied in consecutive windows of 7 s. The reduction of background rate from ∼220 Hz to ∼2.4 Hz provided by the described

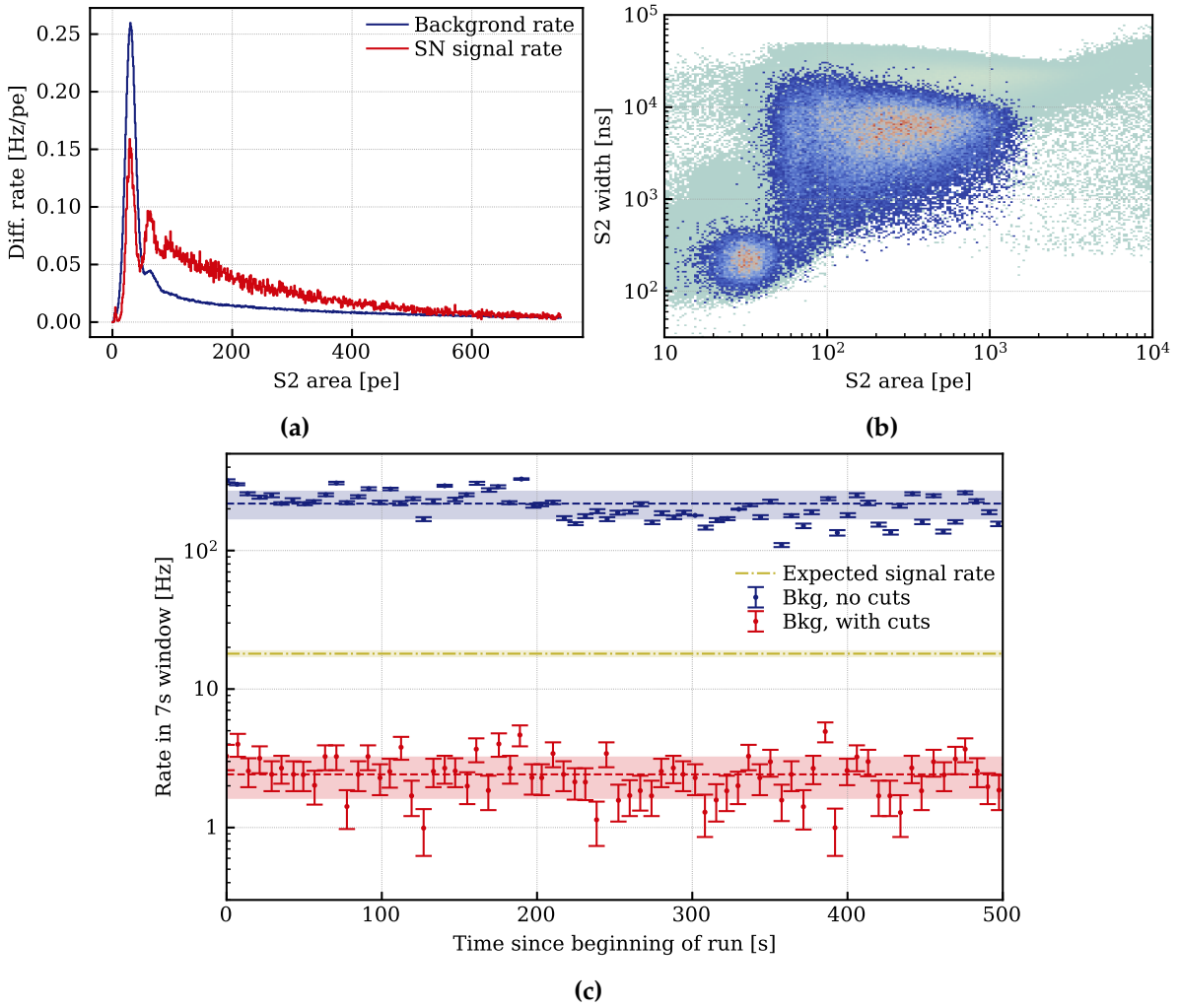

Figure 5.6.: **(a)** Differential rate of background and signal events as a function of the reconstructed S2 area. Both curves are normalised to livetime. **(b)** Signal (blues and reds) and background (semi-transparent greens and yellows) populations in the event width as a function of the event area parameter space. **(c)** Background rate before (blue) and after (red) cuts applied, measured in consecutive windows of 7 s. In gold, the expected number of events integrated over a similar time window of 7 s is shown. The bands represent one standard deviation of the distribution of the observed rates. Figure **(c)** adapted from [322].

selection criteria allows for the detection of the SN events, given the expected rates of $\sim$18 Hz.

5.3.3. Significance of SN detection in current and next generation dark matter experiments

The next generation of LXe TPCs will continue the search for DM while diversifying their science programme(see Chapter 6). With larger active targets, the SN-detection reach of these experiments will be increased when compared to the present. Approximately 100 neutrino events are expected in the current generation of experiments from the benchmark 27 $M_\odot$ SN progenitor at 10 kpc. Targets holding 40 t of LXe, such as the one projected for DARWIN, will increase this number to $\sim$800 events. While this brings challenges such as event pile-up and mis-paired reconstruction, it also extends the reach of detection beyond that of current DM experiments.

Figure 5.7 shows the detection significance for a 27 $M_\odot$ progenitor. The significance of detection is calculated based on the asymptotic formula defined in [323] for a counting experiment with a known number of backgrounds. The null hypothesis tests if the observed events can be entirely attributed to the background, whereas the alternative hypothesis contains in the observed events a combination of both the expected background and SN neutrino signals. Under the assumption that the single and few-electron background scales with the area of the detector, a 60 t xenon target experiment would be able to double the currently surveyed distance from $\sim$30 kpc to $\sim$70 kpc, beyond the Small Magellanic Cloud, at 3 σ significance level. If the background would be improved by a factor of 10, however, the distance at which a detection could be claimed is extended up to $\sim$115 kpc. R&D projects are underway to understand and mitigate the main backgrounds arising from single electrons.

5.4. Implementation of XENONnT in SNEWS

Although out of the scope of this thesis, SNe within $\sim$10 kpc could produce both elastic and inelastic charged-current interactions [316, 324, 325]. For the latter, both the resulting electrons and de-excitation gamma rays contribute as ERs events in the LXe and neutrino-induced neutrons as NRs events are relevant for the next-generation LXe DM detector targets. Moreover, for near-Earth SNe bellow the kpc-scale, LXe targets of might also be used to survey pre-supernova neutrino emission. A significant detection of these interactions is, however, highly dependent on maintaining a sub-keV energy threshold and further reduction of low-energy NR backgrounds [326].

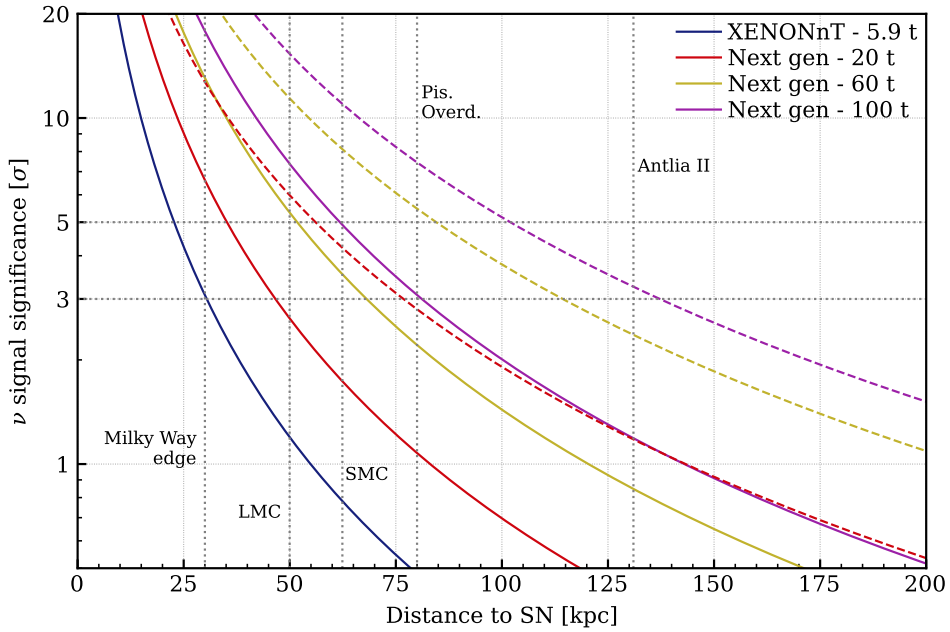

Figure 5.7.: Detection significance for a SN from a 27 $M_{\odot}$ progenitor (Bollig 2016 [270, 282]. Current levels of background at the ROI are scaled by the area of detector assuming a 1:1 heigh-to-diameter ratio. Detection significances for a 10-fold decrease in background levels are shown in dashed-lines.

Another important caveat to mention is the interactions occurring in the water tank which can be detected in the muon and neutron veto of the TPC. The main channel of interaction is through inverse beta decay with the emission of a neutron and positron in the final state. Both the positron itself and ionisation electrons created by scattering will emit Cherenkov radiation, detectable by the muon veto and neutron veto PMTs. In total, $\sim$200 events may be detected in the water tank in the short duration characteristic of the SN neutrino flux, significantly above background level [327]. By requiring a coincidence between the both the TPC and muon veto/neutron veto triggers, the false-alarm rate of a XENONnT-based SNe trigger can be greatly reduced.

XENONnT is the first DM experiment to actively join the SNEWS network. Albeit with limited detection capabilities when compared with massive neutrino observatories such as Super-Kamiokande [328] or Icecube [319, 329], DM experiments have the advantage of detecting all neutrinos flavours and having a chance to reconstruct the full energy curve of the SN neutrinos. In this section, the required implementation of absolute timing in XENONnT is described, followed by a description of the framework implemented to communicate alerts between the experiment and SNEWS.

5.4.1. Absolute timing in XENONnT

The XENONnT TPC DAQ system has 115 digitisers collecting the signals from the experiment's photosensors. The synchronisation between all the digitisers is guaranteed by propagating a calibration signal through the chain. If the synchronisation is broken, the DAQ ceases to acquire data until it is re-established [215]. The DAQ maintains its own high-precision clock, which provides the timestamps to the acquired data (DAQ time). However, while still maintaining the synchronisation of all internal devices, the clock will drift over time from the perspective of an outside viewer from its internal jitter [330]. For a global network like SNEWS that aims to merge incoming inputs from different experiments, a unified measure of time is essential. The accepted standard is global positioning system (GPS) time [305]. Therefore, a framework that converts DAQ time into GPS time and that provides an absolute timestamp for each event record was developed.

The infrastructure to provide GPS time to the underground caverns of LNGS has been in place since 2012 for use in the context of the CERN Neutrinos to Gran Sasso (CNGS) project [331] and updated in 2019 to provide GPS-based timestamps for all the experiments running in the laboratories [332]. The system is composed of a GPS receiver antenna connected to a server above ground, which sends well-defined synchronisation pulses underground via fibre-optics. At the experiments' end, a local GPS module receives the synchronisation pulses and provides absolute timestamps accurate up to $\sim$15 ns (1 σ).

In the XENON DAQ room, a local GPS module receives updates from the GPS main module at 1 Hz, which keeps an internal 50 MHz clock accurately in sync with GPS time. The module has four input channels and outputs through a USB interface. Whenever there is a transistor–transistor logic (TTL) pulse in one of the inputs, the module writes an American Standard Code for Information Interchange (ASCII) entry in a log file with the input channel number and the corresponding GPS timestamp of the trigger pulse. The local GPS module also outputs a 0.1, 1 or 10 Hz analogue signal from its clock for any required use. Since the TPC DAQ is triggerless, meaning all the pulses get digitised and the trigger and pulse selection happen at the processing level, there is no analogue signal to send to the local GPS module and tag each triggered event with a GPS timestamp. Therefore, as depicted in figure 5.8, the method of converting DAQ time to GPS time is less straightforward. TTL pulses at a frequency

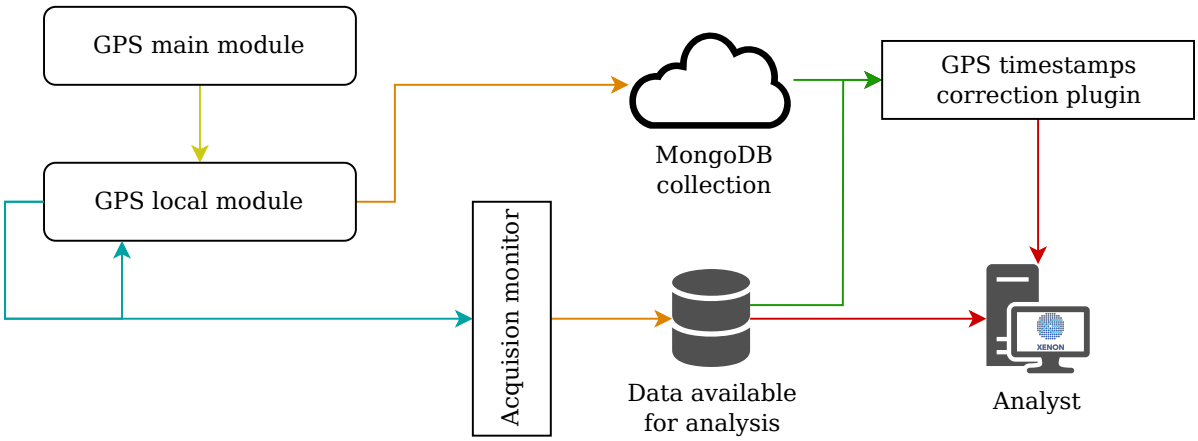

Figure 5.8.: Diagram of the GPS time correction infrastructure. Arrow colour legend: yellow – fibre optic cable from the GPS main module above ground to the local GPS module at the XENON DAQ room underground; blue – 0.1 Hz synchronisation pulse; orange - handling of data by the XENONnT computing infrastructure at LNGS; green – data pipeline during online or offline processing of the GPS timestamp correction; red – data with corrected GPS timestamps upon request by an analyst or by a running script from the XENONnT data analysis front-end.

of 0.1 Hz are sent from the local GPS module to both the acquisition monitor and the GPS module itself.

The acquisition monitor is a v1724 CAEN digitiser dedicated to auxiliary functions such as collecting information about the status of the DAQ, operating the hardware veto modules, collecting the sum analogue waveform of the photosensors, and, for the matter in question, recording the synchronisation pulses from the local GPS module. The data from the acquisition monitor is read out in the same way as the data from the other digitizers and integrated into the larger data processing system. The synchronisation pulses' timestamps provided by the local GPS module are automatically uploaded into a MongoDB [250] "collection", where they become available for querying. When an analyst or automated procedure requests the GPS-corrected timestamps of a given data period, these are computed and provided together with all the other data properties requested. A schematic of the infrastructure described can be found in Figure 5.8.

By correlating the synchronisation pulses in the acquisition monitor data and in the timestamped outputs of the local GPS module, these periodic signals serve as the basis for converting timestamps from DAQ time to GPS time. The corrected GPS

timestamps are calculated by interpolation between the synchronisation pulses:

$$t' = t_0 + \Delta t_0 + \frac{t'_1 - t'_0}{t_1 - t_0} \cdot \Delta t \ , \tag{5.9}$$

where t' is the corrected event timestamp of the event in GPS-time, t_0 is the timestamp of the previous sync pulse in DAQ-time, t'_0 is the timestamp of the previous sync pulse in GPS-time, t_1 is the timestamp of the next sync pulse in DAQ-time, t'_1 is the timestamp of the next sync pulse in GPS-time, Δt_0 is the offset difference $(t'_0 - t_0)$, and Δt is the time span from the previous sync pulse to the uncorrected signal timestamp in DAQ-time. A schematic of the correction effect is shown in Figure 5.9a. The algorithm is robust to missing synchronisation pulses by interpolating between the next available pulse and the start and end of the run by linearly extrapolating from the closest two pulses if required. The correction was implemented in the XENONnT analysis framework as a straxen plugin. An example of the correction can be seen in Figure 5.9b, where, as seen from the GPS-time point of reference, the binned event rate is shown for both uncorrected (DAQ-time) and corrected (GPS-time) timestamps. The result is a shift in the timestamps and, at a too small scale to be noticeable in the figure, a change in the time difference between the two time frames.

The known effect of drift on the DAQ clock over time can also be measured with the timestamps of the synchronising pulses. Over the course of the first science run of XENONnT, the average DAQ time drift was $-0.31\,\mu s_{GPS}/s_{DAQ}$.

5.4.2. Connection and communication to SNEWS

SNEWS is a fast-acting network and relies on the contributing experiments to provide alerts within minutes, at most hours, of a potential astrophysical event. The connection to the SNEWS network is realised through "SNEWS 2.0 Publishing Tools" using a publish-subscribe system built with HopskotchSccima [333, 334]. XENONnT communicates with the "SNEWS 2.0 Coincidence System" at three different levels: send heartbeats, listen to alerts, and publish alerts. Heartbeats are regular messages that test the connection of the experiments to the network and their availability status (regular data taking, calibration ongoing, maintenance). At this moment, SNEWS 2.0 is still finalising its development and how to handle communication with the experiments in a robust way. When fully integrated, XENONnT will be able to send not only the trigger itself but also the significance and timing of the detection.

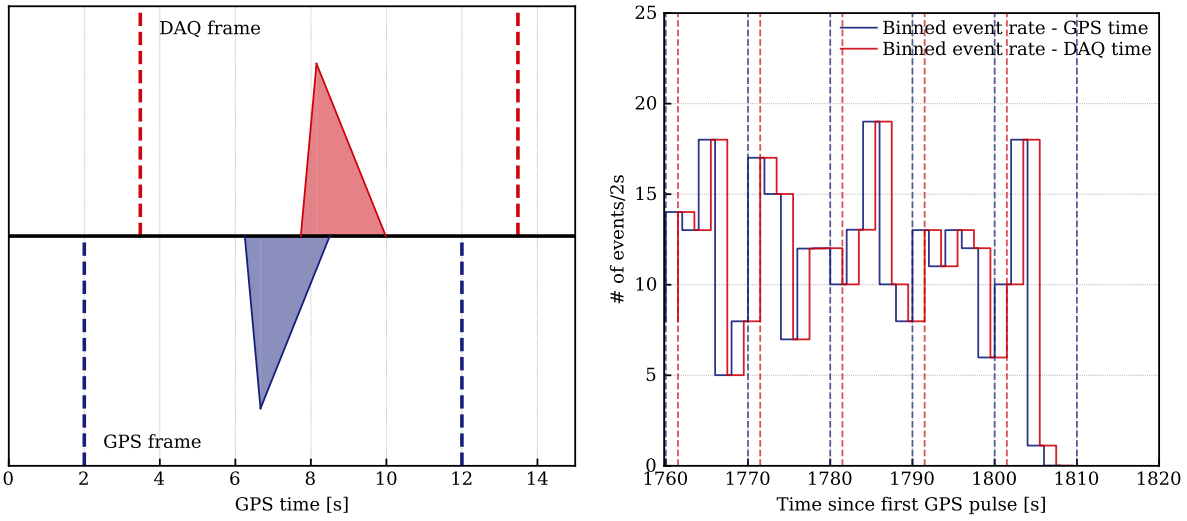

Figure 5.9.: (a) Schematic of the GPS correction. The vertical dashed lines depict the synchronisation pulses as registered in the GPS module (blue) and DAQ AM (red). The triangular shapes represent the same recorded event, seen from both time frames. **(b)** Shift in event times after GPS correction close to the end of a run. The vertical dashed lines depict the synchronisation pulses. On the right side, the last AM pulse is missing since the run was already terminated. In this last region the correction is extrapolated, as detailed in the text.

XENONnT already has several tools in place to monitor the experiment and the data-taking process within seconds to minutes of the data being acquired [215], the XENONnT Online Monitor. An extension to the Online Monitor was developed to apply the cuts described in the previous section and calculate the moving rate of events as they are dispatched. If the computed rate is ever higher than a user-set threshold, an alert is generated. Both the on-site shifters and multi-messenger team are notified by text messages, e-mails, and Slack notifications. In parallel, communication is established with SNEWS and the alert is sent within a minute. The trigger system is being tested in the XENON data infrastructure and will be deployed for continuous monitoring and automatic triggering directly on-site at LNGS. In convergence with the plans of SNEWS 2.0, the system will be online in the second half of 2023. A publication of the work described and commissioning of the XENONnT active SN trigger will then follow.

Chapter 6.

Xenoscope, a full-height DARWIN demonstrator

Following in the steps of the XENON programme, the planned DARk matter WImp search with liquid xenoN (DARWIN) observatory is a next-generation dark matter and neutrinos detector. To develop and test some of the key technologies for DARWIN, a full-scale vertical demonstrator was built at the University of Zurich – Xenoscope. The main goal of the project is to test electron drift in a DARWIN-scale-height TPC.

In this chapter, the DARWIN project and its main goals are described in Section 6.1, followed by a detailed description of the Xenoscope facility in Section 6.2, and an overview of the already completed and planned science runs of Xenoscope in Section 6.3.

6.1. The DARWIN project

The DARWIN observatory is the leading next-generation dual-phase LXe TPC. The main goal of the DARWIN experiment is to probe the spin-independent WIMP-nucleon cross-section down to $\sim 10^{-49}\,\mathrm{cm}^2$ [117, 335] and reach the irreducible neutrino fog [118] (see Figure 1.8 in Chapter 1). In its baseline design, DARWIN will instrument 40 t of liquid xenon (50 t total) in a cylindrical TPC, with 2.6 m height and 2.6 m diameter with two arrays of photosensors, above and below the target. As in current generation dual-phase LXe TPCs, PTFE reflectors cover the sides of the active volume and copper field-shaping rings are distributed vertically around the target

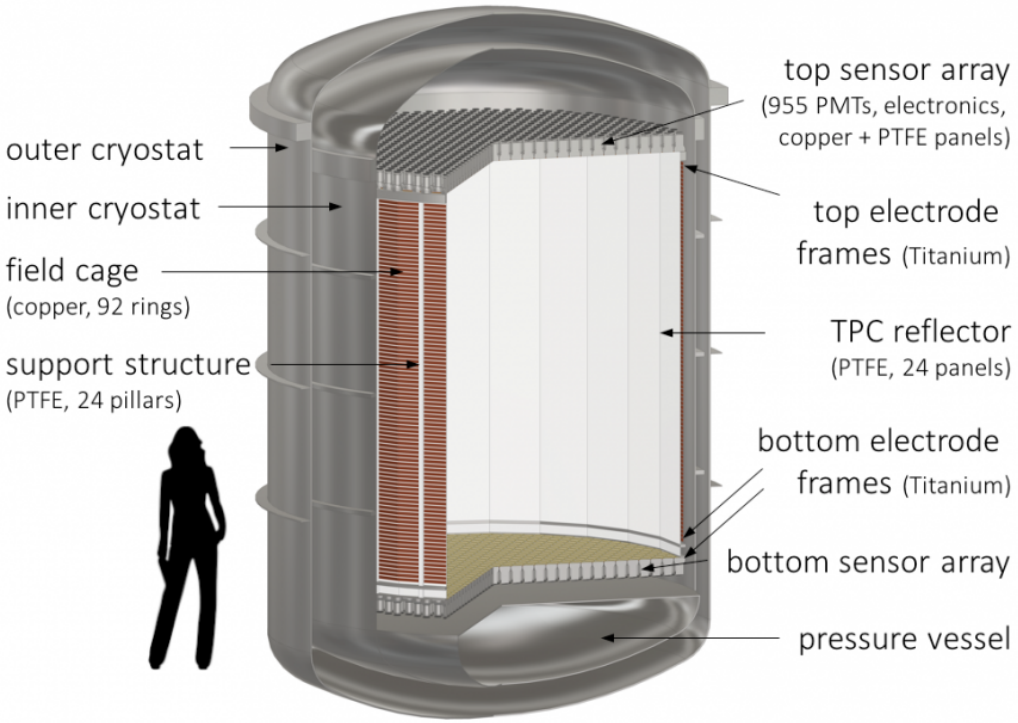

Figure 6.1.: Rendering of the DARWIN TPC baseline design. All the main parts of the detector (excluding veto systems) are depicted and labelled. Figure from [117].

to ensure a homogeneous electric field. A render of the baseline design is shown in figure 6.1.

However, DARWIN's complete science program extends detection beyond DM with broad neutrino and BSM physics searches. Regarding the nature of the neutrino, DAWRIN will be able to search for the neutrinoless double beta decay of ^{136}Xe, with a projected half-life sensitivity of 2.4×10^{27} years, using $50\,\mathrm{t} \cdot \mathrm{yr}$ exposure [138]. DARWIN has the potential to measure the flux of *pp* and ^{7}Be neutrino components with a precision of 1 %, and a 3σ detection of ^{13}N, ^{15}O neutrino components, through electron scattering using $300\,\mathrm{t} \cdot \mathrm{yr}$ exposure [336]. These would improve upon current measurements of the electroweak mixing angle, the electron-type neutrino survival probability and the uncertainty on the component-specific fluxes. Furthermore, DARWIN will pursue further searches for solar axions and ALPs through ER interactions, as well as measurements of ^{8}B solar neutrinos and supernova neutrinos through CEνNS[1].

[1]During the >10 yr lifetime proposed for DARWIN, SN neutrinos will hopefully be detected, not only searched for.

For DARWIN to achieve all its science goals, several technical challenges must be addressed. Regarding background mitigation, XENON1T was limited by ^{222}Rn concentration, and XENONnT successfully demonstrated that this intrinsic and unavoidable radiogenic background can be reduced to $<1\,\mu\text{Bq}\,\text{kg}^{-1}$ with the use of a dedicated distillation column (see Chapter 2). A further reduction down to $0.1\,\mu\text{Bq}\,\text{kg}^{-1}$ is needed to achieve the level required for DARWIN. On the other hand, the ^{85}Kr requirement, set at 0.1 ppt of ^{nat}Kr, is now achieved in current generation LXe TPCs.

Scaling up brings specific challenges related to the size of the future detector. With 2.6 m of diameter, the electrodes need further development to guarantee robustness and minimise any sagging effect while aiming for maximal transparency. In the vertical dimension, the drift of electrons over this unprecedented distance in LXe TPCs requires a long electron lifetime. Subsequently, there is a need for an efficient purification system, a carefully designed field cage to provide electric-field uniformity, ensure spatial, and temporal homogeneity and avoid charge-up of the PTFE panels, and high-voltage transfer to the cathode up to $\mathcal{O}(10-100)$ kV. A high drift field or, at least, a drift field comparable to current generation LXe TPC is vital to DARWIN's physics goals. On the one hand, higher fields allow for better ER and NR band separation and, therefore, better particle discrimination. On the other hand, with a low drift field, leading to low drift speed, the time separation of an S1 signal and its S2 counterpart becomes larger, resulting in higher rates of pile-up and AC events. Finally, with lower drift velocity, drifted electron clouds become increasingly diffused, losing depth resolution and, to some extent, planar reconstruction resolution.

To address the previously stated challenges, several R&D projects are underway and others are planned for the near future [337–340]. Two of these aim at testing the impact of scaling up directly: Xenoscope, at the University of Zurich, Switzerland, and Pancake, at the University of Freiburg, Germany. The first targets the vertical dimension by operating a 2.6 m TPC, albeit with only $\sim$15 cm diameter, while the second targets the horizontal dimension by operating a short but 2.75 m-wide setup. Xenoscope and further details on its facility and operation are discussed in the next section.

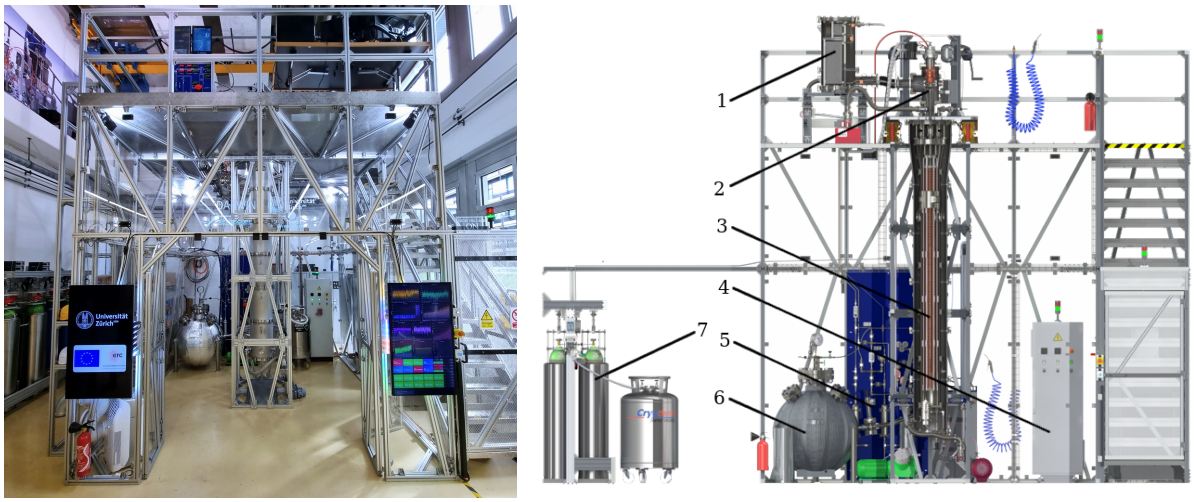

(a) (b)

Figure 6.2.: (a) Front view picture of the Xenoscope facility at UZH. **(b)** Schematic of the sub-systems of the Xenoscope facility. This will be a big caption pointing out the different parts: 1 - Heat exchangers; 2 - Top flange, cold head and feedthroughs; 3 - Main chamber; 4 - Power distribution cabinet; 5 - Main gas panel; 6 - BoX; 7 - Storage array. Figure adapted from [341]

6.2. The Xenoscope facility

Xenoscope is a facility with the main purpose of testing the vertical scalability of the dual-phase LXe TPC concept from the currently achieved ∼1.5 m-long drift up to 2.6 m. The detector resides in a two-floor infrastructure, nested within inner and outer stainless steel vessels, both suspended from a levelling system on the upper floor and makes use of a 400 kg of Xe inventory. The facility is composed of the central detector section and a collection of sub-systems: the cryogenics system, purification and gas handling system, the Xe storage vessel Ball of Xenon (BoX), the Xe storage bottle array, the electrical power distribution sytem, the DAQ, and the slow monitoring and control (SC) system. An extensive description of the Xenoscope facility and its subsystems can be found in [341]. All the subsystems were installed and successfully commissioned. A picture of the full system and a labelled schematic of the facility can be seen in figure 6.2a and figure 6.2b, respectively.

The support structure encompasses a 4 m × 4 m × 4 m volume and is constructed with 50 mm × 50 mm extruded aluminium profiles. It is designed to bear the full load of the structure itself, all the subsystems resting on the frame and the fully-filled cryostat, totalling 1.2 t. The interior of the frame is confined by acrylic panels on all

four sides and is accessed by two double doors at the front. A set of stairs gives access to the upper level.

6.2.1. Cryogenics and xenon circulation

Under operating conditions, the outer vessel is kept under vacuum to thermally isolate the inner vessel from ambient temperature, aided by several layers of biaxially-oriented polyethylene terephthalate (*Mylar*) to reduce radiative losses. The inner vessel is filled with xenon at ∼2 bar, cooled down to LXe temperature (∼177 K) by a copper cold head attached to a PTR from Iwatani Corporation [342], model PC-150, coupled to a 180 W heater unit for precise temperature control. To increase the efficiency of heat transfer from warm circulated xenon gas with cold liquid xenon, a set of two heat exchangers connected in series provides an interface between the cold inner parts of the detector and the rest of the gas system. These have a total heat exchange area of 5.26 m^2 and facilitate heat transfer between cold liquid removed from the top of the cryostat with warm gas incoming from the purification loop. The purified xenon, now cooled to a liquid either in the heat exchanger, the cold head, or in the path in-between, is fed through a hose into the bottom of the inner volume, naturally creating a preferred upward flow in the cryostat, which helps ensure that all the xenon in the cryostat is circulated and purified. Both the cold head and the heat exchangers are equipped with PT100 resistor temperature detectors (RTDs) to monitor the temperature of the xenon at different steps.

The removal of liquid and evaporation to gas is compelled by an under pressure on the return gas lines due to an in-line double-diaphragm xenon compressor model N1400.1.2SP.12E by KNF Neuberger [343]. The compressor produces a pressure difference between the inlet and outlet of up to 3 bar on the system. The gas circulation is then established from the cryostat, through the purification loop, and back to the cryostat. The recirculation mass flow is regulated by an HFC-203 flow controller produced by Teledyne Hastings [344], placed between the return line from the heat exchangers and the xenon compressor. The flow is also measured after the compressor with an HFC-201 flow meter.

In normal operation conditions, the xenon gas is constantly purified by a hot metal getter model PS4-MT50-R-535 from SAES [345]. The efficiency of the getter stays constant over the operational range of xenon flows (from ∼20 to ∼70 standard litres

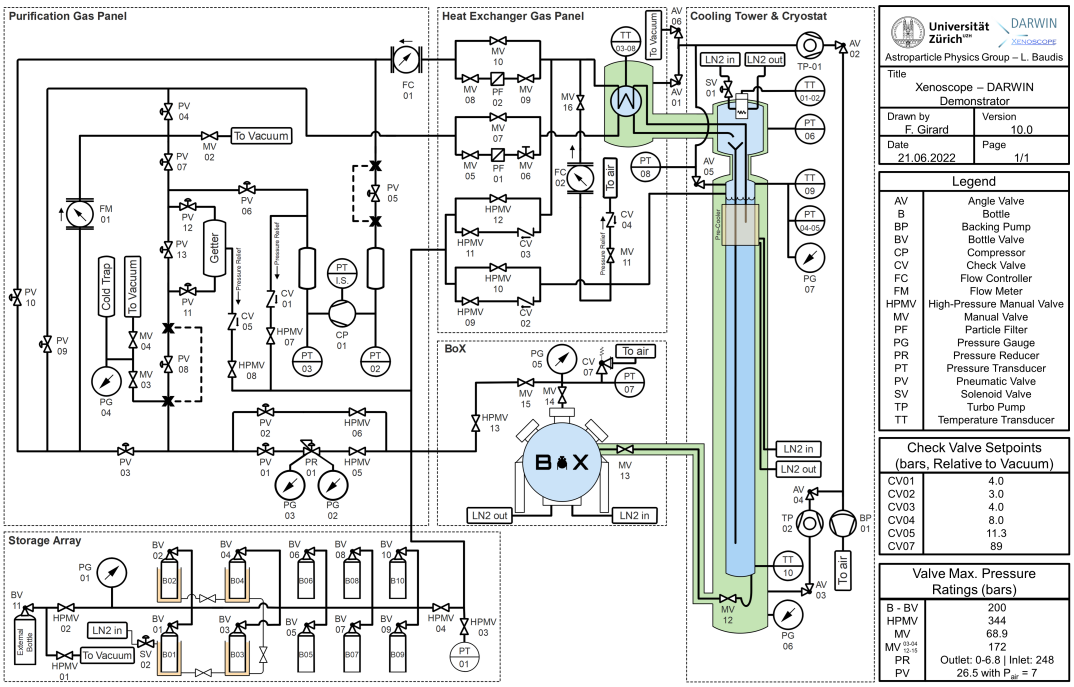

Figure 6.3.: Piping and Instrumentation Diagram of the Xenoscope facility. The facility is separated into five piping sections: purification (main) gas panel, heat exchanger gas panel, storage array, BoX, and cooling tower and cryostat. In regular operation, light blue areas in the diagram represent volumes where gas xenon is maintained, darker blue areas represent volumes with liquid xenon, and green areas represent volumes where vacuum is maintained by the turbopumps. In addition, one or more of the sleeved cylinders on the storage array are kept cold and the high-pressure lines connected to the storage array under cryogenic-pumped vacuum (see text for more details). P&ID up to date as of April 2023, provided by Frédéric Girard [346].

per minute (slpm)), meaning the purification rate is due primarily to the speed at which the full bulk of xenon is circulated through the purification loop. Under proper maintenance, the getter removes oxygen-like impurities down to <1 ppb at flows up to 70 slpm.

The path open to xenon circulation in the main gas panel is defined by the status of dual-acting pneumatic valves that can be actuated remotely. All of the ports with connections to the exterior and valves in contact with the high-pressure sections of the system (bottle rack and BoX) are manual high-pressure-rated valves, as shown in Figure 6.3.

6.2.2. Filling, recuperation and storage of xenon

The filling consists of transferring a set quantity of xenon from the storage systems, either the bottle rack array or BoX, to the cryostat. For both methods, the xenon is transferred in gaseous form and cooled down on the copper cold head, where it liquefies. After a constant gas pressure is established in the whole system and the cooling down of the vessels and xenon starts, the decrease in pressure caused by cooling and liquefying is compensated by continuously supplying more xenon from storage until the desired xenon mass is achieved inside the cryostat. To speed up the process of cooling down the entirety of the stainless steel inner vessel, a pre-cooler is attached to the outside of its highest straight section, encircling it. The pre-cooler consists of four stainless steel sections with a winding path in their interior, where liquid nitrogen can be supplied and undergoes liquid-gas transition. This process cools down the stainless steel parts and, therefore, the vessel which they are in contact with. The first filling of Xenoscope was performed without the presence of the pre-cooler at an observed filling rate of 3.95 kg/h. In subsequent fills, after the addition of the pre-cooler, the observed rate was 16.77 kg/h, $\sim$4.25 times higher than before. Detailed information on the design, commissioning and operation of the pre-cooler can be found in [346, 347]

As a run comes to an end and the xenon must be securely stored, the recuperation process takes place. There are two main methods of recuperation: gas recuperation to bottles with cryogenic pumping, and gravity-assisted liquid recuperation.

The storage array consists of ten[2] 40 L aluminium gas cylinders connected in parallel (bottom left in 6.3). Each row of cylinders is suspended from a weighting system consisting of 250 kg capacity load cells from Mettler-Toledo Schweiz GmbH, providing constant monitoring of the xenon inventory in storage and indicating any xenon losses between run cycles. The two left-most cylinders in both the front and back row are immersed in 1.22 m-tall Dewar flasks for cooling purposes. At room temperature, xenon undergoes a phase change to a supercritical state at 58.4 bar. Although dependent on temperature, the pressure of the total 400 kg inventory of xenon is $<$200 bar, and can, therefore, be safely stored within the ten bottles[2], as shown in figure 6.4.

[2]As of the writing of this thesis, only nine out of the ten cylinders are installed. The total available volume is still large enough to keep all the available xenon stored below the pressure limit of the bottles and valves of 200 bar (see Figure 6.4).

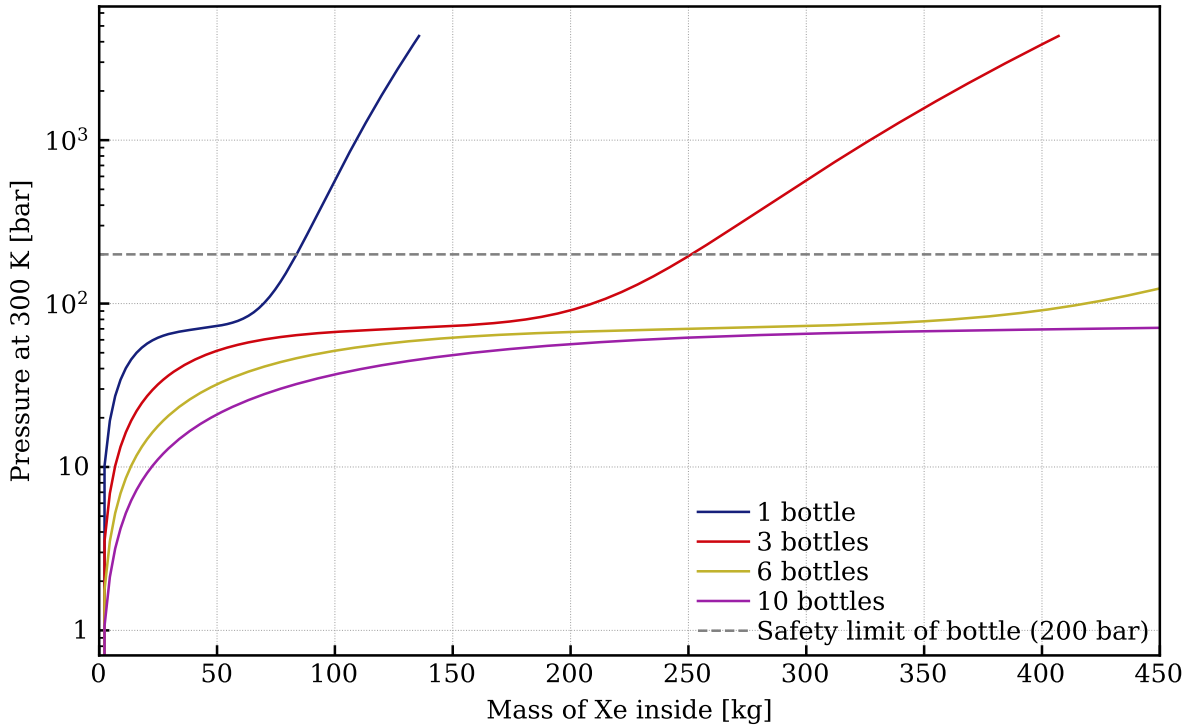

Figure 6.4.: Expected xenon pressure in the storage array bottles for the range of masses of Xenoscope's gas inventory and the number of bottles used at 300 K. The maximum safety pressure of 200 bar is shown by the dashed grey line.

For cryogenic pumping, from one to all four Dewar flasks are filled with LN_2 to cool down the aluminium cylinders and create the desired low-pressure environment caused by the freezing of xenon. Then, gas recuperation consists of connecting the low-pressure environment on the storage array to the main xenon volume within the cryostat to continuously evaporate xenon gas, which flows from the vessel to the storage array and freezes. This is done through the same high-pressure lines used for the filling process. The whole process must be monitored, and the xenon flow is regularly adjusted to keep the pressure at the desired level. In its absence, a sudden change in xenon pressure and temperature inside the cryostat could risk that xenon freezing in certain regions of the system. The recuperation process ends when all of the liquid xenon has been evaporated, and all the gaseous xenon is cryogenically pumped into the storage array. As the process is asymptotic, mbar-level of gaseous xenon pressure is left in the system, which is partly recuperated to the cold trap using the same cryogenic pumping process and partly lost at the end of the cycle. During recuperation, the mentioned cylinders remain cold by the automated regular filling of the Dewar flasks with LN_2. A set of PT100 sensors are installed to tag the level of LN_2 inside the flasks as underfill, low-fill point, high-fill point, and overfill, and

automatically actuate the filling valve or send an alarm to the SC system. Four 1400 W band heaters are installed at the top of each cylinder to maintain the valves at safe operation conditions and prevent ice formation at the exterior. After recuperation has ended and all the recuperated xenon is mainly frozen inside the cold bottles, the storage array is isolated, and the xenon is equalised between all ten cylinders while warming up.

The main drawback of cryogenic pumping is its recuperation speed. From the first commissioning run and first purity monitor run of Xenoscope, recuperation through this method was timed at $\sim$4 kg/h. To recuperate the total amount of xenon when using the full inventory ($\sim$400 kg), one would take around 100 h. The main constraint on speeding up the process is the phase transition from liquid to gas and the necessary energy input. However, even in the case where a heating element would provide direct energy to the process, this would still be unfavoured versus the gravity-assisted recuperation, detailed below.

Gravity-assisted recuperation profits from the fact that there is no need for a liquid-to-gas phase transition. Conceptually, xenon in liquid form is transferred downstream through a vacuum-insulated hose to a cold vessel with a capacity for the full amount of xenon. The pressure on the main vessel is reinstated by connecting it to the top of the storage vessel through the gas system. Once all the xenon in liquid form has been drained, helped by the hydrostatic pressure of the xenon column, the storage vessel is isolated from the rest of the system and the remaining gaseous xenon inside the cryostat and the gas system is recuperated through cryogenic pumping, as described above. This concept, based on [348], was realised in Xenoscope with the design, installation and commissioning of the Ball of Xenon.

BoX is a spherical stainless steel vessel installed on the bottom floor of the Xenoscope facility, in close proximity to the main cryostat (figure 6.2b, marker 2). It can store up to 450 kg of xenon in both liquid and gas phases, has a maximum working pressure of 90 bar and safe operation down to 77 K. A vacuum-insulated cryogenic line connects the bottom of the cryostat with the inlet of BoX and is terminated on both sides by cryogenic bellows sealed valves operated by rotary feedthroughs (MV12 and MV13 in figure 6.3). On the top gas outlet of BoX, a set of valves (MV14, MV15 and HPMV13 in figure 6.3) lead to the safety release valve and the high-pressure side of the gas system. This path is used during recuperation to repressurize the inner vessel and during filling to supply gaseous xenon to the system. For cooling, a copper cooler with spiral channelling is pressed against the spherical vessel. Their thermal contact

is secured with a mixture of cryogenic grease and silver powder. The cooling block is supplied with LN_2 such that, before and during recuperation, the xenon inside the vessel is liquefied or frozen. The pressure is kept at 2 to 3 bar by controlling the flow of gas through the gas system back into the cryostat, and through the liquid recuperation line rotary feedthroughs. Detailed information on the design, commissioning and operation of BoX can be found in [347, 349]

In the last science run to date, the liquid recuperation has been commissioned and successfully used, reaching a xenon recuperation rate of 25.70 kg/h, 6.4 times faster than with gas recuperation only, albeit the last few kilograms of xenon must always be recuperated in gaseous phase.

6.2.3. Slow control system

A slow control system was conceptualised and developed to monitor and control essential parts of the experiment. It provides the users with access to real-time measured values from the experiment's sensors, the ability to actuate several key systems remotely, and aims for 99.99% up-time. In addition, the SC is responsible for dispatching any alarms triggered by user-set-specific conditions. A Programmable Logic Unit (PLC) and a Revolution Pi [350] provide communication to sensors and controllable units, such as pneumatic valves, pumps, flow controllers and the cryogenic control system that powers the cold-head heater. A developed front-end framework allows authorised users to remotely interact with the controllable units of the system. All the time-series data is managed by Prometheus [351] and stored in an InfluxDB [352] database. For monitoring and analysis, all these SC parameters area available and can be visualised through dashboards in a Grafana [353] server. The Grafana application also allows for the configuration of alarms on the accessible parameters, which are sent to a user list by e-mail and SMS. All the different services described above are managed by Kubernetes [354], an open-source orchestration system, which provides automatic restarting of stuck or failing micro-services.

6.2.4. Overview of a Xenoscope run

All the systems detailed in the previous section work together from the start to the end of a Xenoscope run. Excluding the preceding design stage and the proceeding data analysis stage, a standard run of Xenoscope is comprised of the following steps:

- Assembly of the inner detector;
- Checking of electronic connections and test sensors;
- Closing of the inner vessel followed by its covering with Mylar;
- Check inner cryostat for leaks under vacuum;
- Closing of the outer vessel;
- Pump-out of the setup down to 10^{-3} – 10^{-5} mbar to outgas the installed components;
- Filling of the inner volume with gas xenon ($\sim 2\,\text{bar}$);
- Cool down and liquefaction of xenon with the pre-cooler and cold head. Continue filling up to the planned liquid volume;
- Start of circulation through the purification loop;
- DAQ setup and measurements. Constant monitoring through the SC system;
- Stop of purification;
- Recuperation of liquid xenon with the gravity-assisted technique;
- Recuperation of the remaining gas xenon through cryo-pumping to cold bottles on the bottle rack.

6.3. The Xenoscope early science project

The Xenoscope project was designed from the start with a modular approach divided into different stages. In a first commissioning run, the gas system, heat exchangers, cryogenics, purification and slow control subsystems were tested. Results from this initial run were reported in [341]. The following planned stages are a 53 cm-high purity monitor (PM) setup, fully immersed in LXe and a 2.6 m-high TPC, both cylindrical with 15 cm diameter. Albeit with different readouts, for both phases, the main objective is to observe the drift of electrons ejected from a photocathode illuminated by a pulsed xenon flash lamp [355]. For the latter, the drift of electrons over unprecedented lengths in LXe is a major proof-of-principle demonstration of a fundamental requirement of DARWIN and next-generation LXe DM experiments.

6.3.1. Purity monitor phase

After an initial period of commissioning, the first science data apparatus consisted of a 53 cm-tall purity monitor setup, fully immersed in LXe. The main goal of the setup was to evaluate the concentration of impurities diffused in the LXe volume by means of measuring the electron lifetime achievable by the system. The electron lifetime is defined as the time it takes for an electron cloud to be reduced by a factor of e by electron attachment to impurities, such that:

$$N(t_d) = N_0 \, \mathrm{e}^{-t_d/\tau_e} \, , \tag{6.1}$$

where $N(t_d)$ denotes the number of charges in the electron cloud after the drift time, t_d, N_0 is the initial number of charges in the cloud, and τ_e is the electron lifetime.

The PM consists of three main sections, from bottom to top: the charge production and ejection region, the drift region, and the charge collection region. At the bottom of the apparatus, a 30 mm diameter disk of quartz with sputtered gold deposited on top acts as a photocathode. Electron production occurs by the photoelectric effect when the gold substrate is illuminated by a 1 J pulsed xenon flash lamp, placed on the outside of the cryostat, from which the light is guided by a solarization-resistant multimode optical fibre with a 600 µm core. The photocathode disc is placed in the centre of the cathode electrode, a round stainless steel plate covering the bottom of the PM. The ejected electrons are pulled towards the drifting region, starting from the

cathode grid and moving up to the anode grid. The first signal acquired is from the induced charges on the cathode, amplified by a trans-impedance amplifier mounted on the bottom of the setup. The drift region is composed of 35 field shaping rings (FSRs) made from OFHC copper, connected by a double resistor chain. The resistors have a resistance of 1 GΩ and are mounted on small printed circuit boards (PCBs), which are screwed to the FSRs. At the top, after passing the anode grid, the electrons are collected on the anode. The induced charges on the anode provide the second recorded charge signal. Once again, the signal is amplified inside the cryostat by a trans-impedance amplifier before it is read out. During data taking, an external pulser provides a 1 Hz trigger, activating the pulse lamp and initiating acquisition on either an oscilloscope or an ADC. The whole assembly is suspended from the top flange of the inner vessel by six stainless steel rods, with which the vertical position of the PM is defined. The different parts are held together by six polyamide-imide (PAI) pillars axial-symmetrically distributed on the side of the cylindrical setup. Grooves on the pillars secure the electrode disks and FSRs and PTFE parts lock them from the inside.

The PM phase was spread over two trial runs (June-July and October-November of 2021) and one science data run (March-July of 2022). Run 1 was stopped due to a trip on the anode power supply, followed by the inability to establish a current through the electrode and pre-amplifier circuit. Upon opening the setup, it was verified that the pre-amplifier was broken, likely due to excessively applied voltage. In Run 2, during the final stages of filling, the main rubber diaphragm of the xenon compressor ripped, causing a leak from the main volume of the pump to the inner space between the now ripped diaphragm and the backup diaphragm. To prevent the loss of xenon due to an unexpected rupture of the backup diaphragm, the xenon was recuperated, and the run came to an early conclusion.

For Run 3, two sets of data were acquired. First, at a constant drift field of (52 ± 1) V/cm, the electron lifetime was measured for 89 days at three different circulation speeds: 30, 35, and 40 slpm. The expected behaviour of the electron lifetime for each speed of circulation is an initial exponential increase followed by a slower but steady increase until an equilibrium between the production of impurities from outgassing materials and the extraction of impurities by the hot getter is reached. Higher xenon circulation speeds increase the impurities extraction rate, increasing the electron lifetime value for which equilibrium is reached. This effect can be seen in figure 6.6b. Above a flow of 40 slpm, the absolute pressures on the inlet and outlet of

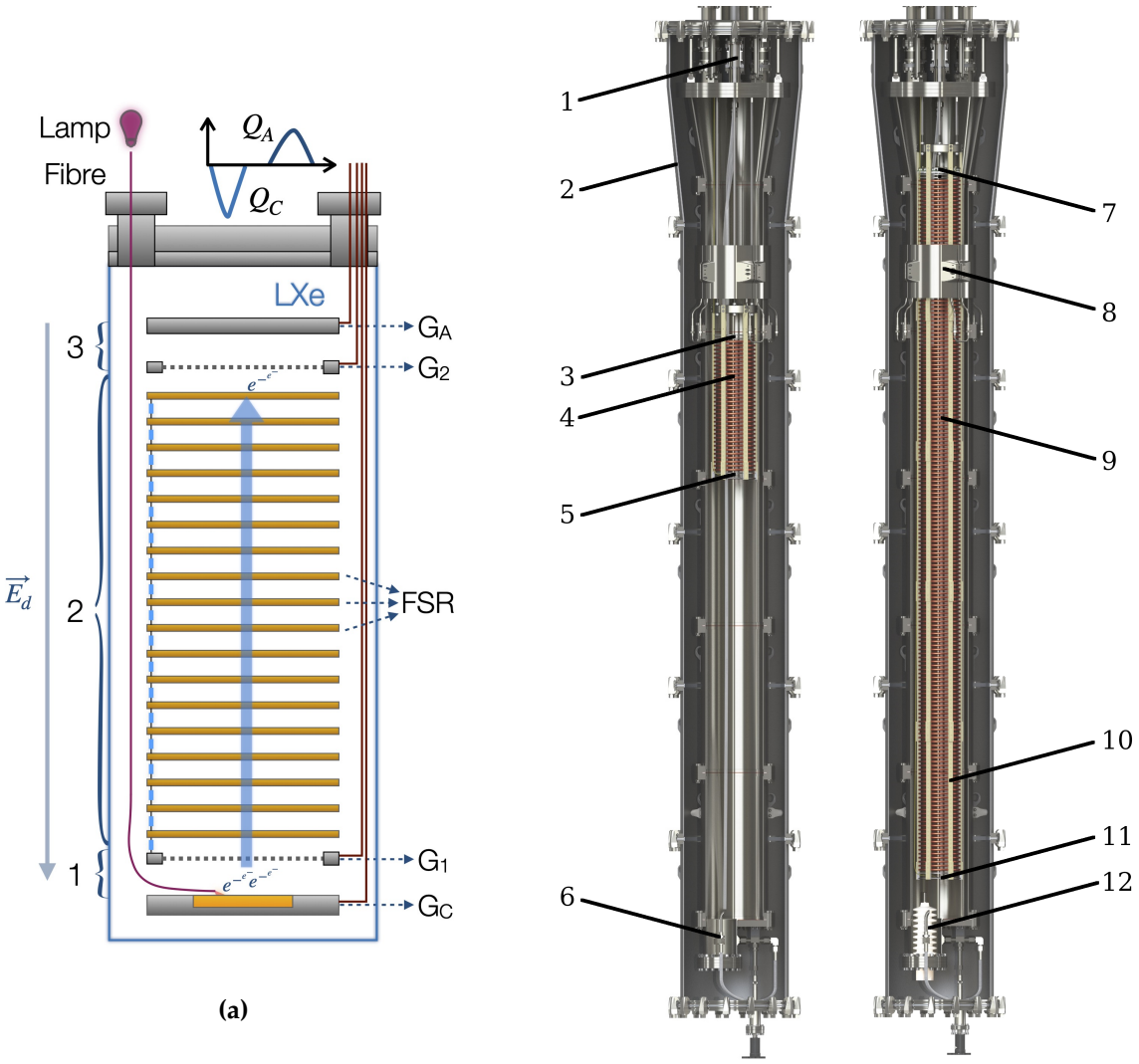

Figure 6.5.: **(a)** Schematic of the purity monitor. A pulse generator triggers a flash from the xenon lamp and the light is transmitted through an optical fibre to the photocathode, where photoelectrons are produced. The electrons are extracted, transported and collected by three electric fields, defined by the cathode (G_C) and cathode grid (G_1), the anode grid (G_2) and the anode (G_A). In the longest region (2), the field shaping rings (FSR) maintain the uniformity of the drift field $\vec{E}_d$ in the vertical direction. **(b)** PM (left) and TPC (right) setups in Xenoscope's cryostat. Legend: 1 - Top flange; 2 - Outer vessel; 3 - Anode grid; 4 - Field cage of the PM: 5 - Cathode disk, cathode grid, and photocathode; 6 - BoX recuperation line; 7 - Anode; 8 - Pre-cooler; 9 - Field cage of the TPC; 10 - Support pillars; 11 - Cathode disk and photocathode; 12 - HV feedthrough. Figure adapted from [347].

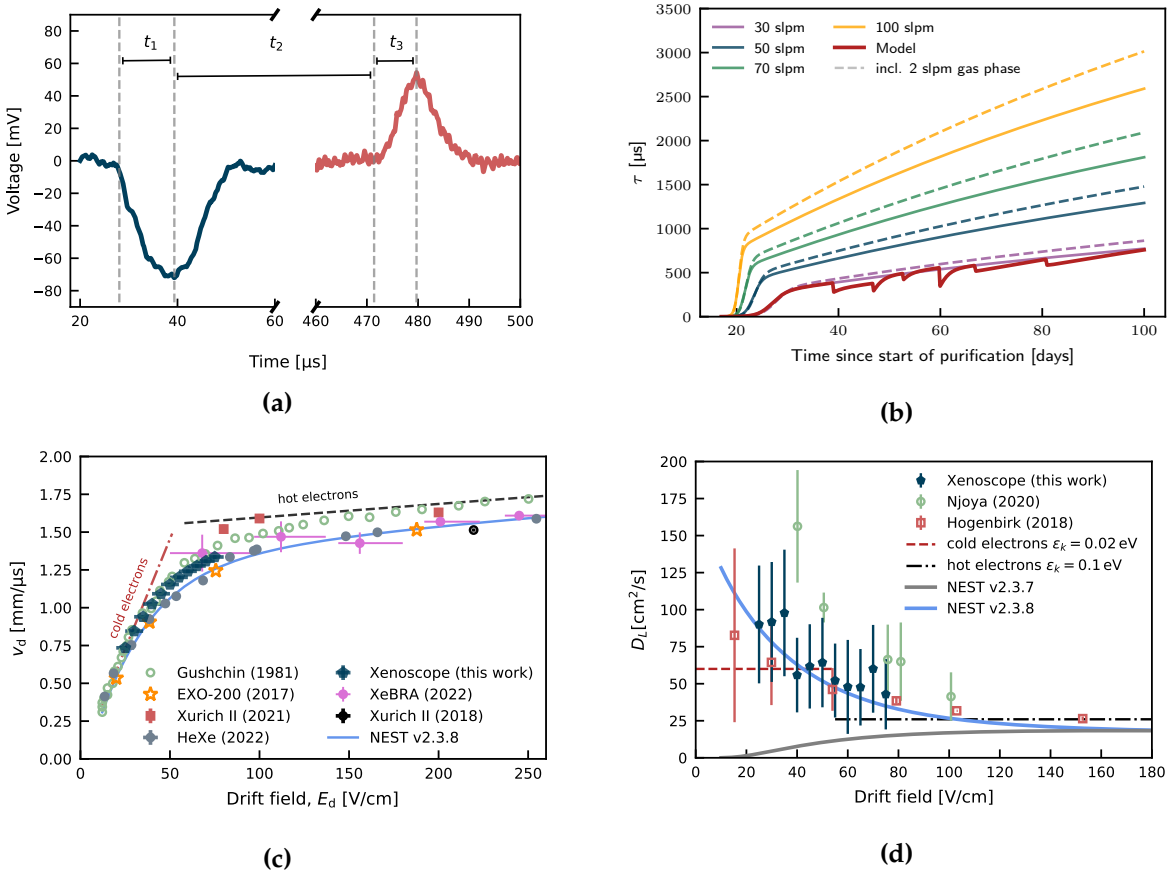

Figure 6.6.: **(a)** Signals acquired at 40 slpm xenon recirculation speed. **(b)** Purification flow-dependent electron drift lifetime data-fitted model. **(c)** Measured drift velocity with electric field values from 25 to 75 V/cm, in steps of 5 V/cm. **(d)** Longitudinal diffusion coefficient measurements, acquired with an electron lifetime of $\tau_e = (649 \pm 23)$ µs. Figures taken from [347], where further details and references can be found.

the xenon compressor were outside the range of normal operation, which determined the endpoint of the different circulation speeds studied.

Following the electron lifetime monitoring campaign, with the circulation flow at 40 slpm, data was taken at different drift fields to study electron velocity and diffusion properties. By varying the applied voltage to the cathode, drift fields were scanned from 25 V/cm to 75 V/cm in steps of 5 V/cm. The main results on the drift velocity and electron longitudinal diffusion in liquid xenon can be found in figure 6.6. The full description of the data taking, analysis, and results are not the subject of this work and can be found in [347] and [356].

6.3.2. TPC phase

In the next stage of the Xenoscope project, the previously described field cage is expanded five-fold and adapted to function as a TPC, as shown in figure 6.5b. The setup is cylindrical in shape, measuring 2.6 m in height and 15 cm in diameter. The field cage now has 173 OFHC copper FSRs from cathode to gate, attached to six PAI pillars, secured with PTFE parts, and hanging as a whole from the top flange of the inner vessel with six stainless steel rods. The connection between each section to the next is done by PAI blocks and four screws connect per pillar.

The upgrade to a dual-phase TPC includes the addition of several subsystems. The charge readout at the bottom and top of the field cage is substituted by a light-based readout with an array of silicon photomultipliers (SiPMs) at the top, which is described in detail in Chapter 7. Because of this change to a light readout at the top, the previous anode grid assumes the role of the gate electrode, and the anode plate is replaced by a wire-mesh anode to allow light transmission ($\sim$ 93% optical transparency). With the presence of a liquid-gas interface, the required liquid-level monitoring will be achieved by three short level meters (SLMs) at the gas-liquid interface and two long level meters (LLMs) for the full height of the LXe column. For liquid-level setting, a weir operated by a magnetically-coupled, linear-motion feedthrough was installed. The weir encompasses an open-top, stainless steel container from which LXe is extracted for recirculation, and an internal cylinder acting as a communicating vessel for the TPC volume. A hole in the internal cylinder lets the liquid pour in, and by adjusting its height, the liquid level of the TPC can be changed. To achieve the design goal for the electric drift field of 200 V/cm, the applied voltage to the cathode plate is $\sim$50 kV. To allow for this electrical potential magnitude, a high-voltage (HV) ceramic feedthrough rated up to 100 kV from CeramTec [357] was installed at the bottom of the cryostat and connected to an Heizinger PNC 100000-1 power supply.

At the start of the TPC-phase data taking, the primary source of signals will be the same as in the PM-phase, ejected electrons from shining the pulsed xenon lamp onto the gold-plated photocathode. The electron cloud is then drifted the full length of the TPC until it reaches the gate. The liquid-gas boundary stands in the middle of the 12 mm extraction field between the gate and anode electrodes. The extraction efficiency of electrons from the liquid phase and proportional amplification in the gas phase is related to the strength of the extraction field. For the nominal value of 10 kV/cm, an

extraction efficiency of $\sim$ 100% [170] is expected. The proportional scintillation light is then detected by the SiPM top array, for which data acquisition was triggered by the same pulse as the xenon lamp, as in the PM setup described above. This method allows for the main goal of Xenoscope to be achieved: proof-of-principle of electron drift in a DARWIN-scale-height TPC.

Since the aspect ratio of $\sim$16:1 highly constrains the LCE of S1 signals from the full xenon column, the design does not include any reflective walls, contrary to past and current DM experiments. As a result, any physics science search in Xenoscope's TPC will be primarily S2-driven. These entail, for instance, calibration campaigns with both internal and external radioactive sources [358], and muon-based measurements [359].

Chapter 7.

The top SiPM array of Xenoscope

SiPMs are a common solution for light detection for a broad spectrum of energies, within and outside research. With a smaller footprint and more consistent manufacturing process, SiPMs are a strong alternative to PMTs as the photosensors of next-generation xenon-based dark matter experiments. For their advantages in high radio-purity and fast pulse timing, SiPMs are far inferior regarding their dark count rate, even at low temperatures, when compared to PMTs. After the successful implementation of a top array of VUV-sensitive SiPMs in the Xurich II dual-phase xenon TPC [168], a larger array was designed, tested and commissioned for the TPC run of Xenoscope.

In Section 7.1 the SiPM concept, modes of operation, and properties are presented. Section 7.2 introduces the design of the top array of Xenoscope, the VUV-sensitive SiPMs employed as photosensors, and its assembly in the TPC of Xenoscope. Section 7.3 describes the characterisation campaign of all the SiPMs in the top array and discusses its results. The first commissioning results of the top array assembled in the TPC of Xenoscope are reported in Section 7.4. Finally, the developed simulation framework to study different configurations of the array layout at different geometrical operating conditions is the subject of Section 7.5.

7.1. Silicon photomultiplier sensors

SiPMs are a type of solid-state photodetector that is increasingly used in a variety of applications, such as medical imaging, particle physics, and industrial sensing. Because of their small size, low power consumption, high gain, and insensitivity

to magnetic fields, SiPMs have largely replaced vacuum-based PMTs over the last decade in most fields. They carry, however, several disadvantages, mainly concerning their higher dark current and reduced linearity at very high illumination. In the following sections, an introduction to silicon photodetectors, the avalanche photodiode (APD) and the SiPM is presented, taking into account their applicability to VUV light detection. The concepts here described will be studied in detail for the SiPM model used in Xenoscope's top array in the remaining parts of the chapter. Overall, this section was written based on references [360–364].

7.1.1. Silicon photodiodes

A pure silicon crystal lattice has, by default, an established equilibrium between charge carriers. In this form, the silicon crystal is called intrinsic and provides high resistance to the passage of charges. However, a PN junction can be made in the silicon lattice by doping it with impurities, one side of the material with electron donors (the N region), and the other side with hole donors (the P region). In the resulting lattice structure, the donated electrons and holes are free to move from one atom to another in the conduction and valence bands, respectively [365–367].

By joining a P (anode) and N (cathode) region into a PN junction, the charge gradient pulls the charge carriers to diffuse into the region of the junction, where electrons and holes recombine. Adjacent to the junction, the doped regions become depleted of majority carriers, forming the depletion layer. Since the heavy ions responsible for donor carriers are immobile in the lattice, after charge recombination within the depletion layer, both sides of the junction become charged with the sign of the carriers donated: the N region (responsible for donating electrons) becomes positively charged, and the P region (responsible for donating holes) becomes negatively charged. From these static charges, an electric field arises, from the positive N region to the negative P region, with peak intensity at the PN junction. This electric field counteracts the natural diffusion process of charge carriers, and an equilibrium is reached. The resulting electric charge distribution, electric field and electric potential are depicted in Figure 7.1a.

The most basic silicon photosensor comes from a PN junction: when the photoelectric effect due to an incident photon provides enough energy to transition an electron in the valence band to the conduction band leaving a hole behind, an electron-hole

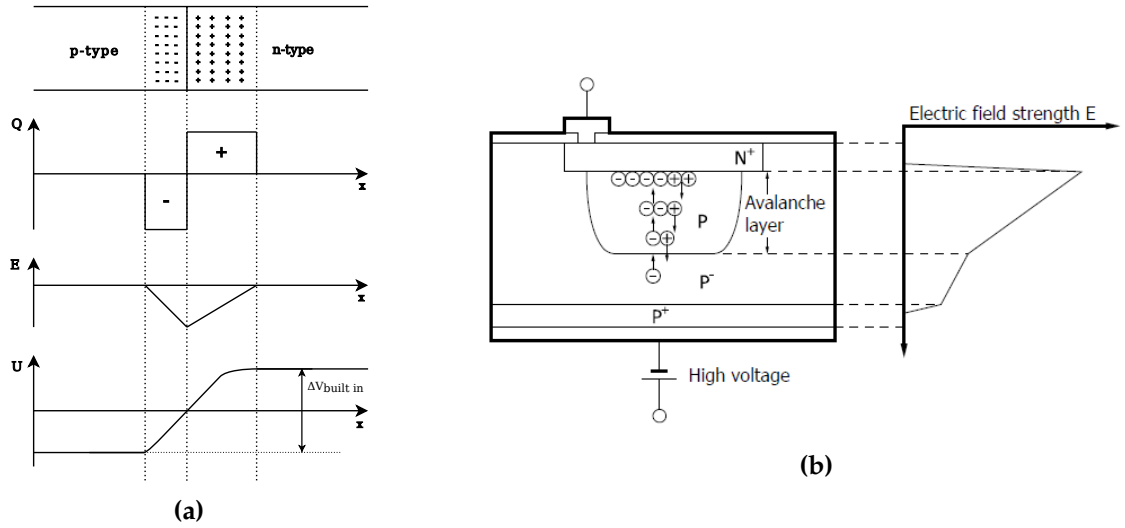

Figure 7.1.: (a) Electric charge, field and potential relationships in the depletion region associated with a PN junction. A PN junction. Figure adapted from [360] **(b)** Schematic of an N-on-P APD. Figure from [363].

pair is created in the depletion layer. In the case of silicon, the band gap is 1.14 eV. Given the intrinsic electric field of this region, the electron and hole drift to opposite sides until they reach the outer edges of the depletion layer. Propelled by diffusion, the electrons accumulate in the N region and the holes in the P region. In the case where these regions are externally connected through a current loop, these charges flow through the loop, creating a photocurrent. The increase in carriers from the initial electron-hole pairs to the final charge signal collected is the gain of the process. From the process described, it follows that PN photodiodes have an absolute gain of one, making them only suitable for high illumination applications, and their readouts are not single-photon sensitive.

The excess energy needed to cross the band gap might come from the thermal energy of the system instead of a photoabsorption effect, giving rise to a dark current. Moreover, in the case where the electron-hole pair is created outside the depletion layer, within the bulk of the P or N regions, due to the lack of an electric field, the pair must rely on Brownian diffusion to enter the depletion layer and is most likely to recombine. To greatly reduce the likelihood of the latter process, the depletion region depth can be expanded by reverse-biasing the PN junction, i.e., applying a higher external potential on the N region (cathode) than on the P region (anode). The depletion layer's size increases with an increasing applied voltage difference, up to the point where the entire bulk of the photodiode is active volume. Because longer

wavelength photons are absorbed deeper inside the silicon material, this technique is especially important for red and near infrared (NIR) applications. As a side effect, enlarging the depletion layer decreases the PN junction's capacitance and, therefore, expands the photodiode's frequency bandwidth. For high-frequency applications, this effect is even deepened by adding an extra layer of intrinsic silicon in between the P and N layers, forming a PIN photodiode.

7.1.2. Avalanche photodiodes

As described above, PN photodiodes operate at a unitary gain and don't usually provide single-photon detection. Therefore, for low-light applications, APDs are more suitable. These devices rely on the fact that increasing the reverse polarity voltage in a PN junction also increases the electric field in the depletion layer. Contrary to the effect of low reverse biasing a PN junction described above, if the electric field's magnitude is large enough such that the accelerated charge carriers' mean energy in-between collisions with the lattice is larger than the band gap energy, they will likely ionise lattice atoms upon impact, releasing another electron-hole pair. This new electron-hole pair will then be accelerated, inducing more impact ionisation and continuing the multiplication process, resulting in an avalanche of carriers. In this case, the gain of the process is larger than one, typically 10 to 1000.

Collisions where the charge carriers have less energy than the band gap result in phonon vibrations in the crystal lattice instead. This stochastic process, in conjunction with the avalanche size depending on the depth of the photoelectric production of the electron-hole pair, results in small yet random fluctuations of the multiplication gain. Other consequences of these two effects are the proportional gain dependence on the incident light wavelength (different avalanche lengths for different penetration lengths) and the inversely proportional dependence on temperature (at higher temperatures, there are more phonon vibrations, resulting in greater losses of kinetic energy during the avalanche process).

The APD gain dependence on reverse bias voltage is divided into three different regions. In the first region, the APD functions as a biased PN-junction with unitary gain. In the second region, the APD gain behaviour is linear with the applied voltage, meaning the output charge signal is linearly proportional to the initial number of electron-hole pairs, where the proportionality constant is the gain of the APD. For

spectroscopy or other applications where the initial deposited energy is of importance, this is the main mode in which APDs are operated. Finally, in the third region at high reverse-bias voltage, the gain of the APD increases exponentially. In this saturation region, also called Geiger mode, the output charge is always the same for a given applied voltage and corresponding gain, independently of the initial number of charge carriers. For this reason, the response of a Geiger-mode APD (GAPD) is binary, indicating only if a signal was triggered or not. The voltage at which the APD starts to behave in Geiger mode is called the breakdown voltage (BV). Moreover, for a GAPD, the gain is given by the output charge derived from a single electron-hole pair and can be written as

$$G = \frac{C_{APD} \cdot (V_{bias} - V_{breakdown})}{q_{e^-}} , \tag{7.1}$$

where C_{APD} is the capacitance of the APD, V_{bias} is the applied reverse voltage and q_{e^-} is the elementary charge of the electron. Typical gain values of GAPDs are on the order of several 10^5 to 10^7, make their usability in low light levels extremely viable and reliable.

During the Geiger multiplication, the avalanching charge carriers behave like a conductor that continually excites valence electrons and sustains the avalanche process, with residual intrinsic resistance to the photocurrent, R_s. To counteract this effect, a quenching resistor, R_q is often added in series with the GAPD with a large enough value such that the current flow from the bias voltage cannot sustain the avalanche process. Once the initial equivalent capacitance, C_d, is discharged and the quenching becomes dominant, the avalanche stops, the junction undergoes a recovery period (characterised by the time constant $R_q \cdot C_d \approx \mathcal{O}(1)$ ns) and the GAPD is prepared for the next multiplication process. During both the avalanche period (characterised by the time constant $R_s \cdot C_d \approx \mathcal{O}(100)$ ns), and the recovery period, the GAPD cannot detect any incident photons.

The APD or GAPD can have either an N-on-P or P-on-N structure, depending if sensitivity to red and NIR or blue and ultraviolet (UV) is needed, respectively. Because minority carriers, i.e. electrons in the P region and holes in the N region, can not cross the junction barrier, by forming the electron-hole pair in the P region of the depletion layer, the electron can more efficiently produce an avalanche process. Since red and NIR photons are deposited deeper in the substrate, an N-on-P setup is favoured. For blue and UV photons, the inverse occurs, and a P-on-N setup is favourable. The latter

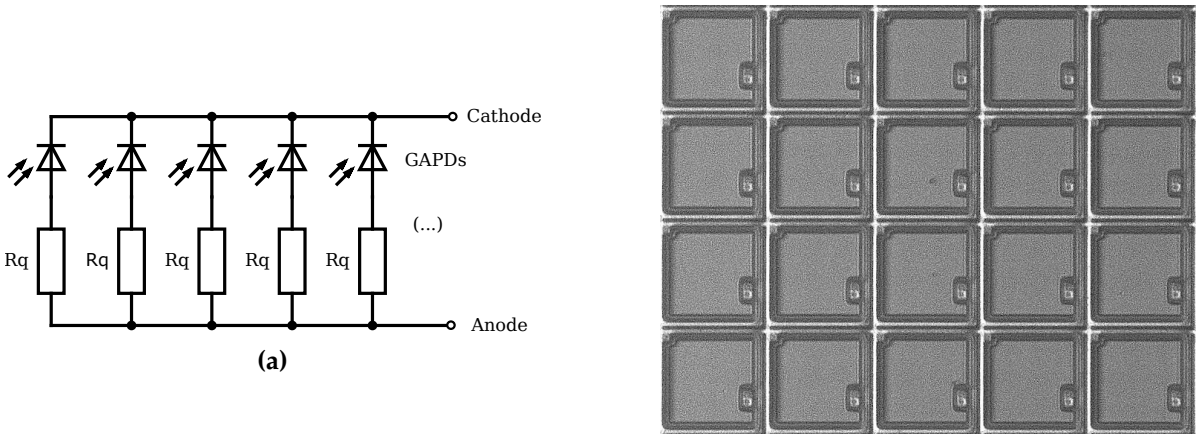

Figure 7.2.: (a) Exemplary circuit of a SiPM. R_q are the quenching resistors and the pictured photodiodes are the GAPDs **(b)** Microscope view of a VUV4 Hamamatus SiPM, a model with 5050 µm pixels. The small rectangles in each APD are the quenching resistors. Also visible are the light trenches around each of the pixels, a measure to reduce cross-talk. Each APD cell is roughly a square with a 50 µm side.

is also the case for VUV-sensitive sensors, such as the ones used for the top array of Xenoscope.

7.1.3. The SiPM unit or MPPC

A SiPM, also known as a Multi-Pixel Photon Counter (MPPC), is a matrix of GAPDs connected in parallel with a common voltage bias and readout (Figure 7.2a). In this context, GAPDs are often called single photon avalanche diodes (SPADs). Each SiPM SPAD pixel is connected in series with a quenching resistor to allow for the recovery process detailed above and is usually on the tens of micrometres-scale (see Figure 7.2b). As in APDs, SiPMs have a characteristic BV value, from which the individual pixels provide a binary response to the interaction of a photon within. The output charge signal of a SiPM is the sum of all the binary responses of the pixels and, conceptually, an integer multiple of the single photon response. However, real SiPM signals have associated noise, which follows a Poisson probability distribution function with the mean as the average number of detected photons and its square root as the standard deviation.

The main characteristics to take into account for SiPM sensors are BV, photon detection efficiency (PDE), gain, dark count rate (DCR), after-pulses, and cross-talk

probability (CTP). For these devices, the PDE is the resulting product of quantum efficiency (QE), the SiPM geometrical fill-factor, ϵ_{geo} and the Geiger-mode avalanche probability, ϵ_{geiger}:

$$PDE = \epsilon_{geo} \cdot QE \cdot \epsilon_{Geiger} \, . \tag{7.2}$$

ϵ_{geo} is dependent on the type of SiPM unit and how the cells and quenching resistance are arranged, with typical values between 60 and 80 %. While QE increases with temperature due to more phonon vibrations, ϵ_{Geiger} decreases. The overall PDE is, therefore, temperature-dependent from the combination of these two effects. Standard values of PDE are 20 to 50 %, depending on the type and wavelength-sensitive region of the SiPM. Moreover, the BV tends to increase as temperature increases, causing the gain to decrease with increasing temperature when the bias voltage stays constant.

DCR is a parameter of particular importance to single-photon counting applications since a high rate of these uncorrelated events greatly reduces the robustness of low-photon counting and increases dead time. If the light level is sufficiently high, the DCR can be easily disregarded by applying a high enough threshold. Increasing the minimum amplitude of the signal by one photoelectron decreases the DCR value roughly by one order of magnitude [363].

Two additional properties are of interest, which are time-correlated to triggered photon signals: after-pulses and cross-talk. After-pulses are delayed signals coming from previously fired pixels of the SiPM, occurring within a few microseconds to several milliseconds after the initial pulse. These spurious pulses come from charge carriers becoming trapped during the avalanche process and released at a later time. If the period before the release of the charge carrier is greater than the recovery time of the SPAD, i.e., the cell is fully recharged, the after-pulse signal will have the same amplitude and topology as a signal from a photon event. In the opposite case, where the period of charge-trapping is smaller than the recovery time of the SPAD, the after-pulse signal amplitude will be a fraction of the typical photo event.

Optical cross-talk, on the other hand, is a correlated effect arising from the emission of light during the multiplication process, at the rate of ~ 10 photons/avalanche of 10^6 e^- [368]. These photons can trigger a secondary avalanche process by interacting with neighbouring SPADs, named internal cross-talk (iCT), escape the silicon bulk and interact with another nearby SiPM, named external cross-talk (eCT), or escape the silicon bulk, get reflected and interact within the same SiPM, named feedback cross-talk

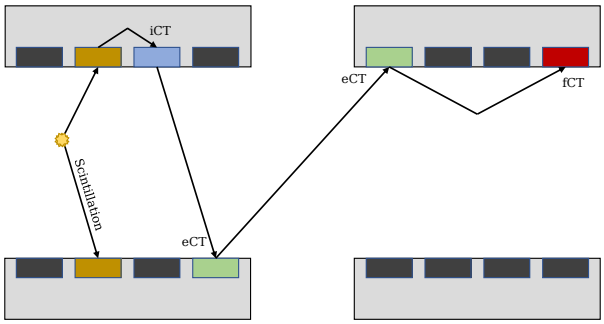

Figure 7.3.: Schematic representation of the different types of cross-talk. The colour code of the schematic is as follows: in yellow, the interaction in a scintillating material, such as LXe, as described in 2; in grey, the various SiPM units; in dark grey, the non-activated SPADs; in gold, the SPADs activated directly by the scintillation light; in blue, the SPADs activated by internal cross-talk (iCT); in green, the SPADs activated by external cross-talk (eCT); in red, the SPADs activated by internal feedback-talk (fCT). The arrows represent the path of photons. Figure adapted from [369].

(fCT) [369]. Figure 7.3 summarises the different types of optical cross-talk processes in a schematic fashion. Depending on the SiPM model and operating conditions, the different cross-talk types will have different time and amplitude responses [370]. In general, if a cross-talk photon interacts within the depletion region of SPAD, the fast timing of the process merges both the initial and cross-talk event in the same collected charge output, making it indistinguishable from a multi-photon signal. This is called prompt cross-talk. In the case where the cross-talk photon created the electron-hole pair outside of the depletion region of a SPAD, the secondary avalanche is only induced if and once the charge carriers reach the depletion layer by diffusion. In that case, the process is called delayed cross-talk, and its topology is similar to after-pulses, albeit with different time constants.

A final important matter on the characteristics of SiPMs, the concepts of linearity and pixel saturation needs to be introduced. Linearity entails the degree to which a photosensor's output and input are linearly related. In particular, the linearity between the number of incident photons in a photosensor and the amplitude (or charge) at its output is of interest. To the system as a whole, further non-linear effects at the readout, amplification or digitisation stage must also be addressed. For the ideal SiPM, its response is given by:

$$N_{fired} = N_{photon} \cdot PDE \,, \tag{7.3}$$

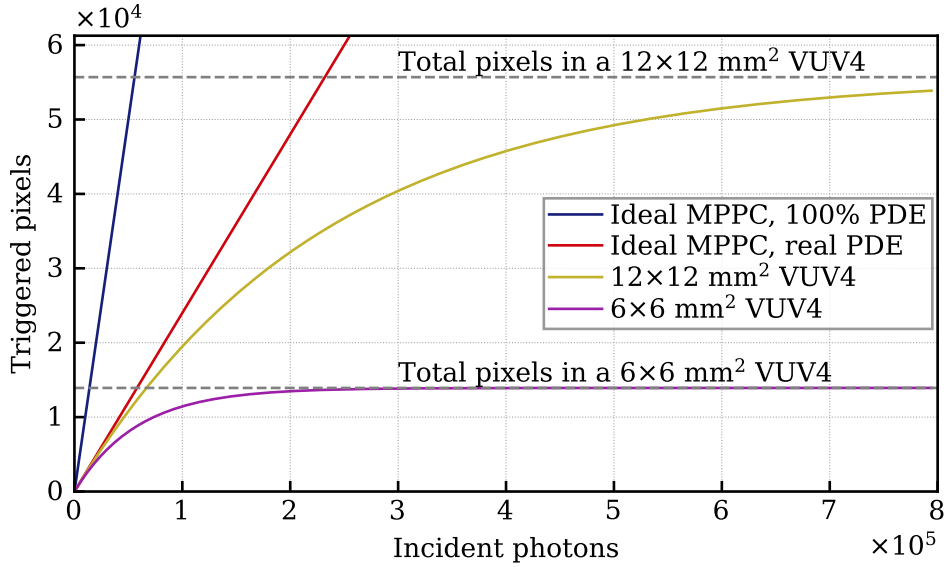

Figure 7.4.: Calculated number of triggered SPADs in a SiPM as a function of the incident number of photons using Equations 7.3 and 7.4, for idealised (with linear response) and real MPPC units, respectively. The solid lines are calculated for the following parameters: in blue, an ideal MPPC with 100 % PDE; in red, an ideal MPPC with realistic a PDE of 24 %; in gold, a $12 \times 12\,\mathrm{mm}^2$ VUV4 unit; in purple, a $6 \times 6\,\mathrm{mm}^2$ VUV4 unit. Dashed grey lines indicate the total number of pixels in $6 \times 6\,\mathrm{mm}^2$ and$12 \times 12\,\mathrm{mm}^2$VUV4 units.

where N_{fired} is the number of SiPM cells fired and contributing to the output signal of the sensor, N_{photon} is the number of incident photons, and PDE is the photon detection efficiency. For a real SiPM, however, if the duration of the pulse, or pulse width, PW, is shorter than the recovery time, the response is described by:

$$N_{fired} = N_{photon} \cdot (1 - e^{\frac{-N_{photon} \cdot PDE}{N_{pixel}}}) \,. \tag{7.4}$$

Or, if the pulse width is longer than the recovery time:

$$N_{fired} = N_{photon} \cdot (1 - e^{\frac{-N_{photon} \cdot PDE \cdot T_{recovery}}{N_{pixel} \cdot PW}}) \,. \tag{7.5}$$

where N_{pixel} is the number of pixel cells in the SiPM active area, PW the pulse width, and $T_{recovery}$ the recovery time of a SPAD.

The effect of this intrinsic non-linearity and saturation effect by the limitation of pixel size and number can be seen in Figure 7.4 with characteristics from the two of the

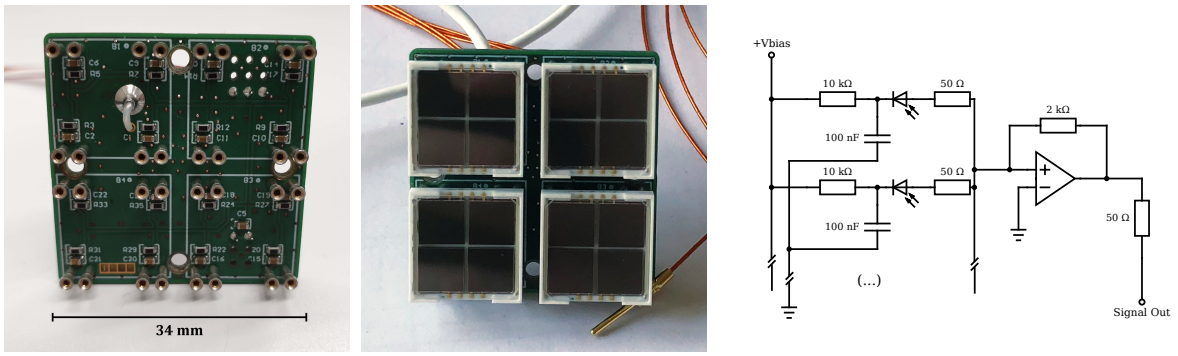

(a) (b) (c)

Figure 7.5.: **(a)** Front side of a tile. The four through-holes are used to fix the tile into the stainless steel plate with screws. Each pair of nearby pins is responsible to power a $6 \times 6\,\mathrm{mm}^2$ MPPC unit. **(b)** Tile fully loaded with four quads. Clearly visible are both the ceramic packaging in off-white, the quartz window and the separate $6 \times 6\,\mathrm{mm}^2$ MPPC units that compose each quad. **(c)** Simplified electronic circuit of the tile power distribution and amplifier circuit.

sensors studied in the following sections: a $6 \times 6\,\mathrm{mm}^2$ and a $12 \times 12\,\mathrm{mm}^2$ MPPC units from Hamamatsu, considering uniform illumination of the full area of the sensors.

7.2. The top array of Xenoscope

Xenoscope will run with SiPMs in its top array as its only light sensors, focusing on recording the S2 signal due to electrons drifted in LXe from the photocathode and extracted into the gas phase, as described in the previous chapter.

The array is made up of 192 $6 \times 6\,\mathrm{mm}^2$ MPPCs. These are packaged in 2×2 quad modules (S13371-6050CQ-02 MPPCs from Hamamatsu) with a total sensitive area of $12 \times 12\,\mathrm{mm}^2$. The four quads are loaded onto printed circuit boards (PCBs) with push-pin connectors, named "tiles" (Figures 7.5a and 7.5b) and there are 12 tiles in the array, named alphabetically from *A* to *M*, excluding the letter *I*, as sketched in Figure 7.6a. The collection of tiles is screwed to a stainless steel plate for mechanical stability with 6 mm PTFE standoffs to ensure the protection of the wiring on the backside of the PCB. The chosen MPPC model is the most recent version produced by Hamamatsu for VUV light detection at the time of this work and was initially develop for the MEG II experiment [371, 372] at Paul Scherrer Institute (PSI). The VUV4 family of sensors considerably improves upon the previous VUV3 generation regarding PDE – from ∼10% to ∼24% at 175 nm) and cross-talk probability. The acquired quad modules have

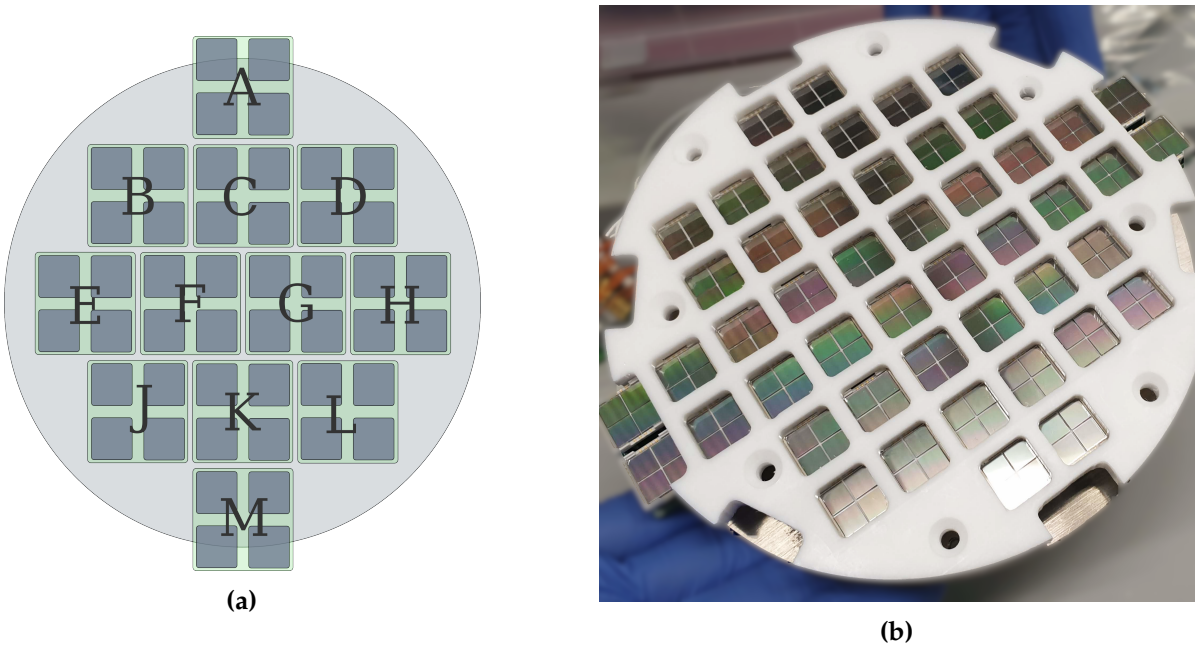

(a) **(b)**

Figure 7.6.: (a) Sketch of the tile distribution and naming in the top SiPM array. **(b)** Fully assembled top array before installation in the time projection chamber.

four distinct channels, each with an effective photosensitive area of 5.9 mm $\times$ 5.85 mm and a geometrical fill factor of 60%. In total, they read a total of 13 923 pixels with 50 µm pitch. The sensors are housed in a ceramic package with a quartz window, which increases their robustness during handling but limits their usability to wavelengths above $\sim$155 nm. In later implementations where radio-purity is a critical parameter, the packaging and covering can be replaced with more appropriate materials or even removed entirely.

The tiles serve at the same time as holders for the SiPM units, voltage distributors, and pre-amplifiers for the signals. The readout scheme is based on the design proposed in [373], where the amplified output is the analogue summed signal, optimised to exclude contributions from non-triggered SiPMs. The pre-amplifier circuit is loaded with an OPA847 operational amplifier from Texas Instruments and provides a $\times$20 amplification factor to the summed signal. Figure 7.5 depicts an empty and fully loaded tile, as well as a simplified amplification circuit. The full circuit can be found in Appendix A. In addition, tiles *B*, *G*, and *M* have been equipped with on-board PT100 sensors to monitor the temperature of the gas in close proximity to the photosensors[1].

[1]The on-board PT100 sensors were introduced during the characterisation campaign later reported in Section 7.3, where only one was used. In Xenoscope, all three PT100 sensors are operational.

There are several advantages and disadvantages of a tiled approach for the photosensor readout. All the sensors within the tile area act, in practice, as one single sensor with a larger active area. When the signal is amplified together on-site, the number of needed operational amplifiers is reduced. As these are power-consuming and cause heat to be introduced to the system in non-negligible amounts, reducing their number is beneficial. Moreover, fewer amplifier circuits translate to fewer electronic components, contributing to a lower radioactivity budget. However, by combining several photosensor units into a single output, the achievable granularity of the set will be broader, which influences the position reconstruction of events, mainly for smaller and more localised events. In total, the array has $\sim$ 36% of its area covered by active sensors.

When assembled in Xenoscope's TPC, the array is secured by the stainless steel plate fitting into grooves in the PAI pillars with the photosensors facing downward, above the anode grid. The distance between the anode mesh and the optical plane is $\sim$15 mm. The plate measures 160 mm in diameter and 4 mm in thickness, and it spans the entirety of the cross-section of the cylindrical TPC. Rounded squares of 27.5 mm length are cut from the plate where the back of the tiles stand, allowing wires to pass without being damaged or excessively bent. Eight M2 threaded holes are axially distributed on the plate to secure the PTFE mask or, during the test phase, to connect to support rods. At the side, six M2 screw-holes match the position of the PAI pillars to securely tighten the array in place with vented screws in conjunction with the grooves (see Figure 7.7a). To ensure that the MPPC modules are secured in place and prevent the dislodging of any units, a perforated PTFE cover made in-house is placed in front of the modules (see Figure 7.7b). Similarly to the stainless-steel plate, the PTFE cover spans the full circular area of the TPC. The mask is 7.5 mm thick, with 3.8 mm between the quartz windows and the bottom. Although these edges cause shadow effects at large incident angles, they are not a major concern since the top array's primary goal is to detect $\mathcal{O}(10^3\text{-}10^4)$ PE S2 signals.

In the Xenoscope TPC, several types of cables with different types of connectors at their ends are used for power supply and signal readout routing. The choice of cable and connector depends on the properties of the signal or voltage requirements where such connection is being used. The low-voltage systems, such as the top array, are serviced by two different wire-connector pairs:

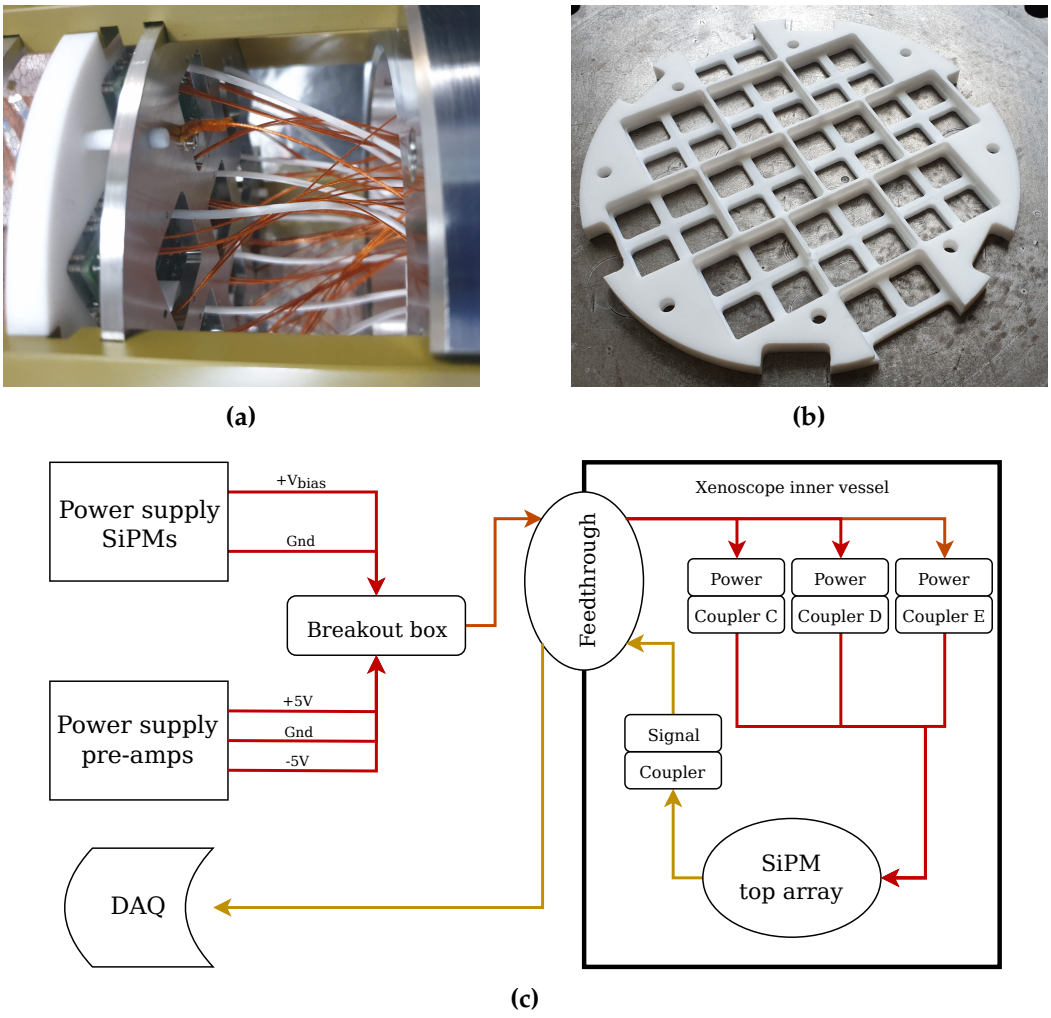

Figure 7.7.: **(a)** Detail of the stainless-steel plate in the assembled first module of the TPC, with the wires for each tile going through the corresponding holes in the plate. **(b)** Detail of the PTFE mask back-side (MPPC-side). Front-facing the page are the larger grooves, where the tiles are laterally secured, and the smaller ones, where the corner of the quad windows come in contact and are locked in place. The eight screw-holes are designed to secure the mask to the stainless-steel plate, while the rectangular grooves at the edge align the array with the PAI pillars. **(c)** Cabling schematic for the top array. Power-related cabling is shown in red and signal-related cabling in gold.

- For power distribution: Kapton insulated copper wires 26 AWG (stranded or single-core) from Accuglass [374] with d-sub pins and sockets connectors, also from Accuglass.
- For signal routing: 50 Ω-impedance coaxial shielded cables from KOAX24 [375] with gold-plated MMCX connectors from Telegartner [376],

Each of the tiles requires five power supply wires (three for the pre-amplifier power and two for the SiPMs' bias voltage) and one signal cable. In total, the twelve tiles sum up to 60 Kapton wires and 12 coax cables needed. Considering these requirements, a custom-made potted electrical feedthrough was commissioned from Vacom [377] to connect wires from the vacuum or xenon gas side to the air side. The potted feedthrough has 63 Kapton-insulated wires, 14 coax PTFE-jacketed cables and two HV-robust single Kapton-insulated wires, and is mounted on a CF40 flange connected on the top of the setup (see Figure 7.8a). To facilitate both single-wire and coax cable connections on the inside, a set of PTFE connectors was used, joining male endings on the wires coming from the tiles to female plugs on the wires going to the feedthrough. These connectors follow the design of the ones developed at the University of Zurich to be used in XENON1T [378] and XENONnT [379]. Each of the single-wire connectors has two distinct PTFE parts for male and female terminations.

Each of the two PTFE plates has 26 holes for individual wire placement, which must travel through the plates before being crimped. Small stainless steel fasteners hold the two sides together and a D-shaped piece of copper attached to the connection block's wire side works as a strain relief (see Figures 7.8b and 7.8c). On the other hand, the coaxial connection blocks are made up of five layers of ridged PTFE and four layers of coaxial wires sandwiched in between. The five pieces of PTFE are secured together by two stainless steel fasteners and the blocks of the male and female connections are securely fastened together using two copper rods at two opposing corners of the block (see Figure 7.8d).

On the outside of the cryostat, after the potted feedthrough, the signal cables are routed from the top of the facility to the lower floor, where the DAQ rack is placed. There, the cables are secured in a patch panel with female SMA connectors on the front, from where a connection can easily and reliably be made to a pulse shaper or a readout device (e.g. oscilloscope, ADC).

As for the 60 power wires of the top array, they are collected in a breakout box (Figure 7.8e). This breakout box merges all the wires at the same potential: SiPM bias voltage, SiPM grounding reference, pre-amplifier positive voltage (5 V), pre-amplifier negative voltage (-5 V), and pre-amplifier grounding reference. After the merge, only five wires need to be routed to the power supplies. While the pre-amplifiers are powered by a standard current-limited power supply, the SiPM bias voltage is supplied by a custom low-noise power supply built by the Physics Institute's

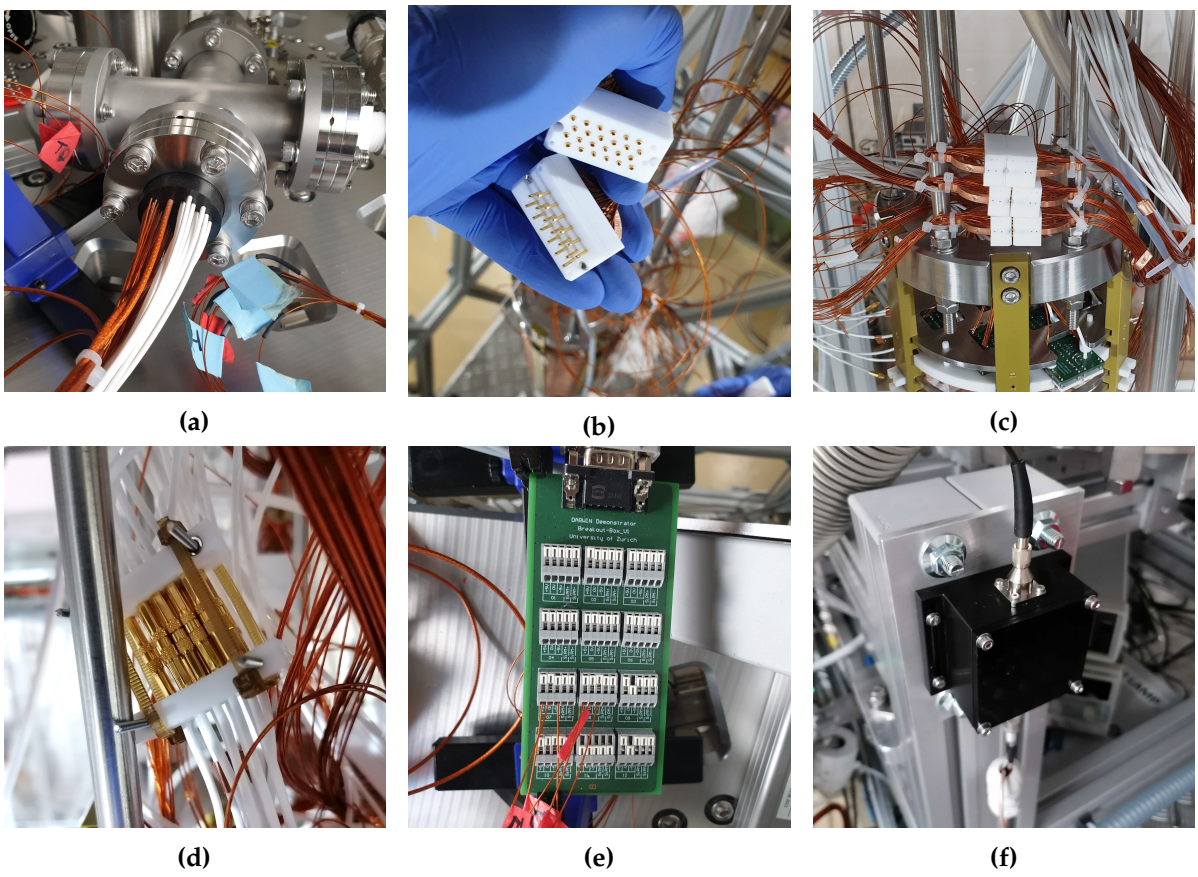

Figure 7.8.: Series of pictures of the cabling of the top array of Xenoscope, taken during the assembly of the TPC. **(a)** Top array custom potted feedthrough for both power and signal cables. **(b)** Female (top) and male (bottom) parts of the PTFE couplers for power distribution ready for connection; **(c)** All three PTFE couplers for power distribution assembled and connected; **(d)** Coupler of the coaxial signal cables; **(e)** Breakout box board before the power cables connected; **(f)** LED box with the 600 µm fibre connected.

electronics workshop. The latter can be controlled either by a touch screen or remotely via a USB connection.

In addition to the photosensors and amplifiers, the three onboard PT100s are serviced by four-wire readouts. These wires are collected in the same PTFE connector blocks as the rest of the single wires, but they are later connected to a dedicated 51-pin feedthrough, through which most of the other temperature sensor connections in the TPC are also made. The temperature sensors are read by a Raspberry Pi-based setup and the values are communicated to the SC system. The full cabling schematic can be found in Figure 7.7c.

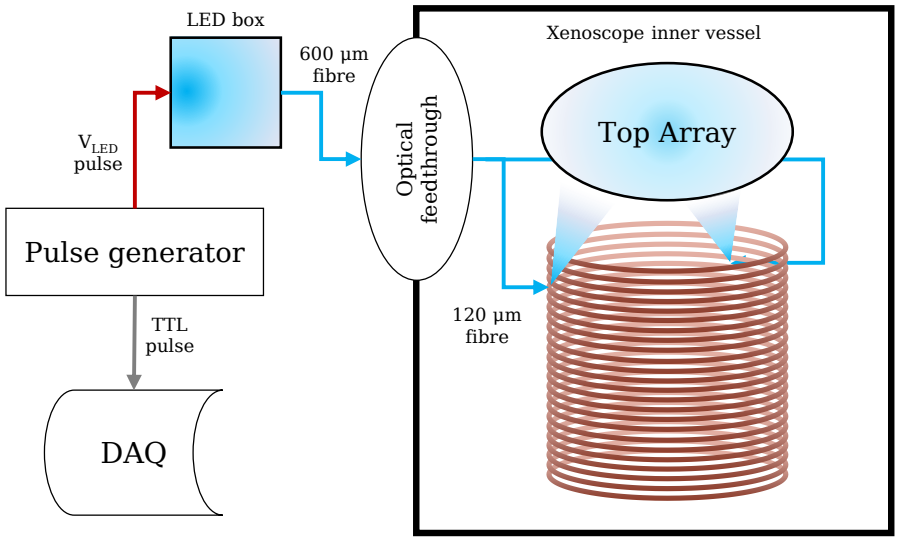

Figure 7.9.: Cabling and fibre routing of the LED calibration system in Xenoscope. Color legend: grey - TTL pulse for triggering the DAQ; red - voltage pulse to activate the LED inside the LED box. The amplitude and frequency of the pulse are defined via a pulse generator; blue - light-guiding fibres, both outside (600 µm) and inside 120 µs the vessel.

To have a triggered calibration light source available during operation in order to monitor the gains of the photosensors, an LED-based calibration system was designed. A KA-4040QBS-D LED from Kinbright stays on the outside of the vessel inside a small dark box, pointed at an SMA 905 connector, pictured in Figure 7.8f. From the LED box connector, a 600 µm optical fibre guides the emitted light to a UV/VIS dual fibre feedthrough from Accu-Glass [374]. The feedthrough is mounted on a CF40 flange on the top flange of Xenoscope and connects to the fibre through another SMA 905 connector. The second connection on the feedthrough is designed to host the fibre coming from the xenon flash lamp. The LED light is split into three 120 µm bare fibres, which are routed into the main volume of the detector alongside the PAI pillars, wrap around the top part of the field cage, and end secured in PTFE holders attached to the pillars and pointing upward to the top array. In the final assembly, two out of the three fibres were verified to be working, situated close to tile A and tile M. A pulse generator on the ground floor sends at the same time the signal to power the LED inside the box with a user-defined shape and amplitude and a TTL pulse to the data acquisition to serve as a trigger. A schematic of the light calibration system can be found in Figure 7.9.

7.3. SiPM characterisation

Before the installation of the SiPM array in Xenoscope, an in-depth characterisation of the SiPM sensors and bases was performed. First, the tile readout was tested and studied by comparing the achievable operating characteristics with those of a single $6 \times 6\,\mathrm{mm}^2$ or a $12 \times 12\,\mathrm{mm}^2$ unit. The main properties studied were breakdown voltage, gain, SPE resolution, DCR, and CTP, all at temperatures from room temperature down to 170 K. Later on, the full set of 50 $12 \times 12\,\mathrm{mm}^2$ units bought to equip the top array were individually characterised with a two-fold purpose: primarily, to test if the unit was working properly at the expected temperature of the gas phase of the TPC, and, further, to characterise their individual breakdown voltage and gain dependence on the applied voltage. The latter allows for the different quads to be distributed so that their gain is as similar as possible per tile, reducing the spread of gains and, as a result, achieving a better SPE resolution. This method is also called "gain matching." Furthermore, the structural integrity, assembling methods, temperature sensors, and cabling of the setup were all tested while the photosensors were being characterised.

The test setup, data acquisition system, and analysis framework used to perform the tests at cold temperatures are described in Subsection 7.3.1. Following the described methodology, the results of the characterisation of a $12 \times 12\,\mathrm{mm}^2$ MPPC unit and the tile readout, as well as the comparison between these, are presented in Subsection 7.3.2. Finally, in Subsection 7.3.3, the results of the full set of SiPM units for the top array are shown and discussed.

7.3.1. Characterisation methodology

Test setup

Initial tests of the photosensors and the readout were performed in SANDBox, a light-tight black box at room temperature and pressure, in the local laboratory. Here, the sensors are illuminated by a blue Light-Emitting Diode (LED) and checked for a binary result of operating or not. The large area of the studied units makes any measurement of single-photon response impossible at room temperature because of high DCR, reaching $\sim$200 MHz.

The full characterisation of the photosensors was performed in the Liquid Argon Setup (LArS), also at the University of Zurich, using the actual array to be later installed in Xenoscope. The setup consists of a double-walled cylindrical vessel with 250 mm diameter sealed to a top flange by an o-ring, where several feed-throughs serve the inner space with connections to electronics, external gas bottles or vacuum pumps. The array is suspended by eight stainless steel rods from a custom-made PTFE holder, which, in turn, is suspended from the top flange with four rods. In the centre of the PTFE holder, the blue LED ($\lambda =\sim$ 420 nm) is placed to illuminate the array. The power transmission wires of the array (Kapton-insulated, stranded copper wires), which supply the bias voltage of the SiPMs and the operational amplifier, are connected to a breakout box on the inside of the vessel, the same to be later used on the outside of Xenoscope as mentioned in the previous section (Figure 7.8e). The five merged power wires are routed to the air-side via an electrical feedthrough connected on the top flange piping and, as in Xenoscope, the pre-amplifier circuit is powered by a standard current-limited power supply, while the SiPM voltage is supplied by a custom-made low-noise power supply. The twelve coax signal cables from each tile are connected directly to another potted feedthrough and are routed to the DAQ. A labelled render and a picture of the setup can be found in Figure 7.10.

The inner volume of the setup is first pumped out to remove atmospheric gases and avoid any residual water vapour in the volume and then filled with a coolant gas, which, in the particular case of this characterisation campaign, was helium. The volume is then cooled via the supply of liquid nitrogen through a copper pipe coiled around the upper part of the chamber, where it undergoes a liquid-to-gas transition, cooling down the system. As the pressure of the He gas decreases during cooling, more is supplied to keep the pressure between 1.9 and 2 bar. The temperature inside the vessel is regulated by the flow of LN_2, from an external Dewar through the copper coil, controlled by a flow valve connected to a Proportional–Integral–Derivative (PID) controller [380]. There are several PT100 temperature sensors inside the vessel to monitor the setup and as reference for the PID controller: one attached to the copper coil, one in the gas volume, close to the PTFE holder, and one on tile *M* of the array. The previously mentioned onboard PT100s of tiles *B* and *G* were not read out during these tests.

Before being digitised, the signals are amplified tenfold with a Phillips Scientific 776 linear amplifier. The data is then acquired with two v1724 digitisers from CAEN [212] and read out through a v2718 VME-PCI [381] optical link bridge module to an on-site

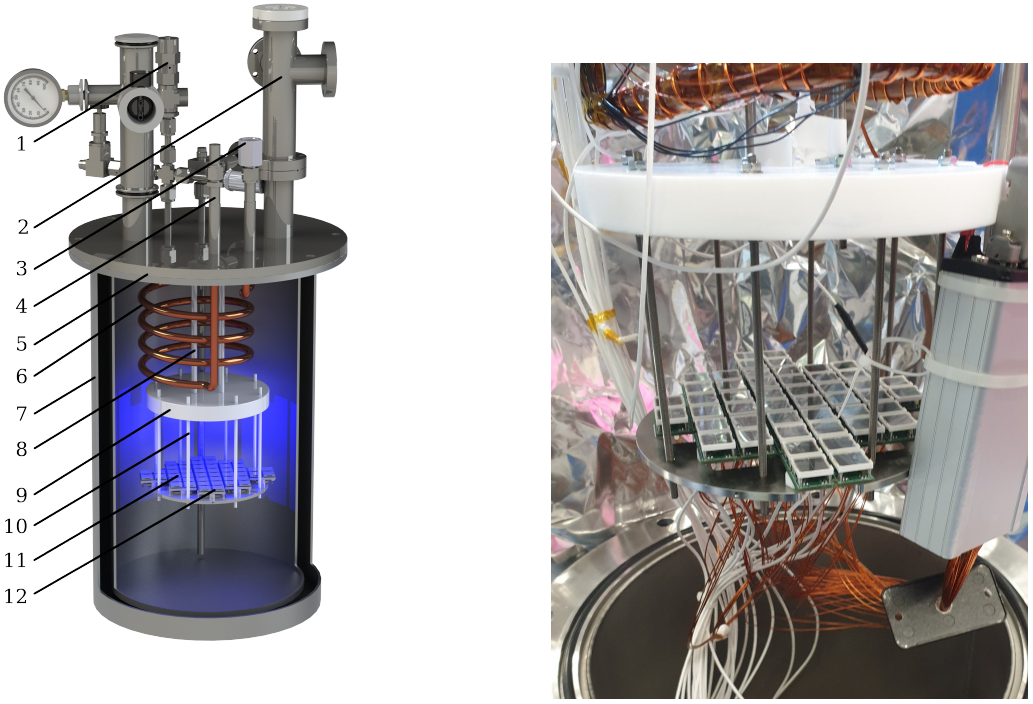

(a) **(b)**

Figure 7.10.: **(a)** Render of top array test setup in LArS. Legend: 1 - Gas inlet; 2 - Electrical and instrumentation feedthroughs; 3 - Pressure relief valve; 4 - Gas outlet; 5 - Top flange; 6 - Copper coil; 7 - Cryostat vessel; 8 - Support rods of the PTFE holder; 9 - PTFE holder; 10 - Support rods of the top array; 11 - Top array; 12 - On-board PT100. **(b)** Picture of the top array fully loaded in the test setup with the vessel open.

computer. In particular, the v1724 is an eight-channel, 14-bit digitiser with a 2.25 V dynamic range and a sampling rate of 100 MHz at the standard 50 Ω impedance. Figure 7.11a schematises the cabling and DAQ apparatus of the test setup.

The LED pulser settings were defined by hand, making sure that none of the channels would saturate from too much light while acquiring data. The pulse shape of choice was a square pulse with 30 ns width, and its frequency was chosen as high as the ADC memory allowed, taking into account the waveform size. For waveforms of ∼1 µs the acquisition rate achieved was ∼2 kHz, while for longer waveforms of ∼0.1 ms the achieved acquisition rate was of ∼200 Hz. A parallel TTL signal is sent from the LED pulser to the ADC to function as the trigger for the acquisition. Similarly, the temperature control on the PID controller was always set and monitored manually. On the other hand, the power supply of the SiPMs was controlled remotely from a

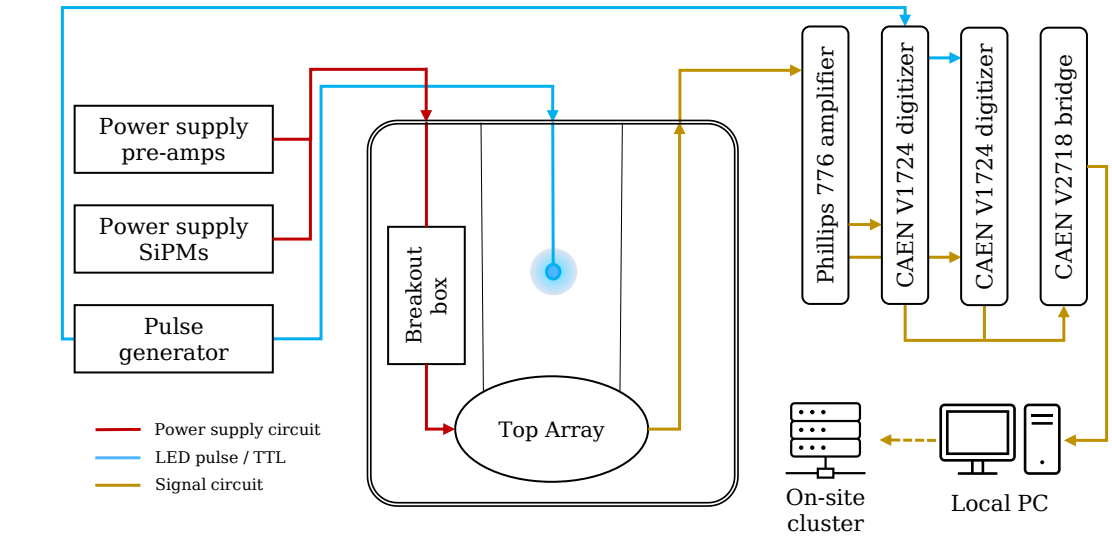

(a)

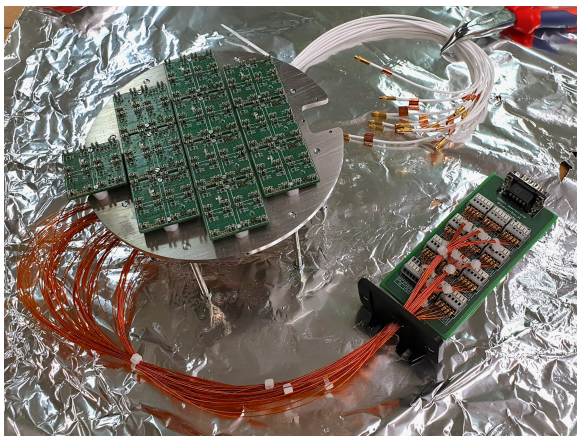

(b)

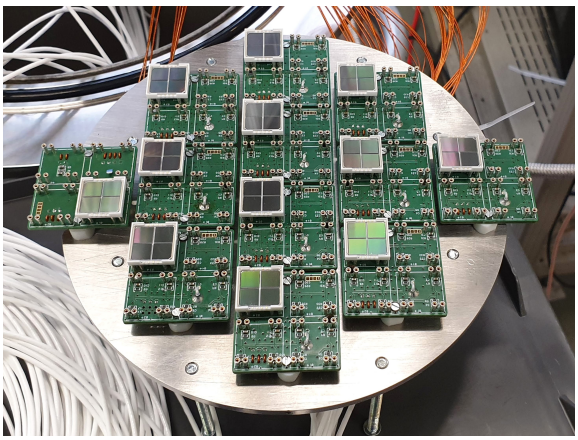

(c)

Figure 7.11.: **(a)** Schematic of the LArS test setup and DAQ cabling. Not represented in the figure are the pressure and temperature regulator circuits, composed of the pressure and temperature sensors, Cryocon with PID controller, and flow valve to control the rate of LN_2 cooling. **(b)** The top array before any sensors are loaded with a focus on the connections of the single-wire power cables inside the breakout box. Tile M was not installed at this time, and later on, added with the onboard PT100. **(c)** The top array loaded with twelve $12 \times 12\,mm^2$ units before a characterisation run.

USB interface connected to the local computer. This allowed for the automation of voltage scans at a given temperature and light level through a Python script.

Data acquisition

The v1724 ADC is programmed with custom C++ software that makes use of the CAEN libraries [382]. Through an instruction file, the user defines the data-taking mode, choosing between an external trigger, periodic internal trigger, or amplitude-based trigger. Also through the instruction file the baseline values of each ADC channel, the duration and position of the waveforms with respect to the trigger, and, in self-trigger mode, the threshold amplitude value at which a waveform is recorded, are defined. The output of a successful data-taking run is a directory with a copy of the instructions file, a summary file with the number of events recorded, the total time the DAQ was running, the UNIX timestamp of the end of the process, and a ROOT file with the recorded waveforms. Further details on the DAQ software can be found in [1]. These files are then copied from the local computer to the computing infrastructure of the physics department, where the data is stored and processed.

Making use of the setup detailed above, there were three stages to the characterisation of the top array:

- Test and benchmark the developed tile readout
- Batch characterise the quad units for Xenoscope
- Test the fully-loaded top array

The first action item was to acquired data from a $12 \times 12\,\mathrm{mm}^2$ quad and a fully loaded 24×24 mm^2 tile, with the main goal to see how the large-area readout affected the typical SiPM characteristics by performing a voltage and temperature scan. Later, with the readout already tuned, the characterisation of all 50 quads was performed in six runs. In each run, twelve quads were characterised, one per available tile readout (Figures 7.11b and 7.11c). Due to time constraints, some of the runs were done only at 190 K, close to the temperature expected in the gas phase of Xenoscope's TPC, where the array will be placed. Finally, after the individual quad data was taken, a run with the top array fully loaded, without special attention to gain-matching the different quads was performed.

For all the runs, data was acquired with both the LED turned ON and OFF. The first can be used to calculate the BV from the collected charge as a function of the applied voltage fit at constant illumination and provides data for high-luminosity effect studies. The latter provides datasets to determine the DCR and CTP but also gain and SPE

resolution by fitting the SPE peak in the charge spectrum with a Gaussian function. For both types of datasets, the triggering of the digitiser is done from the LED pulser. While this decision is easily explained in the LED ON data, it may appear strange in dark datasets. Because the DCR of the quad units is high, when the DAQ was self-triggering with a threshold below 1 pe and reading 12 channels at the same time, it was constantly in busy mode. Without the proper setup to quantify the dead time from the DAQ being busy, there was no handle on the correct livetime of the recorded datasets. The real-time between the start and stop of the DAQ was an overestimation of the livetime because for certain periods the DAQ was not able to record events. By triggering externally, the recorded waveform is uncorrelated to the presence of a dark count event in the waveform, and the total livetime is always the cumulative sum of the waveforms' sizes, i.e., the total number of waveforms multiplied by their sizes. The drawback of such a method is that the large majority of recorded data is noise, and to achieve significant statistics of the dark count signals, the size of the data is significant and limiting. This problem increases at lower temperatures, where the DCR is smaller. For example, at $\sim$170 K, for $\mathcal{O}(10^3)$ SPE events after cuts, the uncompressed ROOT file is $\sim$10 GB. The main advantage is the reliability and reprocessing value of the data acquired since no choice of threshold was done to trigger the DAQ.

There are several improvements that could be implemented in the acquisition framework to more easily and reliably record dark count events. A dead time counter based on propagated busy states, as described in [215, 330], would allow for self-triggered acquisition while maintaining a handle on the true livetime. In addition, the use of ZLE to reduce the memory usage of the ADC during acquisition would greatly reduce the size of the recorded data, although a threshold would then need to be set.

Data processing

The data was processed using PyLArS [383], an in-house developed Python package for pulse finding and analysis. The software was designed with the SiPM characterisation campaign in mind in terms of data structuring and the analysis framework. Its core processing is based on a simple pulse detection algorithm and the extraction of properties from identified pulses. The software defines a signal pulse when ADC counts exceed five times the root mean square (RMS) of the baseline value, defining the integration window on a per-pulse basis. The baseline value and its RMS are defined from the first 50 samples of any given waveform as the median value and the

standard deviation of ADC counts measured the during that interval, respectively. For an identified pulse, $f(x_i), i \in \mathbb{Z}^{0+}$, defined between samples x_0 and x_n, The following properties are determined and saved for each of the found pulses:

- The ADC *module* and *channel* of the data;
- *wf_number*: identifier number of the waveform in the dataset, from 1 to the total number of waveforms;
- *pulse_number*: identifier number of the pulse in the waveform, from 0 to the total number of pulses in the waveform -1;
- *Position* of the pulse, defined as the initial sample of the pulse, x_0;
- *Length* of the pulse, defined as the number of samples from the start to the end of the pulse:

$$Lenght = x_n - x_0 \, . \tag{7.6}$$

- Amplitude of the pulse, defined as the maximum (minimum) value of ADC counts in the pulse if the pulse polarity is positive (negative):

$$Amplitude = \begin{cases} \max\left(f(x_i)\right), & \text{if positive pulse} \\ \min\left(f(x_i)\right), & \text{if negative pulse} \, . \end{cases} \tag{7.7}$$

- *Area* of the pulse, defined as the baseline-corrected, integrated ADC counts from the start to the end of the pulse:

$$Area = p \cdot \Delta t \cdot \sum_{i=0}^{n} \left(f(x_i) - baseline\right), \; p = \begin{cases} 1, & \text{if positive pulse} \\ -1, & \text{if negative pulse} \end{cases} \, . \tag{7.8}$$

Exemplary waveforms are depicted in Figure 7.12 for both an LED-triggered pulse and a spurious dark count event. The computation of these pulse properties was optimised using just-in-time (JIT)-compilation provided by *numba* [384] methods to speed up processing with Python. The processed data is stored in compressed files in the local cluster and methods have been implemented to automatically load the different processed datasets of a run (both at different temperatures, bias voltages and illumination conditions) for analysis.

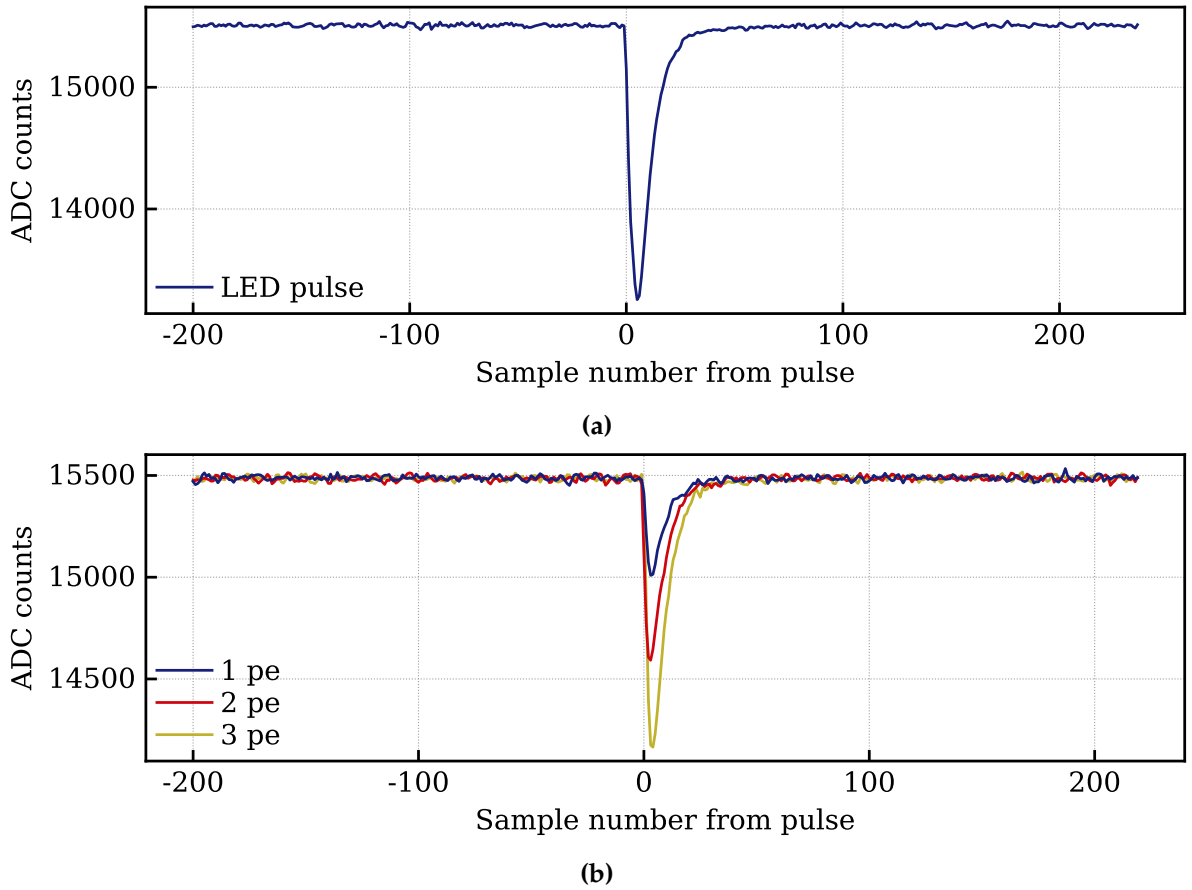

Figure 7.12.: **(a)** Example waveform of an LED pulse taken in triggered mode. The waveform is from a single quad (#309) at 170 K and 52 V V_{bias}. **(b)** Overlapped example waveforms of 1, 2 and 3 PE pulses. The waveforms are from a LED OFF dataset from a single quad (#317) at 170 K and 52 V V_{bias}.

Datasets with the LED at a constant light level are analysed to compute the BV of a given sensor by taking data at different voltages at a constant light level. The resulting pulses are composed of an a priori unknown number of PEs for each voltage, but the number of incident photons stays on average the same through all the datasets. The resulting distribution of pulse areas can be found in Figure 7.13a. For lower voltages, close to the BV, the overvoltage is small and, therefore, so is the gain. On the other hand, for very high applied voltages, the gain is rather large, and the resulting distribution broadens. In Figure 7.13b, the median value of each LED pulse area distribution is shown as a function of the applied voltage. The breakdown voltage, approximated as the voltage at which the gain is zero, is usually found by fitting a linear function to such a plot and calculating the value of V_{bias} for $Area = 0$. However, this procedure is only valid for no or low illumination. As can be noticed, there is a

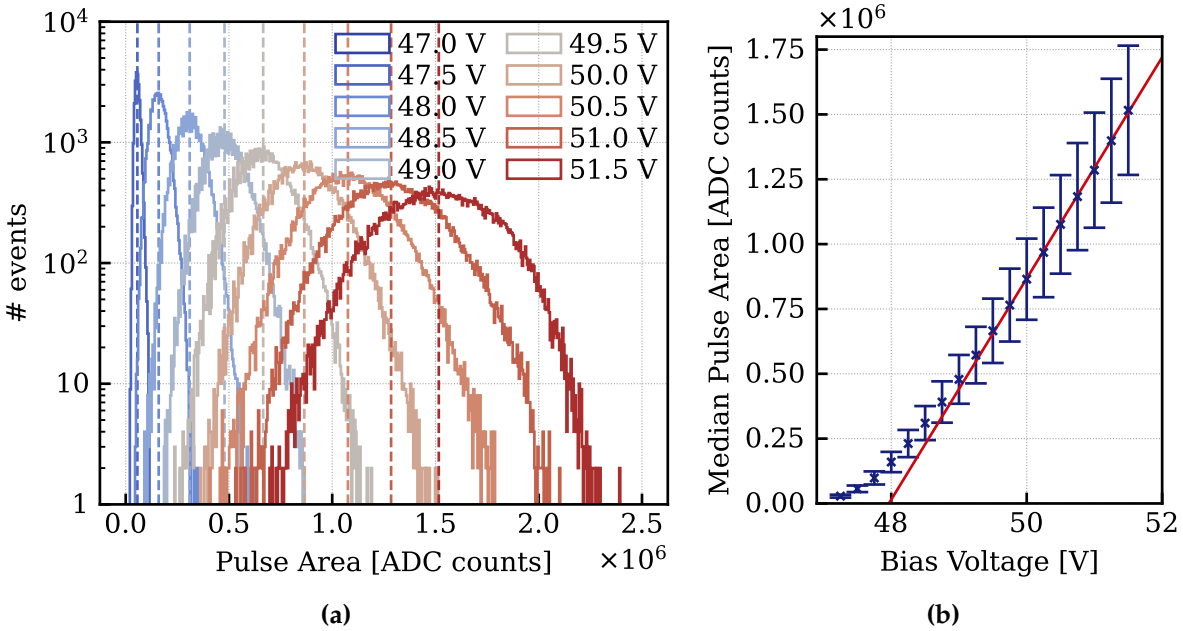

Figure 7.13.: **(a)** Measured area spectra for different bias voltages, after cuts, taken with the LED ON and at a constant illumination for a $12 \times 12\,\mathrm{mm}^2$ unit. The median value of each distribution is shown in dashed lines. **(b)** Median area of the LED pulses as a function of the bias voltage. The error bars represent one standard deviation of the area distribution at each voltage. A linear fit to the data above 48 V is shown in red.

clear deviation from linearity at low bias voltage, which is due to the SPADs operating close to but not yet in Geiger mode. Furthermore, at very high applied voltages, the pulses saturate due to the limited dynamic range of the ADC, although care was taken during data acquisition to minimise this limitation by adjusting the light level accordingly. Another method of calculating the BV will be further explored below, using datasets without illumination.

As previously mentioned, to calculate the gain, DCR, and CTP of the SiPMs, data was taken in a dark environment at different temperatures and voltages. An example of the pulse area spectrum (proportional to charge) of such a dataset without any applied cuts can be found in Figure 7.14a. Such plots are often called *fingerplots* given their finger-like structure composed of the several PE peaks. On the left side of the spectrum, the pedestal of noise is prominent if no cuts are applied, followed by a short tail. The next peak denotes the SPE peak and, in regular intervals, the second and third PE peaks. Unlike other sensors, where valleys between PE peaks are very deep, here a shoulder-like region is observed on the higher-area side. The shape of such pulses mimics the shape of the main peak population, albeit with a higher integrated

area. These events could be due to unresolved fast and correlated avalanches and were similarly observed in [385] when studying the same family of photosensors.

Signal-like events are selected by applying a general quality cut (no sudden baseline shift or very noisy waveform) and a cut on the length of the pulses. Figure 7.14b shows that PE signals have a clearly distinct length population from noise pulses. When properly tuned, the length cut reduces the noise pedestal by $\sim$3 orders of magnitude while retaining $> 99\%$ of the signal pulses, as depicted in Figure 7.14c.

From the clean spectrum, one can make the "step plot" shown in Figure 7.14d. This representation which is frequently used to represent DCR, is created by calculating the number of events above a certain pulse area threshold. Its various “steps” indicate the areas for which there is a clear change in the rate observed, corresponding to each PE peak. In this particular case, the first inflexion point is used to compute the rough position of the SPE, which is then fitted to a Gaussian function in the area spectrum, as shown in Figure 7.14e.

The gain of the photosensor is then calculated as:

$$G = \frac{q_f}{q_i} = \frac{Q}{q_e \cdot A} = \frac{ADC_{range}}{q_e \cdot A \cdot R \cdot ADC_{res}} \int ADC_{counts}\, dt \,, \tag{7.9}$$

where G is the gain of the photosensor, q_i and q_f are the initial and final charge at the end of the Geiger multiplication, respectively, $Q = q_f \cdot A$ is the measured charge during acquisition, R is the impedance of the cables and ADC (50 Ω), ADC_{range} is the dynamic range of the ADC (2.25 V for the v1724), A is the amplification factor on the signal (in the case of this work, usually $\times$20 from the pre-amplifier, $\times$10 from the external linear amplifier), ADC_{res} is the bit-wise resolution of the ADC (2^{14};bit $= 16384$bit for the v1724), and q_e is the elementary charge of the electron. The integral of ADC_{counts} over the pulse time is the above-defined area of the pulses, here taken as the mean of the Gaussian fit to the SPE peak. For the case of Figure 7.14e, Equation 7.9 becomes:

$$G = \frac{2.25\,\mathrm{V}}{1.6 \times 10^{-19}\,\mathrm{C} \cdot 200 \cdot 50\,\Omega \cdot 2^{14}} \cdot 4.3 \times 10^{4}\ \mathrm{s} \approx 0.9 \times 10^{6}\,. \tag{7.10}$$

Also from the fit of Figure 7.14e, the SPE resolution is obtained, defined as:

$$SPE_{res} = \frac{\sigma}{\mu}\,, \tag{7.11}$$

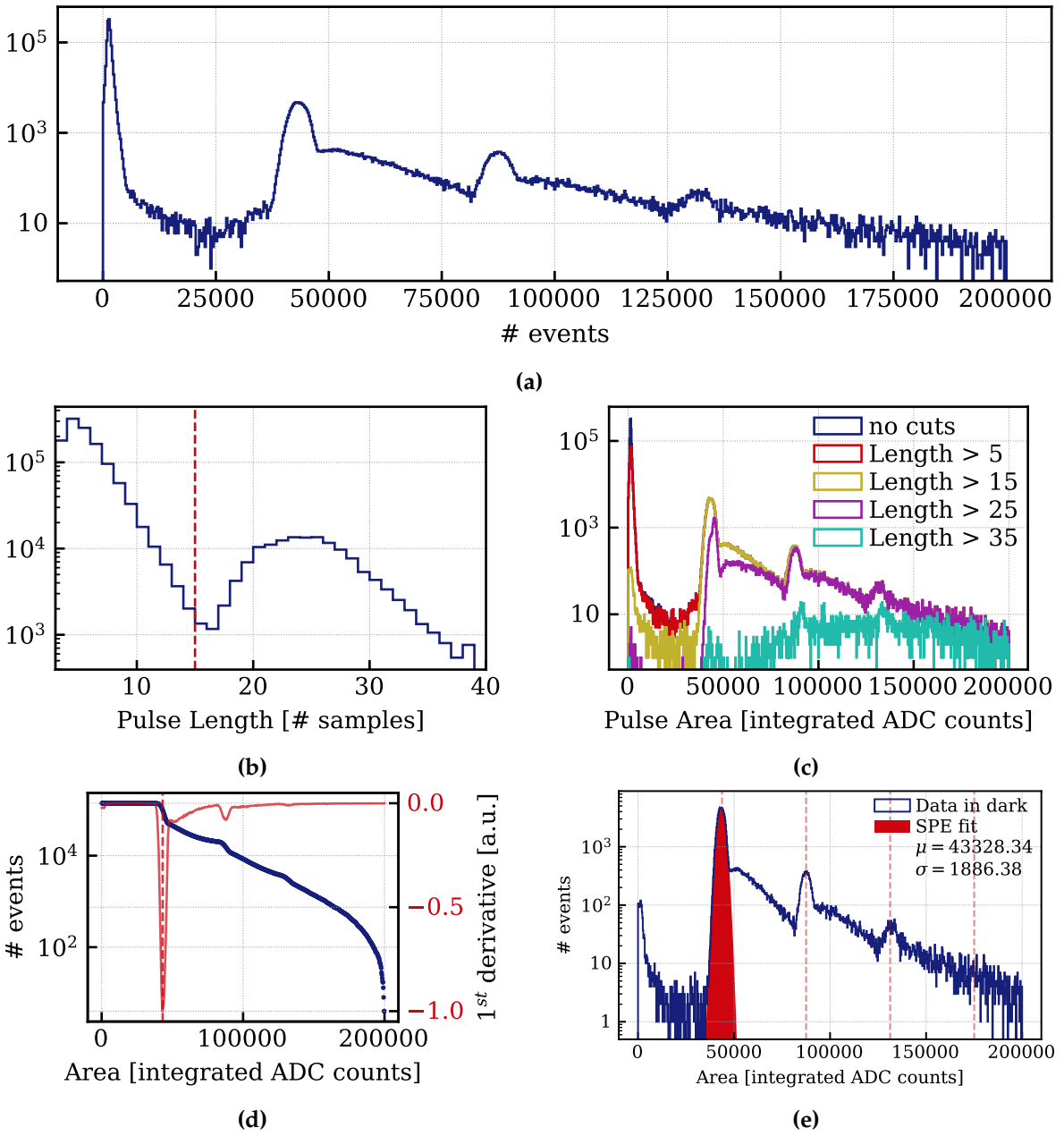

Figure 7.14.: **(a)** Area spectrum of a dark dataset without cuts applied. **(b)** Distribution of the Length values and definition of the selection cut at 15 samples. **(c)** Effect of different pulse length thresholds on the area spectrum. **(d)** Number of selected events as a function of area minimum threshold, commonly named "step plot". The first derivative of the step plot curve is shown in red and used to find the approximate position of the SPE peak, shown as the dashed red line. **(e)** Gaussian fit to the SPE peak, taking as initial parameter the approximate value determined with the step plot. The μ and σ of the Gaussian fit are shown in the legend, in area units.

where μ and σ are the mean value and standard deviation of the fitted normal distribution. With the SPE value determined, the DCR and CTP are calculated from their definitions:

$$DCR = \mathcal{R}_{0.5pe} \,, \tag{7.12}$$

$$CTP = \frac{\mathcal{R}_{1.5pe}}{\mathcal{R}_{0.5pe}} \,, \tag{7.13}$$

where $\mathcal{R}_{0.5pe}$ is the rate of pulses above the 0.5 PE value, computed as the number of pulses divided by the livetime of the dataset, commonly normalised to the sensor area, and $\mathcal{R}_{1.5pe}$ is the rate of pulses above the 1.5 PE value.

The variation of these properties with temperature and the bias voltage is discussed in the next section.

7.3.2. Characterisation of the VUV4 SiPM units and the summed readout

Using the methods described in the previous section, the model S13371-6050CQ-02 MPPC (quad) is extensively characterised in this section at temperatures ranging from 170 K to 210 K. At the same time, a full tile is characterised in similar conditions and its properties are compared to determine if the common readout causes a deviation from the expected behaviour of the photosensors. The setup used was the one described in Section 7.3.1, and all the properties were measured in a dark environment (LED off). A low light level of 1-2 detected photons is commonly used in the field to increase the population statistics of low-PE peaks. However, given the larger area of the sensors considered ($12 \times 12\,\mathrm{mm}^2$ and $24 \times 24\,\mathrm{mm}^2$), the dark count rate is high enough to provide sufficient statistics. Not using the in-situ LED also reduces the noise level and ringing effect sometimes visible when the LED is pulsed.

Gain and breakdown voltage

For each of the recorded datasets, the SPE peak and gain were determined, and its dependence on bias voltage and temperature is shown in Figure 7.15, for both a single

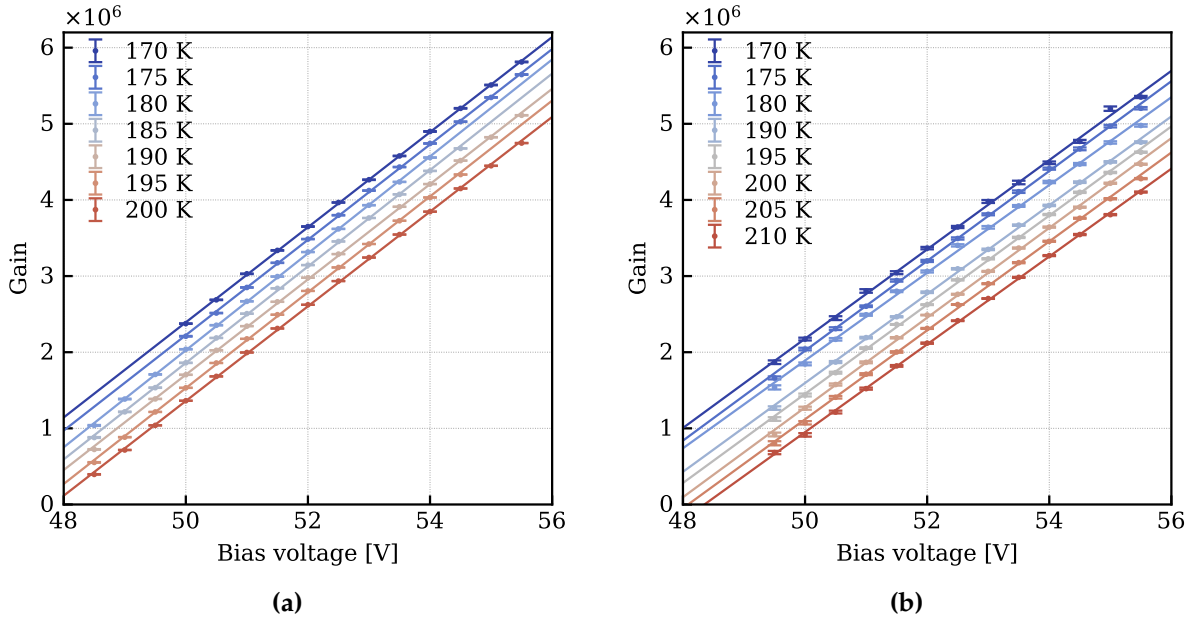

Figure 7.15.: Calculated gain of the photosensor as a function of the applied voltage at temperatures ranging from 170 K to 210 K for a $12 \times 12\,\mathrm{mm}^2$ quad (**a**) and a fully loaded tile (**b**).

$12 \times 12\,\mathrm{mm}^2$ unit and a fully loaded tile. As expected, above the breakdown voltage, the gain is linearly dependent on overvoltage, becoming larger for higher applied voltages. This behaviour is seen at all the temperatures for which data was taken, from 170 K to 200 K (210 K in the case of the tile). Moreover, for a given applied bias voltage, the measured gain increases with decreasing temperature, an effect resulting from a decrease in the corresponding breakdown voltage. For reference, at an applied voltage of 52 V, a gain of $(2.984 \pm 0.001) \times 10^6$ was measured on the quad and a gain of $(2.625 \pm 0.005) \times 10^6$ on the tile, both at 190 K, where the BV is ∼47.3 V.

The breakdown voltage at each temperature was determined by fitting a linear function to the distribution of gains as a function of the applied voltage and finding its x-axis intercept. The results are presented in Table 7.1 and Figure 7.16. A high level of concordance between the single quad and summed readout is shown, with the difference between the two always $< 0.3\%$. The rate of increase in breakdown voltage is $(55 \pm 2)\,\mathrm{mV\,K^{-1}}$ and $(50 \pm 2)\,\mathrm{mV\,K^{-1}}$ for the single quad and tile, respectively, in line with the specifications provided by the manufacturer at room temperature, $54\,\mathrm{mV\,K^{-1}}$.

In LXe TPCs, the typical gain required from the photosensors is dependent on the type of signal and later-stage readout. In general, for the purposes of rare-event

Table 7.1.: Breakdown voltage at different temperatures for a single quad and full tile.

T [K]	BV [V]	
	Quad	Tile
170	46.16±0.02	46.29±0.07
175	46.45±0.02	46.58±0.05
180	46.82±0.01	46.72±0.07
185	47.06±0.02	—
190	47.27±0.02	47.26±0.04
195	47.57±0.01	47.52±0.04
200	47.81±0.01	47.84±0.04
205	—	48.08±0.04
210	—	48.35±0.03

searches, such as in DARWIN, the ability to perform single-photon counting is a necessity for low-energy (and, therefore, low-scintillation) events. For this reason, the typical multiplication gains observed in such experiments are on the order of a few million, tuned photosensor-to-photosensor. In Xenoscope, however, the bias voltage is common to all the tiles, and gains will be slightly different from sensor to sensor. The choice of which bias voltage to use depends, once again, on the desired multiplication gain, and its dependence on the temperature of the sensors. From previous runs, the expected temperature of the gas phase of Xenoscope is ∼190 K. From Figure 7.15, at this temperature, one reads that a gain of 3×10^6 is achieved at a bias voltage of 52 V for the quad, while the full tile shows a slightly lower gain value. This bias voltage corresponds to 4.73 V OV.

SPE resolution

Good single photoelectron resolution is one of the strongest assets of SiPMs when compared to vacuum PMTs by providing photon-counting capabilities up to several PEs, an advantage at low energies. While the latter shows SPE resolution on the order of 25% [180] at a gain of a few million, SiPMs reduce this value almost 10-fold. The effect is most noticeable at low PE counts, where sharp peaks from the integer number of PEs contrast with the wide distributions of a PMT.

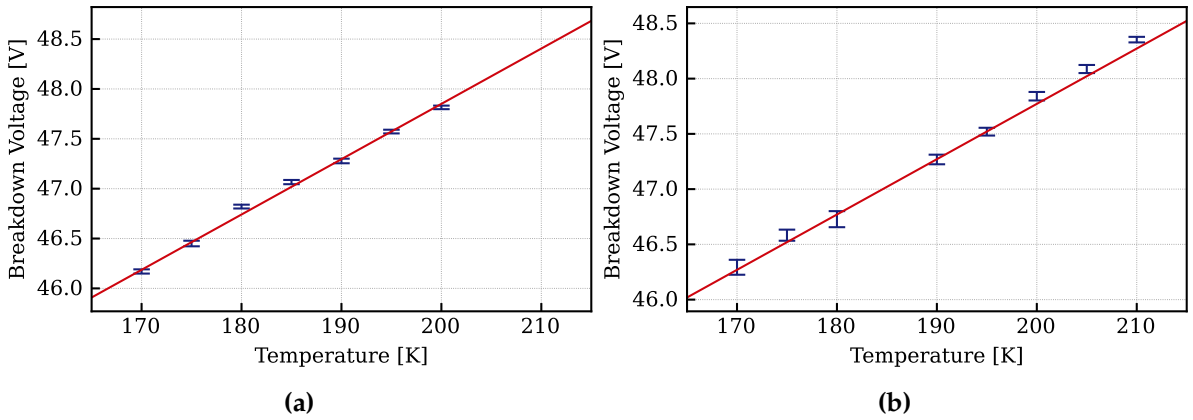

Figure 7.16.: Breakdown voltage as a function of temperature for a single quad (**a**) and a fully loaded tile (**b**) and a linear fit to the data in solid red.

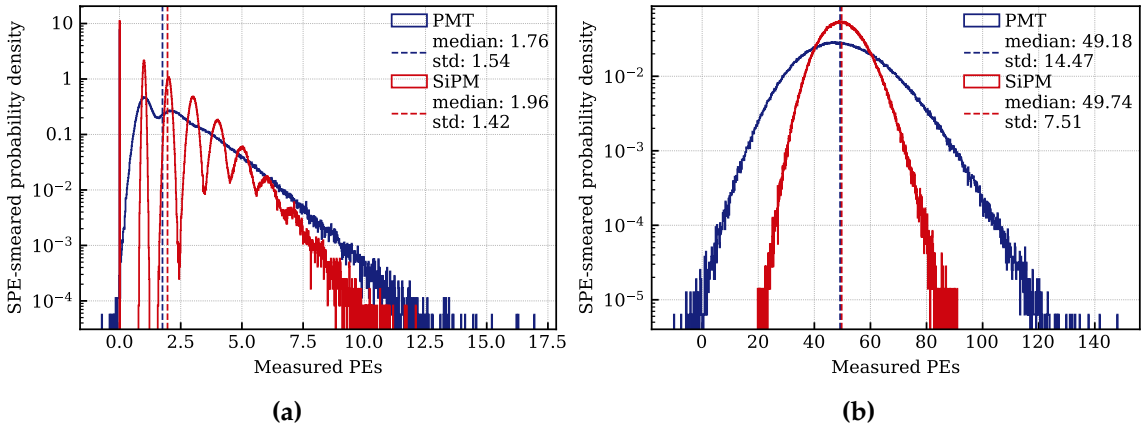

Figure 7.17.: Expected PE spectrum from 2 **(a)** and 50 PEs **(b)**.

Figure 7.17 shows the expected measured signal spectra for both a PMT and a SiPM, assuming 25% and 5% SPE resolution, respectively, for a signal of 5, 10, and 50 PEs. Such spectra are obtained in two steps. To begin, the number of detected photoelectrons is sampled from a Poisson distribution with μ as the initial pe number. The number of photoelectrons detected is then smeared by a normal distribution with a standard deviation, σ, as given by $SPE_{res} \cdot N_{PE}$. At a higher number of measured PEs, the effect of individual photon counting is smeared out, although the SiPM still shows a much narrower distribution of measured PEs than its PMT counterpart.

When considering a summed readout, such as in the tiles of Xenoscope, it is known that the SPE resolution will be one of the factors that will likely be negatively affected. Without gain-matching, the different units in a full tile can have up to a $\sim$1% difference breakdown voltages, resulting in different overvoltages at a given applied voltage.

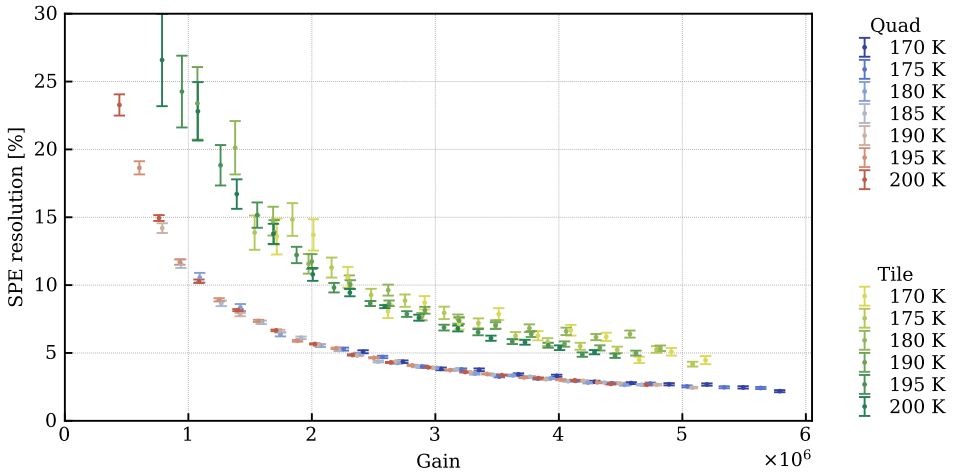

Figure 7.18.: SPE resolution as a function of gain at different temperatures for a single quad (red and blue) and a fully loaded tile (green and yellow).

Furthermore, the amplification process can vary from unit to unit, influencing the observed gain. Such discrepancies will lead to a broadening of the SPE peak in the charge spectrum and, therefore, an increase in SPE resolution. The calculated SPE resolutions of a $12 \times 12\,\mathrm{mm}^2$ quad unit and a fully loaded tile for different temperatures are shown in Figure 7.18. The described effect is clearly visible as, on average, the tile performs two times worse than the solitary quad. Nonetheless, the tile readout remains considerably better than standard vacuum PMTs, with a measured SPE resolution of $(7.78 \pm 0.51)\,\%$ against $(3.90 \pm 0.06)\,\%$ of the single quad for a gain $\sim 3 \times 10^6$ at 190 K. The results show that this property is independent of temperature but highly dependent on gain (or OV), exponentially increasing for lower gains.

Dark count rate

The calculated DCRs are shown in 7.19. As expected, they grow exponentially with increasing gain and temperature. At 190 K and a gain of $\sim 3 \times 10^6$, the calculated DCR for the quad is $(5.41 \pm 0.06)\,\mathrm{Hz\,mm^{-2}}$ and for the tile $(4.94 \pm 0.23)\,\mathrm{Hz\,mm^{-2}}$. At 180 K, closer to the case where the array is submerged in LXe and its temperature is in equilibrium with the medium, the expected DCR at the same gain is considerably smaller: $(1.82 \pm 0.03)\,\mathrm{Hz\,mm^{-2}}$ for the quad and $(1.83 \pm 0.05)\,\mathrm{Hz\,mm^{-2}}$ for the tile. It is noteworthy that the DCR values of the tested SiPM units are still two orders of magnitude above the analogous measurement for the PMTs used in current DM

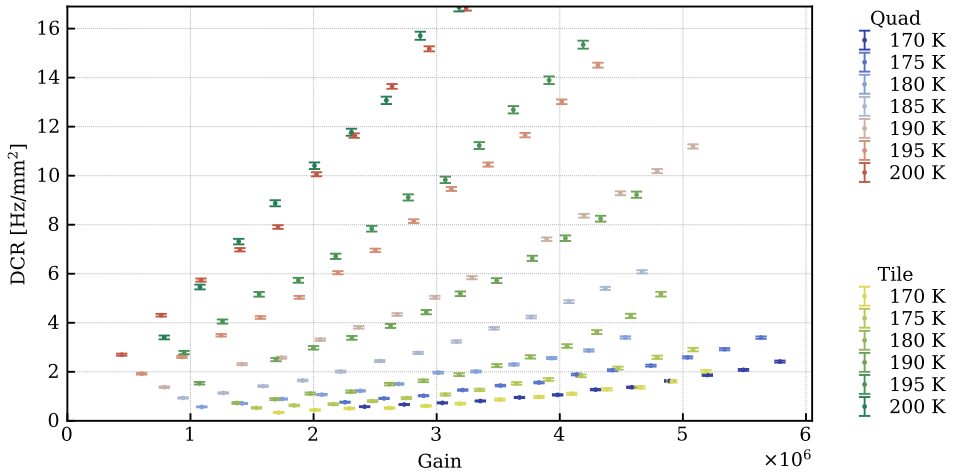

Figure 7.19.: Dark count rate as a function of gain at different temperatures for a single quad (red and blue) and a fully loaded tile (green and yellow).

experiments [179], the latter at $\sim$0.01 Hz mm^{-2}. The observed rates are comparable to current ([385]) and earlier ([386]) versions of this photosensor type.

The calculated DCRs of the quad and the tile agree well at all temperatures studied, staying within 10 % of one another. Since DCR at a given gain and temperature is only dependent on the intrinsic properties of the silicon wafer, no difference is expected between the single or summed readout when normalised to their respective areas, as was observed. In the event that a certain $6 \times 6\,\mathrm{mm}^2$ or $12 \times 12\,\mathrm{mm}^2$ unit has an abnormally high DCR, the spurious events of the tile where it is installed will be dominated by such a unit and will likely show the same order of DCR.

Further analysis of the DCR distribution of the quad was conducted to represent the expected DCR value for any given temperature and gain, within the ranges where the data was taken. The quad data from Figure 7.19 was fitted to an exponential function for each temperature, providing a continuous distribution of DCR values for a reasonable range of gains around the measured data. The modelled data is interpolated between each measured temperature using a Clough-Tocher curvature-minimising interpolator algorithm. The result is shown in Figure 7.20 as a heatmap of the DCR value as a function of temperature and gain. Such a plot is designed to be a practical way to check the expected DCR value of the photosensors of Xenoscope at a given operating condition.

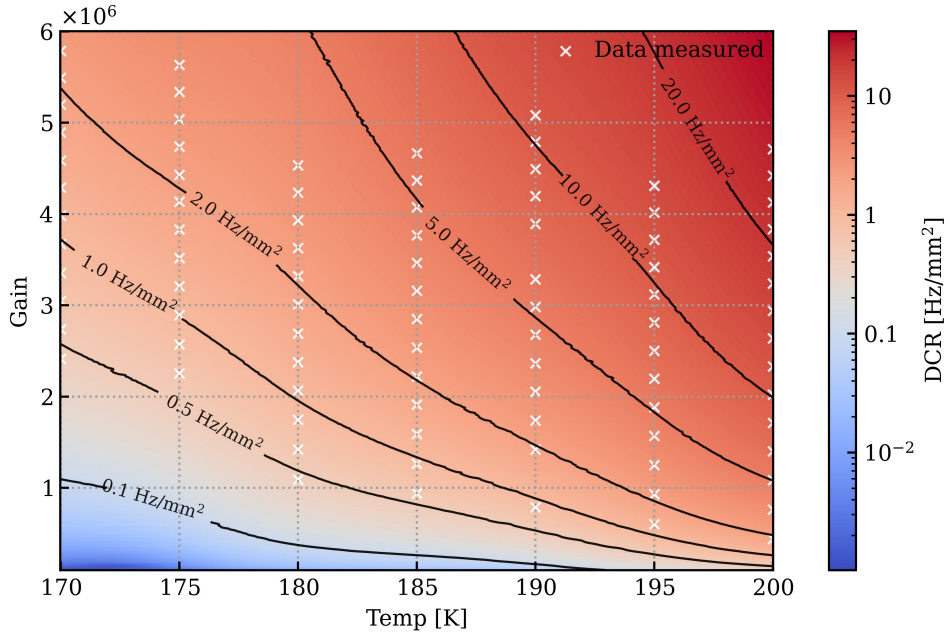

(a)

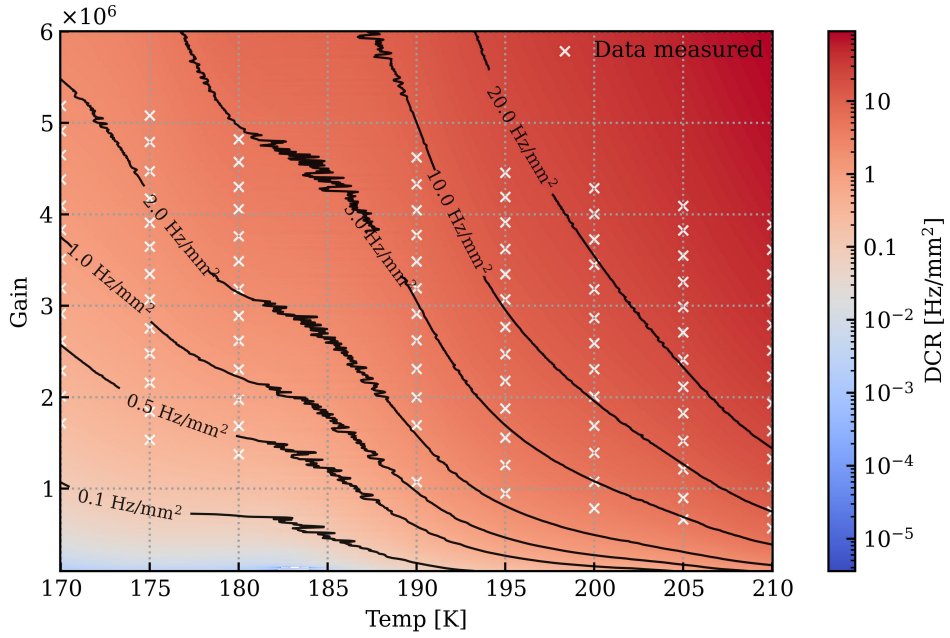

(b)

Figure 7.20.: Heat map of the expected DCR of a $12 \times 12\,\mathrm{mm}^2$ unit as a function of temperature and gain for a quad (**a**) and tile (**b**). The white crosses are the data points used to fit the DCR model with a 2D interpolation of the temperature and gain. In black several contours of DCR values are shown. Due to an issue during data taking, there is no data points for the tile at 185 K, leading to the interpolation problems observed in **(b)** The general trend is, nonetheless, maintained.

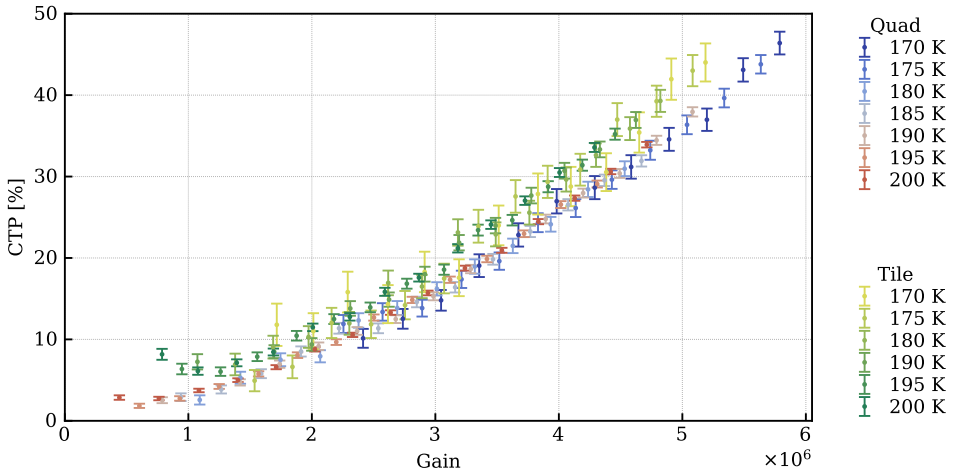

Figure 7.21.: Cross-talk probability as a function of gain at different temperatures for a single quad (red and blue) and a fully loaded tile (green and yellow).

Cross-talk

The final property studied in detail over a range of temperatures and bias voltages was the cross-talk probability. As defined in equation 7.13, no distinction is made between direct, indirect, or feedback cross-talk. Any uncorrelated pulse with an area above 1.5 PE is, therefore, considered a cross-talk event. However, for large area sensors, such as with a summed readout, high values of DCR can lead to pile-up of dark count pulses, mimicking unresolved prompt cross-talk signals.

Figure 7.21 depicts the distribution of CTP as a function of gain for the usual range of temperatures for both the quad unit and the fully-loaded tile. Over the whole range of measured gains, the calculated CTP of the tile exceeds the one from the quad by $\sim 3-5\%$, likely due to the aforementioned chance of pile-up. While the calculated DCR increases with increasing temperature, CTP is temperature independent. At a measured gain of $\sim 3 \times 10^6$, the calculated CTP of a quad is (15.8 ± 0.5) %, while for the fully-loaded tile is (18.9 ± 0.9) %.

Overall, this is a significant improvement from previous versions of the VUV SiPMs from Hamamatsu [386], achieved by adding photon-blocking trenches between the SiPM pixels (as can be seen in Figure 7.2b).

Afterpulses

No quantitative analysis was done to characterise the afterpulse population of the tested sensors. Nonetheless, a large dependence of the aferpulse rate on the light level was observed. In datasets where the SiPMs were highly illuminated by the LED, afterpulses were commonly seen up to several µs after the main pulse. Figure 7.22 portrays such a case, where a high number of afterpulses is seen after the main peak, while no signal is seen before the peak. As mentioned before in Section 7.1, afterpulses can have the same topology as a single-photon signals, including cross-talk effects, contributing as dark-count-like events. Moreover, for primary signals with a duration $\sim\mathcal{O}(1)$ µs, comparable with the characteristic timescale of afterpulses, both will be observed as a single signal with a larger area.

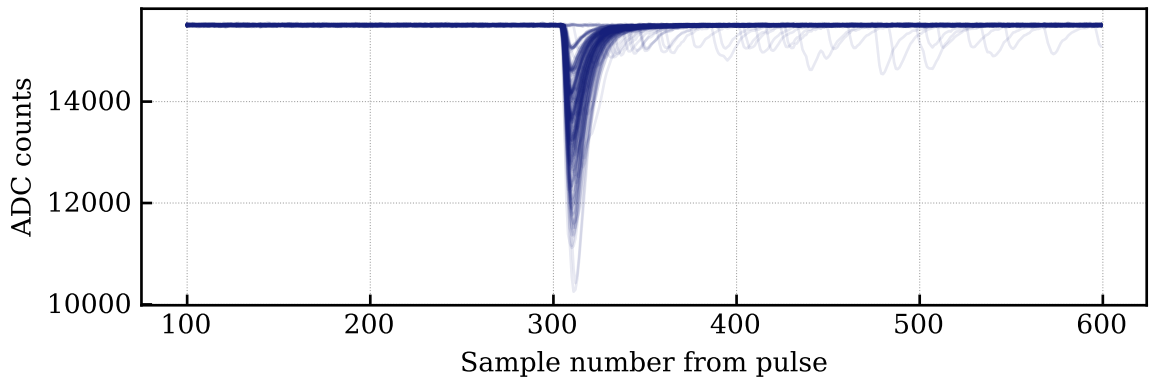

Figure 7.22.: 500 LED waveforms stacked, showing a high number of afterpulses on the right of the main pulse. Also discernible are the discrete amplitudes of PEs on the main LED signal.

7.3.3. The quads of Xenoscope

As described in Section 7.2, all 50 quads purchased for Xenoscope's top array were tested and characterised before installation. This work marks the first batch characterisation of SiPMs in the context of DARWIN. The individual characterisation of quad units was done in two periods, with the first five runs taking place between February and March of 2022 and the final one in July of 2022. An extra run with the array fully loaded with quads took place in September 2022.

Throughout the different runs, the DAQ showed signs of instability: four of the twelve channels systematically yielded bad data, either with a very high noise level,

no signal recorded, or large baseline shifts throughout the acquisition. These channels were excluded from the analysis, and the respective SiPMs were retested later on in the last two runs.

The quad units have a unique identifying number provided by the manufacturer, ranging from 270 to 324 (some numbers are skipped). During the assembly of the test setup for run 6, the array was accidentally pressed against the coiling copper tubing of LArS, and MPPC 321 was broken, as were some of the push pins on two tiles, which were replaced. The data acquired for the remaining 49 quads were processed and analysed as described in Section 7.3.1, and their breakdown voltage, gain, DCR, and CTP were measured. Due to time constraints on the use of the LArS facility, during some of the runs, data was acquired only at a 190 K, the expected temperature of the gas phase of Xenoscope where the array is to be operated. All of the quads were operated at several voltages between 48 V and 55 V. To facilitate the discussion and comparison between the properties of all the units, a bias voltage of 52 V at a temperature of the onboard PT100 of 190 K is taken as the standard, corresponding to an amplification gain on the order of 3×10^6.

The distribution of breakdown voltages at 190 K is shown in Figure 7.23. The median value is (47.08 ± 0.02) V with a standard deviation of 0.13 V. The distribution is skewed toward higher voltages, although all the quads show a BV within 0.4 V of the median value. A deviation to lower values is observed for the first set of SiPMs, from numbers 270 to 283, correlating with the first run of data taking. There was no evidence of failure or problems during the analysis procedure, but a problem with the operating conditions (either temperature or bias voltage) during data acquisition cannot be completely ruled out.

Highly correlated to the breakdown voltages registered, the gain of the characterised photosensors is shown in Figure 7.24. The distribution is similar to the distribution of BVs, this time displaying a larger tail for higher gain values. The median value is $(3.02 \pm 0.02) \times 10^6$ with a standard deviation of 0.12×10^6. Throughout the full collection of quads, at standard conditions, the observed gains are constrained between 2.85×10^6 and 3.35×10^6, or $< 10\%$ from the median value. While in the initial setup of the top array in Xenoscope the applied voltage is common to all the sensors, equalising the gains throughout the array would be possible if each quad was supplied with a voltage dependent on its breakdown voltage.

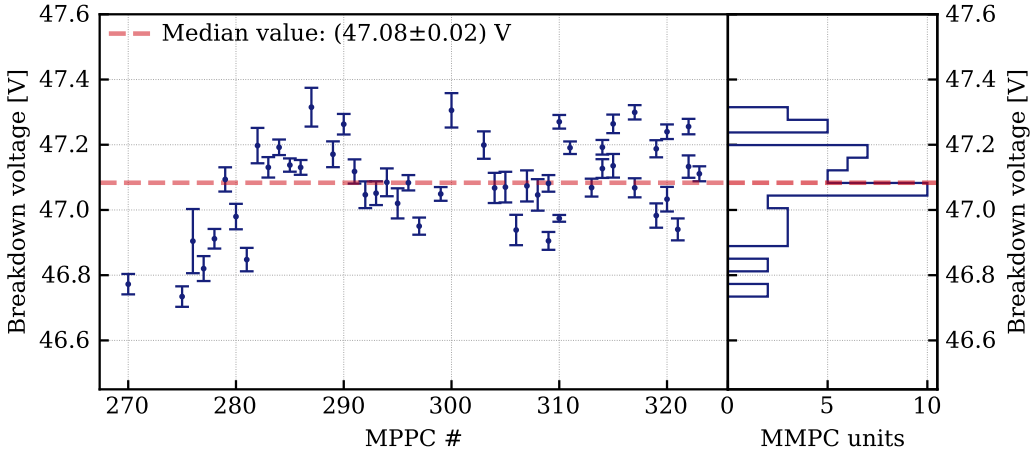

Figure 7.23.: Breakdown voltage calculated for each of the $12 \times 12\,\mathrm{mm}^2$ units of Xenoscope and its overall distribution.

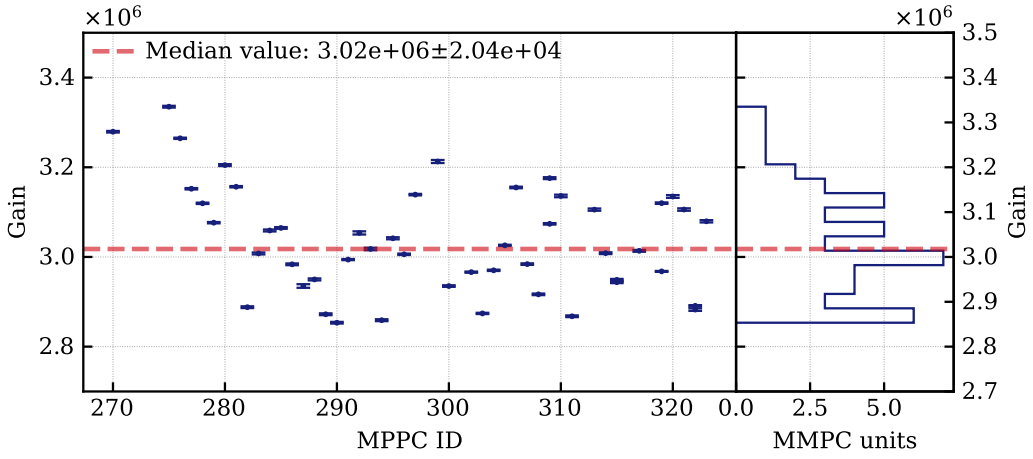

Figure 7.24.: Gain calculated for each of the $12 \times 12\,\mathrm{mm}^2$ units of Xenoscope and its overall distribution.

Figure 7.25 shows the computed SPE resolution values, where a normal distribution is observed. The median value at standard conditions is (4.38 ± 0.08) % with a standard deviation of 0.44 %. In fact, all the quads show SPE resolution values between 3.5 and 5.5% without any clear indication of run dependence. Despite the large relative difference between the extreme ends of the distribution, all the quads display an SPE resolution suitable for clear discrimination between photoelectron pulses up to several PE (see Figure 7.17 in the previous section on the effect of SPE resolution).

Another parameter of interest, under Xenoscope's standard operating conditions, is the distribution of DCR, which is shown in Figure 7.26. The distribution is rather nar-

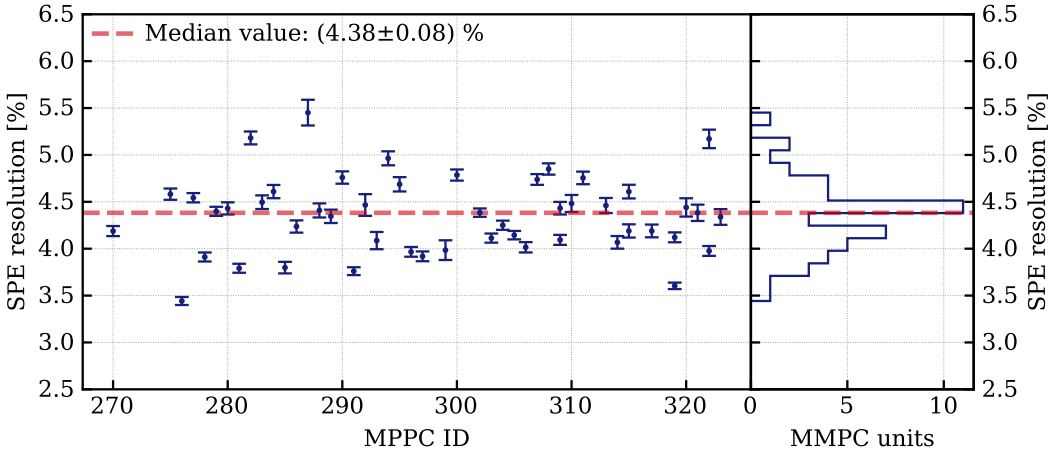

Figure 7.25.: Single photon resolution values obtained for each of the $12 \times 12\,\mathrm{mm}^2$ units of Xenoscope and its overall distribution..

row, with a median of $(2.93 \pm 0.21)\,\mathrm{Hz\,mm^{-2}}$ and a standard deviation of $1.20\,\mathrm{Hz\,mm^{-2}}$. However, the overall DCR of the array will likely be dominated by some outliers, exhibiting rates above double the median value. Due to non-uniformities in the silicon wafers, it is expected that some of the units display a larger DCR. Nonetheless, 90% of the characterised MPPCs show DCRs below $5\,\mathrm{Hz\,mm^{-2}}$ under standard conditions. Summed throughout the sensitive areas[2], the expected DCRs are, on average, $\sim$1.69 kHz for a given tile and $\sim$20.25 kHz for the whole array. Given the nature of signals in Xenoscope's TPC, both triggered and with high PE counts, the rate of spurious pulses at a threshold of 0.5 PE is not an important factor. It is, however, a critical factor for few-photon signals in a next-generation DM experiment, such as DARWIN.

The final property calculated for all the available photosensor units was, as in the previous section, the cross-talk probability. The resulting distribution is shown in Figure 7.27, exhibiting a median value of (14.76 ± 0.34) % and a standard deviation of 1.98 %.

The numerical values of the properties discussed for all of the numbered quads, shown throughout figures 7.23 to 7.27 can be found in Appendix B.

[2]A tile has a sensor area of $12 \times 12 \times 4 = 576\,\mathrm{mm}^2$ and the full array, over the twelve tiles, a sensor area of $6912\,\mathrm{mm}^2$.

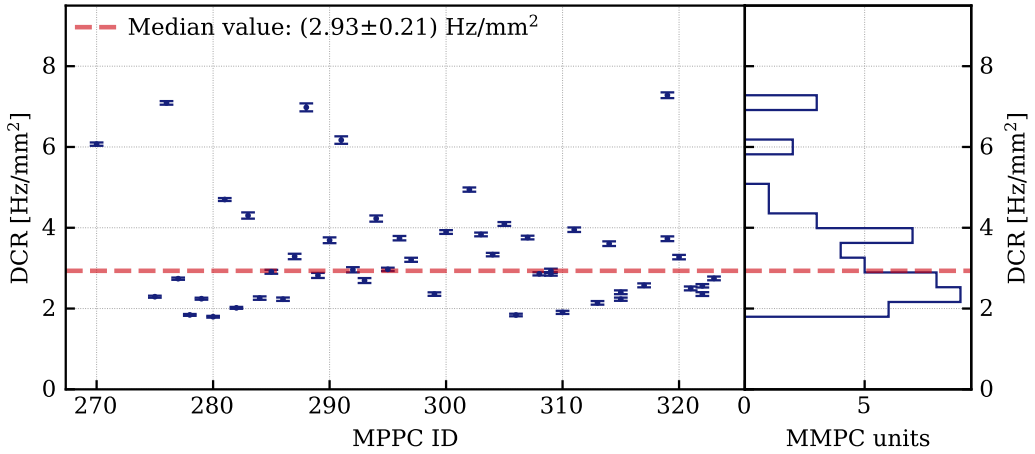

Figure 7.26.: Dark count rate values obtained for each of the $12 \times 12\,\mathrm{mm}^2$ units of Xenoscope and its overall distribution.

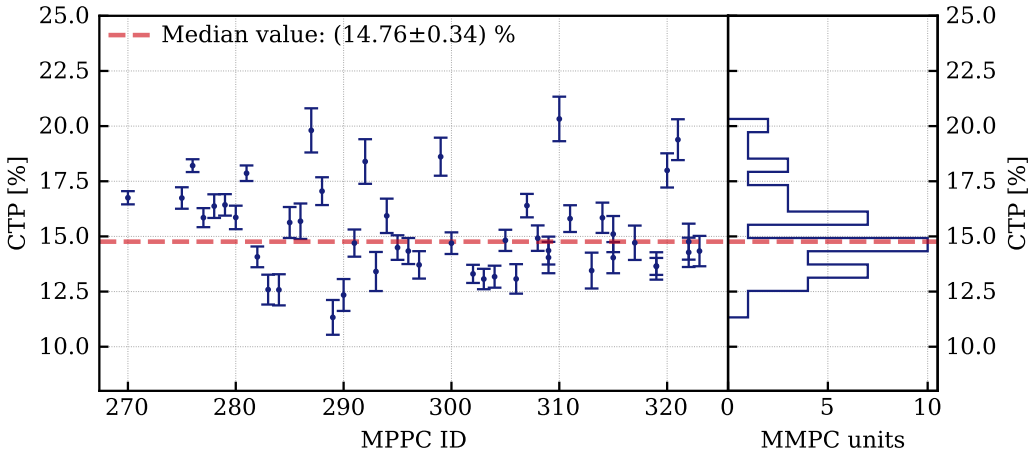

Figure 7.27.: Cross-talk probability values obtained for each of the $12 \times 12\,\mathrm{mm}^2$ units of Xenoscope and its overall distribution.

7.4. First commissioning results of the top array of Xenoscope

In the last quarter of 2022, the second phase of the Xenoscope project started as the TPC and its subsystems were prepared and assembled. As described in Chapter 6, this entailed a thorough cleaning campaign of the different detector parts, the installation of the liquid level monitoring system composed of three short level metres, two long level metres, and a weir, a new fibre feedthrough to host both the Xe lamp fibre and the

LED calibration fibre, the HV connection on the bottom of the vessel, and the assembly and mounting of four more field cage modules.

The top array, in particular, was removed from the test setup after the end of the characterisation campaign and completely disassembled for cleaning before its installation in the first module of the TPC. All the quad units were tested one last time in a dark environment at room temperature with the use of an LED, pulser, and oscilloscope. All sensors were confirmed to be working, except for MMPC number 321, which had previously been broken during testing. Stainless steel parts were cleaned in an ultrasonic bath submerged in a mixture of both ELMA65 soap and ethanol, consecutively, following the recipe used in [249], and wiped with ethanol-soaked low-shedding fibre wipes. The SiPMs' windows and packaging were wiped in the same manner with ethanol. The PCBs were rinsed with ethanol, dried with compressed air, and stored in clean anti-static bags. During the assembly of the first top module of the TPC, all the components were brought into the anti-dust room on the ground floor of the Xenoscope facility, and the array was assembled, including the wiring of the male side of the single-wire PTFE couplers, depicted in Figure 7.8. A four-eyes approach was followed to minimise the risk of miswiring or mislabelling certain cabling components that could endanger the SiPMs or the pre-amplifiers. Continuity checks with a multimeter were made throughout the process to validate the connections.

With the top array fully assembled, it was raised into place and secured to the six rods screwed into the top flange of the inner vessel. The connections of the single-wire and coaxial cables were done with the couplers described in Section 7.2, and the external breakout box was wired to connect the pre-amplifiers and SiPM units to the power supplies. The first set of commissioning tests and measurements was performed before the installation of the HV feedthrough, with just the outer vessel installed to provide a dark environment and allow for the pumping of the system to avoid moisture accumulation. Furthermore, since the setup would be open again for further sub-system installations, an LED was placed at the centre of the TPC, close to the array. The four remaining TPC modules were assembled in parallel in an on-site cleanroom and subsequently installed after the initial tests of the array discussed below.

The initial tests of the array installed in Xenoscope were not successful, indicating severe malfunctioning of the cabling. Some channels exhibited large amplitude noise uncorrelated to any light pulse from the LED, while others showed correlated pulses,

although with overly noisy baselines. In total, half of the channels showed promising behaviour, while for the other half, no proper signal was observed. The outer vessel was opened, and, after some connectivity debugging, several problems were identified and corrected. For the most part, the issue resided in four switched connections in the breakout box, which were not detected during assembly. In two other cases, the problem was traced back to a broken single-wire connector on the female side of a PTFE coupler for channel 08 (tile H) and a non-connected signal cable for channel 10 (tile K). At a second iteration, all the channels of the top array showed clear signals correlated to the LED light and were deemed working.

To further test the good-working state of all the channels of the array, two types of data were acquired:

- At a given bias voltage the LED pulse intensity was changed to test the sensors at different light levels;
- At a given LED intensity, the bias voltage was scanned over several values to calculate the breakdown voltage of photosensors and compare it with the room temperature specifications provided by the manufacturer.

No SPE or *fingerplot* could be investigated in the short time frame available for these initial tests, as the very high dark count rate at room temperature— 4 MHz/quad to 12 MHz/quad, leading to 64 MHz/tile to 192 MHz/tile— greatly complicates these tasks.

Waveforms for each of the tiles at different light levels for an applied bias voltage of 57 V and the response of the different tiles to a constant light level at different bias voltages are presented in Appendix C. It is clear that the tiles are fully working and that the signals resulting from the pulsed LED light are well-behaved. For some of the channels, saturation can be seen at high light levels. This effect is due to the limited range of the pre-amplifier response. As described in Section 7.3.1 and Figure 7.13, the amplitude as a function of the applied voltage of the photosensor at a constant light level can be used to determine the corresponding breakdown voltage by means of a linear fit. As a result, the calculated breakdown voltages are shown in detail in Figure 7.28 and Table 7.2. All the values are in agreement with the specifications from the manufacturer, which quote the breakdown voltage as (53 ± 5) V at 25 °C.

Table 7.2.: Breakdown voltages of each tile in the Xenoscope top array at room temperature.

Channel	Tile	BV [V]	Channel	Tile	BV [V]
01	A	52.98±0.16	07	G	53.07±0.11
02	B	53.24±0.38	08	H	52.95±0.12
03	C	53.18±0.18	09	J	53.03±0.09
04	D	53.19±0.19	10	K	53.05±0.15
05	E	53.02±0.15	11	L	53.00±0.22
06	F	53.16±0.15	13	M	52.94±0.20

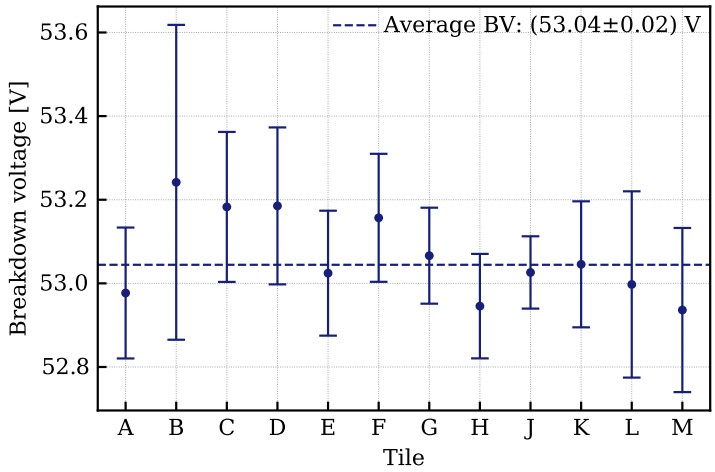

Figure 7.28.: Calculated breakdown voltages of the tiles at room temperature.

Together, the two measurements performed as of the writing of this thesis and reported above, provide broad evidence that all twelve channels of the top array of Xenoscope have been successfully installed and are properly working.

7.5. Top array signal simulation

Time projection chambers are known for providing good background discrimination. This is achieved both by good energy resolution, ER and NR discrimination from their S2/S1 ratio, and the discrimination of single and multiple-site events. As in the case of the distinction between neutrons and WIMP-candidate events or between spatially unresolved electrons and gammas close to the Q-value of the 0νbb of ^{136}Kr, spatial resolution plays an important role in background discrimination. Another example is

the identification of accidental coincidence events, for which the electron cloud size is used to classify the event as a true scatter or a wrongly reconstructed event, as detailed in Chapter 4.

Three effects are mostly responsible for limiting the spatial resolution achievable in a TPC: light sensor size and granularity, understanding of the electric field, and the intrinsic electron cloud diffusion process. While the first two are dependent on detector design and operational choices, the latter arises from the properties of electron transport in the given medium, namely liquid xenon. In next-generation large-scale detectors, such an effect can be ever more prevalent and limiting. Therefore, it is critical to study, precisely measure, and model the electron diffusion process to improve upon current spatial discrimination and know its limits.

Commonly measured electron transport properties are the electron drift speed, the electron cloud longitudinal diffusion, and the electron cloud transversal diffusion. In Xenoscope's first phase, where a liquid xenon purity monitor was operated, the two first properties were measured as a function of the drift field between 25 and 75 V and their results were briefly discussed in Chapter 6. However, the transversal diffusion constant in liquid xenon has only been measured at drift fields from 700 V cm^{-1} to 7.5 kV cm^{-1} [387,388] in $\leq$5 mm-drift apparatus and, more recently, by the EXO-200 experiment in a $\sim$20 cm-max drift length TPC, between 20 V cm^{-1} and 615 V cm^{-1} [167]. Existing measurements of the transversal diffusion coefficient are shown in Figure 7.29. With Xenoscope hosting a dual-phase TPC instrumented by an array of SiPMs, the measurement of transversal diffusion is one of the main studies in the pipeline for the near future.

To predict the expected signals at the SiPM array arising from ejected electrons at the photocathode with a flash of the xenon lamp, a simulation framework, XenoDiffusionScope [389], was developed. The framework provides the basis for the phenomenological study of electron longitudinal and transversal diffusion properties in the context of Xenoscope. The basic principles and steps of the simulation tool and its first results are described below.

The Xe lamp pulse and electron ejection

The triggered production of electrons in Xenoscope's TPC is due to flashing the light from a Xe lamp onto a gold-plated photocathode, as described in Chapter 6. The lamp

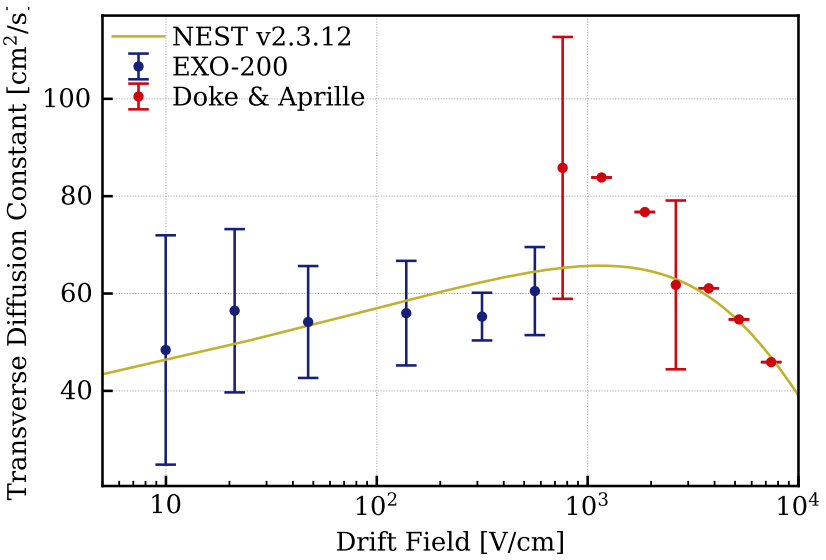

Figure 7.29.: Electron cloud transversal diffusion constant in liquid xenon as a function of the applied electric field. Measurements from EXO-200 (2017, [167], and earlier works by Doke, Aprille and collaborators [387,388] are shown. The parametric model used by the NEST software [157] is displayed in gold for version 2.3.12 (the latest at the time of this work). Figure adapted from [167].

emits a pulse of 1 J with a FWHM of 2.90 µs [355,356], which is modelled as a Gaussian distribution centred at 2.8 µs, as seen in Figure 7.30a. The initial positions of the electrons depend on the light-covered area of the photocathode, which is determined by the numerical aperture, NA, of the fibre and its distance to the surface, d_{pk}. For this work, a numerical aperture of 0.22 and a distance of 2 mm were used, based on the fibre type and assembly on the PM-phase. The initial positions of the electrons are distributed normally from the centre of the TPC at the $z = 0$ plane. The variance is given by the numerical aperture and fibre to photocathode distance, $\sigma = NA \cdot d_{pk}$. The number of electrons ejected during the pulse of the Xe flash lamp is scaled to the expected total number of electrons emitted by the photocathode for 1 J of deposited energy.

Drift and diffusion

Once created in the LXe volume, electrons are drifted from cathode to gate, experiencing longitudinal and transversal diffusion, whose constants are defined by the user. The diffusion processes alone are modelled as random walks with standard deviation D_L and D_T, for longitudinal and transversal diffusion, respectively. By the action

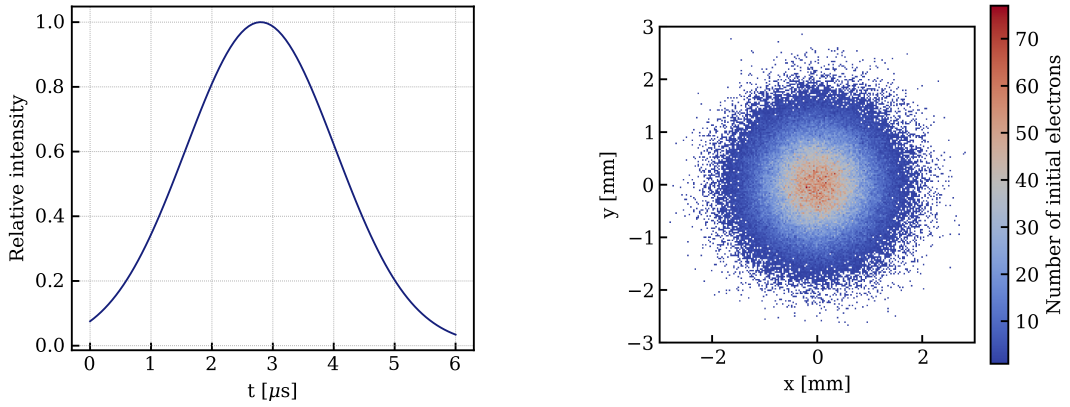

(a) (b)

Figure 7.30.: (a) Normalised time distribution of ejected electrons from the photocathode. **(b)** Initial position of the ejected electrons in the $z = 0$ plane for a full pulse of the lamp.

of the electric field approximated as uniform in the central region of the TPC, the mean position of charge in the z direction will move upwards at a rate of $\frac{dz}{dt} = v_{drift}$, while the x and y mean positions stays at 0. From a point-like source of N electrons, condensed at position $\vec{x} = (0, 0, 0)$ at $t = 0$, the charge density, $n(\vec{x}, t)$ after the time t is given by:

$$n(\vec{x}, t) = \frac{N}{4\pi D_T t \sqrt{4\pi D_L t}} \cdot e^{\frac{-\left(x^2+y^2\right)}{4D_T t}} \cdot e^{\frac{-(z-v_d t)^2}{4D_L t}}, \tag{7.14}$$

which describes the Gaussian diffusion of the charge distribution while drifting in the direction of positive z. The standard distribution of these Gaussian processes is given by $\sigma = \sqrt{2D_L t}$ for the longitudinal diffusion (in the z axis) and $\sigma = \sqrt{2D_T t}$ for the transversal diffusion (in the x and y ax2s).

However, due to the non-negligible space and time distributions of the ejected electrons, a full-track drift is simulated for each of the electrons in the cloud. The code has been optimised to execute each drift step for all the charges at once, greatly reducing the computing time required for the process to complete. At this stage, the boundaries of the TPC are taken into account and electrons reaching the defined maximum radius are not propagated and are considered lost. Upon reaching the gate's height, each electron's times and positions are recorded and the electron transport process stopped. The set of n surviving charges is corrected for electron lifetime, τ_e by randomly removing $n\left(1 - e^{-d_t/\tau_e}\right)$ electrons from the set, where d_t is the expected drift time of the electron cloud.

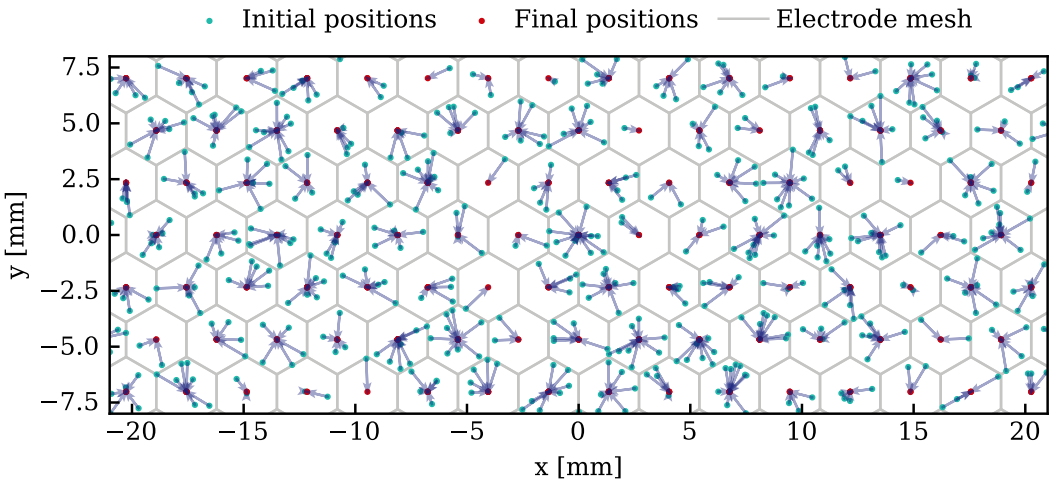

Figure 7.31.: Example of the gate electrode grid focusing effect, showing the position of 200 uniformly sampled electrons at the gate before (turquoise dots) and after (red dots) the focusing effect correction, which is shown as grey arrows.

Electron extraction

To model the extraction of charges from the liquid to the gas phase, two effects are considered: extraction efficiency and charge focusing by the electrode grids.

The extraction efficiency correction is performed similarly to the electron lifetime correction previously detailed, this time with the number of removed charges calculated as $1 - \eta_{eff}$, where η_{eff} is the extraction efficiency defined by the user. On the other hand, the focusing effect is more complex, as it depends on the geometry of the electrodes. In Xenoscope's TPC, the gate and anode electrodes are hexagonal meshes. From previous experience with similar grids [133, 168], it is expected that the electrons are focused to the closest centre of a hexagon of the gate. This effect is modelled by constructing the positions of the hexagons' centres given the grid properties defined by the user (hexagon side length, radius of the grid) and moving the electrons positioned within a given hexagon at the height of the gate to the centre of that hexagon. In practice, all the electron final positions are then constrained to the 2787 centres of the hexagonal grid. An example of this effect is shown in Figure 7.31, where the electron positions before and after the focusing effect correction are shown connected with an arrow.

LCE and scintillation signal production

With the electron extraction process modelled, the next step on the path to simulating waveforms and hit patterns on the top array is the proportional scintillation in the gas phase and geometrical effects on the light collection of the setup. Given the approach established, the final positions of the electrons after drift and extraction are limited to the number of hexagons in the gate grid. Therefore, the LCE maps of interest are only from photons produced at these positions. The approximation is made that any given electron is independent of other electrons in the cloud and that the emission of scintillation photons is isotropic at the final position of the electron in (x, y) and at the middle of the gas gap in z. Moreover, the photon yield of an extracted electron, also known as single electron gain or g2-value is taken as 28.57 PE/e^-, following the values measured in Xurich II [168].

For each centre of an hexagons, i, the pattern resulting from the isotropic emission of photons from the initial position (x_0, y_0, z_0) is computed as an individual LCE_i. The position, (x', y', z'), at which a straight ray crosses the array's plane, z', is given by:

$$\begin{cases} x' = x_0 + (z' - z_0)\cos\varphi\tan\theta \\ y' = y_0 + (z' - z_0)\sin\varphi\tan\theta \end{cases}, \tag{7.15}$$

where ϕ and θ are the azimuthal and polar angles, respectively.

Each LCE_i map is computed with 10^8 toy-photons, considering only angles on the z-positive part of the isotropic emission ($\theta \in [0; \frac{\pi}{2}]$ and $\phi \in [0; 2\pi[$). The maps are then normalised by the number of toy photons and smeared by a 2D interpolation function. The resulting map is the probability distribution function of a photon reaching the array at the position (x', y') from any of the hexagons' centres. In Figure 7.32, the different steps in constructing the LCE_i map for focus point number 2023 are shown.

For a particular signal with a final distribution of extracted electrons and their positions, the number of electrons in each grid focusing point is determined and the corresponding distribution of photons hitting the array is computed. This spatial distribution is given by the sum of all the individual LCE_i patterns, each scaled by the number of electrons counted on the corresponding hexagon centre. It follows that the number of photoelectrons expected in a given area, A, of the array is given by:

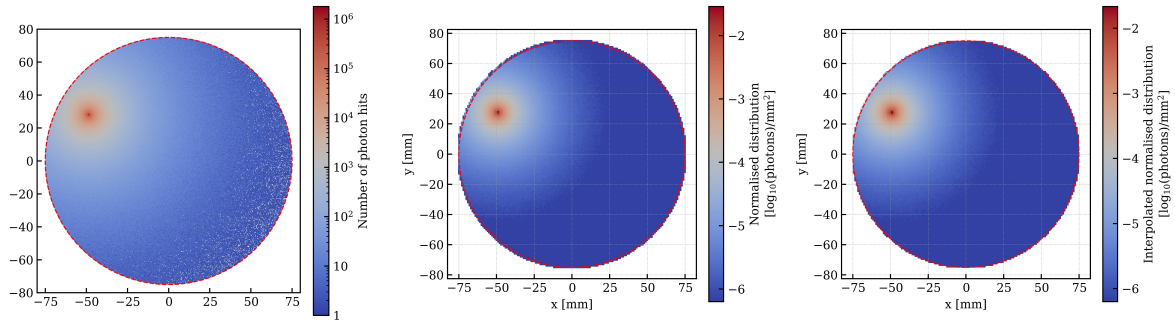

(a) (b) (c)

Figure 7.32.: Process of constructing an LCE map for focus point number 2023. The toy events simulated to construct the pattern (**a**), the event distribution normalised to the number of photons produced (**b**), and the final interpolated pattern to be used (**c**). The radially outer boundary of the TPC is shown as a solid red line.

$$N_{pe} = \sum_{i}^{n_{hex}} \int_{A} LCE_i\,(x,y)\,dxdy\ . \tag{7.16}$$

Signal on the top array of Xenoscope

Since the sensors have finite granularity and the geometrical coverage of the array is not 100%, the final hit pattern must take this into account. Following equation 7.16, the expected number of PE observed for a given active area defined and enclosed on the array can be computed. The specific physical parameters considered for the simulation are detailed in Table 7.3.

In the case of Xenoscope's top array, the sensor geometries of interest are combinations of the different possible granularities of the photosensors acquired, from $6 \times 6\,\mathrm{mm}^2$ active area units to the 24×24 mm^2 tiles with summed readout. Four geometries were coded for testing purposes: the tiled geometry with 12 tiles described in the previous sections and implemented for the first TPC run, a setup where all the $12 \times 12\,\mathrm{mm}^2$ -units are read individually, another where all the $6 \times 6\,\mathrm{mm}^2$ -units are read individually, and a hybrid solution with $6 \times 6\,\mathrm{mm}^2$ units in the centre and $12 \times 12\,\mathrm{mm}^2$ units in the rest of the array. Different geometries may easily be considered for future studies when optimising the array for the next data-taking campaign.

The resulting patterns arising from the simulation of a complete lamp pulse (1 J-mode) considering the different readouts are shown in Figure 7.33.

Table 7.3.: Physical parameters used in the signal simulations of a Xe lamp pulse ejecting electrons from the photocathode. Results shown in Figure 7.33

Parameter	**Unit**	**Value**
Electric drift field	V/cm	100
Electron drift speed	mm/µs	1.364
Longitudinal diffusion coefficient	$mm^2/µs$	0.0027
Transversal diffusion coefficient	$mm^2/µs$	0.0057
Electron lifetime	µs	2000
Extraction efficiency	%	99
Liquid gap (gate to interface)	mm	5
Gas gap (interface to anode)	mm	5

Qualitatively, it is clear that the granularity of the sensor readout scheme is of great importance for any study relying on $x - y$ position reconstruction or pattern recognition. In the tile readout, the two central tiles (F and G) are expected to observe ∼90 % of the total number of produced proportional scintillation photons, while the following two closest tiles (C and K) sum ∼5 % of the photon hits, and the rest of the tiles the remaining ∼5 %. The information available from the measured hit pattern is, therefore, very limited. Although with considerable improvement, the setup with only quads still shows a drop over two orders of magnitude from the centre sensors to the next ones in line.

In a final configuration, optimised for the measurement of transversal diffusion or other xy-pattern-dependent studies on the mm-scale, the photosensor configuration should consider higher granularity, such as a central area covered by $6 \times 6\,mm^2$ units, as tests in the Xurich II TPC. A hybrid solution, as shown in 7.33d, even with the inclusion of some tiles on the outer edges, would be a good compromise between high granularity in the centre and a manageable amount of channels and pre-amplifiers.

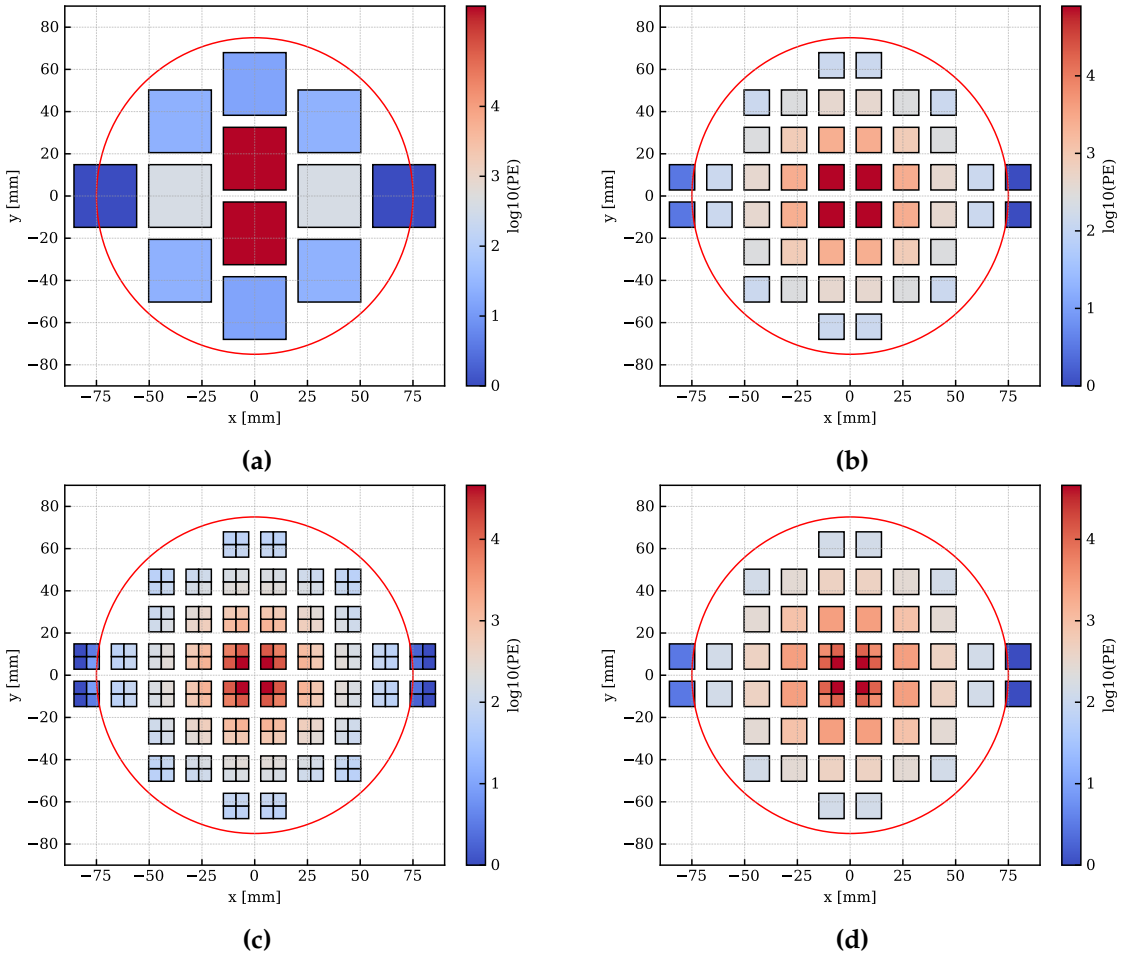

Figure 7.33.: Simulated hit patterns on the top array from a flash of the xenon lamp on the photocathode for different photosensor granularity: current configuration of 12 tiles (**a**), individual readout channel for each quad module (**b**) or $6 \times 6\,\mathrm{mm}^2$ units (**c**), and a hybrid configuration with both quad modules and individual $6 \times 6\,\mathrm{mm}^2$ units (**d**). The radially outer edge of the TPC is shown as a solid red line. The specific parameters used in the simulation are detailed in Table 7.3

Chapter 8.

Summary and conclusions

The existence of dark matter is supported by numerous cosmological and astrophysical evidence. Although not constrained to be a particle, if it is such, then observations point to a stable, non-luminous, non-baryonic unknown particle not described by the SM. Such a solution is widely studied, with particular attention to WIMPs.

The XENON dark matter project has been at the front-end of direct detection of particle dark matter above $\sim 6\,\mathrm{GeV/c^2}$ since 2006. With its first three LXe dual-phase TPCs (XENON10, XENON100, XENON1T), the upper limit on SI WIMP-nucleus was constrained by more than four orders of magnitude. In 2020, the fourth detector of the XENON project, XENONnT, was assembled and commissioned. Surrounded by the muon and neutron veto, the TPC of XENONnT instruments a 5.9 t active target. Updates to the facility infrastructure provide lower impurity levels (through liquid xenon purification) and lower ^{222}Rn concentration (material selection radon, radon distillation column and magnetically-coupled piston pumps in gas recirculation instead of previously used pump solutions).

To characterise the electric field inside the TPC, a full 3D electrostatic field simulation was developed. The framework, which was used to simulate the fields expected from the nominal configuration of XENONnT, includes the 3D geometry of the TPC, charge-density computation with BEM solvers, and subsequent analysis of the calculated fields. The results obtained provide motivation for further development of the technique, in particular for regions of the TPC where the inherently 3-dimensional geometry complexity disallows the use of 2D axial-symmetric simulations, such as the perpendicular wires region. The results were used to study this region and define the near- and far-wire sections of the detector. Later these were updated from data-driven methods. As discussed in the Outlook of Chapter 3 (Section 3.4), in order to reliably

conduct further studies on 3D field simulation, the current framework adapted from Kassiopeia needs robust development or a different solution to be found. Desired features, such as setting constraints on the charge distribution in addition to the voltage of electrodes in order to simulate surface charge-up, is currently not available in the framework and would require further development.

The data acquired by XENONnT between July and November of 2021 constitutes its first science run. SR0 pursued two main science searches: low-energy ER search in order to investigate the excess of events observed in XENON1T below 10 keV, and low-energy NR search to find or constrain WIMP interactions. The data analysis of XENONnT is a complex task and a common effort of the collaboration. Given the low-field conditions of SR0 and the presence of a portion of the active volume influenced by the perpendicular wires, the accidental-coincidence-suppressing event selection criteria are essential. One of the cuts specifically targeting this irreducible background is the S2 width cut. This cut was developed both on data and signal simulations, and tested against data for the calculation of signal acceptance. The cut models the width of the S2 signals as a function of their area and drift time, yielding $\sim$99 % signal acceptance (with lower acceptance at lower S2 signal areas) and $\sim$82.5 % AC events rejection. The cut was determinant on correctly removing background events in both the ROI of the low-energy ER and low-energy NR searches. After unblinding, no excess of low-energy ER events was found, excluding any BSM physics interpretations of the XENON1T excess. More stringent upper limits on solar axions, bosonic DM, and solar neutrinos with an enhanced magnetic moment were set as a result. Moreover, as a consequence of all the radon background mitigation techniques employed, XENONnT achieved the lowest level of ER background rate between 1 and 30 keV of any LXe TPC, measuring $(15.8 \pm 1.3)\,\mathrm{events}/(\mathrm{t}\cdot\mathrm{y}\cdot\mathrm{keV})$. Similarly, no excess was found when unblinding the low-energy NR search data and new upper limits were set for both SI and SD WIMP-nucleon interactions. The lowest upper limit observed for SI WIMP-nucleon interaction cross-section was $2.58 \times 10^{-47}\,\mathrm{cm}^2$ for a WIMP mass of $28\,\mathrm{GeV}/\mathrm{c}^2$.

Apart from DM, the large active target of XENONnT makes it an interesting neutrino observatory for astrophysical neutrinos, in particular ^{8}B solar neutrinos and neutrinos emitted by galactic SNe. Addressing the latter, the emitted neutrinos have energies of $\mathcal{O}(10)$ MeV and mainly interact via CEvNS. As a flavour-insensitive process, measurement of the neutrino luminosity curve in XENONnT and similar detectors allows for the reconstruction of the total neutrino energy emitted in the SN process, un-

like anti-electron neutrino-based detections. A framework was developed to accurately simulate the neutrino signals in the TPC, given a certain neutrino luminosity curve. Moreover, to increase the SNe detection capabilities, a set of background-reducing cuts was formulated, focusing on the single and few-electrons regime, where the signal is concentrated. After cuts, XENONnT is able to detect an average of 137 ± 5 events from a SN progenitor of 27 $M_\odot$ at 10 kpc, approximately ten times above background level. The detector is able to positively identify SNe up to $\sim$30 kpc with 3 σ significance. In the next generation of LXe dual-phase TPCs, profiting from larger active volumes between 40 and 100 t, the detection reach will double the one registered in XENONnT assuming the same background conditions or increase four-fold if backgrounds at the few-electron level can be suppressed ten-fold (to $\sim$115 kpc for a 60 t active target). XENONnT capabilities to significantly detect galactic SNe, albeit with less reach and significance as dedicated neutrino experiments, provide a good addition to the SNEWS network. The structure of an active SNe trigger was defined and developed, including the addition of GPS absolute timestamps to the events reconstructed in the TPC. The active trigger software will be completed and deployed in the near future, ultimately connecting XENONnT to SNEWS.

As a natural successor to XENONnT, DARWIN is a planned dark matter and neutrinos observatory using the LXe dual-phase TPC concept. The baseline design of DARWIN entails a TPC of 2.6 m diameter and height with a planned active target of 40 t. Its primary science objective is to probe the cross-section of the interaction between WIMPs and nucleons with a sensitivity on SI WIMP-nucleon cross-section reaching down to $\sim 10^{-49}$cm^2. Xenoscope was built at the University of Zurich to test the several challenges of a 2.6 m-high TPC and demonstrate the feasibility of electron drift at such unprecedented length. After an initial commissioning run in 2021, a 53 cm purity monitor setup was assembled and operated in 2022. The electron lifetime was measured during 89 days with three different xenon recirculation speeds and a model was fitted to the acquired data. Electron transport studies were also conducted at different drift fields, namely on electron drift velocity and electron longitudinal diffusion.

In the next phase of the Xenoscope project, the PM is replaced by a 2.6 m dual-phase TPC. Among the required updates, the signal readout changes from charge- to light-based. A SiPM array was designed to be placed on the top of the xenon column and detect the secondary scintillation signals from the TPC. The array has twelve summed readout "tiles", each instrumented with four 12×12 mm^2 SiPM units (S13371-6050CQ-

02 MPPCs from Hamamatsu). To each tile corresponds one single signal channel. The necessary cabling and light calibration system were planned and assembled in the Xenoscope facility. In parallel, a characterisation campaign was performed to test and benchmark all the SiPM units used in the array. A data-taking and analysis framework was developed for this task, calculating breakdown voltage, gain, SPE resolution, DCR, and CTP for each unit. For the 50 tested sensors, the median values observed for each of these properties were, respectively, (47.08 ± 0.02) V, $(3.02 \pm 0.02) \times 10^6$, (4.38 ± 0.08) %, $(2.93 \pm 0.21)\,\mathrm{Hz\,mm^{-2}}$, and (14.76 ± 0.34) During the characterisation campaign, the summed readout was also tested and its performance was compared with the readout of a single unit. The striking difference is in SPE resolution, which worsens by a factor of two (from (3.90 ± 0.06) % on a $12 \times 12\,\mathrm{mm^2}$ unit to (7.78 ± 0.51) % in a tile), although still better than the values registered in PMTs (20 to 30 %). The array was assembled in the TPC of Xenoscope at the end of 2022 and the first data in vacuum show that all twelve channels are working properly.

A toy-Monte Carlo simulation framework was developed to study the expected signals in Xenoscope and inform future choices on the optimisation of the array granularity. The framework simulates the drift and extraction of electrons, as well as the focusing effect observed in hexagonal meshes. The software can be used to test different configurations and granularity of the sensors on the SiPM array and different operation conditions, such as electron lifetime, extraction efficiency, and drift field.

The search for dark matter is an exciting and fast-moving field, one where the XENON detector always took the lead. The low background level achieved by the XENONnT detector is a good omen to the progress in each generation of dual-phase LXe TPCs and the potential physics they may find. And whether or not a dark matter particle is detected, it is certain that sooner or later a galactic SN is bound to happen and XENONnT is ready to explore the possibilities that such observation entails. Looking further ahead, attempting to reach where no sole collaboration could go alone, the XLZD consortium [122] joins together the XENON, LZ, and DARWIN collaborations on a long winding road to the next-generation liquid xenon observatory for dark matter and neutrino physics [325].

Appendix A.

Pre-amplification circuit for the "tile" summed readout

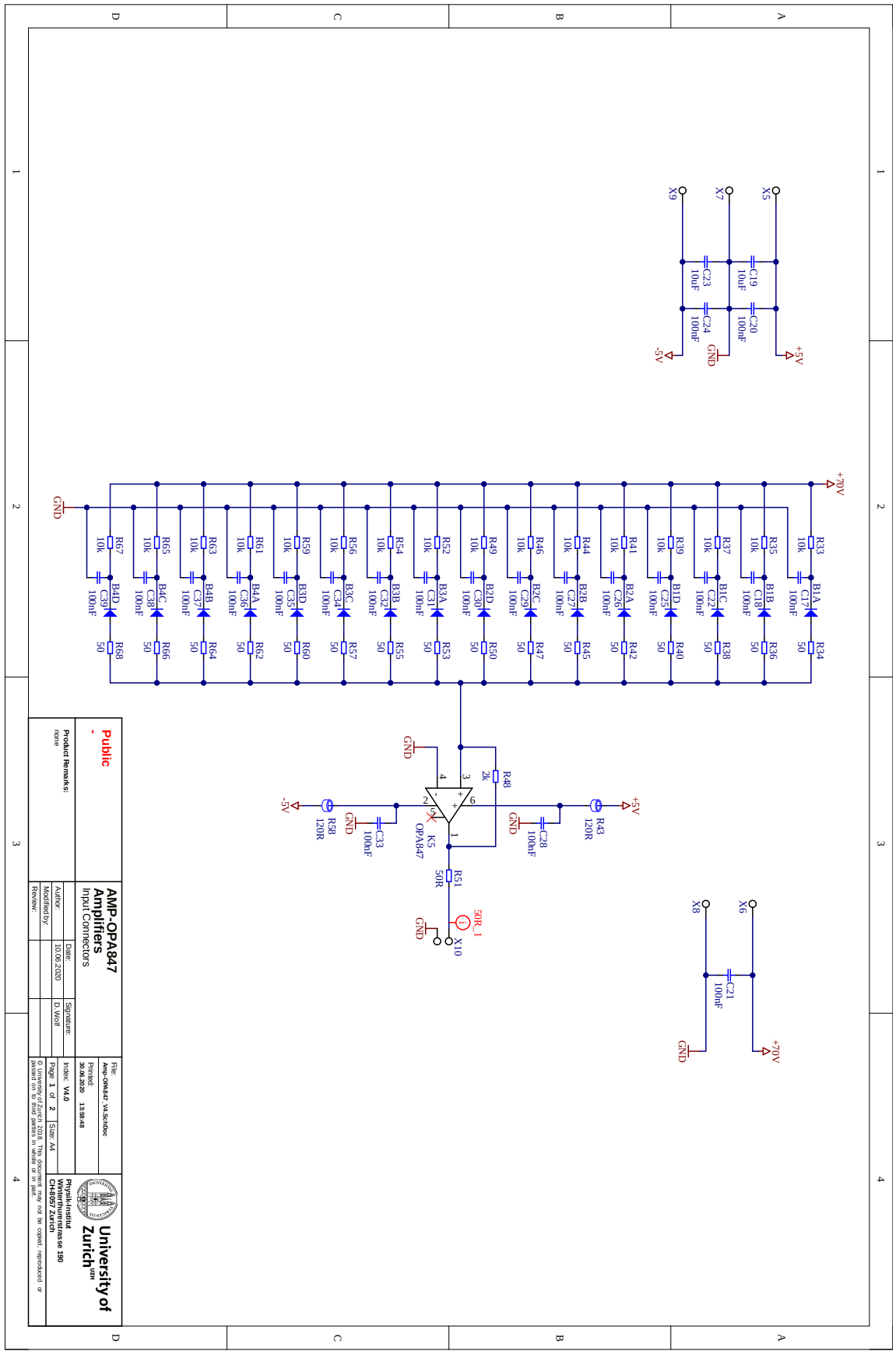

Figure A.1.: Circuit design for the pre-amplification stage of the "tile" summed readout of the top SiPM array of Xenoscope. Circuit from David Wolf based on [373].

Appendix B.

Main characterisation values of the SiPM units of Xenoscope

In order to validate and benchmark the sensors used in the top SiPM array of Xenoscope, a characterisation campaign of all the units was conducted. Details on the campaign, the test setup and its results can be found in Section 7.3. The numerical values obtained for the breakdown voltage of all the tested $12 \times 12\,\mathrm{mm}^2$ units are shown in Table B.1. Table B.2 details the gain, SPE resolution, DCR, and CTP for all the $12 \times 12\,\mathrm{mm}^2$ units tested at 190 K and with a bias voltage of 52 V. As an analogous table could be presented for all the other bias voltages tested (49 to 50 V), 52 V was chosen because it provides a standard gain of $\sim 3 \times 10^6$.

Table B.1.: Breakdown voltage of each $12 \times 12\,\mathrm{mm}^2$ unit tested for Xenoscope. Values shown for 170 K, 180 K and 190 K, when available. Some runs were performed only at 190 K, as this is the expected temperature at the gas phase of the Xenoscope, where the MPPC units stand. Graphic representation and discussion in Chapter 7.

MPPC#	170 K	180 K	190 K
270	45.83±0.034	46.25±0.039	46.77±0.031
275	45.82±0.027	46.75±0.167	46.73±0.031
276	46.00±0.112	46.79±0.307	46.90±0.098
277	45.85±0.033	46.63±0.263	46.82±0.038
278	45.93±0.024	46.79±0.285	46.91±0.030
279	46.09±0.024	47.00±0.542	47.09±0.037

MPPC#	BV at 170K [V]	BV at 180K [V]	BV at 190K [V]
280	45.98±0.038	46.96±0.178	46.97±0.039
281	46.02±0.097	46.80±0.334	46.84±0.035
282	46.19±0.029	46.52±0.042	47.19±0.054
283	—	46.53±0.038	47.13±0.031
284	—	—	47.19±0.023
285	—	—	47.13±0.020
286	—	—	47.13±0.022
287	—	46.67±0.041	47.31±0.059
289	—	46.58±0.040	47.17±0.039
290	—	46.71±0.040	47.26±0.031
291	—	46.56±0.041	47.11±0.037
292	—	46.49±0.061	47.04±0.040
293	—	46.46±0.037	47.05±0.036
294	—	46.58±0.045	47.08±0.042
295	—	—	47.02±0.046
296	—	—	47.08±0.023
297	—	—	46.95±0.026
299	—	—	47.04±0.021
300	—	—	47.30±0.052
303	—	—	47.19±0.042
304	—	—	47.06±0.046
305	—	—	47.07±0.046
306	—	—	46.93±0.046
307	—	—	47.07±0.047
308	—	—	47.04±0.048
309	—	—	46.90±0.027
309	—	—	47.08±0.025

MPPC#	BV at 170K [V]	BV at 180K [V]	BV at 190K [V]
310	—	—	46.97±0.010
310	—	—	47.27±0.020
311	—	—	47.19±0.019
313	—	—	47.06±0.027
314	—	—	47.12±0.028
314	—	—	47.19±0.022
315	—	—	47.26±0.028
315	—	—	47.13±0.036
317	—	—	47.06±0.029
317	—	—	47.29±0.021
319	—	—	46.98±0.037
319	—	—	47.18±0.026
320	—	—	47.03±0.037
320	—	—	47.23±0.022
321	—	—	46.94±0.033
322	—	—	47.13±0.034
322	—	—	47.25±0.023
323	—	—	47.11±0.022

Table B.2.: Computed values for Gain, SPE resolution, DCR, and CTP values of the Xenoscope quad modules at 190 K and bias voltage of 52 V. Graphic representation and discussion in Chapter 7.

MPPC#	**Gain /10^6**	**SPE$_{res}$** [%]	**DCR** [Hz/m^2]	**CTP** [%]
270	3.279±0.001	4.18±0.05	6.07±0.04	16.7±0.29
275	3.335±0.002	4.58±0.06	2.29±0.02	16.7±0.48
276	3.264±0.001	3.44±0.04	7.09±0.04	18.2±0.29
277	3.152±0.001	4.54±0.04	2.73±0.02	15.8±0.43

MPPC#	Gain /10^6	SPE_{res} [%]	DCR [Hz/m^2]	CTP [%]
278	3.119±0.001	3.91±0.04	1.84±0.02	16.3±0.53
279	3.076±0.001	4.39±0.04	2.24±0.02	16.4±0.48
280	3.204±0.002	4.42±0.06	1.79±0.02	15.8±0.53
281	3.156±0.001	3.79±0.04	4.69±0.03	17.8±0.35
282	2.887±0.001	5.18±0.06	2.01±0.02	14.0±0.47
283	3.007±0.002	4.49±0.07	4.30±0.07	12.5±0.67
284	3.059±0.002	4.60±0.07	2.25±0.04	12.5±0.70
285	3.064±0.001	3.79±0.06	2.90±0.04	15.6±0.70
286	2.983±0.001	4.23±0.06	2.23±0.04	15.6±0.80
287	2.935±0.004	5.45±0.13	3.28±0.06	19.8±1.00
288	2.949±0.002	4.40±0.07	6.98±0.09	17.0±0.63
289	2.872±0.002	4.34±0.07	2.81±0.06	11.3±0.78
290	2.853±0.001	4.75±0.06	3.69±0.07	12.3±0.72
291	2.994±0.001	3.76±0.04	6.17±0.09	14.6±0.61
292	3.053±0.003	4.46±0.11	2.95±0.06	18.3±1.01
293	3.017±0.002	4.08±0.09	2.69±0.06	13.4±0.88
294	2.858±0.002	4.96±0.07	4.22±0.07	15.9±0.77
295	3.041±0.002	4.68±0.07	2.97±0.04	14.4±0.55
296	3.005±0.001	3.96±0.05	3.74±0.05	14.3±0.58
297	3.138±0.001	3.91±0.05	3.20±0.05	13.7±0.62
299	3.212±0.003	3.98±0.10	2.35±0.04	18.6±0.86
300	2.935±0.001	4.78±0.05	3.89±0.04	14.6±0.49
302	2.966±0.001	4.38±0.04	4.94±0.05	13.3±0.41
303	2.874±0.001	4.11±0.04	3.83±0.04	13.0±0.46
304	2.970±0.001	4.25±0.04	3.33±0.04	13.1±0.49
305	3.025±0.001	4.14±0.04	4.09±0.04	14.8±0.48
306	3.154±0.001	4.01±0.05	1.84±0.03	13.0±0.66

MPPC#	**Gain /10^6**	**SPE_{res}** [%]	**DCR** [Hz/m^2]	**CTP** [%]
307	2.984±0.001	4.73±0.05	3.75±0.04	16.3±0.53
308	2.916±0.001	4.84±0.06	2.85±0.03	14.9±0.57
309	3.073±0.001	4.09±0.05	2.85±0.04	14.3±0.63
309	3.175±0.002	4.43±0.06	2.93±0.05	14.0±0.71
310	3.136±0.002	4 48±0.09	1.00±0.03	20.3±1.00
311	2.867±0.001	4.75±0.06	3.95±0.05	15.8±0.60
313	3.105±0.002	4.46±0.08	2.14±0.04	13.4±0.81
314	3.008±0.002	4.06±0.06	3.60±0.05	15.8±0.68
315	2.948±0.002	4 60±0.07	2.00±0.03	14.0±0.70
315	2.943±0.002	4.18±0.07	2.40±0.04	15.1±0.81
317	3.013±0.002	4.18±0.06	2.57±0.04	14.7±0.77
319	2.967±0.001	3 60±0.03	7.00±0.07	13.6±0.38
319	3.119±0.001	4.12±0.05	3.72±0.05	13.6±0.62
320	3.134±0.003	4.44±0.09	3.27±0.05	17.9±0.77
321	2.105±0.002	4 38±0.08	2.00±0.04	19.3±0.92
322	2.882±0.002	5.17±0.09	2.35±0.04	14.7±0.81
322	2.891±0.001	3.97±0.05	2.56±0.04	14.2±0.66
323	3.079±0.002	4.33±0.08	2.74±0.04	14.3±0.68

Appendix C.

SiPM data in air

In the last quarter of 2022, several upgrades were implemented in Xenoscope to operate a dual-phase LXe TPC. One of them was the installation of the top SiPM array, described in Chapter 7. Right after installation, two tests were performed at room temperature, before pumping out the vessels:

- At a constant bias voltage, applying different light levels. This dataset is used to observe the pulse shape of the different tiles when exposed to different light intensities.
- At a constant light level, applying a range of bias voltages. This dataset is used to calculate the breakdown voltage of each tile;

Figures C.1 and C.2 denote the obtained results from these first commissioning tests. Further details can be found in Section 7.4 of Chapter 7.

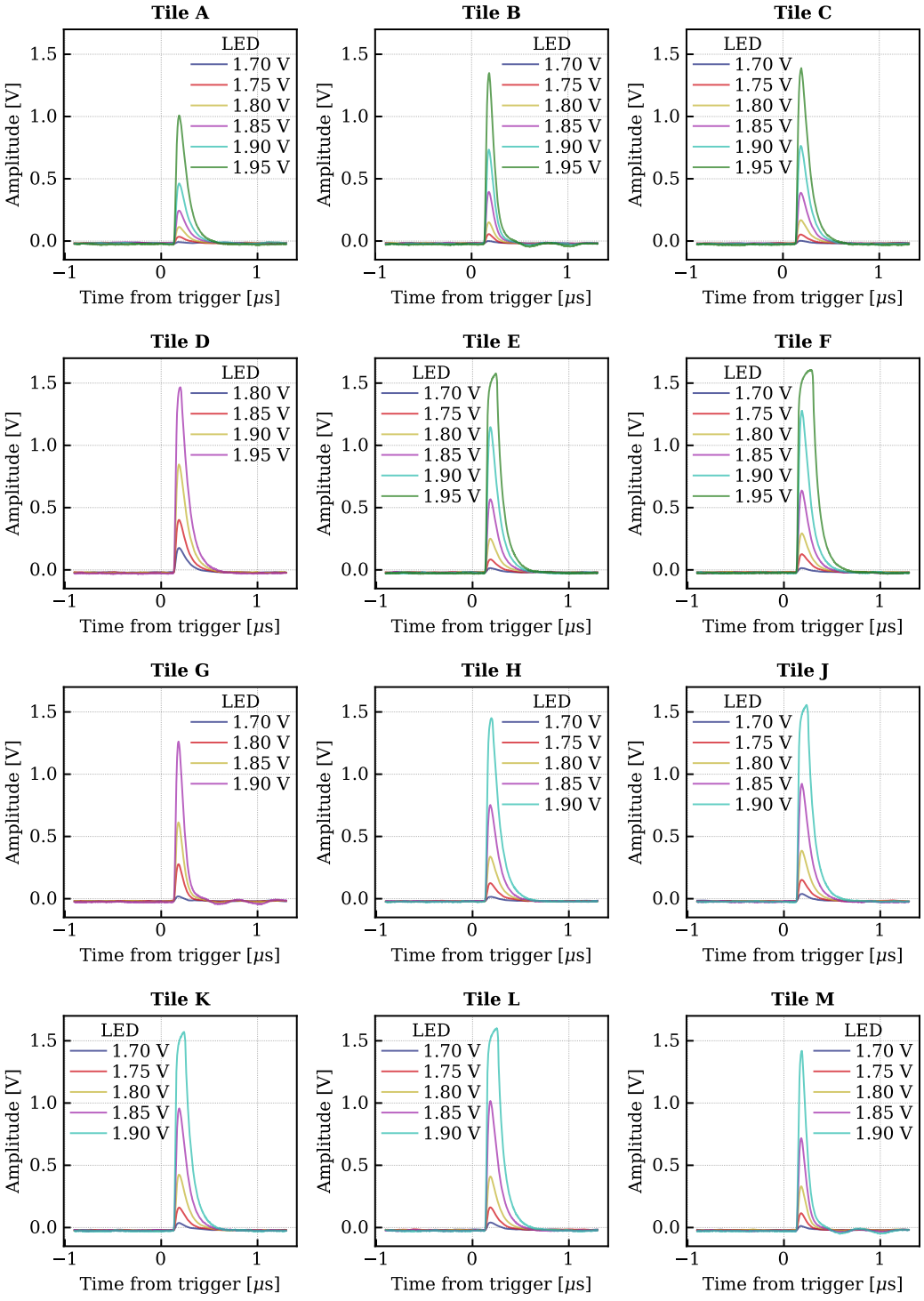

Figure C.1.: Waveforms for different light levels in each tile.

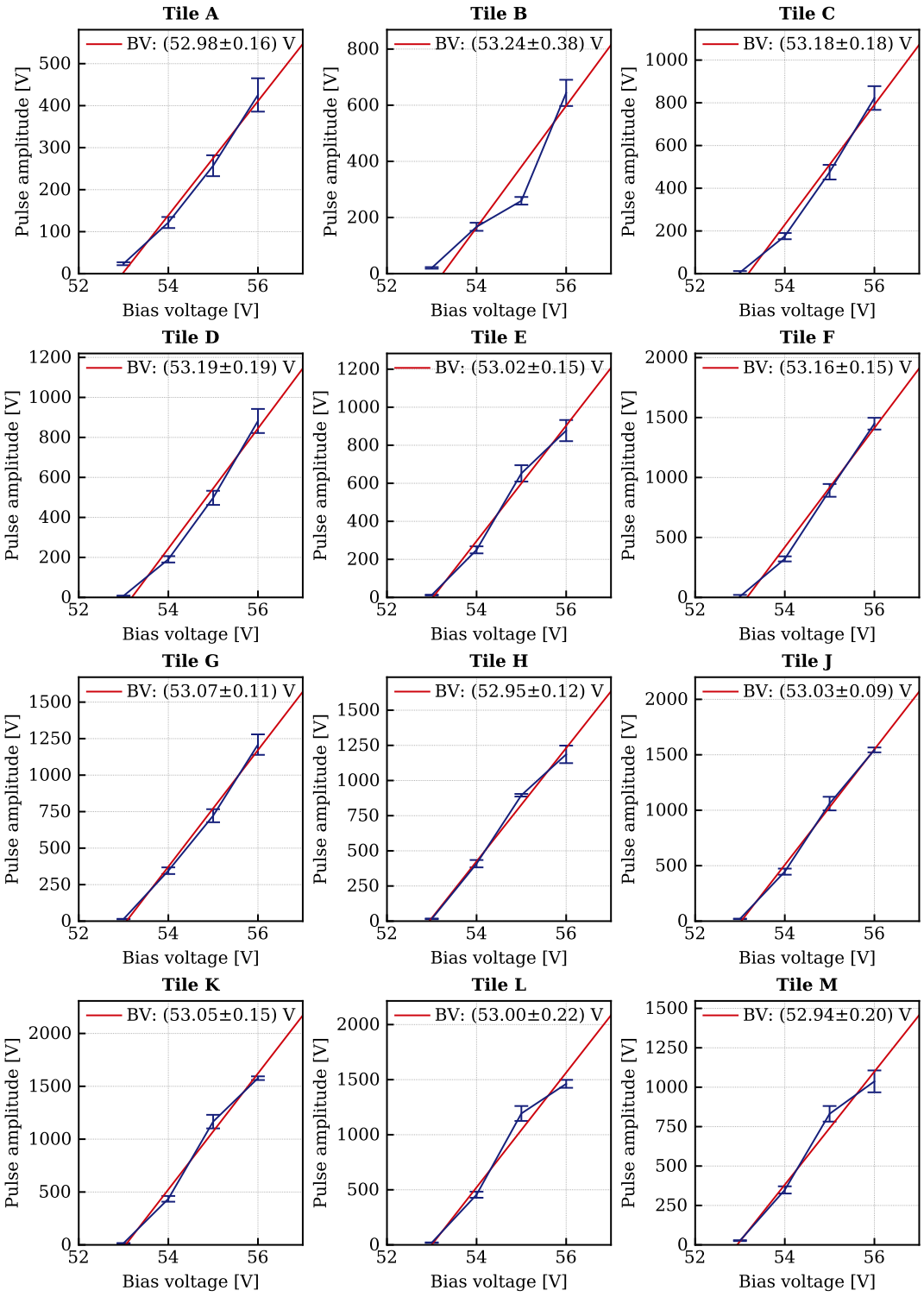

Figure C.2.: Amplitude of signal at different voltages with constant light level (LED V = 12 345 V.

List of figures

List of tables

List of abbreviations

ΛCDM Λ cold dark matter

AC accidental coincidence

ADC analogue-to-digital converter

AFT area fraction top

ALP axion-like particle

APD avalanche photodiode

ASCII American Standard Code for Information Interchange

ASU air separation unit

BDT Boosted Decision Tree

BEM Boundary Element Method

BH black hole

BoX Ball of Xenon

BSM beyond the Standard Model

BV breakdown voltage

CAD computer-aided design

CC charged-current

CEνNS coherent elastic neutrino-nucleus scattering

CMB Cosmic Microwave Background

CNN Convolutional Neural Network

CP charge-conjugation parity

CTP cross-talk probability

DAQ data acquisition

DARWIN DARk matter WImp search with liquid xenoN

DCR dark count rate

DM dark matter

eCT external cross-talk

EM electromagnetic

EOS equation of state

ER electronic recoil

fCT feedback cross-talk

FEM Finite Element Method

FSR field shaping ring

FV fiducial volume

GAPD Geiger-mode APD

GCN Graph Convolutional Network

GdWPS gadolinium water purification system

GPS global positioning system

GPU Graphics Processing Unit

GXe gaseous xenon

HV high-voltage

iCT internal cross-talk

JIT just-in-time

LArS Liquid Argon Setup

LCE light collection efficiency

LED Light-Emitting Diode

LHC Large Hadron Collider

LLM long level meter

LMC Large Magellanic Cloud

LN_2 liquid nitrogen

LNGS Laboratori Nazionali del Gran Sasso

LXe liquid xenon

LY light yield

MACHO massive astrophysical compact halo object

MC Monte Carlo

MLP Multilayer Perceptron

MPPC Multi-Pixel Photon Counter

MSW Mikheyev–Smirnov–Wolfenstein

MV muon veto

NBC Naive Bayes Classifier

NC neutral-current

NEST Noble Element Simulation Technique

NIR near infrared

NLO next-to-leading order

NR nuclear recoil

NS neutron star

nV neutron veto

OFHC oxygen-free high thermal conductivity

PAI polyamide-imide

PCB printed circuit boards

PDE photon detection efficiency

PE photoelectron

PID Proportional–Integral–Derivative

PM purity monitor

PMT photomultiplier tube

PSD pulse shape discrimination

PSI Paul Scherrer Institute

PTFE polytetrafluoroethylene

PTR pulse tube refrigerator

QE quantum efficiency

RGMS rare gas mass spectroscopy

RMS root mean square

ROI region of interest

RTD resistor temperature detector

SC slow control

SD spin-dependent

SE single electron

SI spin-independent

SiPM silicon photomultiplier

SLM short level meter

slpm standard litres per minute

SM Standard Model of particle physics

SN supernova

SNEWS Supernova Early Warning System

SPAD single photon avalanche diode

SPE single photoelectron

TPC time projection chamber

TTL transistor–transistor logic

UV ultraviolet

VUV vacuum ultraviolet

WIMP weakly interacting massive particle

ZLE zero length encoding

Bibliography

[1] J. Wulf, *Electrostatic field simulations and low-temperature measurements for a xenonbased dual-phase noble gas dark matter detector.*, Master's thesis, Karlsruhe Institute of Technolgy, Germany, 2014.

[2] D. Furse et al., *Kassiopeia: A Modern, Extensible C++ Particle Tracking Package*, *New J. Phys.* **19** (2017) 053012 [1612.00262].

[3] PLANCK collaboration, *Planck 2018 results. VI. Cosmological parameters*, *Astron. Astrophys.* **641** (2020) A6 [1807.06209].

[4] B. Thomson and W. Kelvin, *Baltimore Lectures on Molecular Dynamics and the Wave Theory of Light*, Cambridge Library Collection - Physical Sciences, Cambridge University Press (2010 (first edition 1904)), 10.1017/CBO9780511694523.

[5] H. Poincaré, *La Voie lactée et la théorie des gaz*, *Bulletin de la Société astronomique de France* **20** (1906) 153.

[6] J.C. Kapteyn, *First Attempt at a Theory of the Arrangement and Motion of the Sidereal System*, *Astrophys. J.* **55** (1922) 302.

[7] J.H. Oort, *The force exerted by the stellar system in the direction perpendicular to the galactic plane and some related problems*, *Bulletin of the Astronomical Institutes of the Netherlands* **6** (1932) 249.

[8] F. Zwicky, *Die Rotverschiebung von extragalaktischen Nebeln*, *Helv. Phys. Acta* **6** (1933) 110.

[9] H. Katayama and K. Hayashida, *X-ray study of the dark matter distribution in clusters of galaxies with chandra*, *Adv. Space Res.* **34** (2004) 2519 [astro-ph/0405363].

[10] R. Massey, T. Kitching and J. Richard, *The dark matter of gravitational lensing*, *Rept.*

Prog. Phys. **73** (2010) 086901 [1001.1739].

[11] D. Clowe, M. Bradac, A.H. Gonzalez, M. Markevitch, S.W. Randall, C. Jones et al., *A direct empirical proof of the existence of dark matter*, *Astrophys. J. Lett.* **648** (2006) L109 [astro-ph/0608407].

[12] J. Merten et al., *Creation of cosmic structure in the complex galaxy cluster merger Abell 2744*, *Mon. Not. Roy. Astron. Soc.* **417** (2011) 333 [1103.2772].

[13] A.N. Taylor, S. Dye, T.J. Broadhurst, N. Benitez and E. van Kampen, *Gravitational lens magnification and the mass of Abell 1689*, *Astrophys. J.* **501** (1998) 539 [astro-ph/9801158].

[14] A. Mahdavi, H.y. Hoekstra, A.y. Babul, D.y. Balam and P. Capak, *A Dark Core in Abell 520*, *Astrophys. J.* **668** (2007) 806 [0706.3048].

[15] V.C. Rubin and W.K. Ford, Jr., *Rotation of the Andromeda Nebula from a Spectroscopic Survey of Emission Regions*, *Astrophys. J.* **159** (1970) 379.

[16] K.C. Freeman, *On the disks of spiral and SO Galaxies*, *Astrophys. J.* **160** (1970) 811.

[17] Y. Sofue and V. Rubin, *Rotation curves of spiral galaxies*, *Ann. Rev. Astron. Astrophys.* **39** (2001) 137 [astro-ph/0010594].

[18] K.G. Begeman, A.H. Broeils and R.H. Sanders, *Extended rotation curves of spiral galaxies: Dark haloes and modified dynamics*, *Mon. Not. Roy. Astron. Soc.* **249** (1991) 523.

[19] A.A. Penzias and R.W. Wilson, *A Measurement of excess antenna temperature at 4080-Mc/s*, *Astrophys. J.* **142** (1965) 419.

[20] D.J. Fixsen, *The Temperature of the Cosmic Microwave Background*, *Astrophys. J.* **707** (2009) 916 [0911.1955].

[21] C.L. Bennett, A. Banday, K.M. Gorski, G. Hinshaw, P. Jackson, P. Keegstra et al., *Four year COBE DMR cosmic microwave background observations: Maps and basic results*, *Astrophys. J. Lett.* **464** (1996) L1 [astro-ph/9601067].

[22] W. Hu and S. Dodelson, *Cosmic Microwave Background Anisotropies*, *Ann. Rev. Astron. Astrophys.* **40** (2002) 171 [astro-ph/0110414].

[23] A. Liddle, *An introduction to modern cosmology*, John Wiley & Sons (2015).

[24] PLANCK collaboration, *Planck 2015 results. XI. CMB power spectra, likelihoods, and robustness of parameters*, *Astron. Astrophys.* **594** (2016) A11 [1507.02704].

[25] WMAP collaboration, *Nine-Year Wilkinson Microwave Anisotropy Probe (WMAP) Observations: Cosmological Parameter Results*, *Astrophys. J. Suppl.* **208** (2013) 19 [1212.5226].

[26] WMAP collaboration, *Nine-Year Wilkinson Microwave Anisotropy Probe (WMAP) Observations: Final Maps and Results*, *Astrophys. J. Suppl.* **208** (2013) 20 [1212.5225].

[27] PLANCK collaboration, *Planck 2018 results. VII. Isotropy and Statistics of the CMB*, *Astron. Astrophys.* **641** (2020) A7 [1906.02552].

[28] J.L. Feng, *Dark Matter Candidates from Particle Physics and Methods of Detection*, *Ann. Rev. Astron. Astrophys.* **48** (2010) 495 [1003.0904].

[29] E. Morgante, *Simplified Dark Matter Models*, *Adv. High Energy Phys.* **2018** (2018) 5012043 [1804.01245].

[30] M. Davis, G. Efstathiou, C.S. Frenk and S.D.M. White, *The Evolution of Large Scale Structure in a Universe Dominated by Cold Dark Matter*, *Astrophys. J.* **292** (1985) 371.

[31] B. Audren, J. Lesgourgues, G. Mangano, P.D. Serpico and T. Tram, *Strongest model-independent bound on the lifetime of Dark Matter*, *JCAP* **12** (2014) 028 [1407.2418].

[32] CDF collaboration, *Observation of top quark production in $\bar{p}p$ collisions*, *Phys. Rev. Lett.* **74** (1995) 2626 [hep-ex/9503002].

[33] DONUT collaboration, *Observation of tau neutrino interactions*, *Phys. Lett. B* **504** (2001) 218 [hep-ex/0012035].

[34] ATLAS collaboration, *Observation of a new particle in the search for the Standard Model Higgs boson with the ATLAS detector at the LHC*, *Phys. Lett. B* **716** (2012) 1 [1207.7214].

[35] CMS collaboration, *Observation of a New Boson at a Mass of 125 GeV with the CMS Experiment at the LHC*, *Phys. Lett. B* **716** (2012) 30 [1207.7235].

[36] PARTICLE DATA GROUP collaboration, *Review of Particle Physics*, *PTEP* **2022** (2022) 083C01.

[37] M. Herrero, *The Standard model*, *NATO Sci. Ser. C* **534** (1999) 1 [hep-ph/9812242].

[38] SUPER-KAMIOKANDE collaboration, *Evidence for oscillation of atmospheric neutrinos*, *Phys. Rev. Lett.* **81** (1998) 1562 [hep-ex/9807003].

[39] SNO collaboration, *Direct evidence for neutrino flavor transformation from neutral current interactions in the Sudbury Neutrino Observatory*, *Phys. Rev. Lett.* **89** (2002) 011301 [nucl-ex/0204008].

[40] KATRIN collaboration, *Improved Upper Limit on the Neutrino Mass from a Direct Kinematic Method by KATRIN*, *Phys. Rev. Lett.* **123** (2019) 221802 [1909.06048].

[41] A. Boyarsky, M. Drewes, T. Lasserre, S. Mertens and O. Ruchayskiy, *Sterile neutrino dark matter*, *Progress in Particle and Nuclear Physics* **104** (2019) 1.

[42] G. Bertone, D. Hooper and J. Silk, *Particle dark matter: Evidence, candidates and constraints*, *Phys. Rept.* **405** (2005) 279 [hep-ph/0404175].

[43] L. Roszkowski, E.M. Sessolo and S. Trojanowski, *WIMP dark matter candidates and searches—current status and future prospects*, *Rept. Prog. Phys.* **81** (2018) 066201 [1707.06277].

[44] A.B. Lahanas, *LSP as a Candidate for Dark Matter*, *Lect. Notes Phys.* **720** (2007) 35 [hep-ph/0607301].

[45] M.E. Peskin, *Supersymmetric dark matter in the harsh light of the Large Hadron Collider*, *Proc. Nat. Acad. Sci.* **112** (2014) 12256.

[46] D. Hooper and S. Profumo, *Dark Matter and Collider Phenomenology of Universal Extra Dimensions*, *Phys. Rept.* **453** (2007) 29 [hep-ph/0701197].

[47] R.J. Scherrer and M.S. Turner, *On the Relic, Cosmic Abundance of Stable Weakly Interacting Massive Particles*, *Phys. Rev. D* **33** (1986) 1585.

[48] G. Jungman, M. Kamionkowski and K. Griest, *Supersymmetric dark matter*, *Phys. Rept.* **267** (1996) 195 [hep-ph/9506380].

[49] H. Baer, K.-Y. Choi, J.E. Kim and L. Roszkowski, *Dark matter production in the early Universe: beyond the thermal WIMP paradigm*, *Phys. Rept.* **555** (2015) 1 [1407.0017].

[50] J.L. Feng and J. Kumar, *The WIMPless Miracle: Dark-Matter Particles without Weak-Scale Masses or Weak Interactions*, *Phys. Rev. Lett.* **101** (2008) 231301

[0803.4196].

[51] L.J. Hall, K. Jedamzik, J. March-Russell and S.M. West, *Freeze-In Production of FIMP Dark Matter*, *JHEP* **03** (2010) 080 [0911.1120].

[52] J.L. Feng, A. Rajaraman and F. Takayama, *Superweakly interacting massive particles*, *Phys. Rev. Lett.* **91** (2003) 011302 [hep-ph/0302215].

[53] M. Pospelov, A. Ritz and M.B. Voloshin, *Bosonic super-WIMPs as keV-scale dark matter*, *Phys. Rev. D* **78** (2008) 115012 [0807.3279].

[54] G. Ballesteros, J. Redondo, A. Ringwald and C. Tamarit, *Standard Model—axion—seesaw—Higgs portal inflation. Five problems of particle physics and cosmology solved in one stroke*, *JCAP* **08** (2017) 001 [1610.01639].

[55] L. Visinelli and P. Gondolo, *Dark Matter Axions Revisited*, *Phys. Rev. D* **80** (2009) 035024 [0903.4377].

[56] S. Dodelson and L.M. Widrow, *Sterile-neutrinos as dark matter*, *Phys. Rev. Lett.* **72** (1994) 17 [hep-ph/9303287].

[57] B. Holdom, *Two U(1)'s and Epsilon Charge Shifts*, *Phys. Lett. B* **166** (1986) 196.

[58] R. Essig et al., *Working Group Report: New Light Weakly Coupled Particles*, in *Snowmass 2013: Snowmass on the Mississippi*, 10, 2013 [1311.0029].

[59] E.W. Kolb, D.J.H. Chung and A. Riotto, *WIMPzillas!*, *AIP Conf. Proc.* **484** (1999) 91 [hep-ph/9810361].

[60] S.R. Coleman, *Q-balls*, *Nucl. Phys. B* **262** (1985) 263.

[61] A. Kusenko and M.E. Shaposhnikov, *Supersymmetric Q balls as dark matter*, *Phys. Lett. B* **418** (1998) 46 [hep-ph/9709492].

[62] A. Ansari, L. Singh Bhandari and A.M. Thalapillil, *Q-balls in the sky*, 2302.11590.

[63] M. Schumann, *Direct Detection of WIMP Dark Matter: Concepts and Status*, *J. Phys. G* **46** (2019) 103003 [1903.03026].

[64] EROS-2 collaboration, *Limits on the Macho Content of the Galactic Halo from the EROS-2 Survey of the Magellanic Clouds*, *Astron. Astrophys.* **469** (2007) 387 [astro-ph/0607207].

[65] P. van Dokkum et al., *A galaxy lacking dark matter*, *Nature* **555** (2018) 629

[1803.10237].

[66] P. Salati, *Dark matter annihilation in the universe*, in *International Journal of Modern Physics: Conference Series*, vol. 30, p. 1460256, World Scientific, 2014.

[67] FERMI-LAT collaboration, *The Large Area Telescope on the Fermi Gamma-ray Space Telescope Mission*, *Astrophys. J.* **697** (2009) 1071 [0902.1089].

[68] H.E.S.S. collaboration, *Search for a Dark Matter annihilation signal from the Galactic Center halo with H.E.S.S*, *Phys. Rev. Lett.* **106** (2011) 161301 [1103.3266].

[69] CTA CONSORTIUM collaboration, *Design concepts for the Cherenkov Telescope Array CTA: An advanced facility for ground-based high-energy gamma-ray astronomy*, *Exper. Astron.* **32** (2011) 193 [1008.3703].

[70] CTA CONSORTIUM collaboration, *Dark Matter and Fundamental Physics with the Cherenkov Telescope Array*, *Astropart. Phys.* **43** (2013) 189 [1208.5356].

[71] SUPER-KAMIOKANDE collaboration, *An Indirect Search for WIMPs in the Sun using 3109.6 days of upward-going muons in Super-Kamiokande*, *Astrophys. J.* **742** (2011) 78 [1108.3384].

[72] SUPER-KAMIOKANDE collaboration, *Searching for Dark Matter Annihilation into Neutrinos with Super-Kamiokande*, in *Meeting of the APS Division of Particles and Fields*, 10, 2015 [1510.07999].

[73] ICECUBE collaboration, *Improved limits on dark matter annihilation in the Sun with the 79-string IceCube detector and implications for supersymmetry*, *JCAP* **04** (2016) 022 [1601.00653].

[74] J. Goodman and et., *Constraints on Dark Matter from Colliders*, *Phys. Rev. D* **82** (2010) 116010 [1008.1783].

[75] F. Kahlhoefer, *Review of LHC Dark Matter Searches*, *Int. J. Mod. Phys. A* **32** (2017) 1730006 [1702.02430].

[76] ATLAS collaboration, *Dark matter searches with the ATLAS detector*, *EPJ Web Conf.* **158** (2017) 01007.

[77] CMS collaboration, *Search for dark matter, extra dimensions, and unparticles in monojet events in proton–proton collisions at* $\sqrt{s} = 8$ *TeV*, *Eur. Phys. J. C* **75** (2015) 235 [1408.3583].

[78] J.D. Lewin and P.F. Smith, *Review of mathematics, numerical factors, and corrections for dark matter experiments based on elastic nuclear recoil*, *Astropart. Phys.* **6** (1996) 87.

[79] D. Baxter et al., *Recommended conventions for reporting results from direct dark matter searches*, *Eur. Phys. J. C* **81** (2021) 907 [2105.00599].

[80] M.C. Smith et al., *The RAVE Survey: Constraining the Local Galactic Escape Speed*, *Mon. Not. Roy. Astron. Soc.* **379** (2007) 755 [astro-ph/0611671].

[81] J. Bland-Hawthorn and O. Gerhard, *The galaxy in context: Structural, kinematic, and integrated properties*, *Annual Review of Astronomy and Astrophysics* **54** (2016) 529 [https://doi.org/10.1146/annurev-astro-081915-023441].

[82] GRAVITY Collaboration, Abuter, R. and et. al, *Improved gravity astrometric accuracy from modeling optical aberrations*, *A&A* **647** (2021) A59.

[83] J. Aalbers, B. Pelssers, J.R. Angevaare and K.D. Morå, *wimprates: v0.5.0*, 2023. 10.5281/zenodo.7636982.

[84] G. Gelmini and P. Gondolo, *WIMP annual modulation with opposite phase in Late-Infall halo models*, *Phys. Rev. D* **64** (2001) 023504 [hep-ph/0012315].

[85] R.H. Helm, *Inelastic and Elastic Scattering of 187-Mev Electrons from Selected Even-Even Nuclei*, *Phys. Rev.* **104** (1956) 1466.

[86] L. Vietze, P. Klos, J. Menéndez, W.C. Haxton and A. Schwenk, *Nuclear structure aspects of spin-independent WIMP scattering off xenon*, *Phys. Rev. D* **91** (2015) 043520 [1412.6091].

[87] T. Marrodán Undagoitia and L. Rauch, *Dark matter direct-detection experiments*, *J. Phys. G* **43** (2016) 013001 [1509.08767].

[88] PICO collaboration, *PICO-60 Results and PICO-40L Status*, *J. Phys. Conf. Ser.* **1468** (2020) 012043.

[89] P. Collaboration, "Pico-500." https://www.picoexperiment.com/pico-500/.

[90] SUPERCDMS collaboration, *Search for Low-Mass Weakly Interacting Massive Particles with SuperCDMS*, *Phys. Rev. Lett.* **112** (2014) 241302 [1402.7137].

[91] SUPERCDMS collaboration, *Results from the Super Cryogenic Dark Matter Search Experiment at Soudan*, *Phys. Rev. Lett.* **120** (2018) 061802 [1708.08869].

[92] SUPERCDMS collaboration, *Search for Low-Mass Dark Matter with CDMSlite Using a Profile Likelihood Fit*, *Phys. Rev. D* **99** (2019) 062001 [1808.09098].

[93] EDELWEISS collaboration, *Improved EDELWEISS-III sensitivity for low-mass WIMPs using a profile likelihood approach*, *Eur. Phys. J. C* **76** (2016) 548 [1607.03367].

[94] CDEX collaboration, *Limits on Light Weakly Interacting Massive Particles from the First 102.8 kg $\times$ day Data of the CDEX-10 Experiment*, *Phys. Rev. Lett.* **120** (2018) 241301 [1802.09016].

[95] CRESST collaboration, *First results from the CRESST-III low-mass dark matter program*, *Phys. Rev. D* **100** (2019) 102002 [1904.00498].

[96] G. Angloher et al., *The COSINUS project - perspectives of a NaI scintillating calorimeter for dark matter search*, *Eur. Phys. J. C* **76** (2016) 441 [1603.02214].

[97] COSINUS collaboration, *Results from the first cryogenic NaI detector for the COSINUS project*, *JINST* **12** (2017) P11007 [1705.11028].

[98] SBC collaboration, *The Scintillating Bubble Chamber (SBC) Experiment for Dark Matter and Reactor CEvNS*, *PoS* **ICHEP2020** (2021) 632.

[99] SBC collaboration, *The Scintillation Bubble Chamber (SBC) experiment for dark matter and reactor CEvNS*, *PoS* **PANIC2021** (2022) 339.

[100] DAMIC collaboration, *Results on low-mass weakly interacting massive particles from a 11 kg-day target exposure of DAMIC at SNOLAB*, *Phys. Rev. Lett.* **125** (2020) 241803 [2007.15622].

[101] I. Arnquist, N. Avalos, D. Baxter, X. Bertou, N. Castelló-Mor, A. Chavarria et al., *First constraints from damic-m on sub-gev dark-matter particles interacting with electrons*, *Physical Review Letters* **130** (2023) 171003.

[102] SENSEI collaboration, *SENSEI: Direct-Detection Results on sub-GeV Dark Matter from a New Skipper-CCD*, *Phys. Rev. Lett.* **125** (2020) 171802 [2004.11378].

[103] COGENT collaboration, *CoGeNT: A Search for Low-Mass Dark Matter using p-type Point Contact Germanium Detectors*, *Phys. Rev. D* **88** (2013) 012002 [1208.5737].

[104] COGENT collaboration, *Search for An Annual Modulation in Three Years of CoGeNT Dark Matter Detector Data*, 1401.3295.

[105] NEWS-G collaboration, *First results from the NEWS-G direct dark matter search experiment at the LSM*, *Astropart. Phys.* **97** (2018) 54 [1706.04934].

[106] DAMA collaboration, *The DAMA project: Achievements, implications and perspectives*, *Prog. Part. Nucl. Phys.* **114** (2020) 103810.

[107] DAMA collaboration, *First model independent results from DAMA/LIBRA-phase2*, *Nucl. Phys. Atom. Energy* **19** (2018) 307 [1805.10486].

[108] COSINE-100 collaboration, *Three-year annual modulation search with COSINE-100*, *Phys. Rev. D* **106** (2022) 052005 [2111.08863].

[109] COSINE-100 collaboration, *An induced annual modulation signature in COSINE-100 data by DAMA/LIBRA's analysis method*, *Sci. Rep.* **13** (2023) 4676 [2208.05158].

[110] J. Amaré et al., *Dark Matter Annual Modulation with ANAIS-112: Three Years Results*, *Moscow Univ. Phys. Bull.* **77** (2022) 322.

[111] KIMS collaboration, *Limits on Interactions between Weakly Interacting Massive Particles and Nucleons Obtained with NaI(Tl) crystal Detectors*, *JHEP* **03** (2019) 194 [1806.06499].

[112] DEAP-3600 collaboration, *Recent results from DEAP-3600*, *JINST* **18** (2023) C02046 [2302.14484].

[113] XMASS collaboration, *Direct dark matter searches with the full data set of XMASS-I*, 2211.06204.

[114] XENON collaboration, *First Dark Matter Search with Nuclear Recoils from the XENONnT Experiment*, 2303.14729.

[115] LZ collaboration, *First Dark Matter Search Results from the LUX-ZEPLIN (LZ) Experiment*, 2207.03764.

[116] PANDAX-4T collaboration, *Dark Matter Search Results from the PandaX-4T Commissioning Run*, *Phys. Rev. Lett.* **127** (2021) 261802 [2107.13438].

[117] DARWIN collaboration, *DARWIN: towards the ultimate dark matter detector*, *JCAP* **11** (2016) 017 [1606.07001].

[118] C.A.J. O'Hare, *New Definition of the Neutrino Floor for Direct Dark Matter Searches*, *Phys. Rev. Lett.* **127** (2021) 251802 [2109.03116].

[119] DARKSIDE-50 collaboration, *Search for low-mass dark matter WIMPs with 12 ton-day exposure of DarkSide-50*, *Phys. Rev. D* **107** (2023) 063001 [2207.11966].

[120] WARP collaboration, *The WArP dark matter search*, *PoS* **IDM2008** (2008) 016.

[121] ARDM collaboration, *Commissioning of the ArDM experiment at the Canfranc underground laboratory: first steps towards a tonne-scale liquid argon time projection chamber for Dark Matter searches*, *JCAP* **03** (2017) 003 [1612.06375].

[122] XLZD Consortium, "The XLZD dark matter consortium." https://xlzd.org/.

[123] G.A.D.M. Collaboration, "GADMC." https://www.lngs.infn.it/en/darkside.

[124] DARKSIDE-20K collaboration, *DarkSide-20k: A 20 tonne two-phase LAr TPC for direct dark matter detection at LNGS*, *Eur. Phys. J. Plus* **133** (2018) 131 [1707.08145].

[125] CYGNO collaboration, *The CYGNO Experiment*, *Instruments* **6** (2022) 6 [2202.05480].

[126] XENON collaboration, *Light Dark Matter Search with Ionization Signals in XENON1T*, *Phys. Rev. Lett.* **123** (2019) 251801 [1907.11485].

[127] XENON collaboration, *Search for Coherent Elastic Scattering of Solar ^{8}B Neutrinos in the XENON1T Dark Matter Experiment*, *Phys. Rev. Lett.* **126** (2021) 091301 [2012.02846].

[128] DEAP collaboration, *Search for dark matter with a 231-day exposure of liquid argon using DEAP-3600 at SNOLAB*, *Phys. Rev. D* **100** (2019) 022004 [1902.04048].

[129] DARKSIDE collaboration, *DarkSide-50 532-day Dark Matter Search with Low-Radioactivity Argon*, *Phys. Rev. D* **98** (2018) 102006 [1802.07198].

[130] DARKSIDE collaboration, *Low-Mass Dark Matter Search with the DarkSide-50 Experiment*, *Phys. Rev. Lett.* **121** (2018) 081307 [1802.06994].

[131] XENON collaboration, *Design and Performance of the XENON10 Dark Matter Experiment*, *Astropart. Phys.* **34** (2011) 679 [1001.2834].

[132] XENON100 collaboration, *The XENON100 Dark Matter Experiment*, *Astropart. Phys.* **35** (2012) 573 [1107.2155].

[133] XENON collaboration, *The XENON1T Dark Matter Experiment*, *Eur. Phys. J. C* **77**

(2017) 881 [1708.07051].

[134] XENON Collaboration, "XENON Dark Matter Project." https://xenonexperiment.org/.

[135] XENON collaboration, *Double-Weak Decays of ^{124}Xe and ^{136}Xe in the XENON1T and XENONnT Experiments*, *Phys. Rev. C* **106** (2022) 024328 [2205.04158].

[136] PANDAX collaboration, *Determination of Double Beta Decay Half-Life of ^{136}Xe with the PandaX-4T Natural Xenon Detector*, *Research* **2022** (2022) 9798721 [2205.12809].

[137] LZ collaboration, *Projected sensitivity of the LUX-ZEPLIN experiment to the $0\nu\beta\beta$ decay of ^{136}Xe*, *Phys. Rev. C* **102** (2020) 014602 [1912.04248].

[138] DARWIN collaboration, *Sensitivity of the DARWIN observatory to the neutrinoless double beta decay of ^{136}Xe*, *Eur. Phys. J. C* **80** (2020) 808 [2003.13407].

[139] P. Linstrom and W. Mallard, *NIST Chemistry WebBook, NIST Standard Reference Database Number 69*, 20899, National Institute of Standards and Technology, Gaithersburg MD.

[140] E. Lemmon and R. Span, *Short Fundamental Equations of State for 20 Industrial Fluids*, *J. Chem. Eng. Data, 47, 249.* (2006) 785.

[141] M. Berger and et al., *XCOM: Photon cross sections database: NIST standard reference database 8*, *NIST, Gaithersburg, MD* (2013) .

[142] W. Ziegler, J. Mullins and A. Berquist, *Calculation of the Vapor Pressure and Heats of Vaporization and Sublimation of Liquids and Solids below One Atmosphere Pressure. VIII. Xenon*, *Ga. Inst. Technol., Eng. Exp. Stn., Proj. A-764, Tech. Rep. No. 3* (1966) .

[143] M. Juris and et. al, *Atomic weights of the elements 2013 (iupac technical report)*, *Pure and Applied Chemistry* **88** (2016) 265.

[144] I. Fonseca and L. Lobo, *The triple point of xenon as a possible defining point on an international temperature scale*, *Metrologia, 21, 43* (1985) .

[145] R. Kemp, W. Kemp and P. Smart, *Thermodynamics of liquid mixtures of xenon and methyl fluoride*, *Fluid Phase Equilib., 47, 249.* (1989) .

[146] W.M. Haynes, D.R. Lide and T.J. Bruno, *CRC Handbook of Chemistry and Physics*, CRC Press, 99th ed. (2018).

[147] K. Fujii and et al., *High-accuracy measurement of the emission spectrum of liquid xenon in the vacuum ultraviolet region*, *Nuclear Instruments and Methods in Physics Research Section A: Accelerators, Spectrometers, Detectors and Associated Equipment* **795** (2015) 293.

[148] P. Belli and et al., *Liquid Xenon detectors and their applications*, *Nucl. Instrum. Meth. A* **299** (1990) 191.

[149] T. Takahashi and et al., *Average energy expended per ion pair in liquid xenon*, *Phys. Rev. A* **12** (1975) 1771.

[150] T. Doke and et al., *Absolute Scintillation Yields in Liquid Argon and Xenon for Various Particles*, *Jap. J. Appl. Phys.* **41** (2002) 1538.

[151] P. Sorensen and C.E. Dahl, *Nuclear recoil energy scale in liquid xenon with application to the direct detection of dark matter*, *Phys. Rev. D* **83** (2011) 063501 [1101.6080].

[152] S. Kubota, M. Hishida and J. Raun, *Evidence for a triplet state of the self-trapped exciton states in liquid argon, krypton and xenon*, *Journal of Physics C: Solid State Physics* **11** (1978) 2645.

[153] LUX collaboration, *Liquid xenon scintillation measurements and pulse shape discrimination in the LUX dark matter detector*, *Phys. Rev. D* **97** (2018) 112002 [1802.06162].

[154] W.H. Lippincott, K.J. Coakley, D. Gastler, A. Hime, E. Kearns, D.N. McKinsey et al., *Scintillation time dependence and pulse shape discrimination in liquid argon*, *Phys. Rev. C* **78** (2008) 035801 [0801.1531].

[155] DEAP collaboration, *Measurement of the scintillation time spectra and pulse-shape discrimination of low-energy β and nuclear recoils in liquid argon with DEAP-1*, *Astropart. Phys.* **85** (2016) 1 [0904.2930].

[156] SCENE collaboration, *Measurement of Scintillation and Ionization Yield and Scintillation Pulse Shape from Nuclear Recoils in Liquid Argon*, *Phys. Rev. D* **91** (2015) 092007 [1406.4825].

[157] NEST collaboration, M. Szydagis et al., *Noble element simulation technique*, 2023. 10.5281/zenodo.7577399.

[158] NEST collaboration, S. Farrell and et. al., *nestpy: Sync with NESTv2.3.12beta*,

2023. 10.5281/zenodo.7552304.

[159] J. Lindhard, V. Nielsen, M. Scharff and P.V. Thomsen, *Integral equations governing radiation effects. (notes on atomic collisions, iii)*, *Kgl. Danske Videnskab., Selskab. Mat. Fys. Medd.* **33** (1963) .

[160] C.E. Dahl, *The physics of background discrimination in liquid xenon, and first results from Xenon10 in the hunt for WIMP dark matter*, Ph.D. thesis, Princeton University, 2009.

[161] EXO-200 collaboration, *Measurement of the scintillation and ionization response of liquid xenon at MeV energies in the EXO-200 experiment*, *Phys. Rev. C* **101** (2020) 065501 [1908.04128].

[162] L. Baudis, P. Sanchez-Lucas and K. Thieme, *A measurement of the mean electronic excitation energy of liquid xenon*, *Eur. Phys. J. C* **81** (2021) 1060 [2109.07151].

[163] XENON collaboration, *Projected WIMP sensitivity of the XENONnT dark matter experiment*, *JCAP* **11** (2020) 031 [2007.08796].

[164] LZ collaboration, *The LUX-ZEPLIN (LZ) Experiment*, *Nucl. Instrum. Meth. A* **953** (2020) 163047 [1910.09124].

[165] PANDAX collaboration, *Dark matter direct search sensitivity of the PandaX-4T experiment*, *Sci. China Phys. Mech. Astron.* **62** (2019) 31011 [1806.02229].

[166] L.S. Miller, S. Howe and W.E. Spear, *Charge Transport in Solid and Liquid Ar, Kr, and Xe*, *Phys. Rev.* **166** (1968) 871.

[167] EXO-200 collaboration, *Measurement of the Drift Velocity and Transverse Diffusion of Electrons in Liquid Xenon with the EXO-200 Detector*, *Phys. Rev. C* **95** (2017) 025502 [1609.04467].

[168] L. Baudis and et. al, *The first dual-phase xenon TPC equipped with silicon photomultipliers and characterisation with ^{37}Ar*, *Eur. Phys. J. C* **80** (2020) 477 [2003.01731].

[169] E. Aprile, K.L. Giboni, P. Majewski, K. Ni and M. Yamashita, *Proportional light in a dual-phase xenon chamber*, *IEEE Transactions on nuclear science* **51** (2004) 1986.

[170] J. Xu and et. al, *Electron extraction efficiency study for dual-phase xenon dark matter experiments*, *Phys. Rev. D* **99** (2019) 103024 [1904.02885].

[171] O. Njoya et al., *Measurements of electron transport in liquid and gas Xenon using a laser-driven photocathode*, *Nucl. Instrum. Meth. A* **972** (2020) 163965 [1911.11580].

[172] XENON collaboration, *XENON1T Dark Matter Data Analysis: Signal Reconstruction, Calibration and Event Selection*, *Phys. Rev. D* **100** (2019) 052014 [1906.04717].

[173] F. Neves and et al., *Measurement of the absolute reflectance of polytetrafluoroethylene (PTFE) immersed in liquid xenon*, *JINST* **12** (2017) P01017 [1612.07965].

[174] M. Yamashita, T. Doke, K. Kawasaki, J. Kikuchi and S. Suzuki, *Scintillation response of liquid Xe surrounded by PTFE reflector for gamma rays*, *Nuclear Instruments and Methods in Physics Research Section A: Accelerators, Spectrometers, Detectors and Associated Equipment* **535** (2004) 692.

[175] V.A. Kudryavtsev, P. Zakhary and B. Easeman, *Neutron production in (α, n) reactions*, *Nucl. Instrum. Meth. A* **972** (2020) 164095 [2005.02499].

[176] L. Althüser, S. Lindemann, M. Murra, M. Schumann, C. Wittweg and C. Weinheimer, *VUV Transmission of PTFE for Xenon-based Particle Detectors*, *JINST* **15** (2020) P12021 [2006.05827].

[177] Hamamatsu Corp., "Photomultiplier Model R11410-21." https://www.hamamatsu.com/us/en/product/optical-sensors/pmt/pmt_tube-alone/head-on-type/R11410-20.html.

[178] L. Baudis, A. Behrens, A. Ferella, A. Kish, T. Marrodan Undagoitia, D. Mayani et al., *Performance of the Hamamatsu R11410 Photomultiplier Tube in cryogenic Xenon Environments*, *JINST* **8** (2013) P04026 [1303.0226].

[179] P. Barrow et al., *Qualification Tests of the R11410-21 Photomultiplier Tubes for the XENON1T Detector*, *JINST* **12** (2017) P01024 [1609.01654].

[180] V.C. Antochi et al., *Improved quality tests of R11410-21 photomultiplier tubes for the XENONnT experiment*, *JINST* **16** (2021) P08033 [2104.15051].

[181] CAEN, "HV power supply A1526." https://www.caen.it/products/a1526/.

[182] Heinzinger, "PNChp 150000-1." https://www.heinzinger.com/en/products/pnc-serie.

[183] CAEN, "HV power supply A1580H."

https://www.caen.it/products/a1580h/.

[184] F. Toschi, *Design of the field cage and charge response of the XENONnT dark matter experiment*, Ph.D. thesis, Albert-Ludwigs-Universität Freiburg im Breisgau, Germany, 2023.

[185] Iwatani Industrial Gas Co., "Model PC150." https://www.iwatani.co.jp/eng/.

[186] Lakeshore Cryotronics, "Cryogenic Temper Controller Model 340." https://www.lakeshore.com/products/categories/overview/discontinued-products/discontinued-products/.

[187] SAES, "PS4-MT Series Rare Gas Purifier, Model PS4-MT50-R." http://www.saespuregas.com/Library/specifications-brochures/s110-233_a_521.pdf.

[188] D. Schulte, M. Murra, P. Schulte, C. Huhmann and C. Weinheimer, *Ultra-clean radon-free four cylinder magnetically-coupled piston pump*, *JINST* **16** (2021) P09011 [2107.00755].

[189] CHART QDrive technologies. https://www.chartindustries.com/.

[190] Barber Nichols, "Pump Model BNCP-32C-000." https://barber-nichols.com.

[191] K. Morå, *Xenonnt first results on electronic recoil events*, 2022. Talk at International Dark Matter 2022, Vienna, Austria [accessed May 2023].

[192] G. Plante, E. Aprile, J. Howlett and Y. Zhang, *Liquid-phase purification for multi-tonne xenon detectors*, *Eur. Phys. J. C* **82** (2022) 860 [2205.07336].

[193] XENON collaboration, *Search for New Physics in Electronic Recoil Data from XENONnT*, *Phys. Rev. Lett.* **129** (2022) 161805 [2207.11330].

[194] XENON collaboration, *Removing krypton from xenon by cryogenic distillation to the ppq level*, *Eur. Phys. J. C* **77** (2017) 275 [1612.04284].

[195] B. Singh and J. Chen, *Nuclear Data Sheets for A=85*, *Nucl. Data Sheets* **116** (2014) 1.

[196] S. Lindemann and H. Simgen, *Krypton assay in xenon at the ppq level using a gas chromatographic system and mass spectrometer*, *Eur. Phys. J. C* **74** (2014) 2746 [1308.4806].

[197] XENON collaboration, *Dark Matter Search Results from a One Ton-Year Exposure of XENON1T*, *Phys. Rev. Lett.* **121** (2018) 111302 [1805.12562].

[198] M. Murra, D. Schulte, C. Huhmann and C. Weinheimer, *Design, construction and commissioning of a high-flow radon removal system for XENONnT*, *Eur. Phys. J. C* **82** (2022) 1104 [2205.11492].

[199] XENON collaboration, *Online ^{222} Rn removal by cryogenic distillation in the XENON100 experiment*, *Eur. Phys. J. C* **77** (2017) 358 [1702.06942].

[200] XENON collaboration, *Material radioassay and selection for the XENON1T dark matter experiment*, *Eur. Phys. J. C* **77** (2017) 890 [1705.01828].

[201] XENON1T collaboration, *Conceptual design and simulation of a water Cherenkov muon veto for the XENON1T experiment*, *JINST* **9** (2014) P11006 [1406.2374].

[202] Hamamatsu Corp., "Photomultiplier Model R5912ASSY." https://www.hamamatsu.com/us/en/product/optical-sensors/pmt/pmt_tube-alone/head-on-type/R5912.html.

[203] Hamamatsu Corp., "Photomultiplier Model R5912-100-10 WA-D30." https://www.hamamatsu.com/us/en/product/optical-sensors/pmt/pmt_tube-alone/head-on-type/R5912.html.

[204] L. Marti et al., *Evaluation of gadolinium's action on water Cherenkov detector systems with EGADS*, *Nucl. Instrum. Meth. A* **959** (2020) 163549 [1908.11532].

[205] A. Manalaysay et al., *Spatially uniform calibration of a liquid xenon detector at low energies using 83m-Kr*, *Rev. Sci. Instrum.* **81** (2010) 073303 [0908.0616].

[206] L.W. Kastens, S.B. Cahn, A. Manzur and D.N. McKinsey, *Calibration of a Liquid Xenon Detector with Kr-83m*, *Phys. Rev. C* **80** (2009) 045809 [0905.1766].

[207] R.F. Lang, A. Brown, E. Brown, M. Cervantes, S. Macmullin, D. Masson et al., *A ^{220}Rn source for the calibration of low-background experiments*, *JINST* **11** (2016) P04004 [1602.01138].

[208] XENON collaboration, *Low-energy Calibration of XENON1T with an Internal ^{37}Ar Source*, 2211.14191.

[209] J. Scherzinger et al., *Tagging fast neutrons from an ^{241}Am/^{9}Be source*, *Appl. Radiat. Isot.* **98** (2015) 74 [1405.2686].

[210] R.F. Lang, J. Pienaar, E. Hogenbirk, D. Masson, R. Nolte, A. Zimbal et al., *Characterization of a deuterium–deuterium plasma fusion neutron generator*, *Nucl. Instrum. Meth. A* **879** (2018) 31 [1705.04741].

[211] XENON collaboration, *Energy resolution and linearity of XENON1T in the MeV energy range*, *Eur. Phys. J. C* **80** (2020) 785 [2003.03825].

[212] CAEN, "V1724 flash ADC." https://www.caen.it/products/v1724/.

[213] J. Aalbers and et al., *AxFoundation/strax: Streaming analysis for xenon experiments, v1.2.3*, 2021. 10.5281/zenodo.5576034.

[214] XENON collaboration, *XENONnT/straxen: Streaming analysis for XENON(nT), v1.2.8*, 2022. 10.5281/zenodo.6102391.

[215] XENON collaboration, *The Triggerless Data Acquisition System of the XENONnT Experiment*, 2212.11032.

[216] J. Cardoso et al., *Experience with a Slow Control system based on industrial process control hardware and software for the XENON1T dark matter search*, in *20th IEEE-NPSS Real Time Conference*, 8, 2016, DOI.

[217] K.-J. Bathe, *Finite element method*, *Wiley encyclopedia of computer science and engineering* (2007) 1.

[218] COMSOL, "COMSOL Multiphysics®." www.comsol.com.

[219] ADINA, "ADINA Multiphysics." https://adina.com/adina-multiphysics.shtml.

[220] Ansys, "Ansys Maxwell." https://www.ansys.com/products/electronics/ansys-maxwell.

[221] W.S. Hall, *The boundary element method*, vol. 27, Springer Science & Business Media (2012).

[222] KATRIN collaboration, *KATRIN: A Next generation tritium beta decay experiment with sub-eV sensitivity for the electron neutrino mass. Letter of intent*, hep-ex/0109033.

[223] NVIDIA Corporation, "NVIDIA V100." https://www.nvidia.com/en-us/data-center/v100/.

[224] NVIDIA Corporation, "NVIDIA Tesla T4." https://www.nvidia.com/en-us/data-center/tesla-t4/.

[225] LUX collaboration, *3D Modeling of Electric Fields in the LUX Detector*, *JINST* **12** (2017) P11022 [1709.00095].

[226] D. Cubric, B. Lencova, F. Read and J. Zlamal, *Comparison of fdm, fem and bem for electrostatic charged particle optics*, *Nuclear Instruments and Methods in Physics Research Section A: Accelerators, Spectrometers, Detectors and Associated Equipment* **427** (1999) 357.

[227] T. Corona, *Methodology and Application of High Performance Electrostatic Field Simulation in the KATRIN Experiment*, Ph.D. thesis, North Carolina U., 2014.

[228] J. Wulf and R. Peres, "XSLAP - xenon simulation and analysis package." https://github.com/Physik-Institut-UZH/XSLAP, 2022.

[229] P. Lazić, H. Štefančić and H. Abraham, *The robin hood method – a novel numerical method for electrostatic problems based on a non-local charge transfer*, *Journal of Computational Physics* **213** (2006) 117.

[230] P. Lazic, H. Stefancic and H. Abraham, *The robin hood method¿a new view on differential equations.*, *Engineering Analysis With Boundary Elements* **32** (2008) 76.

[231] J.A. Formaggio and et al., *Solving for Micro- and Macro- Scale Electrostatic Configurations Using the Robin Hood Algorithm*, 1111.5035.

[232] D.F.R. Hilk, *Electric field simulations and electric dipole investigations at the KATRIN main spectrometer*, Ph.D. thesis, KIT, Karlsruhe, 2017. 10.5445/IR/1000065869.

[233] C. Geuzaine and J.-F. Remacle, *Gmsh: A 3-d finite element mesh generator with built-in pre-and post-processing facilities*, *International journal for numerical methods in engineering* **79** (2009) 1309.

[234] Autodesk. https://www.autodesk.com/products/fusion-360.

[235] W. "Schroeder, K. Martin and B. Lorensen, *The Visualization Toolkit (4th ed.)*, Kitware (2016).

[236] J. "Ahrens, B. Geveci and C. Law, *ParaView: An End-User Tool for Large Data Visualization*, Elsevier (2005).

[237] R.L. Amey and R.H. Cole, *Dielectric constants of liquefied noble gases and methane*,

The Journal of Chemical Physics **40** (1964) 146.

[238] R. Peres, "PyKeField - Python-based KEMfield analysis." `https://github.com/ricmperes/pykefield`, 2022.

[239] A. Weiser and S.E. Zarantonello, *A note on piecewise linear and multilinear table interpolation in many dimensions*, *Mathematics of Computation* **50** (1988) 189.

[240] "Regulargridinterpolator; scipy." `https://docs.scipy.org/doc/scipy/reference/generated/scipy.interpolate.RegularGridInterpolator.html`.

[241] P. Virtanen et al., *SciPy 1.0–Fundamental Algorithms for Scientific Computing in Python*, *Nature Meth.* **17** (2020) 261 [1907.10121].

[242] S.E. Derenzo, T.S. Mast, H. Zaklad and R.A. Muller, *Electron avalanche in liquid xenon*, *Phys. Rev. A* **9** (1974) 2582.

[243] COMSOL, "8 Uses of COMSOL Multiphysics® in the Biomedical Industry." `https://www.comsol.com/blogs/8-uses-of-comsol-multiphysics-in-the-biomedical-industry`.

[244] COMSOL, "The Use of COMSOL Multiphysics® in the Food Industry." `https://www.comsol.com/blogs/the-use-of-comsol-multiphysics-in-the-food-industry`.

[245] COMSOL, "10 Real Uses of COMSOL Multiphysics® in the Power Industry." https://www.comsol.com/blogs/10-real-uses-of-comsol-multiphysics-in-the-power-industry.

[246] COMSOL, "COMSOL Multiphysics® version 5.3 - AC/DC module." `https://www.comsol.com/release/5.3/acdc-module`.

[247] V.H.-S. Wu, "Simulations and wire tests for the electrodes design." Internal DARWIN note.

[248] XENON collaboration, *Excess electronic recoil events in XENON1T*, *Phys. Rev. D* **102** (2020) 072004 [2006.09721].

[249] XENON collaboration, *Material radiopurity control in the XENONnT experiment*, *Eur. Phys. J. C* **82** (2022) 599 [2112.05629].

[250] MongoDB Database. `https://www.mongodb.com/`.

[251] M. Barisits et al., *Rucio - Scientific data management*, *Comput. Softw. Big Sci.* **3** (2019) 11 [1902.09857].

[252] S. Liang and et al., *Domain-Informed Neural Networks for Interaction Localization Within Astroparticle Experiments*, *Front. Artif. Intell.* **5** (2022) 832909 [2112.07995].

[253] XENON collaboration, *Detector signal characterization with a Bayesian network in XENONnT*, 2304.05428.

[254] F. Jörg and et al., *Characterization of alpha and beta interactions in liquid xenon*, *Eur. Phys. J. C* **82** (2022) 361 [2109.13735].

[255] G. Carugno, B. Dainese, F. Pietropaolo and F. Ptohos, *Electron lifetime detector for liquid argon*, *Nucl. Instrum. Meth. A* **292** (1990) 580.

[256] XENON collaboration, *Emission of single and few electrons in XENON1T and limits on light dark matter*, *Phys. Rev. D* **106** (2022) 022001 [2112.12116].

[257] A. Kopec and et al., *Correlated single- and few-electron backgrounds milliseconds after interactions in dual-phase liquid xenon time projection chambers*, *JINST* **16** (2021) P07014 [2103.05077].

[258] XENON collaboration, *XENONnT/WFSim: v1.0.2*, Oct., 2022. 10.5281/zenodo.7216324.

[259] P. Sorensen, *Anisotropic diffusion of electrons in liquid xenon with application to improving the sensitivity of direct dark matter searches*, *Nucl. Instrum. Meth. A* **635** (2011) 41 [1102.2865].

[260] A. Bollhöfer, C. Schlosser, S. Schmid, M. Konrad, R. Purtschert and R. Krais, *Half a century of krypton-85 activity concentration measured in air over central europe: Trends and relevance for dating young groundwater*, *JER* **205-206** (2019) 7.

[261] GEANT4 collaboration, *GEANT4–a simulation toolkit*, *Nucl. Instrum. Meth. A* **506** (2003) 250.

[262] EXO-200 collaboration, *Improved measurement of the* $2\nu\beta\beta$ *half-life of* ^{136}*Xe with the EXO-200 detector*, *Phys. Rev. C* **89** (2014) 015502 [1306.6106].

[263] J.N. Bahcall and C. Pena-Garay, *Solar models and solar neutrino oscillations*, *New J. Phys.* **6** (2004) 63 [hep-ph/0404061].

[264] W.C. Haxton, R.G. Hamish Robertson and A.M. Serenelli, *Solar Neutrinos: Status*

and Prospects, *Ann. Rev. Astron. Astrophys.* **51** (2013) 21 [1208.5723].

[265] BOREXINO collaboration, *Comprehensive measurement of pp-chain solar neutrinos*, *Nature* **562** (2018) 505.

[266] XENON COLLABORATION collaboration, *XENONnT/pema: v0.6.4*, 2022. 10.5281/zenodo.7219740.

[267] D. Ramirez García, *Simulating the XENONnT dark matter experiment: backgrounds and WIMP sensitivity*, Ph.D. thesis, Albert-Ludwigs-Universität Freiburg im Breisgau, Germany, 2022.

[268] H.-T. Janka, *Explosion Mechanisms of Core-Collapse Supernovae*, *Ann. Rev. Nucl. Part. Sci.* **62** (2012) 407 [1206.2503].

[269] K. Scholberg, *Supernova Neutrino Detection*, *Ann. Rev. Nucl. Part. Sci.* **62** (2012) 81 [1205.6003].

[270] A. Mirizzi, I. Tamborra, H.-T. Janka, N. Saviano, K. Scholberg, R. Bollig et al., *Supernova Neutrinos: Production, Oscillations and Detection*, *Riv. Nuovo Cim.* **39** (2016) 1 [1508.00785].

[271] H.A. Bethe and J.R. Wilson, *Revival of a stalled supernova shock by neutrino heating*, *Astrophys. J.* **295** (1985) 14.

[272] A. Burrows and D. Vartanyan, *Core-collapse supernova explosion theory*, *Nature* **589** (2021) 29.

[273] H.-T. Janka, K. Langanke, A. Marek, G. Martinez-Pinedo and B. Mueller, *Theory of Core-Collapse Supernovae*, *Phys. Rept.* **442** (2007) 38 [astro-ph/0612072].

[274] A. Mezzacappa, *ASCERTAINING THE CORE COLLAPSE SUPERNOVA MECHANISM: The State of the Art and the Road Ahead*, *Ann. Rev. Nucl. Part. Sci.* **55** (2005) 467.

[275] A. Burrows and J. Goshy, *A theory of supernova explosions*, *Astrophysical Journal Letters v. 416, p. L75* **416** (1993) L75.

[276] R. Fernandez, *Hydrodynamics of Core-Collapse Supernovae at the Transition to Explosion. I. Spherical Symmetry*, *Astrophys. J.* **749** (2012) 142 [1111.0665].

[277] O. Pejcha and T.A. Thompson, *The Physics of the Neutrino Mechanism of Core-Collapse Supernovae*, *Astrophys. J.* **746** (2012) 106 [1103.4864].

[278] B. Müller and H.T. Janka, *Non-Radial Instabilities and Progenitor Asphericities in Core-Collapse Supernovae*, *Mon. Not. Roy. Astron. Soc.* **448** (2015) 2141 [1409.4783].

[279] L. Wolfenstein, *Neutrino Oscillations in Matter*, *Phys. Rev. D* **17** (1978) 2369.

[280] S.P. Mikheyev and A.Y. Smirnov, *Resonance Amplification of Oscillations in Matter and Spectroscopy of Solar Neutrinos*, *Sov. J. Nucl. Phys.* **42** (1985) 913.

[281] H. Nagakura, *Roles of fast neutrino-flavor conversion on the neutrino-heating mechanism of core-collapse supernova*, 2301.10785.

[282] "The garching core-collapse supernova archive." https://wwwmpa.mpa-garching.mpg.de/ccsnarchive/, 2023.

[283] G.G. Raffelt, *Supernova neutrino observations: What can we learn?*, *Nucl. Phys. B Proc. Suppl.* **221** (2011) 218 [astro-ph/0701677].

[284] W.D. Arnett, J.N. Bahcall, R.P. Kirshner and S.E. Woosley, *SUPERNOVA SN1987A*, *Ann. Rev. Astron. Astrophys.* **27** (1989) 629.

[285] KAMIOKANDE-II collaboration, *THE KAMIOKANDE-II DETECTOR*, in *7th Workshop on Grand Unification: ICOBAN 86*, 4, 1986.

[286] KAMIOKANDE-II collaboration, *Observation of a Neutrino Burst from the Supernova SN 1987a*, *Phys. Rev. Lett.* **58** (1987) 1490.

[287] L.R. Sulak et al., *THE FIRST THIRD OF A YEAR...: PROTON DECAY PHYSICS FROM THE IMB DETECTOR*, *Hadronic J.* **6** (1983) 1391.

[288] R.M. Bionta et al., *Observation of a Neutrino Burst in Coincidence with Supernova SN 1987a in the Large Magellanic Cloud*, *Phys. Rev. Lett.* **58** (1987) 1494.

[289] A.A. Pomansky, *The Baksan Neutrino Observatory of the Nuclear Research Institute of the Academy of Sciences of the USSR*, *Sov. Atom. Energ.* **44** (1978) 433.

[290] E.N. Alekseev, L.N. Alekseeva, V.I. Volchenko and I.V. Krivosheina, *Possible Detection of a Neutrino Signal on 23 February 1987 at the Baksan Underground Scintillation Telescope of the Institute of Nuclear Research*, *JETP Lett.* **45** (1987) 589.

[291] M. Aglietta et al., *On the event observed in the Mont Blanc Underground Neutrino observatory during the occurrence of Supernova 1987a*, *EPL* **3** (1987) 1315.

[292] K. Rozwadowska, F. Vissani and E. Cappellaro, *On the rate of core collapse*

supernovae in the milky way, *New Astron.* **83** (2021) 101498 [2009.03438].

[293] M.D. Kistler, W.C. Haxton and H. Yüksel, *Tomography of Massive Stars from Core Collapse to Supernova Shock Breakout*, *Astrophys. J.* **778** (2013) 81 [1211.6770].

[294] P. Antonioli et al., *SNEWS: The Supernova Early Warning System*, *New J. Phys.* **6** (2004) 114 [astro-ph/0406214].

[295] SNEWS. https://snews2.org/about.

[296] SUPER-KAMIOKANDE collaboration, *The Super-Kamiokande detector*, *Nucl. Instrum. Meth. A* **501** (2003) 418.

[297] LVD collaboration, *The Large Volume Detector (Lvd) of the Gran Sasso Laboratory*, *Nuovo Cim. C* **9** (1986) 237.

[298] ICECUBE collaboration, *The IceCube Neutrino Observatory: Instrumentation and Online Systems*, *JINST* **12** (2017) P03012 [1612.05093].

[299] KAMLAND collaboration, *KamLAND: A reactor neutrino experiment testing the solar neutrino anomaly*, *Nucl. Phys. B Proc. Suppl.* **91** (2001) 99.

[300] T.C. Shantz, *Design and construction of the helium and lead observatory*, Master's thesis, Laurentian University, 2010.

[301] SNO+ collaboration, *Development, characterisation, and deployment of the SNO+ liquid scintillator*, *JINST* **16** (2021) P05009 [2011.12924].

[302] NOVA collaboration, *The NOvA Technical Design Report*, .

[303] BOREXINO collaboration, *The Borexino detector at the Laboratori Nazionali del Gran Sasso*, *Nucl. Instrum. Meth. A* **600** (2009) 568 [0806.2400].

[304] DAYA BAY collaboration, *The Detector System of The Daya Bay Reactor Neutrino Experiment*, *Nucl. Instrum. Meth. A* **811** (2016) 133 [1508.03943].

[305] SNEWS collaboration, *SNEWS 2.0: a next-generation supernova early warning system for multi-messenger astronomy*, *New J. Phys.* **23** (2021) 031201 [2011.00035].

[306] LIGO SCIENTIFIC collaboration, *Advanced LIGO*, *Class. Quant. Grav.* **32** (2015) 074001 [1411.4547].

[307] KM3NET collaboration, *Letter of intent for KM3NeT 2.0*, *J. Phys. G* **43** (2016) 084001 [1601.07459].

[308] N. Astrophysics Science Division, Goddard Space Flight Cente, "General coordinates network." https://gcn.nasa.gov/.

[309] LIGO SCIENTIFIC, VIRGO collaboration, *Observation of Gravitational Waves from a Binary Black Hole Merger*, *Phys. Rev. Lett.* **116** (2016) 061102 [1602.03837].

[310] P. Mészáros, D.B. Fox, C. Hanna and K. Murase, *Multi-Messenger Astrophysics*, *Nature Rev. Phys.* **1** (2019) 585 [1906.10212].

[311] S. Chakraborty, P. Bhattacharjee and K. Kar, *Observing supernova neutrino light curve in future dark matter detectors*, *Phys. Rev. D* **89** (2014) 013011 [1309.4492].

[312] R.F. Lang, C. McCabe, S. Reichard, M. Selvi and I. Tamborra, *Supernova neutrino physics with xenon dark matter detectors: A timely perspective*, *Phys. Rev. D* **94** (2016) 103009 [1606.09243].

[313] D.Z. Freedman, *Coherent Neutrino Nucleus Scattering as a Probe of the Weak Neutral Current*, *Phys. Rev. D* **9** (1974) 1389.

[314] COHERENT collaboration, *Observation of Coherent Elastic Neutrino-Nucleus Scattering*, *Science* **357** (2017) 1123 [1708.01294].

[315] CONUS collaboration, *Constraints on elastic neutrino nucleus scattering in the fully coherent regime from the CONUS experiment*, *Phys. Rev. Lett.* **126** (2021) 041804 [2011.00210].

[316] P. Bhattacharjee, A. Bandyopadhyay, S. Chakraborty, S. Ghosh, K. Kar and S. Saha, *Inelastic charged-current interactions of supernova neutrinos in two-phase liquid xenon dark matter detectors*, *Phys. Rev. D* **106** (2022) 043029 [2012.13986].

[317] M. Hoferichter, J. Menéndez and A. Schwenk, *Coherent elastic neutrino-nucleus scattering: EFT analysis and nuclear responses*, *Phys. Rev. D* **102** (2020) 074018 [2007.08529].

[318] A. Gallo Rosso, *Supernova neutrino fluxes in HALO-1kT, Super-Kamiokande, and JUNO*, *JCAP* **06** (2021) 046 [2012.12579].

[319] ICECUBE collaboration, *IceCube Sensitivity for Low-Energy Neutrinos from Nearby Supernovae*, *Astron. Astrophys.* **535** (2011) A109 [1108.0171].

[320] J. Bland-Hawthorn and O. Gerhard, *The galaxy in context: structural, kinematic, and integrated properties*, *Annual Review of Astronomy and Astrophysics* **54** (2016)

529.

[321] P. Sorensen and K. Kamdin, *Two distinct components of the delayed single electron noise in liquid xenon emission detectors*, *JINST* **13** (2018) P02032 [1711.07025].

[322] A. Depoian Baxter, *FEW-ELECTRON SIGNALS AND THEIR IMPLICATIONS IN LIQUID XENON TIME PROJECTION CHAMBERS*, Ph.D. thesis, Purdue University, United States of America, 2022.

[323] G. Cowan, K. Cranmer, E. Gross and O. Vitells, *Asymptotic formulae for likelihood-based tests of new physics*, *Eur. Phys. J. C* **71** (2011) 1554 [1007.1727].

[324] P. Pirinen, J. Suhonen and E. Ydrefors, *Neutral-current neutrino-nucleus scattering off Xe isotopes*, *Adv. High Energy Phys.* **2018** (2018) 9163586 [1804.08995].

[325] J. Aalbers et al., *A next-generation liquid xenon observatory for dark matter and neutrino physics*, *J. Phys. G* **50** (2023) 013001 [2203.02309].

[326] N. Raj, V. Takhistov and S.J. Witte, *Presupernova neutrinos in large dark matter direct detection experiments*, *Phys. Rev. D* **101** (2020) 043008 [1905.09283].

[327] D. Layos Garcia and A. Molinario, "Supernova neutrinos in the Muon and Neutron Vetoes." XENON internal communication.

[328] Y. Suwa, K. Sumiyoshi, K. Nakazato, Y. Takahira, Y. Koshio, M. Mori et al., *Observing Supernova Neutrino Light Curves with Super-Kamiokande: Expected Event Number over 10 s*, *Astrophys. J.* **881** (2019) 139 [1904.09996].

[329] ICECUBE collaboration, *Constraining High-Energy Neutrino Emission from Supernovae with IceCube*, 2303.03316.

[330] XENON collaboration, *The XENON1T Data Acquisition System*, *JINST* **14** (2019) P07016 [1906.00819].

[331] B. Caccianiga et al., *GPS-based CERN-LNGS time link for Borexino*, *JINST* **7** (2012) P08028 [1207.0591].

[332] M. De Deo and et al., *Accurate GPS-based timestamp facility for Gran Sasso National Laboratory*, *JINST* **14** (2019) P04001 [1903.00233].

[333] P. Godwin and et al., *scimma/hop-client: v0.2 release of scimma/hop- client*, Sept., 2020. 10.5281/zenodo.4033483.

[334] SCiMMA, "Hopskotch." https://hop.scimma.org/, 2023.

[335] M. Schumann, L. Baudis, L. Bütikofer, A. Kish and M. Selvi, *Dark matter sensitivity of multi-ton liquid xenon detectors*, *JCAP* **10** (2015) 016 [1506.08309].

[336] DARWIN collaboration, *Solar neutrino detection sensitivity in DARWIN via electron scattering*, *Eur. Phys. J. C* **80** (2020) 1133 [2006.03114].

[337] K. Ozaki, S. Kazama, M. Yamashita, Y. Itow and S. Moriyama, *Characterization of New Silicon Photomultipliers with Low Dark Noise at Low Temperature*, *JINST* **16** (2021) P03014 [2007.13537].

[338] F. Kuger, J. Dierle, H. Fischer, M. Schumann and F. Toschi, *Prospects of charge signal analyses in liquid xenon TPCs with proportional scintillation in the liquid phase*, *JINST* **17** (2022) P03027 [2112.11844].

[339] J. Dierle and et al., *Reduction of ^{222}Rn-induced backgrounds in a hermetic dual-phase xenon time projection chamber*, *Eur. Phys. J. C* **83** (2023) 9 [2209.00362].

[340] D. Baur et al., *The XeBRA platform for liquid xenon time projection chamber development*, *JINST* **18** (2023) T02004 [2208.14815].

[341] L. Baudis and et al., *Design and construction of Xenoscope — a full-scale vertical demonstrator for the DARWIN observatory*, *JINST* **16** (2021) P08052 [2105.13829].

[342] ULVAC Technologies Inc. Iwatani. https://www.ulvac-cryo.com/products-en/refrigerator-en/cryocoolers/?lang=en.

[343] KNF Neuberger GmbH. https://knf.com/en/ch.

[344] Teledyne Hastings. https://www.teledyne-hi.com/.

[345] SAES Pure Gas. https://www.entegris.com/shop/en/USD/Products/Gas-Filtration-and-Purification/Gas-Purifiers/c/gaspurifiers.

[346] F. Girard, *Design, Construction and Operation of Xenoscope and Photosensor Characterisation for the DARWIN Observatory*, Ph.D. thesis, University of Zurich, Switzerland, 2023.

[347] L. Baudis et al., *Electron transport measurements in liquid xenon with Xenoscope, a large-scale DARWIN demonstrator*, 2303.13963.

[348] L. Virone et al., *Gravity assisted recovery of liquid xenon at large mass flow rates*,

Nucl. Instrum. Meth. A **893** (2018) 10.

[349] K. Thieme, *The Low-Energy and Large-Scale Frontier of Dual-Phase Xenon Time Projection Chambers for Dark Matter Search*, Ph.D. thesis, University of Zurich, Switzerland, 2022.

[350] Raspberry Pi. `https://www.raspberrypi.org/`.

[351] Prometheus. `https://prometheus.io/`.

[352] InfluxData Inc. `https://www.influxdata.com/`, 2023.

[353] Grafana. `https://grafana.com/`.

[354] Kubernetes. `https://kubernetes.io/`.

[355] H. Photonics, "L7685 xenon lamp." `https://www.hamamatsu.com/content/dam/hamamatsu-photonics/sites/documents/99_SALES_LIBRARY/etd/L7684_L6604_TLSX1029E.pdf`.

[356] Y. Biondi, *Sensitivity of DARWIN to Rare Events and the Purity Monitor for Xenoscope*, Ph.D. thesis, University of Zurich, Switzerland, 2022.

[357] CeramaSeal catalogue. `https://www.ceramtec.com/files/us_ceramaseal_feedthroughs.pdf`.

[358] S. Hochrein, *Background measurement and mc simulations for the darwin demonstrator*, Master's thesis, University of Zurich, Switzerland, 2021.

[359] S. Joshi, *Cosmic muons to calibrate xenoscope*, Master's thesis, University of Zurich, Switzerland, 2021.

[360] N. Arora, *Review of basic semiconductor and pn junction theory*, in *MOSFET Models for VLSI Circuit Simulation: Theory and Practice*, (Vienna), pp. 15–68, Springer Vienna (1993), DOI.

[361] *Semiconductor physics and devices : basic principles*, Irwin, Chicago [etc, second ed. ed. (1997 - 1997).

[362] D. Renker and E. Lorenz, *Advances in solid state photon detectors*, *JINST* **4** (2009) P04004.

[363] A. Ghassemi and K. Kobayashi, *A technical guide to silicon photomultipliers (mppc)*, Tech. Rep. Hamamatsu Photonics K. K. (2018).

[364] S. Gundacker and A. Heering, *The silicon-photomultiplier: fundamentals and applications of a modern solid-state photon detector*, *Phys. Med. Biol.* **65** (2020) 17TR01.

[365] K. McAfee and G. Pearson, *The electrical properties of silicon pn junctions grown from the melt*, in *Physical Review*, vol. 87, pp. 190–190, AMERICAN PHYSICAL SOC ONE PHYSICS ELLIPSE, COLLEGE PK, MD 20740-3844 USA, 1952.

[366] G. Pearson and P. Foy, *Silicon pn junction diodes prepared by the alloying process*, in *PHYSICAL REVIEW*, vol. 87, pp. 190–190, AMERICAN PHYSICAL SOC ONE PHYSICS ELLIPSE, COLLEGE PK, MD 20740-3844 USA, 1952.

[367] G.K. Teal and E. Buehler, *Growth of silicon single crystals and of single crystal silicon pn junctions*, in *Physical Review*, vol. 87, pp. 190–190, AMERICAN PHYSICAL SOC ONE PHYSICS ELLIPSE, COLLEGE PK, MD 20740-3844 USA, 1952.

[368] M. Teshima, B. Dolgoshein, R. Mirzoyan, J. Nincovic and J. Popova, *SiPM development for Astroparticle Physics applications*, in *30th International Cosmic Ray Conference*, vol. 5, pp. 985–988, 7, 2007.

[369] A. Razeto and N. Rossi, *Challenges for dark matter direct search with SiPMs*, 2209.09224.

[370] M.G. Boulay et al., *SiPM cross-talk in liquid argon detectors*, 2201.01632.

[371] MEG II collaboration, *Liquid xenon calorimeter for MEG II experiment with VUV-sensitive MPPCs*, *Nucl. Instrum. Meth. A* **845** (2017) 528.

[372] MEG II collaboration, *The design of the MEG II experiment*, *Eur. Phys. J. C* **78** (2018) 380 [1801.04688].

[373] F. Arneodo and et al., *Cryogenic readout for multiple VUV4 Multi-Pixel Photon Counters in liquid xenon*, *Nucl. Instrum. Meth. A* **893** (2018) 117 [1707.08004].

[374] Accu-Glass Products. https://www.accuglassproducts.com/.

[375] Koax24. https://www.koax24.de/.

[376] Telegärtner. https://www.telegaertner.com/.

[377] VACOM. https://www.vacom.net/en/home.html.

[378] G. Kessler, *Inelastic WIMP-Nucleus Interactions in XENON100 and Cables and*

Connectors for XENON1T, Ph.D. thesis, University of Zurich, Switzerland, 2016.

[379] A. Brown, *Search for Elastic and Inelastic Dark Matter Interactions in XENON1T and Light Detection for XENONnT*, Ph.D. thesis, University of Zurich, Switzerland, 2020.

[380] Cryo-Con, "Model 32 Cryogenic Temperature Controller." `https://ww.cryocon.com/M32ProdFolder.php`.

[381] CAEN, "V3718 VME to USB 2.0/Optical Link Bridge." `https://www.caen.it/products/v2718/`.

[382] F. Girard, K. Thieme and J. Wulf, "DAQ." `https://github.com/Physik-Institut-UZH/DAQ`, 2020.

[383] R. Peres, "Python-based SiPM analysis package." `https://github.com/ricmperes/PyLArS/`, 2022 (accessed November 8, 2022).

[384] S.K. Lam, A. Pitrou and S. Seibert, *Numba: a LLVM-based Python JIT compiler*, 2015, DOI.

[385] G. Gallina et al., *Characterization of the Hamamatsu VUV4 MPPCs for nEXO*, *Nucl. Instrum. Meth. A* **940** (2019) 371 [1903.03663].

[386] L. Baudis, M. Galloway, A. Kish, C. Marentini and J. Wulf, *Characterisation of Silicon Photomultipliers for Liquid Xenon Detectors*, *JINST* **13** (2018) P10022 [1808.06827].

[387] T. Doke, *Recent developments of liquid xenon detectors*, *Nuclear Instruments and Methods in Physics Research* **196** (1982) 87.

[388] E. Aprile and T. Doke, *Liquid xenon detectors for particle physics and astrophysics*, *Rev. Mod. Phys.* **82** (2010) 2053.

[389] R. Peres and Y. Biondi, "Toy-MC Diffusion Studies for Xenoscope." `https://github.com/ricmperes/XenoDiffusionScope/`.

[390] A. Buckley, "hepthesis v1.5.2." `https://www.ctan.org/pkg/hepthesis`, 2017.

[391] J.D. Hunter, *Matplotlib: A 2d graphics environment*, *Computing in Science & Engineering* **9** (2007) 90.

Acknowledgements

A PhD dissertation is, in its essence, a book about a journey. The author, or student, overcomes a myriad of challenges to achieve their single goal of taking their research from the already known to beyond the uncertain and unknown. It's an arduous task that would not be possible to complete without the help of many, to whom I, the author, would like to extend my heartfelt gratitude.

First and foremost, my gratitude goes to Prof. Laura Baudis. She accepted me in her group and propelled me to overcome the many challenges of a PhD. Her passion for Science and Physics stands as one of my greatest inspirations and her trust in moments of doubt was essential to the completion of this thesis. I would like like to thank Dr. Michelle Galloway for supporting me, even before the start of my PhD in Zurich. We met during a XENON shift at LNGS and since then she has been a core part of my scientific development. I would also like to express my gratitude to Prof. Benjamin Kilminster for the discussions and support as part of the doctoral committee.

I would like to thank all the members of the Baudis group with whom I was lucky to work side by side: Adam, Ale, Alex, Chiara, Christian, Diego, Fred, Gabriela, Giovanni, Jose, Kevin, Mariana, Neil, Paloma, Pin-Jung, Yanina, and Yannick. Our regular physics discussions, coffee breaks, and bar evenings across all the ups and downs of research made it ever more compelling to come to work and regain focus. I am very fortunate to have had the chance to share my PhD journey with Giovanni. Your friendship, fearless approach to hard problems and your complaining skills make you the best PhD partner I could have hoped for. To Alex, Paloma, and Jose, thank you for making our office "The Cool Office". A special thank you goes also to Diego, Jose, Christian and Michelle, who took time to review parts of this thesis.

Doing a PhD as part of the XENON collaboration has been a privilege. I extend my thanks to all of those with whom I crossed paths – whether inside a cleanroom, during a shift, over Slack threads, or at collaboration dinners. The Science that we do together would not be possible without the overwhelming sense of communal work.

Although coming to Zurich was a leap to the foreign and unknown, I found in this city kind and amazing people that over the course of the last few years have become a family away from home. I owe this accomplishment also to them. To Raquel, Raúl, Catarina, André, António, Cata, and Ana Rita, thank you for all the dinners, hikes, game nights, and friendship. Andrea, Ahmed, Aren, Anil, Pragnya, and Marta, I feel very fortunate to have met you and learnt so many different things from you. In particular throughout the last year and the writing of this thesis, I would like to thank Daniela for her permanent availability for cake and complaining. We were there for each other in a period of immense difficulty and stress and now that we are both out of it, I can not be more grateful. However, in making Zurich an enjoyable place, there is no bigger responsible than Samuel. There is no doubt that there is a before and after meeting you in Zurich (they do say the third time is the charm!). I can not express in words how fortunate I feel to be your friend and how thankful I am for your support. Your kindness, care, and sense of adventure are unparalleled and a source of inspiration.

To all my friends in Portugal, I'm very grateful for your patience and availability whenever a visitor from the Alps arrived. Thank you Filipa, Bernardo, Rita, Fred, Daniel, and Daniel for keeping me up to date on Tuna gossip and the lovely reunions. Thank you Maria João and João for your kind hearts and for calling me back to reality when needed. Back in Tomar, thank you Pedro, Soraia, and Joel for your everlasting friendship. To Henrique, five years ago I wrote: "the friend with whom too much time is invested to consider going back". I am extremely proud of the investment made and would not trade it for anything. Thank you for 25 years of friendship, for all the walks around town to catch up and the feeling that your number is always available no matter how much time passes between calls.

Lastly, I want to thank Leonor and my family. Thank you for supporting my move abroad, despite how hard distance can be on the heart. Thank you Leonor for your care, your patience, your love, and your courage on supporting this adventure from day one. You are a wonderful and loving person and I could not be more proud and happy to be sharing my life with you. Por fim, aos meus pais e avós, quero agradecer todo o apoio incondicional que me deram. A sua força interior e dedicação ao que lhes é querido é uma enorme inspiração para mim. Apesar da dor latente em cada acenar da varanda ou partida no aeroporto, acompanharam-me incansavelmente pelos melhores e piores momentos desta aventura. Este documento é, por isso, a eles dedicado.

Colophon

This thesis was made in LaTeX using a modified version of the "hepthesis" class [390]. All the diagrams and figures, apart from cited work, use the font DejaVu Serif Font Family. All the plots were made using the open-source `matplotlib` package [391]. The colours of the points and lines use the pallet, in hex values: `16207B`, `CE050F`, `C1B22D`, `9C20A7`, `21BAAB`, `1F7915`, `707084`. The colourmap used is `coolwarm` from the matplotlib colourmap library. Most of the figures presented can be found at and reproduced from `https://github.com/ricmperes/thesis_plots/`, with the exception of the ones with XENONnT data under embargo.